A Thesis entitled

A STUDY OF THE PERFORMANCE OF A CASCADE IMAGE INTENSIFIER

by

François Charles DELORI, E.E.

Submitted for the degree of PhD
in the University of London

Applied Physics Section
Physics Department
Imperial College of Science
and Technology
London S.W.7.

August 1971.

ABSTRACT

The basic requirements for the detection of faint optical images are discussed, and the superiority of vacuum devices employing a photoemissive surface as primary image detector is indicated. Various photoelectric image detectors are reviewed and compared, more emphasis being placed upon image intensifier photography and in particular upon cascade intensifiers employing phosphor–photocathode multiplying dynodes. The requirements and properties of photocathodes and phosphor screens are discussed in view of their use in imaging devices.

A brief description of the Imperial College three stage cascace intensifier is followed by an enumeration of the various techniques employed in its manufacturing and processing. The construction and requirements of the ancillary equipment are discussed and some measurements of their characteristics are reported.

The theoretical and practical performance of the cascade intensifier are then investigated. Measurements of light gain, photometric linearity, statistics of intensification, time resolution, modulation transfer function, geometrical distortions and spurious instrument background are reported. The influence of various parameters upon these characteristics are analysed and discussed. A detailed study is made of the signal induced background occuring in this intensifier and its origin and possible cures are analysed

A medical application of the cascade intensifier is described and other utilizations of this instrument are briefly reported.

Future possibilities for improvement of construction, performance and versatility of the cascade intensifier are proposed.

CONTENTS

CHAPTER 1.

IMAGE DETECTION

1.1. PERFORMANCE OF IMAGE DETECTORS

The information contained in an optical image can be expressed as a spatial and temporal distribution of photons. To achieve ideal image detection it is necessary to register each photon in its spatial and temporal element by the production of an identical and independent event. The accuracy of such a detector would be limited only by the statistical fluctuation in the arrival of individual photons. Since photons occur independently and collectively at random, the probability of detecting one photon in a spatial element during a specified time will obey a Poisson distribution. (Fry, 1929). The fluctuations in the detection of an average of $\overline{N}$ photons can be expressed by the mean square deviation $\overline{\Delta^2 N}$, which, in the case of a Poisson distribution equals $\overline{N}$. It is convenient to adopt the concept of signal power to noise power ratio used in electrical engineering for the assessment of image detectors. For an ideal image detector this ratio will be given by

$$\left(\frac{S}{N}\right)^2 = \frac{\overline{N}^2}{\overline{\Delta^2 N}} = \overline{N} \qquad (1.1)$$

independently of the wavelength of the incident photon.

1.1.1 The Signal to Noise Ratio of a Real Detector

The light intensity distribution of any two dimentional image detail can be broken down by means of Fourier analysis into a sum of sine wave function terms of particular spatial frequency and amplitude. The light intensity distribution in a picture element of an image incident on a detector is thus fully characterised by its signal power spectrum SP(w), which may be defined as the deviation of the energy per unit area from its mean value as a function of the spatial frequency. The modulation transfer function MTF (w) of a detector is the ratio of modulation* in the output image to that in the incident image. The output signal power can thus be expressed by MTF (w). SP (w) at any spatial frequency. The noise power spectrum NP (w) in an output image is the variation with spatial frequency of the mean square deviation from the mean output signal power when the detector is uniformly illuminated.

The signal to noise ratio of any detector can be factorised by:

$$\left(\frac{S}{N}\right)^2_w = \frac{MTF^2(w) \; . \; SP(w)}{NP(w)} \qquad (1.2)$$

The signal power SP(w) is a property of whatever is imaged on a detector and is generally assumed to be independent of the spatial frequency w when image detectors are compared. The modulation transfer function generally decreases with increasing spatial frequency and since it enters eqn. 1.2. as a squared term, MTF (w) will dominate the expression of signal to noise ratio in most practical cases. This means that as the spatial frequency increases the $(S/N)^2$ will eventually tend to zero. The value of w for which $(S/N)^2$ becomes $(2 \text{ to } 5\%)^2$ of the $(S/N)^2$ at $w = o$ is called the limiting spatial frequency.

1.1.2 The Equivalent Quantum Efficiency. (EQE)

The concept of EQE introduced by Rose(1948.A) and further developed by Felgett(1956) and Jones(1955) is ideally suited to the comparison of the performance

---

*Modulation: If S_M and S_m are respectively the maximum and minimum amplitude of the sine wave distribution, modulation is given by $S_M - S_m \;/\; S_M + S_m$.

of all types of detectors. The EQE compares the $(S/N)^2$ obtained with an actual detector with that attainable by an ideal detector working at the same exposure level.

$$\mathrm{EQE}\,(w) = \frac{(S/N)^2_w \text{ actual}}{(S/N)^2_w \text{ ideal}} \qquad (1.3)$$

The $(S/N)^2$ of the ideal detector is constant for all spatial frequencies and is equal to the average number of incident photons, if the signal power in the incident image is constant. Therefore the EQE may be regarded as the reciprocal of the factor by which it is necessary to increase an input photon flux in order to produce a $(S/N)^2$ in the output of the real detector equal to that which would be produced in the output of the ideal detector. Substitution of equation 1.2 into 1.3 gives:

$$\mathrm{EQE}\,(w) = \mathrm{EQE}(o)\,.\,\frac{\mathrm{MTF}^2_\tau\,(w)}{\mathrm{NP}_\tau\,(w)} \qquad (1.4)$$

where EQE(o) is the equivalent quantum efficiency for $w = 0$ (macroscopic EQE) and $\mathrm{MTF}_\tau\,(w)$ and $\mathrm{NP}_\tau\,(w)$ are normalised values such that $\mathrm{MTF}_\tau(0) = \mathrm{NP}_\tau\,(o) = 1$.

A unique value of EQE(w) cannot be assigned to a detector since it will depend upon the wavelength distribution and the intensity of incident light and upon the operating conditions of the detector. If a single value is quoted it will refer to the maximum attainable at low spatial frequency.

1.1.3 Minimum Detectable Contrast.

This concept is used when a weak signal is to be detected against background. If $SP_S\,(w)$ is the signal power of that small object and $SP_b\,(w)$ that of the background at a particular spatial frequency w, then that signal will be detected in the final image if :

$$\mathrm{MTF}^2(w)\,.\left[SP_s\,(w) - SP_b\,(w)\right] = K^2\left[NP_s(w) + NP_b(w)\right]$$

where K is a factor of certainty (≈ 5). The noise power from the signal is negligible compared to that of the background.

If contrast is defined as

$$C^2(w) = \frac{SP_s(w) - SP_b(w)}{SP_b(w)} \qquad (1.5)$$

then the minimum detectable contrast is given by

$$C^2_{min}(w) = K^2 . \frac{NP_b(w)}{MTF^2(w)\, SP_b(w)} = K^2 . \left(\frac{N}{S}\right)^2_w \qquad (1.6)$$

C_{min} will thus generally increase as the spatial frequency is increased. It should be noted that the EQE(w) of a detector is often defined by :

$$EQE(w) = \frac{C^2_{min} \quad . \ \text{ideal}}{C^2_{min}(w) \quad . \ \text{actual}} \qquad (1.7)$$

since the same coefficient of certainty K must be used for both detectors.

A real detector cannot store an infinite amount of information and there will be a maximum signal power in the final image that a detector can store. This will, according to eqn. 1.6, set a limit to the minimum detectable contrast. Conversely, the higher the storage capacity of a detector, the lower the ultimate detectable contrast will be.

1.2 IMAGE DETECTORS FOR SCIENTIFIC APPLICATIONS.

The most universal image detector is the human eye combined with the brain. Although quite efficient as a detector of images between 3500 and 7000 Å ; maximum EQE of 5.0 and 0.9% have been quoted by Rose (1948.B) and Jones (1959) respectively; the eye is limited as an image detector for scientific purposes mainly because of its inability to integrate and permanently record information.

1.2.1 The Photographic Emulsion.

The photographic plate has long been used as an image detector for scientific observation and has been developed to satisfy a wide range of spectral sensitivities, speeds and spatial resolutions. The information is recorded in the developed emulsion as concentrations of silver grains and can be analysed visually or by densitometry. In the latter case, an expression for the EQE at low spatial frequencies has been derived by Felgett (1956), Shaw (1963) and Jones 1958):

$$\mathrm{EQE}\left(o\right) = \frac{\varepsilon}{U} \frac{(\log_{10} e)^2}{\mathrm{NP}(o)} \gamma_U^2 \qquad (1.8)$$

where U is the exposure (in erg/cm^2), ε the photon energy (in erg), γ_U the slope of the characteristic curve (Density D $\log_{10}$ units versus $\log U$) for the exposure U , and NP (o) the low frequency value of the noise power spectrum at the density corresponding to the exposure U . Measurements made by Felgett (1958), Jones (1958.) and Shaw (1962 and 1965) on commercially available emulsions show a maximum in EQE (o) of 0.5 to 0.9% occurring at rather low densities of 0.10 to 0.25 $\log_{10}$ units. (tab. 1.1.). At densities corresponding to the linear region of the density - log. exposure characteristic (about 0.6 $\log_{10}$ units) the EQE (o) falls to 0.05 to 0.20%. This would suggest that in order to derive maximum information it is better to make a series of exposures corresponding to the maximum EQE than to use the full available storage capacity of the plate. However, the summation of data recorded in the different exposure would be an arduous procedure.

A further disadvantage of the photographic plate is known as the reciprocity law failure. To produce a given density with very low (or very high) light intensity a greater exposure will be needed than that required to obtain this density at intermediate light levels. As a result, the EQE at extreme light levels will be further reduced. The detection of very faint objects against background, requiring long

Manufacturer Type	Kodak RoyalX	Kodak Tri X	Kodak IIa 0	Ilford HPS	Ilford HP3	Units
Max. EQE	0.90 [1]	0.58 [1]	0.62 [9]	0.20 [2]	1.05 [2]	%
at density	0.21	0.14	0.25	0.45	0.20	$\log_{10}$
EQE at 0.6 $\log_{10}$	0.25	0.15	0.25	0.15	0.20	%
EQE at 1.0 $\log_{10}$	0.01	0.02	0.10 [6]			%
Fog Level	0.105 [1]	0.050 [1]	0.060 [4]	0.150 [7]	0.200 [7]	$\log_{10}$
Grains/cm^2 X10^{-7}	1.20 [8]	0.56 [8]	0.91 [8]			
Granularity (10μ)						
$\overline{\Delta^2 D}$ at Fog	0.104	0.064	0.070			
$\overline{\Delta^2 D}$ at 0.6 $\log_{10}$	0.185	0.110	0.120	0.200	0.750	
Relative MTF	[3]	[3] [4]	[6] [5]	[7]	[7]	
15 c/mm	75	96-95	70-92	75	68	modu-lation %
30 c/mm	49	79-72	45-60	45	49	
45 c/mm	37	62-55	32-45	33	22	
60 c/mm	29	47-39	22-35	27	17	
75 c/mm		34-24	14	20	12	
90 c/mm		20-10	7	17	8	

<u>References:</u> 1.Jones 1958 A. 2.Shaw 1962. 3.Lamberts et al.1958 4.Kodak Data 1962. 5.Kahan et al. 1969. 6.Beckman 1966. 7.Ilford Data 1962. 8.Reynolds 1966 A. 9.Wilcock 1964.

TAB. 1.1 PHOTOGRAPHIC PLATE DATA

exposure time, will thus be limited by the storage capacity and by the lowering of the EQE of the emulsion. A compilation of data for several commercially available photographic plates is given in tab. 1.1.

1.2.2 The Photoemissive Surface.

The photoemissive surface used as a primary image detector has several outstanding qualities as compared with other detectors. The quantum efficiency QE (number of photoelectrons per incident photon) is high, ranging from 10 to 40% for wavelengths of 4000 to 5000 Å (§ 3.1.2) and photocathodes can be prepared to cover partially the wavelength range of 1000 to 12000 Å. The photocurrent, which is generated practically instantaneously upon incidence of light, is proportional to the illumination intensity over a wide range of intensities. Furthermore, the extreme thinness of the photoemissive surface prevents any appreciable lateral diffusion of light, such that very high spatial resolutions are attainable in the photoelectron image.

A disadvantage of the photoemissive surface is that of spurious electrons, liberated from the surface as a result of thermionic emission. Rates in the order of 1 to 500 electrons/cm^2/sec are encountered for most photocathodes or can be achieved by adequate cooling (§3.1.2). This effect will be neglected for the purpose of simplicity in the following considerations.

The signal to noise ratio in the "photoelectron image" of a photocathode can be derived from general equations for the fluctuations resulting from an interaction involving stochastic processes. If in an interaction, a primary particle gives rise to λ secondaries (where λ is a stochastic variate), n incident particles making independent interactions will give rise to μ secondaries such as (Mandel 1959)

$$\begin{aligned} \overline{\mu} &= \overline{n}\;\overline{\lambda} \\ \overline{\Delta^2 \mu} &= \overline{\lambda}^2\;\overline{\Delta^2 n} + \overline{n}\;\overline{\Delta^2 \lambda} \end{aligned} \qquad (1.9)$$

where a bar denotes the average and Δ the mean deviation.

The photoelectric effect may be described as a "go-not-go" process, such that the probability of emission of one photoelectron will follow a binomial distribution, thus $\overline{\lambda} = QE$ and $\overline{\Delta^2 \lambda} = QE\,(1 - QE)$. The number of photoelectrons Ne resulting from the incidence of N_i photons is thus given by: (eqn. 1.9 and 1.1)

$$\left.\begin{aligned} \overline{Ne} &= \overline{N_i}\ .\ QE \\ \overline{\Delta^2 N_e} &= QE^2 .\ \overline{\Delta^2 N_i} + \overline{QE\,(1 - QE)}\,\overline{N_i} = \overline{N_i}\ .\ QE \end{aligned}\right] \quad (1.10)$$

and the signal to noise ratio by:

$$\left(\frac{S}{N}\right)^2_{w=o} = \frac{(\overline{N_i}\ QE)^2}{\overline{N_i}\ QE} = \overline{N_i}\ .\ QE \qquad (1.11)$$

Therefore, the $(S/N)^2$ of the incident photon flux is reduced by QE but the statistics in the photoelectron image still obey a Poisson distribution. The latter fact has been confirmed experimentally by Sauter (1949).

1.2.3 Image Detectors using the Photoemissive Effect.

In order to take full advantage of the high performance of a photocathode three conditions must be satisfied:

-Each photoelectron should be recorded in the final image.

-All these records should have equal weight.

-No additional spurious noise should be introduced.

In that case the $(S/N)^2$ in the final image will be that of the photoelectron image and the equivalent quantum efficiency will be:

$$\text{EQE}\ (\ o\ )\ \text{system} = QE \qquad (1.12)$$

Of the three conditions mentioned above, the last is the most closely achieved in practice and can be assumed so for the purpose of the following calculation. However, the other two conditions are never satisfied. Only a fraction RE (the recording efficiency) of the photoelectrons will lead to an output event, such that the number N_{er} of recordable photoelectrons is given by: (eqn. 1.9 and 1.10)

$$\left.\begin{array}{l} \overline{N_{ez}} = \overline{N_i} \cdot QE \cdot RE \\ \overline{\Delta^2 N_{ez}} = RE^2 \cdot QE \cdot \overline{N_i} + \overline{N_i} \cdot QE\ \overline{\Delta^2 RE} = RE.QE.\overline{N_i} \end{array}\right] \quad (1.13)$$

where $\overline{\Delta^2 RE} = RE\,(1 - RE)$ since a loss process can be described as a"go-not-go" process. Furthermore, these photoelectrons will be recorded with unequal weight as a result of fluctuations in the recording process. If $\overline{G}$ is the average weight of the records of photoelectrons and $\overline{\Delta^2 G}$ the mean square deviation from $\overline{G}$, then the number $\overline{P}$ of recorded events is given by: (eqn. 1.9)

$$\left.\begin{array}{l} \overline{P} = \overline{G}\ \overline{N_{er}} \\ \overline{\Delta^2 P} = \overline{G}^2\ \overline{\Delta^2 N_{er}} + \overline{N_e}\ \overline{\Delta^2 G} \end{array}\right] \quad (1.14)$$

The $(S/N)^2$ in the final recorded image can be found by substitution of eqn. 1.13 by eqn. 1.14, and is given by:

$$\left(\frac{S}{N}\right)^2 = \frac{\overline{P}^2}{\overline{\Delta^2 P}} = \frac{\overline{N_i} \cdot QE \cdot RE}{1 + \overline{\Delta^2 G}/\overline{G}^2} \quad (1.15)$$

The general expression of the EQE (o) of photoelectronic devices is then:

$$EQE = \frac{QE \cdot RE}{1 + \overline{\Delta^2 G}/\overline{G}^2} \quad (1.16)$$

where QE is the quantum efficiency of the primary photocathode, RE is the recording efficiency of the system and $\frac{\overline{\Delta^2 G}}{\overline{G}^2}$ is the relative fluctuation of the recording system.

Both RE and $\overline{\Delta^2 G} / \overline{G}^2$ will depend upon the method used for recording the photoelectron image. It will be seen in Chapter 2. that ratios EQE / QE as high as 0.85 can be achieved in some practical devices, corresponding to equivalent quantum efficiencies at low spatial frequencies of 8 to 35%. Modulation transfer function comparable to the most efficient photographic plates can be achieved in practical devices using a photoemissive surface as primary detector.

The minimum contrast detectable with a photoelectric image detector can be calculated from eqn. 1.7. If N is the number of photons from the image background which land on the detector per cm^2 and per sec., and if A is the area of the faint object and t the integration time, then the minimum contrast detectable by an ideal detector is $K/\sqrt{N.A.t}$. K is the factor of certainty which is generally taken as 5 for small objects. Therefore, using eqn. 1.16, the minimum contrast detectable with a photoelectric detector becomes:

$$C_{min} = \frac{C_{min.id}}{\sqrt{EQE}} = \frac{\sqrt{1 + \frac{\overline{\Delta^2 G}}{G^2}}}{\sqrt{N.A.t.\ QE\ .RE}} \qquad (1.17)$$

Obviously the EQE must be as high as possible. The ultimate threshold will be approached when the integration time t approaches its limiting value due to the finite storage capacity of the detector.

1.2.4 <u>Photoconductive Image Detectors.</u>

The quantum efficiency of a photoconductive layer is basically much higher than that of photoemissive layers, and can approach unity at long wavelengths and low temperatures. (Gaucher, 1950, Spencer, 1958). The incorporation of efficient photoconductive layers in practical image detectors has been slow because of the difficulties encountered in controlling their other properties. The spread of light and carrier migration in the layer limits the attainable resolution while the inherent lag limits the rate at which information can be treated. Furthermore, relatively high illuminations are required to produce acceptable signal to noise ratios. Photoconductive layers are used as primary detector in television camera devices, i.e. the Vidicon (Weimer et.al. 1950) and the Plumbicon (de Haan et.al. 1964), in which detection and storage of information are combined in the layer. Jones (1959) calculated that the maximum EQE of the Vidicon is about 0. 1% at an exposure level about 100 times higher than that required for optimum use of a photographic plate. Photoconductive layers are also used in conjunction with electro-luminescent panels in the so-called solid-state image detectors (Kazan, 1957, Szepesi, et.al. 1969). However, these devices have low resolution, long lag, and cannot be considered for low light level application because of their high input threshold.

1.2.5 Conclusions.

The superiority of detectors employing a photoemissive surface as primary detector results from the high value of quantum efficiency, the linearity of the photoemissive effect and the absence of any lag and loss in spatial resolution in the generation of the photoelectron image. Methods of recording the latter image will be discussed in the next chapter.

CHAPTER 2.

PHOTOELECTRIC IMAGE DETECTORS

The various means of recording a "photoelectron image" will be discussed in this chapter. Three major methods are used:

- The photoelectron image is recorded on an electron sensitive emulsion: Electronography.
- The photoelectron image is recorded on a light sensitive emulsion after intensification and reconversion to a photon image: Image Intensifier Photography.
- The photoelectron image is transformed into a charge image which, in turn, is transformed into a coded electric signal by an electron beam scanning technique.

2.1 ELECTRONOGRAPHIC IMAGE DETECTORS.

Electron sensitive emulsions are the most logical means of recording photoelectron images. These emulsions* have several marked advantages over photographic materials:

- the proportionality of recorded density with electron exposure up to high optical densities (4 – 5 $\log_{10}$ units)
- the strict observance of the reciprocity law
- very fine grains and low fog level
- a high storage capacity.

The photoelectron image is accelerated and focused on the emulsion. Each photoelectron (30KV) renders several grains developable (4 – 7), thus producing a record with high certainty because of low fog level.

---

* most commonly used are ILFORD L4, G5 and XM.

The major problem in using this technique is the protection of the photocathode from detrimental effects due to gases released under vacuum by the emulsion. Three important instruments based on these principles will be discussed below. Other devices have been developed (Kiepenheur, 1934, Hiltner et.al., 1960 and 1962) and are under investigation (Combes et.al., 1969, Deckers et.al. 1969 and McMullan, 1970).

2.1.1 Lallemand's Camera.

(Lallemand, 1936, 1960, 1962 and 1966. Duchesne, 1962. Bied-Charrenton et.al., 1969). The development of electronographic image recording technique is due mainly to the pioneering work done by Lallemand since 1936. In this device the photoelectrons from a 18mm diameter S9 or S11 photocathode are accelerated to 25KeV energy and focused electrostatically with a demagnification of 0.8 on the electron sensitive emulsion. Both cathode and emulsion are refrigerated (-196°C) to minimize the gas poisoning of the cathode. Residual gas is removed with a getter pump and, more recently, with titanium ion pumps. In spite of these precautions, the useful life of the photocathode is usually not greater than two days. The system must be exposed to atmospheric pressure in order to remove the plates after each series of exposures, and a new preformed photocathode must be introduced into the vacuum for each observational run (12 exposures).

2.1.2 Kron's or US-Navy Electron Camera.

Kron, G.et.al. 1962, 1966 and 1969) This device is essentially the same as Lallemand's camera, except that a special "coin" valve can be closed to protect the photocathode (S9 or S11 type; 40mm diameter) during recovery and insertion of plates. (6 exposures per plate). Electrostatic focusing with 0.4 magnification is employed at 30 KV. An ion pump which runs continuously maintains the high vacuum against small leaks around the valve. Liquid nitrogen cooling of the plates reduces the release of gases. Kron reports that the photocathode shows little deterioration during time spans as long as 14 months.

2.1.3 McGee's Electronic Camera : The Spectracon.

(McGee, et.al. 1962.A, 1966.A and 1969.A) The Spectracon is a sealed-off vacuum system requiring no continuous pumping as in the previously mentioned systems. Photoelectrons are accelerated with sufficient energy to penetrate a 3 to 4 microns thick vacuum-tight mica membrane. The transmitted electron image is then recorded on an emulsion pressed against this membrane with a special mandrel. Thus the operation of this device is greatly facilitated in comparison with other cameras described. Moreover, its electromagnetic focusing produces an image of high resolution and low distortion, while the good vacuum conditions tolerate the use of any preformed photoemissive layer (S11, S20 and S1 cathodes). The fragility of the mica window and the limited size of the photocathode (30 x 10mm) are the two main disadvantages of this camera.

2.1.4 Performance of the Electronographic Cameras.

Inherent high efficiency, linearity, highresolution and storage capacity are the main characteristics of electronographic devices. If each recorded photoelectron produces an average of $\overline{G}$ developable grains and if $\overline{\Delta^2 G} = k\overline{G}$, where k is a constant ($\precsim 1$) indicating the deviation from a Poisson distribution, then the EQE (o) for grain counting analysis of the electronographic emulsion can be calculated from: (eqn. $1.\overset{16}{20}$).

$$\text{EQE (o)} = \frac{\text{QE . RE}}{1 + \frac{k}{\overline{G}}} \qquad (2.1)$$

In the case of devices where the photoelectrons have a direct impact on the emulsion, the relative fluctuation in the number of developable grains is about $k/\overline{G} = 0.3/6 = 0.05$ (Pniewski, 1951) for 25 KeV electrons and the recording efficiency about

0.90 (Jeffers, 1968) such that EQE (o)/QE = 0.86. The relative fluctuation in a Spectracon record is increased by the spread of energies of the electrons transmitted by the mica window and the recording efficiency is decreased by transmission losses. Measurements made by Khogali (1964) indicate that $k/\overline{G}$ = 0.6/4.5 = 0.13 and RE = 0.75 for photoelectrons with 40 KeV energy, such that EQE (o) / QE = 0.66. However, Jeffers (1968) predicted that the difference in EQE of these two types of devices would be less if the information is analysed by densitometry. Indeed, the exposure required to reach a given density is smaller in the case of the Spectracon because the sensitivity of the emulsion is not lowered by cooling and because the most probable energy of the electrons transmitted by the mica is higher (33 KeV) than that currently used in the Lallemand (25 KeV) and Kron (30 KeV) cameras.

The limiting resolution of electronographic cameras is high (70 - 120 lp/mm) and determined by the type of emulsion used. Speed gains over direct photography using Kodak IIa - o of 20 to 30 have been reported using electronographic cameras with Ilford G5 emulsion. (Kron, G. et.al., 1969; Kahan, et.al., 1969).

2.2 IMAGE INTENSIFIER PHOTOGRAPHY.

In this family of devices the photoelectron image is converted into a luminescent image after acceleration and eventual multiplication of the electrons. The phosphor image can be visually observed or recorded on a photographic emulsion by means of an optical coupling system.

2.2.1 Condition for Photoelectron Recording.

It is important to determine the conditions under which single photoelectrons are recorded on a photographic emulsion. It can be seen from tab. 1.1 that Kodak Tri-X and Kodak IIa - O are best suited to this purpose because they combine good quantum efficiency with low fog level and good modulation transfer function.

Assuming that one photoelectron produces N photons at the emulsion inside a disk of diameter d (disk of confusion of the complete system : intensifier, coupling optics and emulsion). This event will be recorded if it produces a density D_R given by:

$$D_R = D\,\text{fog} + k\,\sigma \tag{2.2}$$

where Dfog is the fog density, σ the standard deviation in the fog density and k a factor of certainty. There is good evidence that σ is proportional to d^{-1} for areas much greater than the average grain size (Jones, 1958.). If the density - log exposure relation and the standard deviation σ for a given area are known for a given emulsion,it is then possible to calculate the required number of photons N with

$$N = \frac{\pi .\, d^2 .\, U}{4 .\, \mathcal{E}} \tag{2.3}$$

where $\mathcal{E}$ is the energy of the photons (erg) and U the exposure (erg/cm^2) needed to produce a density D_R . This calculation was carried out for Kodak TRI -X using published data for $D = f(U)$ and σ . (Jones, 1958. Data from Kodak, 1962). No accurate data could be found for Kodak IIa - O, but one could expect similar performance as Kodak TRI - X because the slightly higher speed of the former is offset by the lower granularity of the latter. (tab. 1.1). The required number of photons per photoelectron was calculated using eqn. 2.2 and 2.3 for $\mathcal{E} = 4.6\ 10^{-12}$ erg (λ = 4300 Å), k = 1 and k = 5. The results are shown on fig. 2.1 as a function of the diameter d or the corresponding system resolution. Also shown are the number of photons needed to produce given values of density above fog level.

2.2.2 Single Stage Intensifier.

A Photoelectron, accelerated with 20 KeV onto the best available high efficiency-high resolution phosphor screen available, i.e., a P.11 screen with 15% effective efficiency and 120 lp/mm limiting resolution (§ 3.2) will cause the emission of about

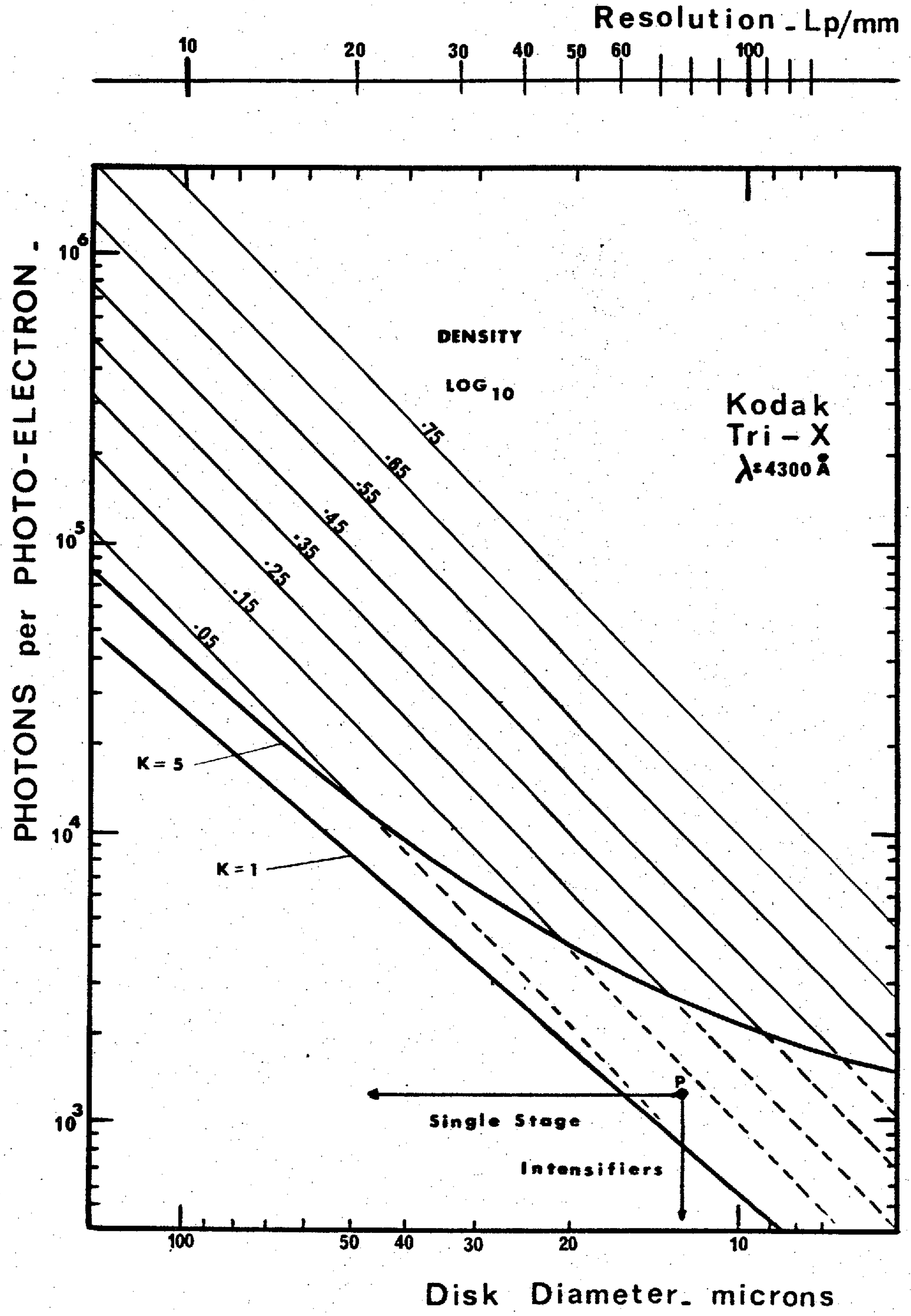

FIG 2.1 PHOTO-ELECTRON RECORDING

1200 photons in the forward direction (eqn.3.5). If all these photons are transferred to the emulsion without loss in resolution, then silver grains will be rendered developable inside a disk of 13 microns diameter, corresponding to the combined resolution of the phosphor and the film (100 lp/mm). This situation is represented in fig.2.1 by the point P, which corresponds with marginal detection. However, no optical system can transfer an image to the emulsion without loss of photons and/or resolution. Therefore, single photoelectron detection is not at present possible with a single stage device.

2.2.3 Image Intensifiers with Internal Electron Multiplication.

It is obvious from the previous considerations that the recording of single photoelectrons requires some sort of electron multiplication between the photocathode and the phosphor screen. The multiplication should be sufficient to cancel out the losses in the optical coupling system and to provide a record of adequate density (0.6 $\log_{10}$ units) on the emulsion.

If a lens of transfer efficiency T_L is used to record the phosphor image with a typical system resolution of 30 lp/mm, then, according to fig.2.1, an internal multiplication of:

$$\frac{10^5 \text{ (photons/photoelectron)}}{T_L \times 1200 \text{ (photons/electron)}} = \frac{83}{T_L}$$

is needed to record photoelectrons with a density of 0.6 $\log_{10}$ units above fog level. Therefore, the required multiplication is 830 for f / 1.2 since $T_L = 10\%$, and 16600 for f / 5.6 since $T_L = 0.5\%$.* Although such a multiplication cannot for the present be achieved in one step, it is fairly easy to accomplish it in two or more steps by cascading multiplying dynodes. Low individual dynode gains will not only reduce the limiting resolution of the system because a greater number of stages will be needed to produce the required gain, but will also reduce the statistical performance of the system.

---

* T_L is given by eqn. 6.2

The equivalent quantum efficiency EQE of any photoelectric device is given by eqn. 1.16. The fraction $\overline{\Delta^2 G}/\overline{G}^2$, this is the relative fluctuation in the weight of the recorded photoelectrons, has been calculated in appendix I for a mulstistage intensifier coupled to an emulsion by means of an optical system:

$$\frac{\overline{\Delta^2 G}}{\overline{G}^2} = \overline{\Delta^2_g} \cdot \frac{1 - g^{-m}}{g(g-1)} + \frac{K}{\beta . g^m} + \frac{1 - M.T_L}{M.T_L.g^m.\beta} \qquad (2.4)$$

where G is the number of developable grains produced by one photoelectron (weight), g the dynode electron gain, m the number of dynodes, M the quantum efficiency of the emulsion ($\approx 10^{-3}$ grains / photon), T_L the transfer efficiency of the coupling lens (10^{-1} to 5.10^{-3} photons/photon for f/1.2 and f/5.6 respectively), β the quantum efficiency of the output phosphor (1.2×10^3 photons/electron) and finally K a constant expressing the deviation from a Poisson distribution for the statistics of the luminescent process ($K \approx 1$).

If the condition, $g^m \gg 83/T_L$, of single electron recording is obeyed and using the abovementioned values for M, T_L, β and K, then the second term of eqn. 2.4 is always smaller than 10^{-6} and the thrid term has a magnitude of about 10^{-2} independently of the aperture of the recording lens. These two terms are thus negligible in comparison to 1 in the substitution of eqn. 2.4 in eqn. 1.16, so much so that the EQE (o) of a multistage intensifier system becomes:

$$\text{EQE (o)} = \frac{\text{RE . QE}}{1 + \frac{\overline{\Delta^2 g}}{\bar{g}(\bar{g}-1)}} \qquad (2.5)$$

The EQE (o) will thus be dependent on the recording efficiency RE, the quantum efficiency QE of the primary photocathode and on the gain and statistics of the individual dynodes. In order to achieve the highest possible EQE (o), this is this is RE . QE; $\overline{\Delta^2 g}$ must be $\ll \bar{g}(\bar{g}-1)$. It will be seen in the following discussion of practical multistage devices that this is not always possible.

2.2.4 Transmission Secondary Emission Multiplication or TSEM Image Intensifiers.

Orvin (1934) first suggested the use of transmission secondary emission as a possible method for producing internal electron image multiplication. If primary electrons are accelerated to a sufficient energy onto a film made of a suitable secondary emitting material (KCL, BaF_2), secondary electrons will be ejected from the other side. Since the multiplication involved is of the order of 4 to 7 per dynode, several TSE - films are to be cascaded in order to produce sufficient electron gain.

Early TSEM - image intensifiers incorporated 4 to 6 dynodes made of KCl or $Ba\,F_2$ films to produce multiplications of 1500 to 2500 (Watchel, et.al. 1960). Work at Imperial College by Wilcock et.al. (1960) produced the first TSEM - device with sufficient gain to enable the recording of photoelectrons. The multiplying screens consisted of 500 Å thick KCl layers and a 200 Å layer of aluminium (to produce electrical contact) deposited on a 450 Å self-supporting film of aluminium oxide. Using 5 dynodes of this type, each with $g = 5$, electron multiplication of 3200 to 3500 was achieved leading to light gains of about 10^5 with a limiting resolution of 15 to 20 lp/mm. Further work on TSEM - intensifiers by English Electric Valve Co. (Slark, et.al. 1962) and by 20th Century Electronics (Emberson, et.al., 1962) has led to improved performance both in light gain ($\sim 9.10^5$) and resolution (20 - 45 lp/mm).

The performance of TSEM - intensifiers is very much degraded by the poor statistics of its multiplication process. Wilcock, et.al. (1966 A, 1969) made accurate measurements of the statistics of individual dynodes and found that the probability of producing a secondary electron obeys a nearly geometric distribution. In that case, $\overline{\Delta^2 g} = k\,\bar{g}^2$ (Miller, 1956), where k is close to one.

Substitution in eqn. 2.5 gives

$$EQE(o) = \frac{RE \cdot QE\ (g-1)}{g(1+k) - 1} \qquad (2.6)$$

Therefore, even if the dynode gain g is high, the EQE will never be more than 50% of RE. QE. (k = 1). The single electron response of the complete intensifier is approximately exponential as it was measured by several investigators. (Emberson, et.al., 1962 and 1966, Binnie, et.al., 1963, Baldwin, et.al., 1965). There is furthermore a high possibility of photoelectrons impacting on the first dynode not producing any secondaries (Wilcock, 1969), such that the recording efficiency RE is only 20 to 45%. (Iredale, et.al., 1964, Reynolds, 1966, A.B.). By the substitution of RE = 0.20 to 0.45 and g = 5 into equation 2.6 it can be seen that the EQE (o) of the TSEM - intensifier will be only 9 to 20% of the quantum efficiency of the primary photocathode.

Another important drawback is the poor contrast in the final image resulting from penetration of electrons through the dynodes and the consequent out of focus positioning in the next stage.

Hence, the poor statistics, the low EQE, the large signal induced background component of TSEM - image intensifiers place severe limitations on the use of these devices in practical applications. A higher dynode gain would improve somewhat the resolution (less stages required) and statistical performance, but the EQE would still be limited to 50% of RE. QE. Although methods of achieving high gain TSEM - dynodes (g = 40-60) with "low density" films have been described (Goetze, 1962. Dietz, et.al. 1967), the author is not aware of the existence of any multistage intensifier using these high gain dynodes.

2.2.5 Channel Image Intensifiers.

Electron multiplication of the photoelectron image in channel intensifiers is achieved by a two dimensional array of individual secondary emission multipliers.

Early devices (McGee, et.al. 1960, Burns, et.al. 1960, Flinn, 1962) incorporated ingenious dynode structures designed to "channel" electrons from one secondary emitting surface to another, without any magnetic focusing. Although high multiplication could be achieved, the resolution was very low (1 - 2 lp/mm), limited by the size of dynode structures.

The advance in glass-fibre technology has made it possible to develop continuous channel multipliers consisting of an array of thin hollow glass tubes (40 microns internal diameter) coated internally with high resistive secondary electron emitting material, or made of special electronically conducting glass. (Adams, 1962. Manley, et.al. 1969, Eschard, et.al. 1969). With a potential drop of a few kilovolts across such a channel, electron multiplication from 10^3 to 10^6 are achieved as a result of multiple reflection secondary emission of electrons on the inner walls of the fibre.

Although two dimensional arrays of fibres can be produced quite successfully (Adams, et.al., 1967) the major problems remain the inefficient coupling of the array to the photocathode and phosphor screen, the low limiting resolution (5-15 lp/mm) and recording efficiency (30-50%), and the poor statistics resulting from the low value of the individual multiplication ($\bar{g} = 2 - 3$) (Sackinger et.al., 1969, Adams et.al., 1966). Output pulses of nearly the same amplitude can be obtained by operating the channels in the 'pulse saturation mode". This occurs, at gains in excess of 10^6 , when the electric field in the output section of a fibre is sufficiently distorted by space charge that no further electron gain is achieved.

Intensive research is continued on these channel multipliers; the small size, weight and low operating voltage of which are highly advantageous for may practical applications.

2.2.6 Cascade Image Intensifiers.

High electron multiplication can be obtained by efficient coupling of a phosphor screen with a photocathode. A dynode gain of 40 to 120 can be achieved (§ 3.3) such that only two or three dynodes would be needed to meet the requirements of a single electron detection as discussed in § 2.2.1.

Cascade intensifiers can be ~~as~~ thought of as several single stage devices linked together by means of an optical coupling. This can best be achieved by a very thin transparent membrane onto which a phosphor screen is deposited on one side and a photocathode is evaporated on the other. This method was first suggested by scientists at Philips Gloeilampen Fabrieken(Philips, 1928). The transmission of such a coupling is about 95% and its limiting resolution can be as high as 200 lp/mm (§ 8.4.).

The alternative method of fibre optic coupling (Kapany, 1961, 1967) is attractive because a cascade tube could be assembled from several vacuum sealed single stage devices. This would facilitate the manufacture of such intensifiers and increase the probability of producing a device with all photocathodes of high quality. When used in conjunction with electrostatically focused tubes, fibre plates can be made curved in order to adopt the shape of the electron image plane, at the expense of uniformity of light transmission across the plate. For a faceplate made of the smallest diameter fibres now technically possible, i.e., 5 microns diameter with a numerical aperture of about 1.0, it has been calculated by Dolon et.al. (1961) that only about 50% of the light is transmitted by the faceplate. The limiting resolution of such a faceplate is 80 to 100 lp/mm. Furthermore, the problems involved in manufacturing perfectly registered matching pairs of fibre plates result in this type of coupling being inferior to the thin membrane solution.

Cascade image intensifiers have been made in various forms by a number of workers and there is a fairly large choice of commercially available devices. A compilation of published results is given in tab.2.2, showing physical characteristics

Authors (references) & Manufacturers		N° of STAGES	PHOTOCATHODE DIAMETER in MM	STAGE COUPLING tf; thin film thickness in μm f.op; fiber optic	PHOTOCATHODE TYPE [3]	SENSITIVITY in μA/Lm	OUTPUT PHOSPHOR [4]	FOCUSING	OVERALL POTENTIAL in KV	CENTER RESOLUTION Lp/mm	EDGE RESOLUTION Lp/mm	GAIN [2]	BACKGROUND EL/CM²/SEC	IONS/CM²/SEC	DISTORTION in o/o [5]	AXIAL MAGNIFICATION
Schaffernicht	1946	2		tf 100	S1			ES	40	10						
Krizek	1946	2		tf 30	S1			ES								
Eckart	1954	2		tf 30	S9			ES	30	8		$1.5\ 10^2$				
Zavoiskii	1955	5		tf				EM		10		$1.0\ 10^5$	-	$5\ 10^2$		
Davis.E.(IC)[1]	1959	2	40	tf 15	S9	35	P11	EM	20	14		$9.0\ 10^2$	$5.0\ 10^6$			
Stoudenheimer	1960	2	24	tf	S20		P11	ES	24	18	4	$1.0\ 10^3$	$3.0\ 10^4$		32	
Stoudenheimer	1961	2	88	tf	S11		P11	EM		25		$5.0\ 10^3$				
Stoudenheimer	1961	3	38	tf	S11		P11	EM		18	9	$1.0\ 10^5$				
Davis.G.	1962	4	40	tf 5	S24		P11	EM	45	17		$1.0\ 10^5$	$3.1\ 10^4$	$5\ 10^2$		
Gildermeister	1962	4		tf 10				EM	56	5		$2.0\ 10^6$	$3.2\ 10^4$			
Catchpole(IC)[1]	1963	3	40	tf 5	S9	40	P11	EM	40	22		$1.0\ 10^5$		10		
Habel	1966	3		tf 4	S9		P11	ES	50	10		$3.0\ 10^4$				
Randall	1966	4	40	tf 4	S20	150	P11	EM	45	22	17	$9.0\ 10^5$	$7.5\ 10^2$	10		1.00
Powell (IC)[1]	1967	3	40	tf 4	S11	60	P11	EM	40	45	25	$6.0\ 10^5$	50-500	1-5		
Varma (IC)[1]	1968	3	9x29	tf 4	S11	60	P11	EM	40	52	40	$7.0\ 10^5$	50-200	0.1-2		
Collings	1969	2	40	f.op	S25	225	P20	ES	30	17		$9.5\ 10^4$	$3.0\ 10^4$	15	2	0.40
EMI 9694 fc[6]		4	48	tf 4	S20	110	P11	EM	40	25		$1.0\ 10^6$	$5.0\ 10^2$	1-10		0.99
EMI 9723		2	48	tf 4	S20	110	P11	EM	20	40		$5.0\ 10^3$	$2.0\ 10^2$			
RCA 33011[7]		2	38	tf	S20	130	P11	EM	20	40	10	$4.6\ 10^3$	$2.0\ 10^3$		3	1.00
RCA C33063		2	38	tf	S20		P11	EM		55		$7.0\ 10^3$				
RCA C70021 SP2		3	38	tf	S20		P11	EM		40		$1.2\ 10^5$	$3.4\ 10^2$			
RCA C70055 GP2		3	89		S20		P11	EM		28		$1.2\ 10^5$				
RCA C33074-P2		4	32	tf	S20		P11	EM		25		$1.7\ 10^6$	$3.4\ 10^2$			
ITT F 4710		3	60	f.op	S20R	175	P20	ES		25		$9.4\ 10^4$	$2.1\ 10^4$		25	0.82
Machlett ML 8858		3	18	f.op	S25	210	P20	ES	36	32	29	$1.6\ 10^5$	$6.0\ 10^3$		15	0.87
VARO 8858		3	25	f.op	S20R	175	P20	ES	38	32	28	$1.1\ 10^5$	$2.1\ 10^4$		21	0.85
EMR 549-125 ReV		3	40	f.op	S20		P11	EM	45	35		$1.3\ 10^5$				
Mullard XX 1060		3	30	f.op	S20R	175	P20	ES	45	25	23	$1.1\ 10^5$	$2.2\ 10^4$		25	0.90
Westingh..WX32002		2	40	f.op	S25	225	P20	ES	30	17		$9.4\ 10^4$	$2.8\ 10^4$	15	2	0.40

TAB. 2.2. CASCADE IMAGE INTENSIFIERS.

SEE NOTES ON NEXT PAGE

and performance of various intensifiers.

Notes to tab.2.2. (1) Refers to work carried out in the department of Applied Physics of Imperial College, under the direction of Professor J.D. McGee. See also McGee et.al. (1966.C and 1969.B). (2) Gain: Light gain is quoted for intensifiers having P11 output phosphor and luminous gain for intensifiers with a P20 output phosphor. (§ 7.1 - 2) (3) § 3.1. (4) § 3.2. (5) distortion as defined by eqn. 9.4 (6) These data were obtained from up to date leaflets released by the commercial manufactures. (7) This two-stage intensifier has been developed by R.C.A. under the guidance of the Carnegie Committee on Image Tubes for Telescopes. A critical study of its performance has been made by Cromwell (1969).

It can be seen that if the required gain is generally achieved for three or more stage devices, it is often done at the expense of resolution, especially in intensifiers using fibre optics coupling. The background, which was initially very high, has been reduced to levels corresponding to the thermionic emission of the primary photocathode. The occurrence of ion (bright) scintillations is generally thought to be caused by the desorption of ions in the first stage (§ 10.4). Electrostatic focusing as compared to electromagnetic focusing causes degradation of the geometry, while the resolution is prevented from decreasing for off-axis points by the use of curved fibre optics coupling plates. However, this should cause an important decrease of gain at the edge of the field (vignetting).

The statistics of cascade intensifiers are by far superior to that of the previously discussed multistage devices owing to high dynode gains and good statistical properties of the multiplication in each dynode. Assuming that one electron is accelerated onto the phosphor of a dynode (quantum efficiency β), that all the emitted photons reach the photocathode (quantum efficiency QE) to produce g secondary electrons, that the luminescence process obeys a near Poisson distribution, such that $\overline{\Delta^2\beta} = k\overline{\beta}$ and that $\overline{\Delta^2 QE} = QE\,(1 - QE)$ (§1.2.2), and using eqn. 1.9, it is possible to show that:

$$\bar{g} = QE \cdot \bar{\beta}$$

$$\overline{\Delta^2 g} = QE \cdot \bar{\beta} \cdot \left[QE\ (k-1) + 1 \right] = \bar{g} \left[QE\ (k-1) + 1 \right]$$

It can be seen that even if the luminescence process deviates srongly from Poisson statistics, the term QE (k - 1) is much smaller than one, ~~such as~~ so that $\overline{\Delta^2 g} \approx \bar{g}$. Substitution in eqn. 2.5 gives:

$$EQE\ (o) = \frac{QE \cdot RE\ (g-1)}{g} \qquad (2.7)$$

Since g is large (40 to 120), the equivalent quantum efficiency of the cascade intensifier is practically equal to QE. RE. Measurements have indicated that the recording efficiency RE of cascade intensifiers is high ~ 70 to 85% (Powell, 1967, Water, et.al. 1962) so that the equivalent quantum efficiency EQE (o) can be expected to be 0.70 to 0.85 . QE. Good resolution (30 - 55 lp/mm) and high EQE (o) make cascade intensifiers superior to any other multistage devices available now. This thesis is concerned with the evaluation of the performance of the three, stage cascade intensifier developed in the Department of Applied Physics of Imperial College.

2.3 PHOTOELECTRIC IMAGE DETECTION BY CHARGE STORAGE.

An alternative technique for the detection of the photoelectron image will be briefly mentioned here. The photoelectron image is transfomed into a positive charge image created either on the photocathode itself, deposited in a large number of insulated islands, by the release of these same photoelectrons* or on a target plate bombarded by photoelectrons, by the emission of secondary electrons **. The information stored on the target is extracted by a "reading" process in which the charge is scanned with an electron beam. This restores the surface to its initial

---

* Emitron, Iconoscope, CPS Emitron, Orthicon.

** Super Emitron, Image Iconoscope, Image Orthicon.

potential and enables an electrical signal to be generated. This "video" signal carries the information in a coded form, which, after amplification can be stored on tape or displayed on a CRT.

Besides the television systems developed for entertainment application, a number of devices using charge storage have been developed to meet the requirements of low light level applications. The image orthicon (Rose et.al. 1946) has a maximum EQE of about one third of the QE of the primary photocathode, at exposure levels slightly smaller than those required for optimum use of the best photographic plates. (Jones ,1959). The limiting resolution is 700 to 800 TV lines or about 3 lp/mm. The performance may be extended to even lower light levels by incorporating an intensifier preceding the image orthicon (Morton, 1955). The CPS Emitron (McGee, 1955) has a lower sensitivity than the image Orthicon, but owing to its linear response to light, and large target capacity, has superior performance in low contrast image detection. Finally, the secondary electron conductivity (SEC) camera or SEC - Vidicon (Goetze, 1969) has, when coupled to an image intensifier section, a sensitivity and resolution comparable to those of the intensifier orthicon, but with lower lag, better low contrast performance and wider dynamic range.

2.4. CONCLUSIONS

Cascade intensifers are superior to any other intensifier photography system because of their higher resolution, better signal to noise ratio and larger photoelectron recording efficiency. Although electronography has superior performance as compared to the other image detector techniques, its complexity of use and lack of versatility makes it applicable only to a narrow range of practical uses.

CHAPTER 3.

PHOTOCATHODES AND PHOSPHOR SCREENS.

It has already been stressed that the performance of image intensifiers is strongly dependent upon the characteristics of their photocathodes and phosphor screens. It is therefore useful to analyse in this chapter the properties of different photoemissive and cathodoluminescent surface in view of their use in image devices. Photocathodes or Phosphors are often characterised by a single S or P code symbol which describes only a standardized relative spectral sensitivity or spectral emission characteristic. (JEDEC 1960 and 1964).

The terminology "spectral matching factor" will be used widely in this thesis. If a detector with relative spectral sensitivity $D_{\lambda r} = D_\lambda / D_{max}$ is coupled with a source with relative spectral emission $F_{\lambda r} = F_\lambda / F_{max}$, then the response of this detector is

$$R = D_{max} F_{max} \int_0^\infty D_{\lambda r} \,.\, F_{\lambda r} \,.\, d\lambda$$

$$R = D_{max} \,.\, M(F, D) \int_0^\infty F_\lambda \,.\, d\lambda \qquad (3.1)$$

with

$$M(F, D) = \frac{\int_0^\infty F_{\lambda r} \,.\, D_{\lambda r} \,.\, d\lambda}{\int_0^\infty F_{\lambda r} \,.\, d\lambda} \qquad (3.2.)$$

$M(F, D)$ is the spectral matching factor between the source (F_λ) and the detector (D_λ).

3.1 PHOTOCATHODES.

The basic advantages of the use of photocathodes as primary image detectors have already been discussed in § 1.2.2. This section is concerned with the practical aspects of their use in image devices.

3.1.1 Quantum Efficiency. Radiant and Luminous Sensitivity.

The relation between the quantum efficiency QE_λ and the radiant sensitivity S_λ at a wavelength λ is given by

$$QE_\lambda = S_\lambda \frac{hc}{e\lambda} = S_\lambda \frac{12395}{\lambda} \qquad (3.3)$$

(where S_λ is expressed in Amps/Watt, λ in Å) and between the luminous sensitivity R_L and the maximum radiant sensitivity S_M by (Eberhardt, 1968):

$$R_L = \frac{S_M}{680} \frac{M\,(CAL.\ S-)}{M\,(CAL.EYE)} \qquad (3.4)$$

(where R_L is expressed in Amps/Lumen, S_M in Amps/Watt). M(CAL.EYE) is the spectral matching factor between the calibrated source, i.e. a tungsten lamp operated at a colour temperature of 2854°K, and photopic vision and equals 0.071. M(CAL.S-) is the matching factor of the same source and the photocathode.

3.1.2 Characteristics of Useful Photocathodes (semitransparent).

Typical and maximal sensitivities of some of the most important photocathodes are given in tab.3.1, together with typical dark current data and spectral matching factors of these cathodes with the 2854 °K calibrated source and various phosphor materials. Typical radiant sensitivity curves are given on Fig.3.2. in function of wavelength.

The S.1 photocathode, or Ag-O-Cs, (Koller, 1930) is the only known semitransparen beyond 9000 Å – photocathode with a useful response in the infra-red region of the spectrum (Malherbe, et.al. 1966) but has a very high thermionic emission at room temperature. The S.9 cathode, or Cs_3Sb, (Görlich, 1936) is probably the easiest cathode to process and is for that reason still used in certain image devices (§ 2.1.1 and 2.1.2). The sensitivity of the Cs_3Sb cathode can be increased by processing it on a substrate of manganese oxyde (Polkosky, 1951). This improved cathode, the S.11 or MnO - Cs_3Sb, is widely used in image tube work. The MnO substrate is thought to cause a favourable band bending at the interface between the MnO layer and the Cs_3Sb

Photocathode Type Composition	S1 AgOCs	S9 SbCs	S11 MnOSbCs	S20 CsNaKSb	S24 NaKSb	S25 CsNaKSb	Units
Typical Data [1,3,8]							
Luminous Sensitivity	25	30	60	150	40	200	μA/Lm
Max.Radiant Sensitivity	2.4	22.0	48.0	64.0		42.0	mA/W
at wavelength	8000	4800	4300	4200		4300	A
Max.Quantum Efficiency	0.4	5.0	13.6	18.9	11.0	12.0	%
at wavelength	7900	4700	4000	4100	3800	4200	A
Maximum Data		[6]	[4]	[5]		[7]	
Luminous Sensitivity	30	50	110	250		310	μA/Lm
Max.Quantum Efficiency		10.3	17.0 [4]	26.0			%
Dark Current (20°C) [1,3,8]	10^4–10^8	50–500	50–300	500–10^3	1–50	500–10^3 [7]	el/cm^2/sec
Spectral Matching [2]							
M(Cal.S–)	0.516	0.071	0.060	0.112		0.227	–
M(P11.S–)	0.217	0.930	0.914	0.877		0.953	–
M(P20.S–)	0.395	0.560	0.427	0.583		0.782	–
M(P22.S–)	0.217	0.923	0.960	0.927		0.979	–

References: 1.RCA Manual 1963. 2.Eberhardt 1968. 3.Sommers 1968. 4.Westlake 1970. 5.Spicer 1958. 6.Powell 1967. 7.Collings 1969. 8. EMI Data 1969.

TAB_3_1 PHOTOCATHODE CHARACTERISTICS

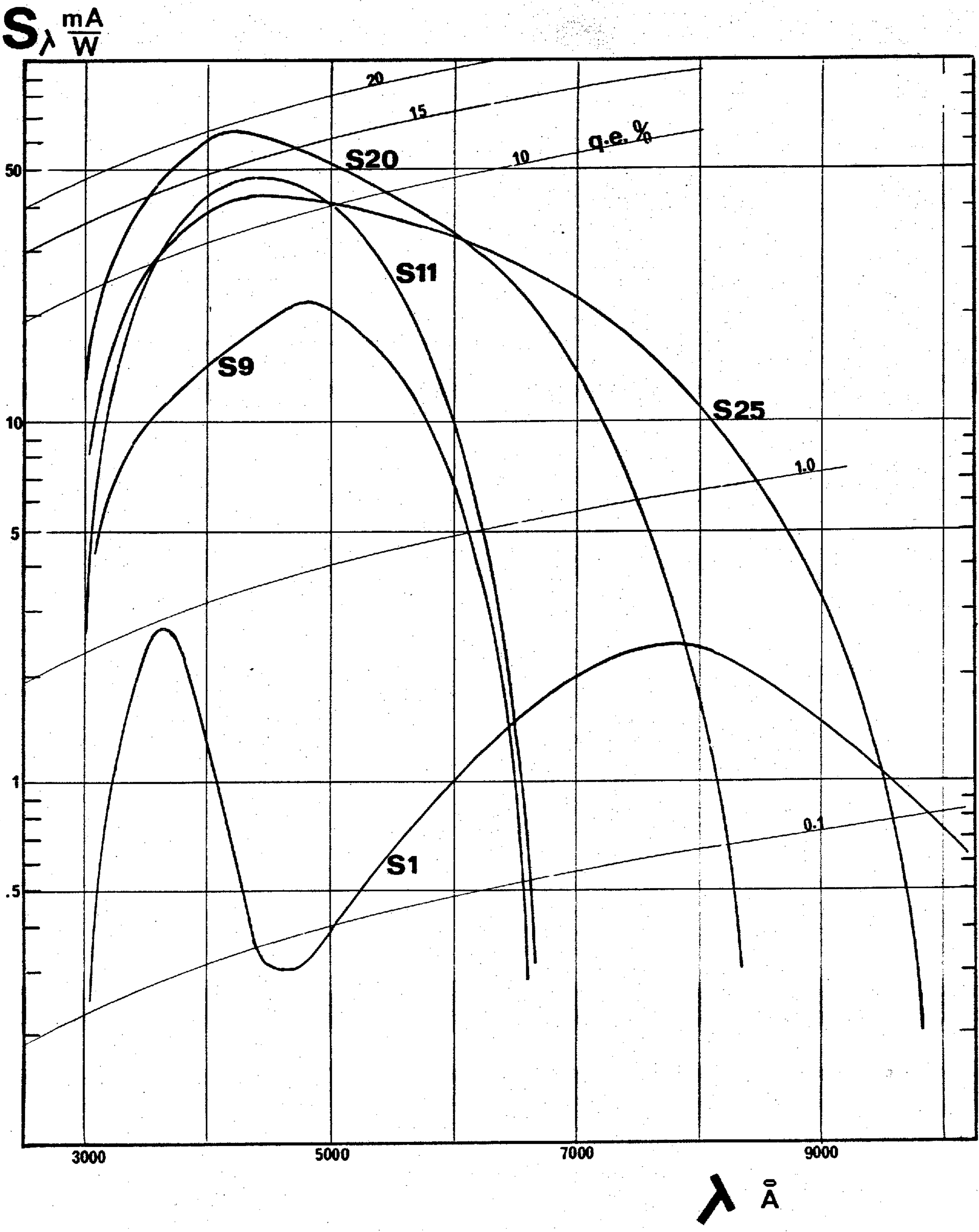

FIG 3.2 TYPICAL RADIANT SENSITIVITY PLOTS

layer (Wooten, 1966). Photocathodes of higher sensitivies are obtained by combining more than one alkali metal (K, Cs, Na,) with antimony. The most successful of these multialkalies is the S20 or (Cs).Na$_2$ .K.Sb discovered by Sommer (1955). A good S.20 cathode has a higher quantum efficiency throughout the visible range than any other semitransparent photoemissive surface, and is therefore almost universally adopted by commercial image intensifier manufacturers. The S24 or Na$_2$.K.Sb cathode (Jědlicka, 1969) is characterised by the absence of Caesium such that its thermionic emission is extremely low. Recently new multi-alkali cathodes have been discovered and some are already used in commercial devices. Both the S25 and the multi-alkali with extended red response (ERMA) cathodes have the same composition as the S20 cathode, but higher sensitivities in the near infra-red and lower sensitivities at short wavelengths (Collings et. al. 1969. Data from Varo, 1971 and ITT, 1971).

The S.11 cathode has been adopted in the IC cascade intensifier because its favourable spectral matching with the high efficiency P11 phosphor (§ 3.3) and its relative easy processing procedure in comparison with the multialkali cathodes. Fig.3.3. shows the quantum efficiency versus wavelength curves of three S11 cathodes prepared for this intensifier and measured with the calibrated apparatus developed by Wilcock (1966.B).

3.1.3 Effects of various Parameters on Photocathode Characteristics .

Variation in quantum efficiency with illumination intensity has never been reported for the illuminations currently used with image devices (corresponding to photocurrents of 10^{-6} Amps/cm^2 maximum). However, fatigue effects may occur through temporary surface decomposition if higher light levels are used.

Lowering the temperature of a photocathode has only a minor effect on its sensitivity (Murray, et.al. 1960) but causes a drastic reduction of its thermionic emission. A temperature change of +20°C to - 20°C reduces the dark emission

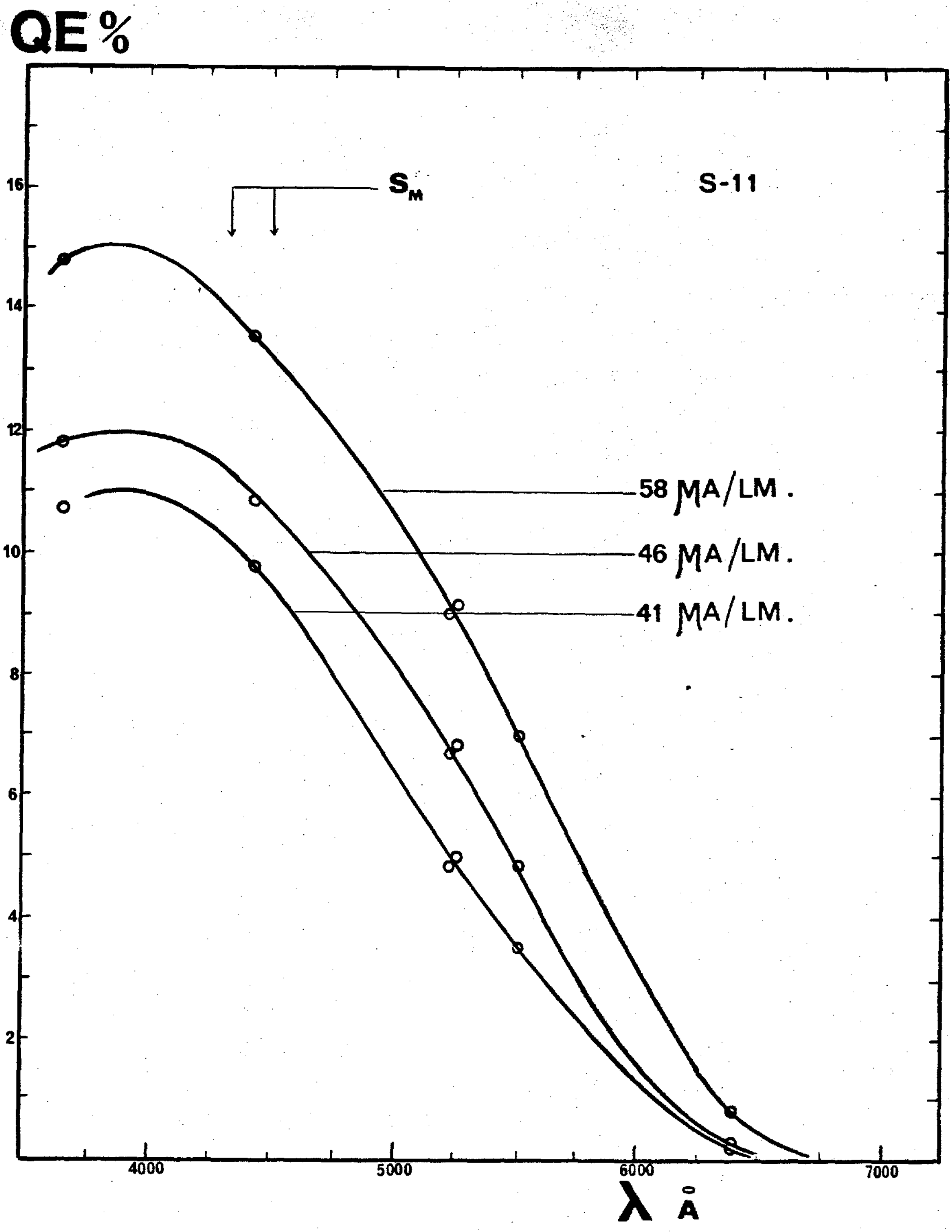

FIG 3.3 QUANTUM EFFICIENCY MEASUREMENTS

by a factor of about 100 for the S.1 photocathode, 10 to 20 for the S.11, and 20 to 50 for the S20 cathode. (Data from RCA, 1963, Engstrom, 1947, Charman, et.al. 1966). The conductivity of the cathodes decreases with decreasing temperature and this can create problems at very low temperatures for large photocathodes. A voltage drop across the surface dependent upon the photocurrent could affect the focusing conditions in an image tube. (Hopmann, 1966).

Photoemission is slightly enhanced as a result of the applied electric field at the cathode, which aids emission by reducing the voltage barrier at the surface associated with the photoelectric work function. Sometimes this is referred to as the photoelectric Schottky effect and it results in a shift of the spectral response towards longer wavelengths. This effect has been reported in the literature for the photoelectric effects of metals (Lawrence, et.al. 1930) and of photocathodes (Lawrence et.al., 1942; Crowe, et.al. 1967).

3.1.4 Practical Considerations on Photocathode Processing.

In choosing a photocathode type for a practical application, one would naturally select the photocathode with the highest quantum efficiency in the wavelength range of the illumination. Limitations, however, will arise if the difficulty in processing certain types of cathodes is considered in a particular image tube configuration. The conventional technique is to process the photocathodes in situ by thermal evaporation of alkali metals and antimony from sources mounted inside the tube. This not only restricts the number of possible electrode configurations, but also allows the alkali vapours to diffuse throughout the tube during processing. Alkali vapour often interacts chemically with the surface of the electrodes and enhances undesirable effects such as ohmic leakage and spurious photoemission. Most important however, is the fact that alkali vapour reduces the work function of metals and thus seriously increases the field emission (McGee, 1956 A. Hiltner, 1956). In spite of these drawbacks photocathodes of a large number of image tubes are still processed in situ, because to do otherwise would be difficult and expensive.

McGee (1956.B) has suggested a partial solution to these problems by processing the cathodes in a separate compartment inside the tube. The caesium vapour is prevented from diffusing into the high field region of the device by separating the processing compartment with the photocathode substrate plate. The processed cathodes are moved to their permanent position after the device is sealed off the pump. Another solution is to process the cathodes outside the device but within the same vacuum (Backwill, et.al., 1959) or outside the tube in a completely separate envelope. In the latter case, a thin glass membrane is broken under vacuum to introduce the preformed photocathode into the device. This technique, first introduced by Lallemand on his electronographic camera (§ 2.1.1.) and adapted by McGee on the Spectracon (§ 2.1.3.), not only solves the problem of alkali vapour contamination but permits the use of one or more preselected photocathodes of practically any type. Recently, a very ingenious photocathode transfer system was developed by Dolizy, et.al.(1969) where the preformed photocathode is introduced directly into its working location in the device, prior to the completion of the tube under vacuum. This technique will without doubt be universally adopted in the near future for the manufacturing of photoelectric devices.

3.1.5 Stability of Photocathodes.

In the absence of leaks in the vacuum envelope the stability of a photocathode will depend upon the amount of residual gases, the intensity of the incident illumination and the electric field at the photocathode. A vacuum in the region of 10^{-6} torr, corresponding to a mean free path for electrons of about 10^{4} cm, may be considered adequate for satisfactory operation of a cathode. The residual gas must not contain oxygen, water vapour, CO_2 and halogenes or any other material that reacts with alkali metals (Theodorou, 1966. Deckers, 1969). Contamination of the photocathode by seal-off gases in glass systems (mostly H_2O,

CO, CO_2 , H_2 and F_2) causes deterioration of sensitivity. Particularly this is the case for cathodes transferred to alkali free envelopes, since the seal-off gases cannot be absorbed by any alkali metal adsorbed on the surrounding glass walls (Charrier, et.al. 1962). Several precautions can be taken to minimize this effect: degassing by heating of the seal-off region before activation, the use of a special cold trap to increase the pumping speed during sealing off and the protection of the photocathode from seal-off gases by the use of getters (Barium). This problem could be completely solved by means of "cold-seal-offs" but such a technique is expensive and necessitates sophisticated equipment. Other sources of sensitivity drop during the operation of the device are positive ion bombardment of the cathode and electrolytic or thermal decomposition of the surface if high photocurrents are (accidentally) used.

3.2 PHOSPHOR SCREEN.

Phosphor screens used in image intensifiers are subjected to very strict requirements. They must ensure the highest possible conversion of electrons to photons and the spectral matching factor of the phosphor with the detector of its radiation (photocathode, film, etc.) must be high. Furthermore, the screen material must be deposited in a very thin, uniformly packed layer of small phosphor particles in order to produce high resolutions.

3.2.1 Intrinsic, Effective and Quantum Efficiency.

The instrinsic efficiency of a phosphor material is the ratio of radiated light power in all directions to the absorbed electrical power. The effective efficiency η_{eff} of a practical phosphor screen is the ratio of radiated light power in the forward direction to the power in the exiting electron beam. The quantum efficiency β of a phosphor screen, i.e., the total number of photons emitted per exiting electron, can be calculated using the following equation (Eberhardt, 1968):

$$\beta = V \cdot \eta_{eff}(V) \cdot M\left(P \cdot \frac{\lambda}{1200}\right) \qquad (3.5)$$

where V is the potential used for acceleration of the electrons, $\eta_{g}(V)$ the effective efficiency at V and M a factor depending upon the spectral emission of the phosphor material (tab.3.4).

3.2.2 Intrinsic Efficiency of Useful Phosphor Materials.

The most efficient phosphor materials for electron beam excitation are the Zinc-Sulphides and the Cadmium Sulphides activated with Silver (and coactivated with Chlorine or Aluminium). The characteristics and relative spectral emission curves of three of these phosphors (the P11, P20 and P22B) are shown in Fig.3.4. The P.11 phosphor emits actinic blue fluorescence which makes it particularly suited as an output phosphor for photographic recording and for coupling with an S.11 photocathode (§ 3.3). The P.20 phosphor emits yellow-green fluorescence and has consequently a higher spectral matching factor with photopic vision than the P11 type phosphor*. It is therefore currently used as an output phosphor when not dark adapted visual observation is required. The P.22 B, recently introduced by RCA (1969), seems to have characteristics superior to the P11 type. However, little is known about the fabrication process of this phosphor and its availability in very fine grains. Two other phosphors have been used in image tube work when short persistence is needed. They are both Zinc-Oxyde phosphors activated with Zinc (P 24 and P 15). However, their efficiency is much lower than the Zinc-Sulphides (tab.3.4).

3.2.3 The Effective Screen Efficiency.

All practical phosphor screens consist of a thin layer of phosphor material deposited on a transparent support. A highly reflective aluminium backing (normally 500 to 1000 Å thick), deposited on the phosphor surface, forces the light

---

* This relation is reversed for scotopic vision (Eberhardt, 1968)

Phosphor Type Composition activated by	P11 ZnS Ag	P20 ZnCdS Ag	P22B ZnS [5] Ag	P24 ZnO Zn	P15 ZnO Zn	
Peak Emission at	4600	5550	4400	5100	3900	Å
Intrinsic (15–20 KV) Efficiency [1234]	20–26	17–22		5–8	9–13	%
Decay [56] Type	1/t	1/t	1/t	e^{-t}	e^{-t}	–
Time to 10%	34	60	22	1.5	2.0	μsec
Spectral Matching						
M(P–.Eye)	0.201	0.707	0.150	0.540	0.376	–
M(P–.λ/1200) [7]	0.392	0.476	0.377	0.437	0.401	–
Typical Screen [5] Efficiency (RCA)	10	14	15	2.6	5.0	%

References: 1.Leverenz 1950. 2.Garlick 1966. 3.Bril 1952 4.Longini 1949. 5.RCA Data 1969. 6.Westinghouse Data 1964 7.Eberhardt 1968.

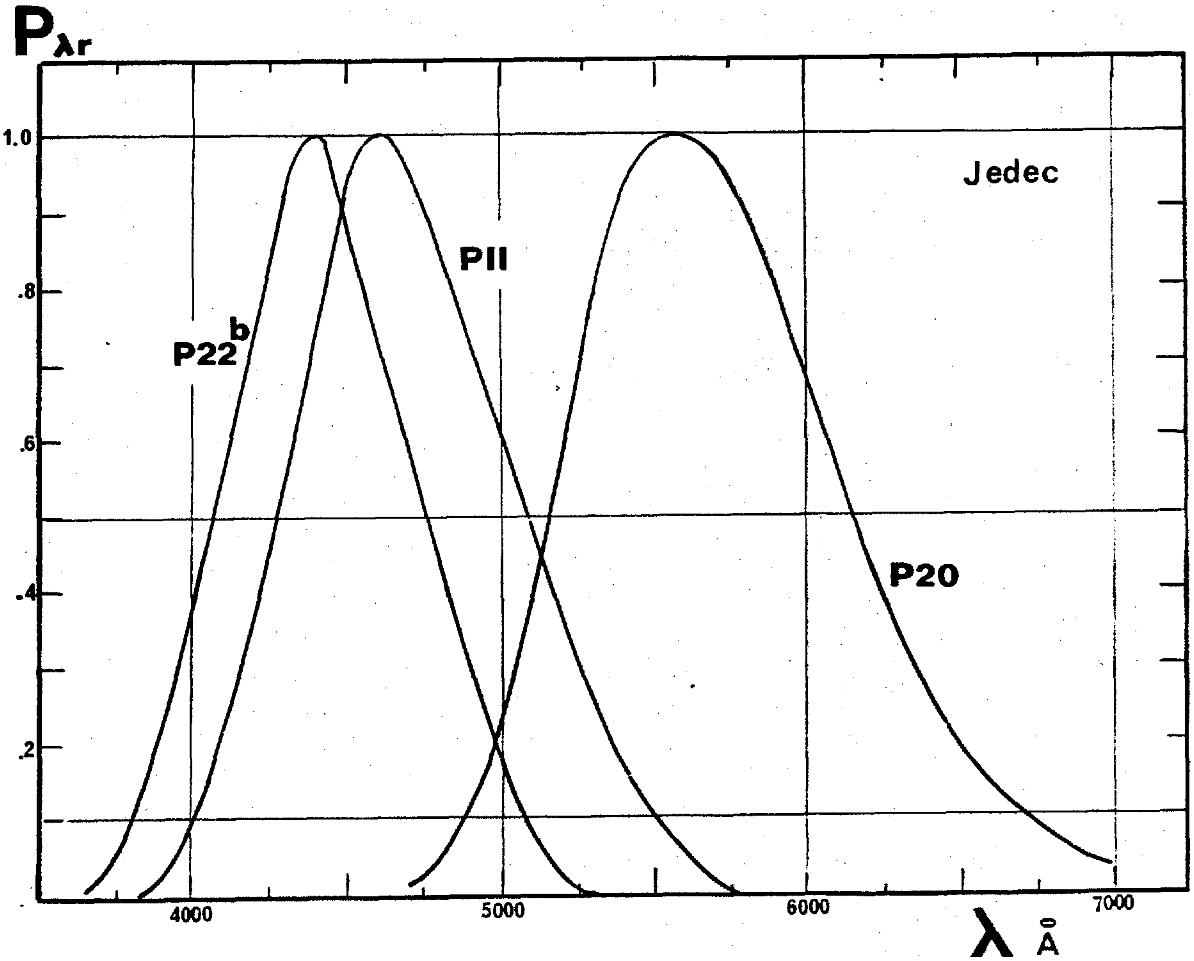

FIG 3.4 PHOSPHOR CHARACTERISTICS

emitted towards the electron beam side to be reflected in the forward direction to increase the light output of the phosphor and prevents light feedback in the device. The conductive layer also stabilizes the phosphor potential and protects it from contamination during processing and from negative ion bombardment during operation of the device.

The effective screen efficiency depends upon the intrinsic efficiency and upon the losses in beam energy and light intensity occurring in the screen. Transmission through the aluminium backing causes a loss of about 3% in beam energy for 15 KeV electrons (Zworykin et.al. 1949). Backscattering of electrons at impact with the screen result in a loss of 15 to 25% of the electrons (Meyer 1970, see also § 11.4.5). Complete conversion of the remaining energy will occur in phosphor layers of about 4 microns (Ehrenberg, et.al. 1953 and 1963). If the layer thickness is further increased, the self absorption of emitted light will increase, so much so that an optimum thickness can be expected to give the highest efficiency for a given electron energy.

Such a layer will emit about 45% of the light in the forward direction, 45% in the direction of the backing, while 10% will be absorbed in the phosphor material (Bril, et.al. 1952). If the reflectivity of the aluminium backing is 50 to 80%, depending on its flatness, and if a further 10% of the reflected light is absorbed in the layer, one may expect a fraction:

$$\left[(0.50 \text{ to } 0.80) \times 0.45 \times 0.90\right] + 0.45 = 0.65 \text{ to } 0.77$$

of the originally emitted light to emerge in the forward direction.

Combining the above estimation of losses with the intrinsic efficiency of the P11 phosphor material (20 to 26%), one can expect the effective screen efficiency to be 9 to 17% for a screen bombardment with 15 KeV electrons. Measured values of this efficiency between 7 and 15% have been reported in the literature for P.11 screens. (Data from RCA, 1969; McGee et.al., 1966, D; Francis et.al., 1960).

3.2.4 Screen Resolution.

Loss of resolution in a phosphor screen is the result of the finite size of the phosphor grains, of scattering of electrons by the aluminium backing and by the phosphor grains,and of the spread of emitted light by multiple reflections and refractions as it emerges from the screen. The latter effect is increased by the presence of an aluminium backing since effectively light emitted in the backwards direction will have to cross a thicker layer. The phosphor layer can be said to be homogenous if its thickness is much greater than the average grain size. The resolution of an optimum layer ($\sim$ 5 microns thick) will not be dependent on the grain size if the latter is in the order of one micron. Measurements made by Longini (1949) on scattering of electrons by the backing have shown it to be a negligible contribution. It is extremely difficult to calculate the relative contributions of scattering of electrons and light in the grains to the radius of the disk of confusion. However, extrapolation from the results obtained by Ehrenberg, et.al.(1953, 1963) for unbacked screens shows that the radius of confusion resulting from these two causes, should be about equal to the screen thickness. Similar results were observed by projecting an illuminated resolution pattern on unbacked screens of various thicknesses (McGee, et.al. 1966 D; Csorba, 1969) One might conclude that the contribution of the scattering of electrons is small compared to that of the spread of light. The presence of the reflective backing will, in the worst case, decrease the resolution by a factor of two. However, since most of the light is generated close to the aluminium backing (Koller, 1951) a much lower reduction in resolution can be expected. Ultimately, this will depend on the intimacy of contact between the top layer of phosphor grains and the aluminium film.

3.2.5 High Efficiency and High Resolution Screens.

If both the requirements of high resolution and high effective efficiency are to be met, a compromise must be made with regard to screen thickness.

Moreover, if tight packing of the phosphor grains affects favourably both resolution and efficiency, the intimate contact of the aluminium film favours resolution at the expense of efficiency, since it will result in a poor reflectivity of the backing. Intensive research in this department (McGee, et.al. 1966 D and E) into how these conditions could be met has resulted in adopting the electrophoretic technique for grain deposition of the P.11 phosphor and the organic film procedure for application of the aluminium backing (§ 5.1). This phosphor deposition technique leads to about 25% better packing than the more classical sedimentation method (Aslam, 1965; Zworykin, et.al. 1954); while the adopted filming procedure although leading to a smaller efficiency, gives about 30% improvement in resolution over the "floated-on" filming method (Aslam 1965). Phosphor screens of this type, with EMI-214.P.11 phosphor grains (1 micron average diameter), are currently used in this department in conjunction with the three stage cascade tube. The average effective efficiency was measured as 15 ± 2% for a 1 mg/cm^2 layer (about 6 microns thick) at 15 KV, and the limiting resolution is about 120 lp/mm (Powell, 1967; McGee et.al. 1966 D).

3.2.6 Measurements of Effective Efficiency.

The screen efficiency of these phosphors was remeasured by the author on a demountable system. Electrons from a gun are accelerated and focused on the phosphor screen. Measurements of the bombarding voltage, variable from 3 to 25 KV, and of the beam current permit the calculation of the beam power. Light emitted in the forward direction passes through the faceplate of the demountable system onto a S.11. photocell and the photocurrent is measured. Readings R_H of relative efficiency in μA photocurrent per μwatt beam power are thus obtained. The photocurrent measured by the cell is:

$$I \text{ (Amps)} = \int_0^\infty W_\lambda \,.\, T_\lambda \,.\, S_\lambda \,.\, d\lambda$$

where W_λ (Watts) is the light power emitted at a wavelength λ, T_λ is the transmission of the faceplate and S_λ (Amps/Watt) the radiant sensitivity of the cell at λ . Using eqn.3.1 and 3.3 and introducing the total radiated power Wtt, one finds:

$$I \text{ (Amps)} = \frac{Wtt}{12395} \; \frac{\int_0^\infty W_{\lambda t} \cdot T_\lambda \cdot QE_\lambda \cdot \lambda \cdot d\lambda}{\int_0^\infty W_{\lambda t} \; d\lambda}$$

Measured values for the product $T_\lambda \cdot QE_\lambda$, using the apparatus described by Wilcock (1966.B), and values for $W_{\lambda t}$ given by fig.3.4 for the P.11 phosphor, were used to perform the numerical integrations. After adjustment of units a relation between R_H and the effective efficiency η_{eff} was found:

$$\eta_{\mathrm{eff}} = 44.1 \times R_H \left(\frac{\mu A}{\mu W}\right) \tag{3.6}$$

Fig.3.5 shows the relation between the effective efficiency and screen thickness for three different bombarding potentials. The maximum efficiency is 12 ± 1% for a 1 mg/cm^2 . phosphor screen at 15 KeV.

3.2.7 Influence of Various Parameters on the Characteristics of Phosphor Screens.

It is found that the efficiency of phosphor under electron bombardment is independent of current density between 10^{-7} and 10^{-5} Amps/cm^2 . (Garlick 1950). As the current density is increased, a saturation is observed, setting in at 1.5 to 5.0 x 10^{-4} Amps/cm^2 for P.11 phosphor (Martin, et.al. 1939). However, phosphors used in cascade tubes, are bombarded with much lower current densities (10^{-16} to 10^{-7} Amps/cm^2). A number of statements have appeared in the literature concerning non-linearities between light output intensity and current density at these low levels (Lasof 1947. Francis, et.al. 1960. Randall, 1966). Decreases in efficiency as the current density is decreased are reported. Similar behaviour was observed with ultra-violet excited phosphors (Urbach, et.al. 1947; Nail, et.al. 1949 and Klassens, et.al. 1948). The latter studies indicate that the presence of impurities (Co, Ni) in the phosphor favours a non-linear behaviour which is accompanied by a shift in the spectral emission to higher wavelengths as

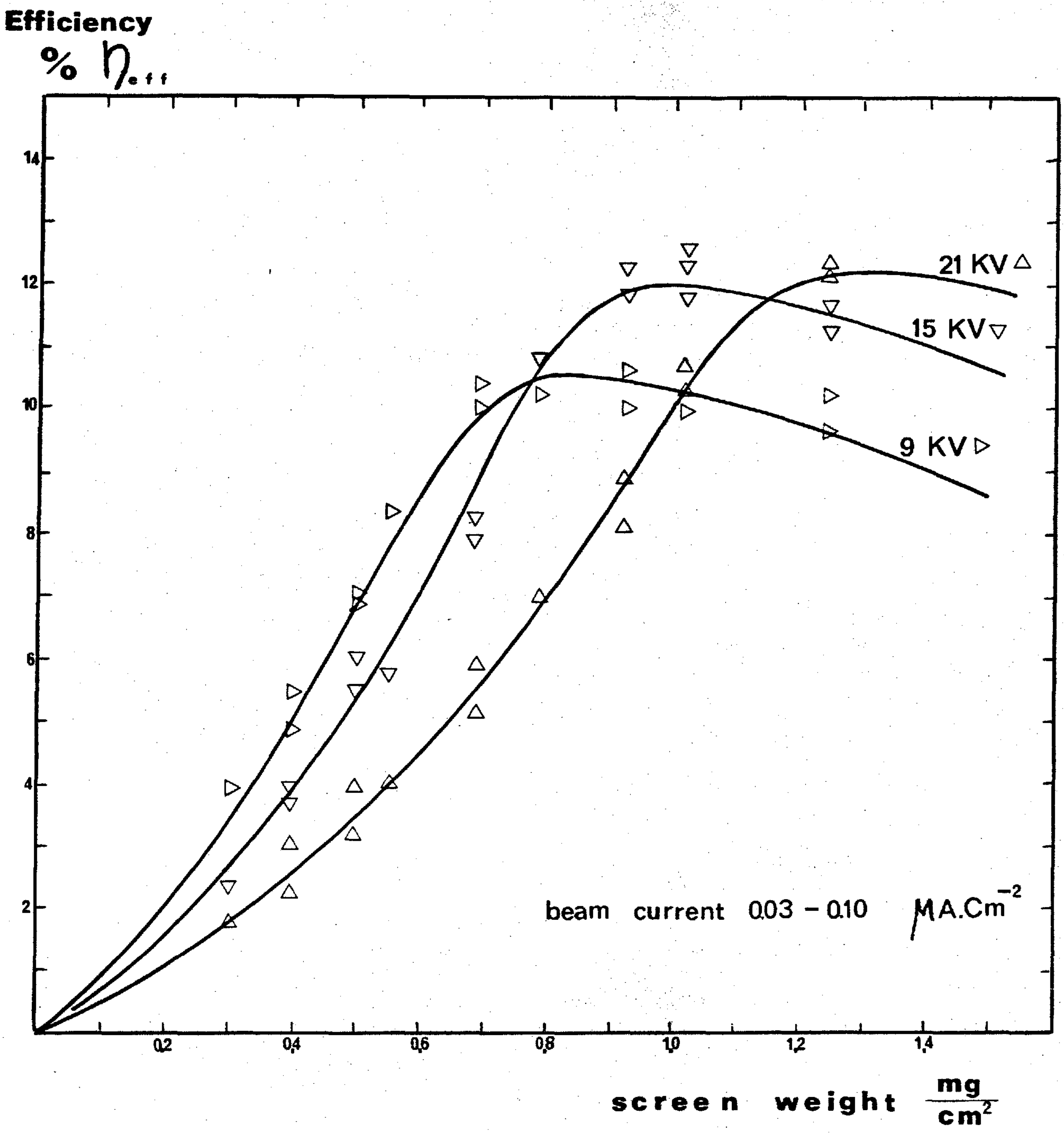

FIG 3.5. SCREENS : EFFICIENCY MEASUREMENTS.

the excitation density is decreased. Schön (1942) and Klassens, et.al. (1948) have proposed a theory explaining this phenomenon involving a migration of holes from luminescent levels to impurity levels. Measurements made by the author (§ 7.3) on the linearity of the cascade tube show however, that no such variation in efficiency (within 6%) occurs when the phosphors screens are bombarded with current densities ranging from 10^{-15} to 10^{-4} Amps/cm^2. This would tend to indicate that the phosphor material used is free from impurities and that the processing and manufacturing procedure does not favour their introduction.

An increase in phosphor efficiency with decreasing temperature has been reported by several workers (Klassens, et.al. 1948, Lehman, 1958, Charman, et.al. 1966). An increase in phosphor efficiency of 16% was measured by Charman on P.11 screens as the temperature was decreased from +19 to −22°C. This effect is enhanced by the presence of impurities.

3.3 DYNODES OF THE PHOSPHOR-PHOTOCATHODE TYPE.

The performance of cascade image intensifiers will depend on the efficiency with which the internal electron multiplication is achieved. If P_λ is the light power emitted by the phosphor at a wavelength λ (maximum P_M at λ_{PM}) and S_λ is the radiant sensitivity of the cathode at λ (maximum S_M at λ_{SM}) then the photocurrent I_2 from the photocathode is given by:

$$I_2 = \int_0^\infty T_D \cdot P_\lambda \cdot S_\lambda \cdot d\lambda = P_M \cdot S_M \cdot T_D \int_0^\infty P_{\lambda r} \cdot S_{\lambda r}\, d\lambda$$

where $P_{\lambda r} = P_\lambda / P_M$ and $S_{\lambda r} = S_\lambda / S_M$ and T_D the transmission efficiency of the coupling.

The total light power emitted by the phosphor is

$$P = P_M \int_0^\infty P_{\lambda r}\, d\lambda = \eta_{eff} \cdot I_1 \cdot V$$

where I_1 is the beam current impacting on the phosphor at a bombarding voltage V and η_{eff} the effective efficiency at V.

The current gain of the dynode is thus:

$$g_D = \frac{I_2}{I_1} = \eta_{eff} \cdot V \cdot S_M \cdot T_D \frac{\int_0^\infty P_{\lambda r} . S_{\lambda r} . d\lambda}{\int_0^\infty P_{\lambda r} . d\lambda}$$

and using eqn 3.2:

$$g_D = \eta_{eff} \cdot V \cdot S_M \cdot T_D \cdot M\,(P- . S-) \qquad (3.7)$$

It is convenient to express the dynode gain as a function of the luminous efficiency of the cathode.

Then using eqn. 3.4, the electron gain of a dynode is given by:

$$g_D = \eta_{eff} \cdot V \cdot T_D \cdot R_L \cdot \frac{680\ M\,(cal.eye) M\,(P-, S-)}{M\ (cal,\ S-)} \qquad (3.8)$$

Values for M (P-.S-) and M (CAL, S-) are tabulated in tab. 3.1 and M (Cal.eye) = 0.071. The dynode gains of several combinations of phosphors and photocathodes were calculated using eqn. 3.8 for V = 15KV and $T_D \approx 1.0$ (mica membrane) and the results are shown in fig. 3.6. It can be seen, for example, that the gain of a typical S20 - P11 dynode (150 μA/lm, 12.5%) will be 35% superior to that of a typical S11- P11 dynode (60 μA/lm; 12.5%). If fibre optics are used for coupling the phosphor to the photocathode $T_D \approx 0.5$ should be used (§ 2.2.6.).

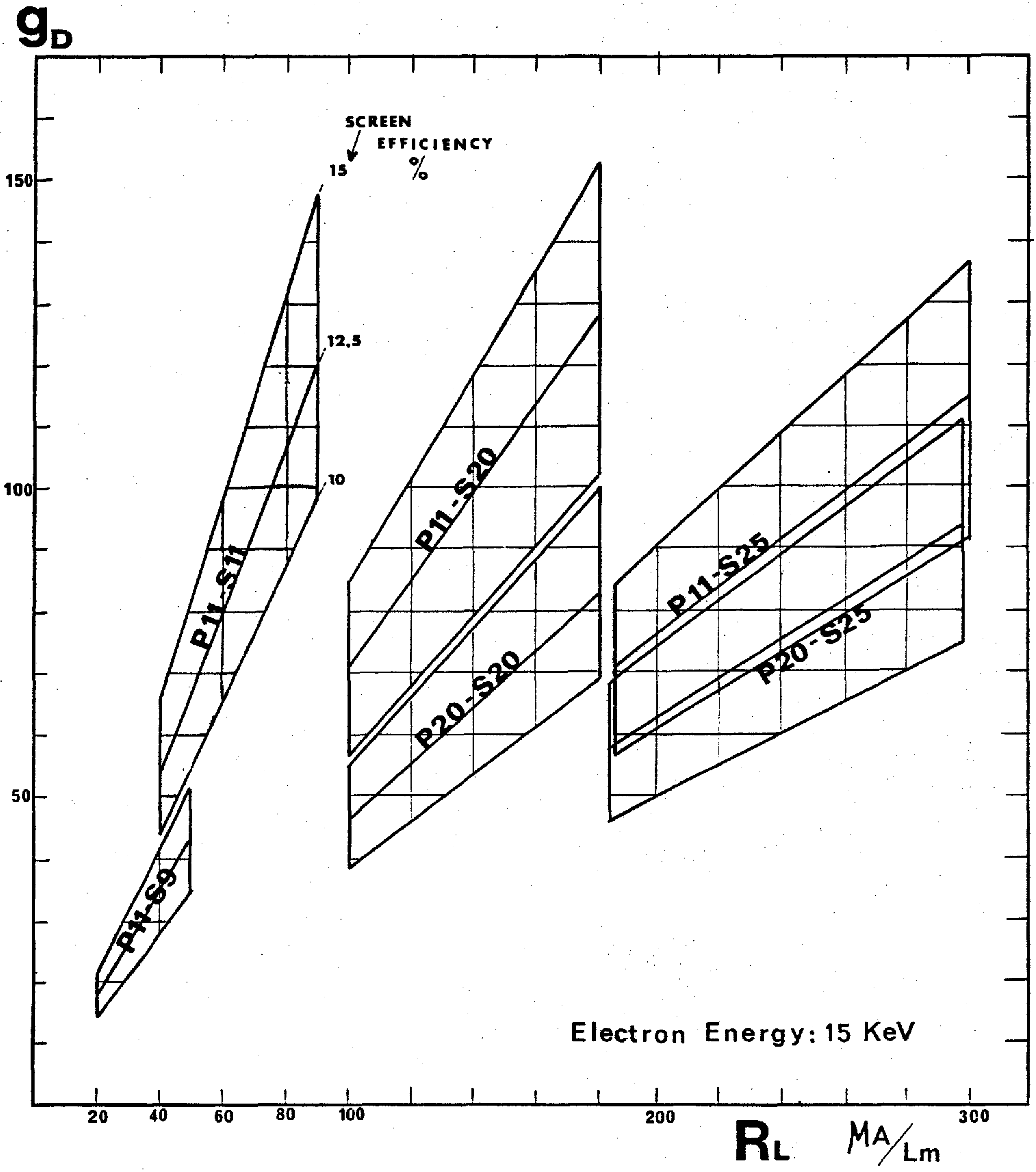

FIG 3.6. DYNODE CURRENT GAIN, g_D

CHAPTER 4.

THE IMPERIAL COLLEGE CASCADE IMAGE INTENSIFIER.

Work at Imperial College on the development of cascade intensifiers began in 1956 in the Applied Physics Department under the direction of Professor J.D. McGee. Early work on an electromagnetically focused two stage tube is reported by Davis.E (1959). This intensifier already incorporated a scheme suggested by McGee (1956.B) for the exclusion of alkali vapour from the high field region of the tube (§ 3.1.4). The acquired experience and techniques were extended by Catchpole (1963) to a three stage intensifier (tab.2.2). Drastic improvements in the performance were obtained after the development of the high quality phosphor screens discussed in § 3.2.5. These new screens and improved photocathodes of the S.11 type were incorporated in the device by Powell (1967), who succeeded, by means of other modifications to the design and processing methods, in improving the performance of the intensifier to a degree which makes its use in various applications possible and quite successful. His latest devices had a resolution of 45 to 50 lp/mm with a quoted light gain of 2 to 10 x 10^5, while the background was sufficiently low to make long exposures possible (tab.2.2). A special cascade intensifier, developed to meet the requirements of sepctroscopy was designed by Varma (1968). The major innovation in this intensifier was the introduction of preformed photocathodes made possible by their small size.

4.1 DESCRIPTION OF THE IMPERIAL COLLEGE CASCADE TUBE.

This intensifier is a three stage magnetically focused cascade image tube with circular working area of 40mm in diameter (12.5 cm^2). All the photosensitive surfaces are $M_nO - Cs_3Sb$ or S11 photocathodes (§3.1.2) and all phosphor screens are made of fine grain ZnS (Ag) or P.11 phosphor (§3.2.5.).

The dynode support membranes are made of mica 4 microns thick.

Fig.4.1 shows a diagram of this intensifier. The envelope (19) is made of precision bore Pyrex tubing and is equipped with two flat Pyrex end-windows. (15 and 16). Metal annuli (9) serve primarily to define the equipotential planes in the accelerating electric field, but also to screen the working space of the tube from spurious optical and electrical phenomena on the glass walls. No electric field is applied in the processing compartment (IV), the advantages and purpose of which were discussed in § 3.1.4.

Annuli are made of springy molybdenum and spring into slots (11) cut into the inner wall of the envelope. The photocathode holder (5), the dynode holders (6 and 7), the processing shelf (8) and the output phosphor holder (10) are all made of stainless steel and are held in position by means of wire springs. A thin carbon layer deposited on these metal parts minimizes reflections of light transmitted by the photocathodes. Thin platinum or tungsten tapes, sealed through the glass wall provide electrical contact between the internal electrodes and metalized rings on the outside wall of the envelope.

The two dynodes (2 and 3) are mounted during assembly of the device respectively on top (cc) of the output phosphor screen (4) and in a dimple (bb, 14) in the processing compartment(IV). The three phosphor screens are facing the envelope wall in order to protect them from caesium contamination during activation. The primary photocathode plate (1) is mounted (aa) on the processing shelf(8) and separates the accelerating region of the tube (III) from the processing compartment (IV) during simultaneous activation of the cathodes.

After processing and seal-off, the photocathode plate and the dynodes are moved through the specially shaped annuli (fig.5.3) and locked in their permanent positions by means of magnetically operated catches.

The resistor chain (20)connected to the metalized rings supplies the desired potentials to the metal parts. Three high voltage cables (21) are connected to

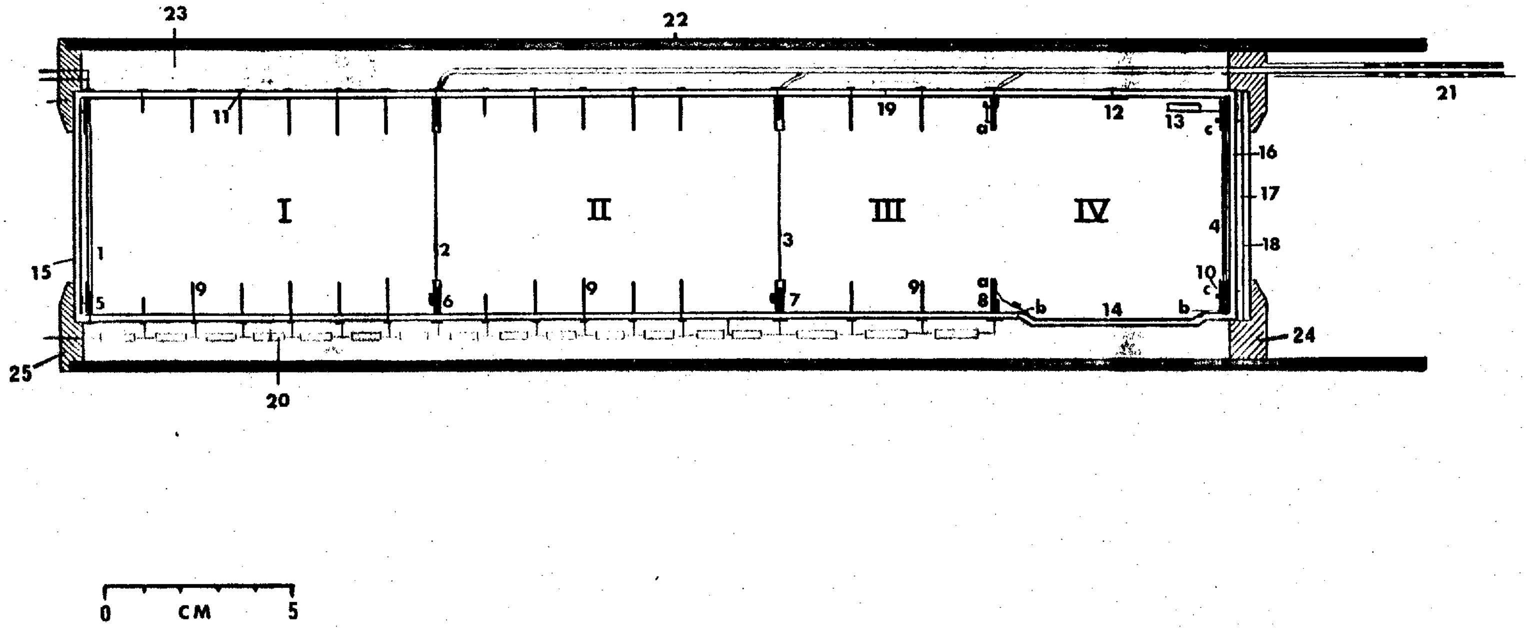

FIG 4_1_ THE CASCADE IMAGE INTENSIFIER

the two dynodes and the output phosphor (the phosphor holder is internally connected to the processing shelf), while the primary photocathode is grounded. The complete tube, coated with black paint, is encapsulated in a Perspex cylinder (22) filled with high insulating material (23).

The following chapter gives a detailed account of the methods used for manufacturing and processing the I.C. Cascade intensifier, a photograph of which is shown on Fig. 4.2.

4.2. OPERATION OF THE I.C. INTENSIFIER.

The encapsulated tube is positioned in a focusing solenoid (§6.1) powered by a highly stabilized current supply, and provides a uniform magnetic field over the whole working space of the image tube. The required accelerating voltages are provided by a high voltage stabilized supply and the potential of each stage can be adjusted by an external potential divider box.

The focusing condition for each stage is given by (Appendix III):

$$L = \sqrt{\frac{2 . \pi^2 . m}{e}} . n . \frac{\sqrt{V_T}}{H} = 335.19 . n \frac{\sqrt{V_T}}{H} \qquad (4.1)$$

where V_T is the stage potential in KV, H the magnetic flux density in Gauss, n the order of the image (or number of loops) and L the equivalent length * of the stage in cm. The design of the tube is such that the three stages have equivalent lengths, so that theoretically the same accelerating voltage is to be used for each stage.

Every tube requires individual adjustment in order to obtain optimum

---

* For stages I and II : L = physical length
for stage (III + IV) : L = (length of III) + $\frac{1}{2}$ (length of IV)

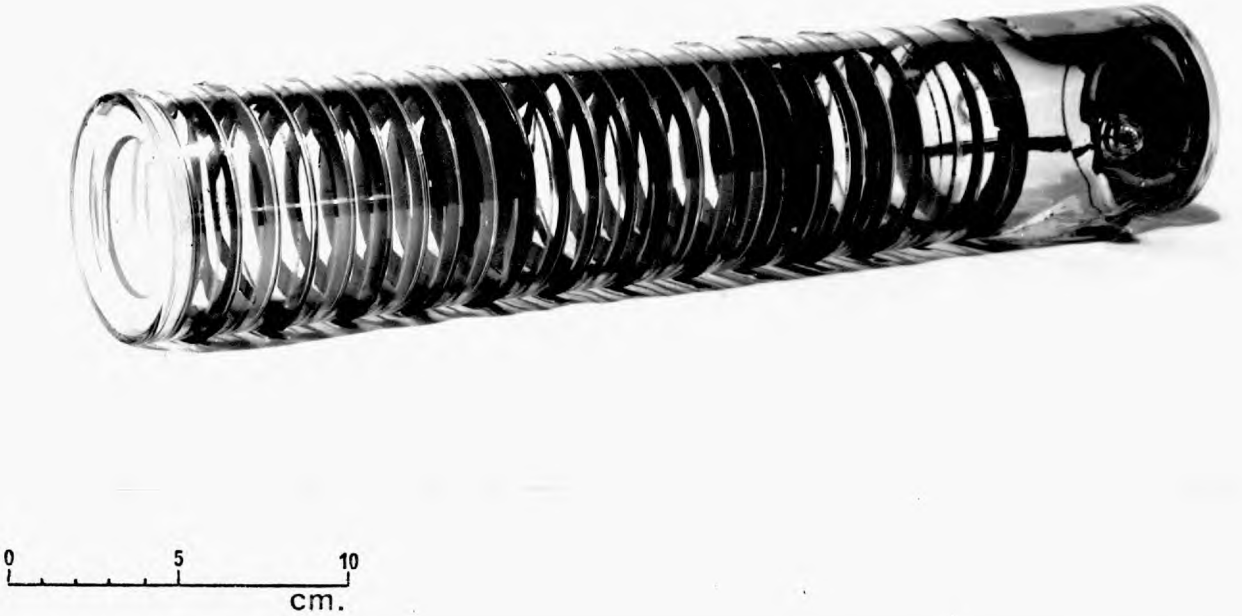

FIG 4.2 THE CASCADE INTENSIFIER

focus. A Baum pattern is projected onto the photocathode (Baum 1962) and the ouput image is observed with a low power microscope (x30). The overall potential is slowly raised to 40 KV and the individual stage potentials (V_T about 13 KV) as well as the magnetic field (H about 135 Gauss for n = 1) are adjusted to give best stage focus. The tube normally requires about 5 minutes to stabilize before final adjustments are made.

4.3 GENERAL PERFORMANCE.

A list of different intensifiers manufactured* in the Applied Physics department and used by the author for the assessment of performance and for experimental investigations is given on tab. 4.3. Several intensifiers, not mentioned in this list, failed mainly because the occurrence of vacuum leaks and accidental damage during the transfer of the dynodes. Much effort was put into minimizing these causes of failure and to increase the sensitivity of the photocathodes.

Tab.4.3. also indicates the major characteristics of the I.C. intensifiers. A constant, limiting resolution of 48 to 55 lp/mm is obtained in all intensifiers but the light gain varies between 7.10^4 and 2.10^5 depending on the success with which the photocathodes were activated. Background and geometry are generally acceptable for most practical applications.

---

* Messrs. B.Weekly, R. Rainger, G. Busby.

CASCADE INTENSIFIERS . No.	Photocathode Sensitivity in μA/Lm.	Resolution in Lp/mm.	Blue Light Gain .	Notes.
73	40	52	$3.5\ 10^4$	
76	48	53	$1.0\ 10^5$	
78	43	55	$1.2\ 10^5$	
82	45	53	$9.0\ 10^4$	
91	36	52	$7.5\ 10^4$	
94	51	50	$2.3\ 10^5$	
95	45	50	$9.0\ 10^4$	
97	56	50	$1.1\ 10^5$	Angiograph I.
99	40	48	$8.7\ 10^4$	
100	70	45		P20 Output Phosphor.
103	38	51	$3.6\ 10^4$	
104	45	49		
107	56	56	$1.0\ 10^5$	
108	44	50	$7.5\ 10^4$	
109	50	53	$9.0\ 10^4$	
112	30	50		Equal Stages .
113	58	52	$1.2\ 10^5$	Angiograph II.
Single Stage Intensifiers				
A	50		56	30 cm long.
B	59		69	30 cm long.
C	65	132	71	9 cm long.

TAB. 4.3 PERFORMANCE

CHAPTER 5.

MANUFACTURING AND PROCESSING METHODS.

5.1 THE PHOSPHOR SCREENS.

5.1.1. Transparent Substrate Preparation: The output phosphor screen support is a 1 mm thick soda glass disk (45 mm OD), while the dynode substrate is a 3 to 4 microns thick mica[a] disk (44 mm OD) sealed between two 0.020" thick titanium rings (40 mm I D; 45 mm OD) with low melting point (400°C) solder glass[b]. Each titanium ring is glazed with solder glass by RF heating. The mica sheet is placed on the glazed surface and heated on an electric hot plate (fig.5.2.a) until the glass melts. The work is allowed to cool slowly before the other titanium ring is sealed in a similar manner. Because of the slightly higher coefficient of thermal expansion of mica, 9 to 12 x 10^{-6} compared with 8.5 x 10^{-6} for titanium (Rosebury 1964), the mica membrane is left under slight tension and hence is very flat. A small ring of fired bright platinum paint[c] provides good electrical contact between the titanium ring and the photocathode or phosphor backing.

5.1.2 Temporary Conducting Layer: A layer of aluminium about 500 Å thick (10% transmission) is evaporated onto the substrates in a demountable vacuum chamber in order to provide a conductive film for the electrophoretic deposition of the phosphor grains (Airey 1964).

5.1.3 Preparation of the Phosphor Powder Suspension: Two stock solutions are prepared; Solution A: 1.0 gr. Lanthanumnitrate, 0.5 gr. Aluminium nitrate,

---

a. The letter indexes refer to a list of products and manufacturers given in Appendix V.

95 ml. isopropyl alcohol and 5 ml. distilled water.
Solution B: equal volumes of glycerol and isopropyl alcohol.
750 mg. phosphor powder[d] are dispersed into a mixture of 2 ml. of solution B and 3 drops of solution A. Continuous rotation in a flask containing glass beads for about 5 min. provides a viscuous suspension. 195 ml. of isopropyl alcohol, 3 ml. of solution A and 5 ml. of double distilled water are then added and the mixture is subjected to ultrasonic agitation for a further 5 min.

5.1.4 Electrophoretic Deposition: The aluminized substrate is immersed in this suspension in the apparatus shown in fig.5.1.b. A suitable potential is applied between the substrate and the anode to give a current of 20 m A. The highly charged Al^{+++} and La^{+++} ions on the surface of the phosphor grains cause the acceleration of the suspended positively charged particles towards the substrate to form a compact layer. The duration of this process is about 60 sec. for a 1 mg/cm^2 layer. The screen is then dried and weighed. The increase in weight of the substrate gives the "thickness" of the screen in mg/cm^2.

5.1.5 Etching of the Aluminium Film: The screen is immersed in a bath, containing 3.5 gr. of ammonium persulphate, 5 ml. of ammonium hydroxide (0.88 sg.) and 200 ml. double distilled water; during 10 to 15 minutes. This dissolves the aluminium film without evolution of gas, leaving the phosphor layer adhering to the insulating surface. The screen is washed thoroughly in running distilled water for several hours to remove all traces of this chemical bath.

5.1.6 The Aluminium Backings:

By covering the phosphor layer with an organic film, as it is currently used for CRT application (Epstein, et.al. 1946. Bayford, 1952), it is possible to evaporate a continuous layer of Aluminium in close contact with the phosphor

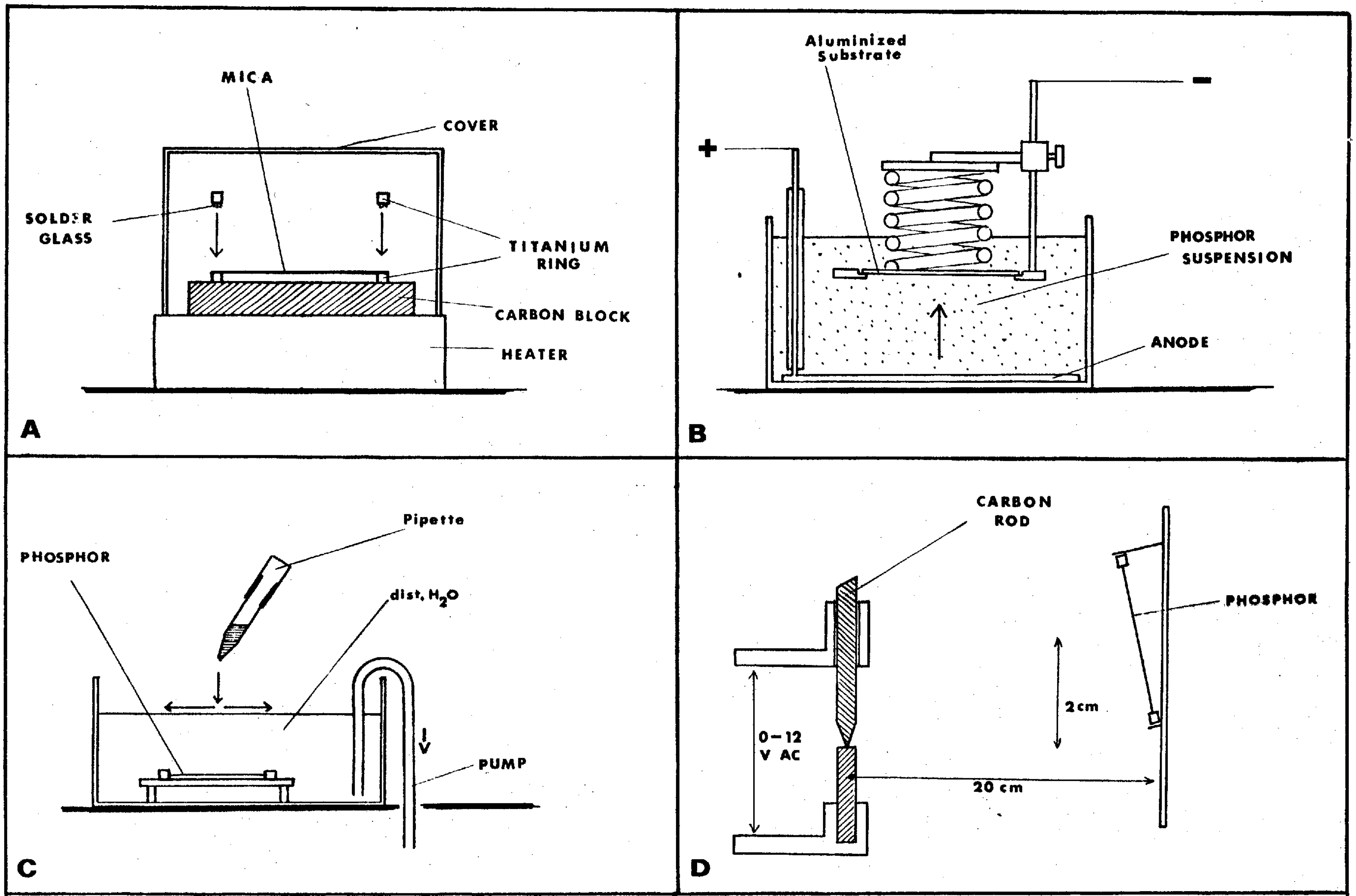

FIG 5.1 SCREENS PREPARATIONS

grains. The filming solution is a nitro-cellulose compound[e] to which a plasticizer (Bytyl, Phthalate or Butyl benzoate) and a solvent (Amyl acetate, n butyl acetate or ethyl lactate) are added. The phosphor screen is immersed in double distilled water (fig.5.1.c) and a drop of filming solution is added. The solution spreads out over the surface in a very thin layer (about 1000 Å). The water is syphoned away allowing the film to drop evenly onto the phosphor surface. Aluminium is evaporated onto the organic film at a pressure of about 10^{-5} torr. Its thickness is monitored visually until complete loss of transmission occurs, corresponding to a film of about 800 Å (Zworykin, 1954). The organic film is then removed by baking the screen at 360°C for 10 min. in air.

5.1.7 Anti-Reflection Coating:

A thin layer of carbon is evaporated onto the phosphor screen from an arc produced between the ends of two spectrographically pure carbon rods (fig. 5.1.d). This is done in a demountable pump at a pressure of about 10^{-5} torr (Rhoads, 1962).

5.2 THE VACUUM ENVELOPE.

5.2.1 Glass Work:

Glass envelopes are prepared by the departmental glass-blowers* from precision bore Pyrex glass tubing (57.2 ± 0.1 mm. ID; 2.7 ± 0.4 mm thick walls). The glass used is similar to Corning type 7740 (Rosebury, 1964) Fig.5.2 shows a sectional diagram of the envelope. Slots are cut in the inside wall of the tube with a diamond wheel at the location to be occupied by each metal part.(depth: 0.75 mm. width: 0.50 mm). A small recess is cut at the cathode side of each slot as shown in fig.5.2 (detail). Because of the reduced

---

*Messrs. Beseigel and Yarwood.

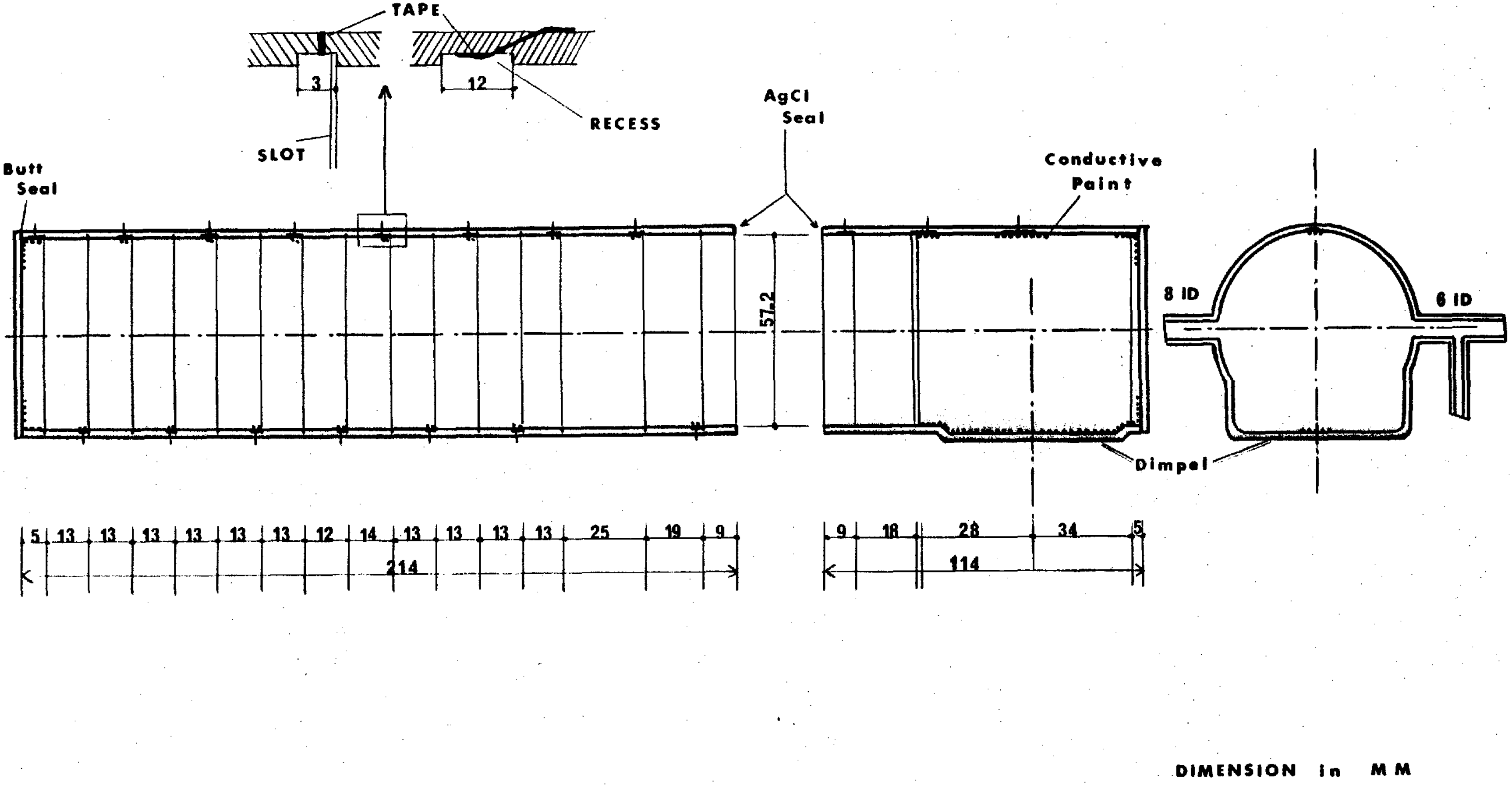

FIG 5.2 THE GLASS ENVELOPE

thickness of the wall, the insertion of a tape in this area can be performed with little glass distortion and conductive paint connecting the metal part to the tape is localized in this area only.

5.2.2 Electrical Connections: Contact between each metal part and the outside of the tube has been successfully achieved, since early work on this device, by a thin platinum tape (expansion: 90×10^{-7}) inserted into the Pyrex glass wall (expansion: 36×10^{-7}). (Davis, E. 1958; Rosebury, 1964). To remedy recent systematic leaks occurring at these contacts, the use of a better matched seal using tungsten tapes (expansion: 46×10^{-7}) was introduced by Airey (1970) This seal relies on the formation of oxides, which are readily "wetted" by the fused glass. Tungsten tapes [g] (0.27" wide, 0.02" thick, 1" long) are electrolytically cleaned (Rosebury, 1964) and beaded with Pyrex glass leaving only one end exposed. Each tape is inserted, exposed end inside, into the recessed area using a highly localized flame, as shown in fig. 5.2 (detail). The outside end of each tape, beaded with glass to protect the tungsten from burning under the flame, is exposed by careful removal of the glass with a carborandum wheel.

All internal slots are flame-polished to avoid any sharp glass edges, the processing compartment is equipped with sidearms and two Pyrex end windows (62 mm diameter, 2.5 mm thick) are sealed to the tube by means of "butt-seals" (Barr, et.al. 1949). The open ends of the two halves of the body are cut and polished to the correct dimensions.

5.2.3 Final Preparation of the Envelope: Both ends of the tungsten tapes are again electrolytically cleaned and gold plated. Conductive platinum paste [h] is applied in the recesses of the cleaned tube between the tape end and the adjacent slot into which annuli are sprung. Further platinum paste[h] connections are made to the output phosphor plate (there is no tape in this location) and to the small anode (12) used for monitoring the processing of the cathodes. Rings of silver paste[i] , making contact to each tape, are painted on the outside wall of the envelope and bright platinum[c] is applied on the polished end faces to provide a wettable surface for a silver chloride seal. All these paints are fired into the glass by heating the work to 600°C for 10 min. The platinum paste surfaces are polished to a smooth finish before final cleaning and drying of the envelope.

5.3. METAL PARTS

5.3.1 Design and Materials: Complete plans of the metal parts used in recent tubes are shown in fig. 5.3. Several modifications in their design have been carried out as compared to that adopted by Powell(1967) . All photocathode surfaces are now mounted in the plane of the anode side surface of their holder. This has produced marked improvements in tube geometry (§ 9.3). An alternative mounting method of the processing shelf between two small molybdenum annuli has greatly facilitated the assembly of this component and has improved the separation of the processing compartment during activation. A new design of the photocathode holder, locked against the end window with a small annulus, and the introduction of "butt" sealed end windows has made it possible to minimize the distance (4 to 6 mm) between the photocathode surface and the outside surface of the front end window. This is important when high speed input optics are to be used because of the short backdistance of such lenses.

5.3.2 Preparation of the Metal Parts: The parts, manufactured in the departmental workshop* are degreased, electropolished (Rosebury, 1964) and vacuum stoved to 1000°C for stainless steel and to 700°C for molybdenum.

---

* Mr. R. Barr

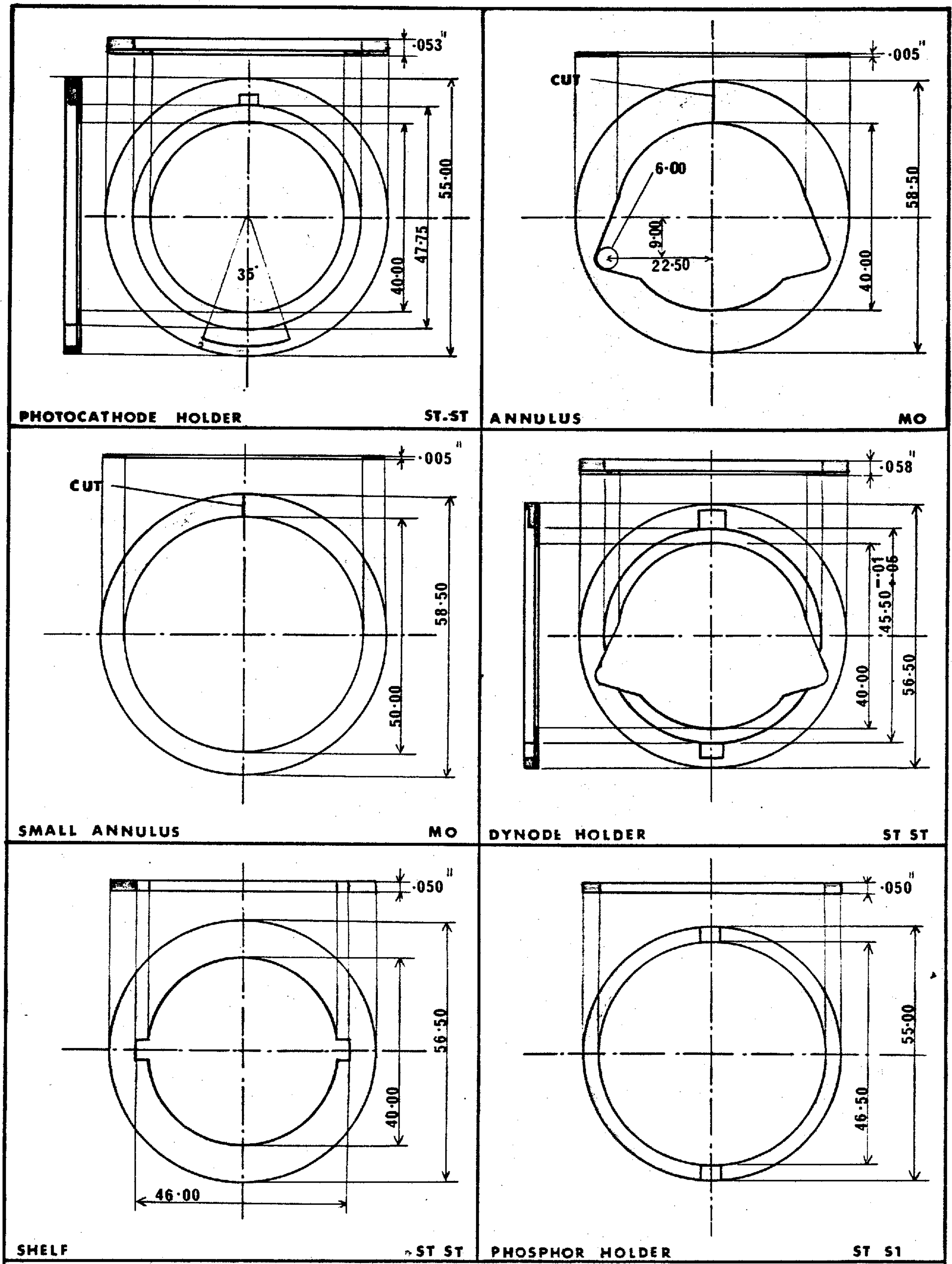

PHOTOCATHODE HOLDER ST.ST

ANNULUS MO

SMALL ANNULUS MO

DYNODE HOLDER ST ST

SHELF ST ST

PHOSPHOR HOLDER ST S1

SCALE 4/5 DIMENSIONS IN MM

FIG 5.3 METAL PARTS

They are equipped by spotwelding with various springs, clips, stops and catches made of Nimonic wire[k], soft[l] and hard[m] Inconel strips. (fig. 5.4) Sharp points are removed by buffing and additional electropolishing is performed. The annuli and dynode holders are etched chemically (Rosebury, 1964) or by sand blasting to produce a surface onto which carbon can adequately be evaporated. This is done in a demountable vacuum system at a pressure of 10^{-5} torr. All the parts are finally degassed in a good vacuum (10^{-7} torr) by eddy current heating to a dull red. Fig. 5.4 shows a photograph of all the components prior to assembly.

5.4 ASSEMBLY AND PREPARATION OF PHOTOCATHODE PROCESSING.

5.4.1 Assembly: The metal parts are assembled in the glass envelope under conditions of high cleanliness. Fig. 5.5.A. shows how the output phosphor (4), the two dynodes (b and c) and the photocathode substrate (a) are assembled in the processing compartment (IV). A flashless getter (13) is attached to the phosphor holder. The two parts of the tube are joined together by means of a silver chloride seal (19) under a steady stream of argon to avoid oxidation of the metal parts and the complete tube is joined to the pump by sidearm Q. The pumping system is a mercury vapour diffusion pump equipped with two coldtraps. A third coldtrap (J), located above the pumptable, is filled during seal-off to provide extra pumping speed. The pressure is monitored with an Alpert gauge M.

5.4.2 Sources for the MnO - Sb - Cs Photocathode Activation: The manganese evaporator (A) is omnidirectional and consists in a simple RF pick-up coil connected to a thin tungsten wire, electroplated with Mn in a special bath (50 gm $MnSO_4 \cdot 2H_2O$, 37.5 gm $(NH_4)_2SO_4$, 30 gm NH_4CNS and H_2O to make 500 cc.) The oxygen source (B) is a bulb containing $KClO_3$ which liberates O_2 upon gentle heating. The pumping speed can be reduced by a ball valve (H). The

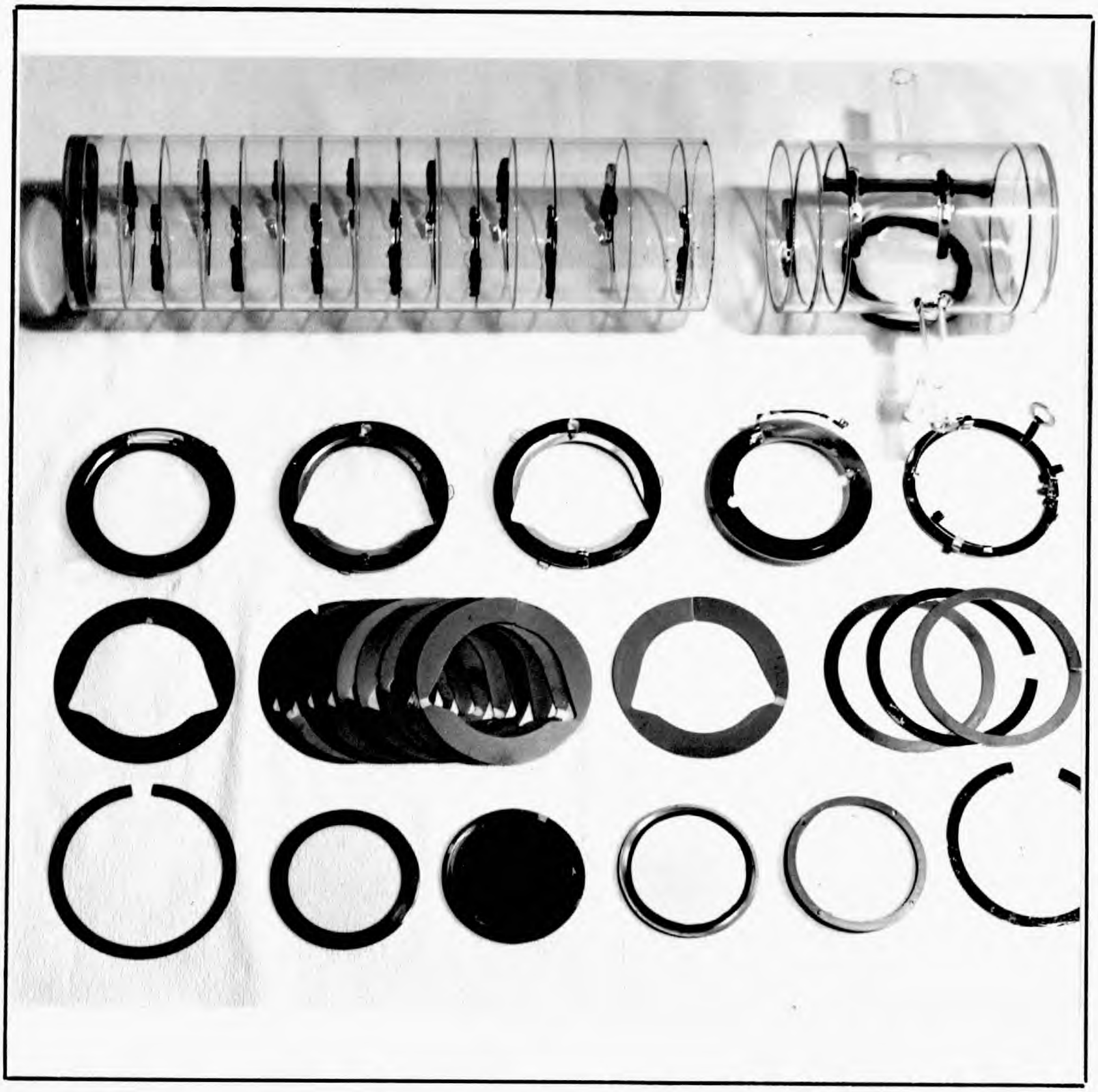

FIG 5.4 ENVELOPE & COMPONENTS

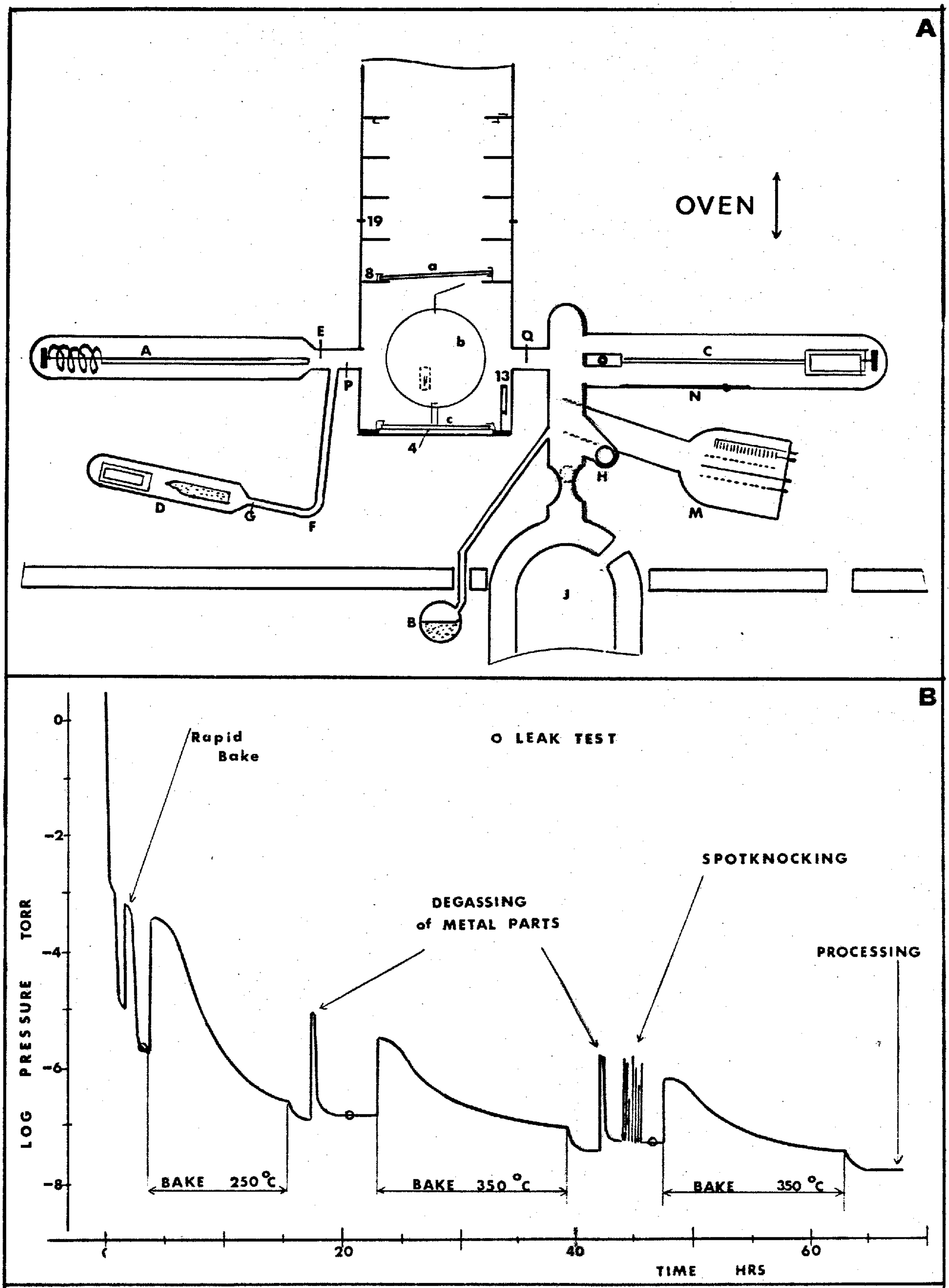

FIG 5.5 PUMPING SET - UP & SCHEDULE

Antimony evaporator(c) is shielded to allow evaporation of each surface separately. A composite mesh is interposed to provide uniformity of evaporation. Eddy currents induced by a low coupling pick-up coil, heat a tantalum filament which supports an Sb bead on a nickel disk. The caesium source (D) is an ampoule into which Cs has been distilled from a mixture of $Cs_2\ Cr\ O_4$ (1 part), Al-powder (1 part) and W-powder (5 parts). This capsule is broken under vacuum with a glass covered magnetic hammer.

5.4.3 Pumping and Baking: A typical schedule of evacuation and baking is shown in Fig.5.5.B. in the form of a pressure - time diagram. Leak testing is done by applying CCl_4 on possible leak locations and watching for any rise or fall in pressure. The annuli are degassed by heating them to dull-red with an eddy current heater. "Spot - knocking" is an operation performed in order to minimize the amount of sharp emission points on metal parts and at painted electrical contacts. A voltage of 10 to 25 KV is applied between two consecutive annuli (in the first two stages only) during the time required to make eventually resulting fluorescent streaks on the glass walls and localized emission points disappear. The tube is ready for processing when a pressure of about 10^{-8} torr is achieved.

5.5 ACTIVATION OF THE S.11 PHOTOCATHODES.

Oxygen is released by heating bulb B with the ball valve H closed. A white discharge is generated in the processing compartment with a Tesla coil for about 60 sec. This process cleans the substrates and possibly introduces an adsorbed layer of oxygen.

5.5.1 Manganese Evaporation and Oxidation: Manganese is then evaporated onto the three substrates simultaneously. The amount deposited on the primary photocathode plate is monitored to give a decrease in transmission of 5 to 10%. The thickness is not considered critical (RCA. 1961). The manganese layer is then oxidized by readmitting oxygen and generating a discharge for about 30 sec. The transmission goes up to reach a value close to 100%. The manganese sidearm is sealed off at E. All the metal parts are degassed again and the top part of the tube is baked with an electric heater tape to 300°C for about 60 min. After cooling, the photocathode plate a is allowed to fall flat on the processing shelf by magnetic operation of catch (K). This produces an efficient separation of the active region of the device from the processing space (§ 3.1.4). The caesium capsule (D) is broken, caesium is driven into the sidearm (F) and the source is sealed off at (G).

5.5.2 Precaesiation: A heater wire is wound around the caesium sidearm from (G) to (P) and a photosensitivity monitoring system is installed so that photoemission from the cathode plate a can be detected (collector 12). The temperature of the complete system is raised to 160°C while caesium is kept in the sidearm by a flow of cold air at (P). Caesium is released into the processing chamber by stopping the air flow and heating the sidearm with the heater wire until a first maximum in photoemission is detected (0.05 to 0.20 μA/lm).

5.5.3 Antimony Evaporation: The system is cooled to room temperature and antimony layers are evaporated onto the three surfaces in turn. The thickness of each layer is accurately monitored to correspond to a 28 % increase in reflection on the two micas and a 28% decrease in transmission on the photocathode plate for a light beam incident at 45°.

5.5.4 Final Caesiation. The temperature of the system is then raised again to 160°C and left to stabilize for 15 min. Caesium is introduced as before and photosensitivity of the primary cathode is monitored. The sensitivity first rises rapidly to a maximum (about 40 μA /lm). Caesium admission is stopped to allow any excess to be baked away. The sensitivity reaches a minimum and more caesium is then introduced. The temperature of the oven is allowed to drop slowly while more caesium is introduced whenever the sensitivity falls to a minimum. Successive maxima of increasing photosensitivity are obtained until the temperature is about 100°C, after which the tube is cooled rapidly to room temperature. The final sensitivity is usually 50 to 100 μA/lm.

5.5.5 Seal-off.

The cold trap (J) is filled with liquid nitrogen to provide additional pumping speed while the sidearm is sealed off at (P) and the complete tube is sealed off from the pump at (Q). The sensitivities of all cathodes are then measured with a standard lamp.

5.6 TRANSFER AND ENCAPSULATION.

The photo surfaces are moved to their respective final positions in the intensifier. The resistor chain is soldered directly onto the metalized rings so that the resistance between two metal parts is 40 MΩ, made up of four 10 M resistors[n]. (1 Watt. 500 V max.). The outside wall of the processing compartment is painted with Aquadag and the whole envelope with non-conductive black paint[p] leaving the two end windows clear. A silica window[q] is mounted on the high tension end of the tube to prevent electrical breakdown. (Fig. 4. 1) It (18) is cemented onto a small glass disk(17), itself cemented onto the end window with cold setting optical resin[r]. A Perspex end cap (24) fits onto these windows producing a reliable high voltage insulation. After connection of the high voltage cables[s], the complete work is primed[t] and located centrally in a Perspex cylinder (88 mm OD) with the two endcaps (24 and 25). The space between the tube and the Perspex cylinder is subsequently filled with cold setting silicone rubber[v] previously degassed in a desmountable pump. Finally the outside wall of the encapsulation is coated with a conductive layer to prevent any charge build-up upon its surface. A Photograph of an encapsulated intensifier is shown on Fig. 5.6.

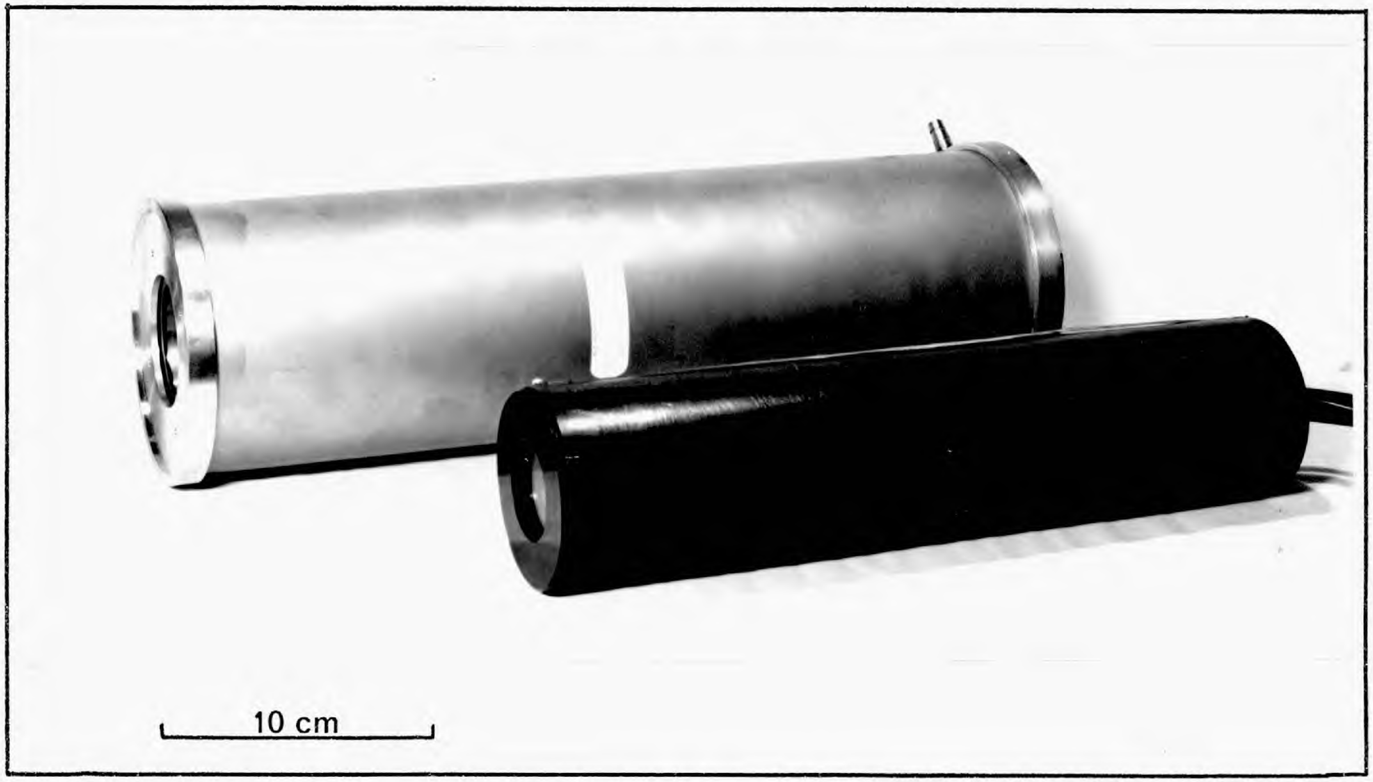

FIG 5.6 INTENSIFIER & SOLENOID

CHAPTER 6.

ANCILLARY EQUIPMENT.

6.1. THE FOCUSING SOLENOID

A light weight solenoid has been designed for operation of the three stage cascade tube to replace the heavy and bulky focusing coil used by previous investigators in this department (Powell, 1967). This new type of solenoid, supplied by a low voltage - high current source, produces a maximum field of about 300 Gauss with a field uniformity better than ± 1%. The solenoid is cooled and shielded from external field interference.

Lack of uniformity in the magnetic field causes geometrical S-distortion of the image due to radial field components. As will be shown in § 8.3.2 it can also result in a deterioration of resolution. The absence of magnetic shielding from external fields can also cause geometrical distortion, loss in resolution and drift of the image if this external field is variable both in intensity and direction with respect to the intensifier (For example, the case of operation on a telescope in the earth's magnetic field).

The advantages of winding a solenoid with large, as compared to small diameter wire, result from the fact that the thickness of the insulation of any circular conductor is practically independent of its diameter. Therefore, the ratio of active (conductor) volume to total volume increases as the core diameter increases. This increase in packing with conductor diameter will result in a decrease in required power for a solenoid of fixed geometry designed to produce a given field, and in an increase in thermal conductivity of the bulk (conductor plus insulation) of the windings. (Kroon, D. 1968).

6.1.1 Design of the Solenoid.

Fig. 6.1 shows a sectional plan of the solenoid. Dotted lines indicate the position of the image tube. The distance between the photocathode and the front end of the solenoid is kept small (3 to 4 cm.), permitting the use of high aperture input optical systems. The cooling jacket (W), located between the encapsulation of the intensifier and the windings, is made of two concentric copper cylinders soldered to two brass end pieces (A and B). The coolant (normally tap water) entering the coil is driven directly to the front end by a partition inside the jacket. Magnetic shielding is achieved by two concentric high permeability MU - metal cans. A flange (F) attached to the front end of the solenoid and the back end piece (B) serve to support the coil without damaging the strain sensitive MU - metal cans.

6.1.2 Required Number of Windings.

The solenoid should produce a magnetic field of about 300 Gauss in order to be able to focus the intensifier operated at 45 KV with 2 loops (eqn.4.1).

It is important to consider first the characteristics of the current supply to be used in conjunction with the solenoid. To obtain the maximum field using a supply, with maximum current I max and maximum voltage Vmax, the solenoid resistence should be Vmax / I max. If the coil resistance is made greater than Vmax / I max by the addition of windings no further increase in the magnetic field will result. Although the number of windings increases, the current (Vmax divided by the coil resistance) decreases so that the number of Ampere - turns remains constant*. The power supply** chosen to operate with the solenoid has Vmax = 60V and I max = 5 A and a maximum solenoid resistance of 12 ohm will lead to the

---

* The number of A.T. will actually decrease slowly as the number of turns is increased, since a turn added on the outside of the coil has a larger resistance and creates a lesser field than one located closer to the axis. ** Roband Type 60:5 - Charlwood - Surrey.

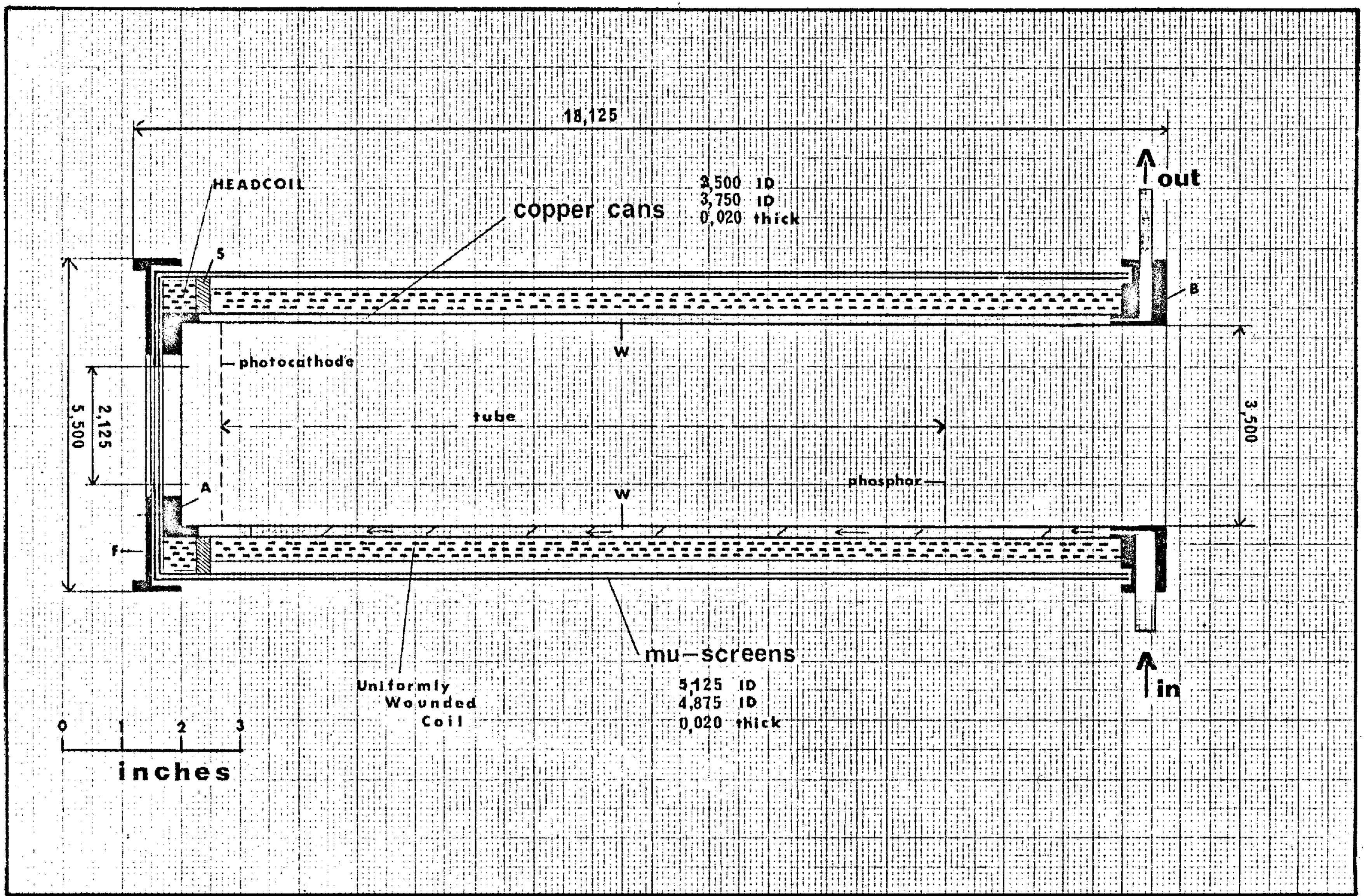

FIG 6.1 THE SOLENOID

maximum field.

The windings of the solenoid consist in a 40 cm. long uniformly wound coil and of a headcoil, necessary for the rapid rise in magnetic field at the front of the solenoid. The required number of windings for a uniformly wound coil were calculated by means of equations published by Kron. D (1968) and Montgomery (1969). It was found that the two conditions, 60 Gauss/Amp (300 Gauss at 5 Amps) at the centre of the solenoid and a resistance of 10 ohm (in order to allow for additional resistance of the headcoil), are achieved if 7 layers of 350 windings each of 18 BSG copper wire are used. The use of wire with bondable insulation greatly facilitates the winding of a coil and improves the thermal conductivity of the bulk. Unfortunately, this wire is not available commercially for gauges lower than 20 BSG. Therefore, the coil is made in two sections of 20 ohm resistance connected in parallel. This is equivalent to a single coil delivering 120 Gauss/Amps with an equivalent resistance of 40Ω. Calculations show that this can be achieved by winding 20 BSG copper wire in two sections, each having 10 layers of 205 windings.

6.1.3 Winding and Correction of the Solenoid.

Four 10 cm. long sections (20 BSG wire) each having 10 layers of about 100 windings, were wound onto mandrels and mounted on the cooling jacket. They are connected two by two in series and these two sections in parallel. The field distribution from this coil is shown in Fig. 6.2. In order to determine the required number of Ampere - turns for the headcoil, an arbitrary headcoil of Na turns is connected to a second current supply. The current I_a in this coil is adjusted so that the resulting field maximum at the front end of the solenoid is equal to that in the centre of the main coil, supplied with a current I_0 (Fig.6.2) The number of turns in the permanent headcoil will be given by $I_a \cdot Na / I_0$ It was found that the sharpest rise in magnetic field was obtained if a gap (S in Fig.6.1) was left between the headcoil and the main windings of the solenoid.

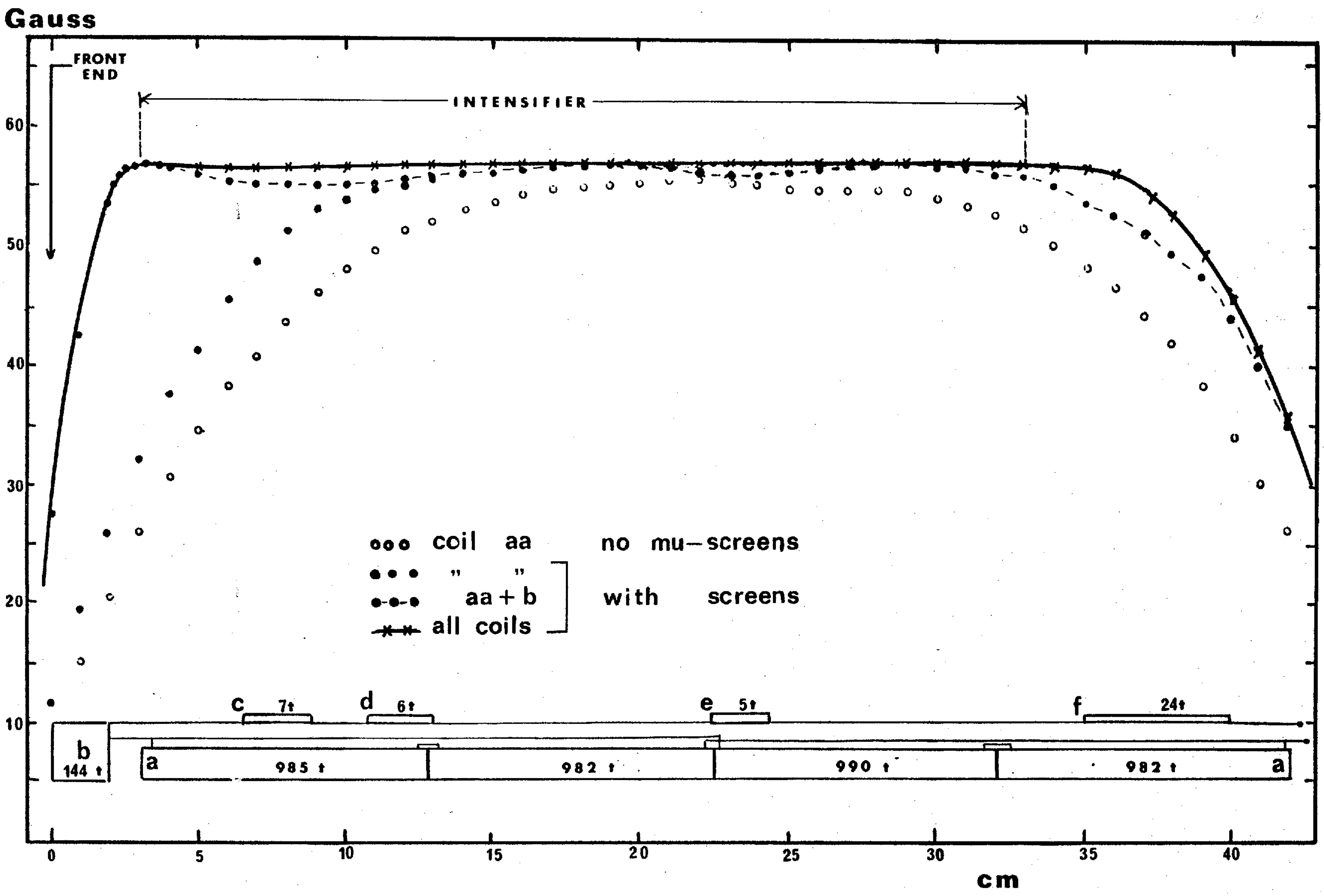

FIG 6.2. CORRECTION of FIELD COIL C

This corresponds with the negative windings added behind the headcoil in the Spectracon - solenoids (McGee 1970). Additional turns are placed at the back of the coil to increase the region of uniformity up to about 33 cm. from the front of the coil. The uniformity of the field is at that stage well within ± 1%. Eventual positive or negative turns are added where the field profile still contains some marked irregularities.(Fig.6.2). Tab. 6.3 shows the characteristics of several solenoids developed in this department under the supervision of the author for various applications.

6.1.4 Efficiency of the Screening.

Mu - metal has, according to data from the manufacturer* , an initial permeability of 45,000, a maximum permeability of 100,000 and a saturation of 8000 Gauss. Assuming a flux density of 300 Gauss inside the coil (section: 61 cm^2) and equal penetration of the field lines through the two shields (section: 5.08 cm^2), then the flux density in the Mu - metal is about 3600 Gauss, well below saturation.

The screening efficiency of a typical solenoid (D) was measured by a similar method as that used by McGee et.al. (1969.A). An efficiency of 950 was found for a field perpendicular to the axis of the solenoid. A deflection of 5 microns would be significant for an image resolution of 50 lp/mm. Therefore, according to eqn.6.1, it is undesirable to have a transverse field variation inside the solenoid higher than 5.10^{-3} Gauss during an exposure. A transverse field variation outside the solenoid of 4.5 Gauss can thus be tolerated, which is much higher than the eventual changes in the earth's magnetic field.

---

*Magnetic Shield Ltd. Staplehurst, Kent.

COIL symbol	B[5]	C	D	E	BX[4]	
Main Coil . Gauge	18[3]	20	20	20	20	BSG
Total Length	40	4x10	4x10	4x9.7	4x9.7	cm
Number of Layers	7	10	9	10	10	-
Head Coil . Gauge	18	20	20	18	20	BSG
Number of Turns	272	150	144	164	-	-
Solenoid Resistance	16.0	11.0	12.0	10.3	10.6	ohm
Gauss / Amps	80	63.2	58.0	61.5	62.1	G/A
Maximum Field	300	316	290	308	310	Gauss
Dissipation[1] 1 loop	46	51	66	48	54	Watts
2 loops	184	204	264	194	215	Watts
Gauss / Watt "	1.48	1.33	1.03	1.40	1.26	G/W
Axial Uniformity	±0.7	±0.35	±0.25	±0.55	±0.25	%
Edge Uniformity[2]	-	1.00	0.35	0.90	0.40	%
Scanning Coils	0	1	2	0	0	-

Notes: 1.for 136 & 272 Gauss. 2.at 2 cm from the axis. 3. wire with no bondable insulation. 4.for Dr.Boksemberg.University College .London. 5.for Angiograph.

FIG 6.3 SOLENOID DATA

6.1.5 Deflection Coils.

The possibility of displacing an output image across the phosphor screen without altering the position at the photocathode is a very attractive one. The image of a spectrum, for example, could be broadened in a direction perpendicular to that of dispersion, enabling the registration of more information. It also makes it possible to use phase resolving techniques for images whose intensity varies periodically in time. Furthermore, it could be used for taking several exposures of a small image without altering the ancillary optics. Image deflection in an electromagnetically focused image tube can only be achieved successfully by applying a transverse magnetic field (H_T). If Ha is the axial magnetic flux density and L the length of a stage, then the total deflection δ in the cascade tube is given by (Bǎćik, 1970):

$$\delta = 3\left[\left(\frac{H_T}{Ha}\,L\right)^2\left(1+\frac{1}{n^2\pi^2}\right)\right]^{\frac{1}{2}} \approx 3\,\frac{H_T}{Ha}\,L \qquad (6.1)$$

where n is the number of loops used for focusing. The angle between the transverse field and the direction of the deflection is given by arctg $1/\pi n$, which equals 17.6° and 9.0° for one and two loops focusing respectively (Ha = 135 Gauss and Ha = 270 Gauss).

Deflection coils have been placed in two of the solenoids described above. They are located between the MU - metal screens and the windings and extend over the full length of the solenoid. With 25 turns of 30 BSG wire a deflection sensitivity of 5.6 mm/Amp and 2.8 mm/Amp is obtained when the intensifier is focused in one and two loops respectively.

6.1.6 Cooling

The solenoid is normally operated with tap water cooling (12 to 15°C) at a rate of ~ 1 litre/min. The temperature of the primary photocathode of a simulated tube, measured with a calibrated thermocouple, was found to be 19 to 24°C when the coil dissipation is 250 W. If more cooling is required, a closed circuit refrigeration system could be used or thermoelectric cooling devices (Peltier - effect) could be incorporated in the vicinity of the photocathode (McMullan et.al. 1968).

6.2 POWER SUPPLIES

In order to permit long exposures without altering the optimum focusing conditions, both high voltage supply (providing the accelerating potentials) and low current supply (providing the current for the solenoid) must be highly stabilized. According to measurements reported in § 8.3.3 a change of 0.5% in the magnetic field or a change of 1.0% in the overall accelerating voltage will affect the limiting resolution of the intensifier by 4% (50→48 lp/mm). In terms of power supply specification this means that the sum of load regulation, line regulation and drift for the duration of the exposure and the expected changes in load and line potential should be smaller than 0.5 and 1.0% for current and voltage supply respectively. These conditions are met for both supplies* used in conjunction with the cascade tube according to specifications of the manufacturers and measurements of drift made by the author (10% change in load and line potential during 60 min.) The effect of another important specification, the ripple on the output voltage or current of the supply has been investigated (§ 8.3.3) and it was found to be more important for the solenoid supply (50 cps ripple; 0.25%rms tolerable) than for the high voltage supply (8 Kcps ripple; 0.75% rms tolerable).

The stage potentials are defined by an external divider chain made up of high stability and high voltage resistors and potentiometers.

---

* current supply : 60 V ; 5 A. Roband Type 60:5.

H.V. supply : 50 KV; 1 mA. Brandenburg Type MR 50 R.

6.3 TRANSFER OPTICS

A lens is used to transfer the output image of the intensifier to a suitable recording system (photographic plate, television camera ...). The requirements of high transfer efficiency and good modulation transfer function of this lens have already been discussed in § 2.2.2 and 2.2.6. A magnification of one is used as being the best compromise between high transfer efficiency and low resolution limitation of the lens.

6.3.1. Canon Lenses

One system currently used with the cascade tube consists of a pair of commercially available 35 mm camera lenses (Canon: f = 50 mm, f/1.2 to f/22) connected front to front. Unit magnification is obtained by focusing each lens at infinity and by placing both object and image in the focal planes of the two lenses. Such a lens arrangement suffers from two disadvantages. Firstly, vignetting will occur as a result of the presence of two different aperture stops. This restricts the usable field to a circle of 22 mm at f/1.2. Secondly, all the rays of an off-axis pencil will suffer high aberrations in one of the two lenses, causing a rapid deterioration of the image quality for off axial objects. Additional aberrations will be introduced by the presence of the end windows of the intensifier.

6.3.2. Wynne-Wray or WW lens

A new lens has been designed by Wynne et. al. (1969) in the Applied Optics Section and prototypes of this design have been made by Wray Optical Works.** This lens has an aperture ratio of f/2.8 with a focal length of 75 mm, and is designed for unit magnification of a 35 mm diameter object. Its effective aperture ratio is thus f/5.6 for 1 : 1 image transfer. The correction of the aberrations of this lens, which is designed to operate over the wavelength range 4000 to 5500 Å (emission of P11 phosphor) takes into account the total end window

---

** Wray Optical Works Ltd., Bromley, Kent.

thickness (3.5 ± 2.0 mm) of the image tube. The lens must be used with a glass plate of identical optical thickness placed between the lens and the photographic plate.

6.3.3. The Transfer Efficiency of the Coupling Lens

The theoretical transfer efficiency of a lens, for light emitted from a perfect diffusing surface (Lambertian emitter) is given by:

$$T_L = \frac{K}{1 + 4\,(f/\text{-})^2\,(1 + \frac{1}{m})^2} \qquad (6.2)$$

where K is the transmission of the lens (reflections at interfaces and bulk absorption), m the magnification and $f/$- the aperture ratio (f - number). The factor K can easily be evaluated by measuring the transmission of the lens for a parallel beam of blue light (Wratten 47B filter).

For the Canon lenses K was found to be 0.68 so that, with $m = \infty$ (first lens), the transfer efficiency becomes $T_L = 10.0\%$ for $f/1.2$ and $T_L = 0.54\%$ for $f/5.6$.

For the WW lens it was found that $K = 0.64$ so that, with $m = 1$, the transfer efficiency becomes $T_L = 0.51\%$ for $f/5.6$. This is in good agreement with the value $T_L = 0.50 \pm 0.03\%$ measured by Airey (1971) for light from a diffusing glass plate.

The angular intensity distribution of the light emerging from the end window of the cascade intensifier was found to be slightly more peaked than a Lambertian distribution. (Fig. 6.4 A). This is the result of Fresnel reflections occuring at the interface between the phosphor grains and the glass support plate of the output screen (§ 8.4.1)*. Therefore a higher transfer efficiency than that predicted by the use of eqn. 6.2, can be expected if the lenses are used in conjunction with the intensifier. Numerical integration of the angular distribution shown in Fig. 6.4 A

---

*Calculation of the angular distribution of the light emerging from the substrate, using the measured angular distribution of the light inside the substrate (§ 8.4.1.) gave results similar (within 5%) to those presented in Fig. 6.4 A.

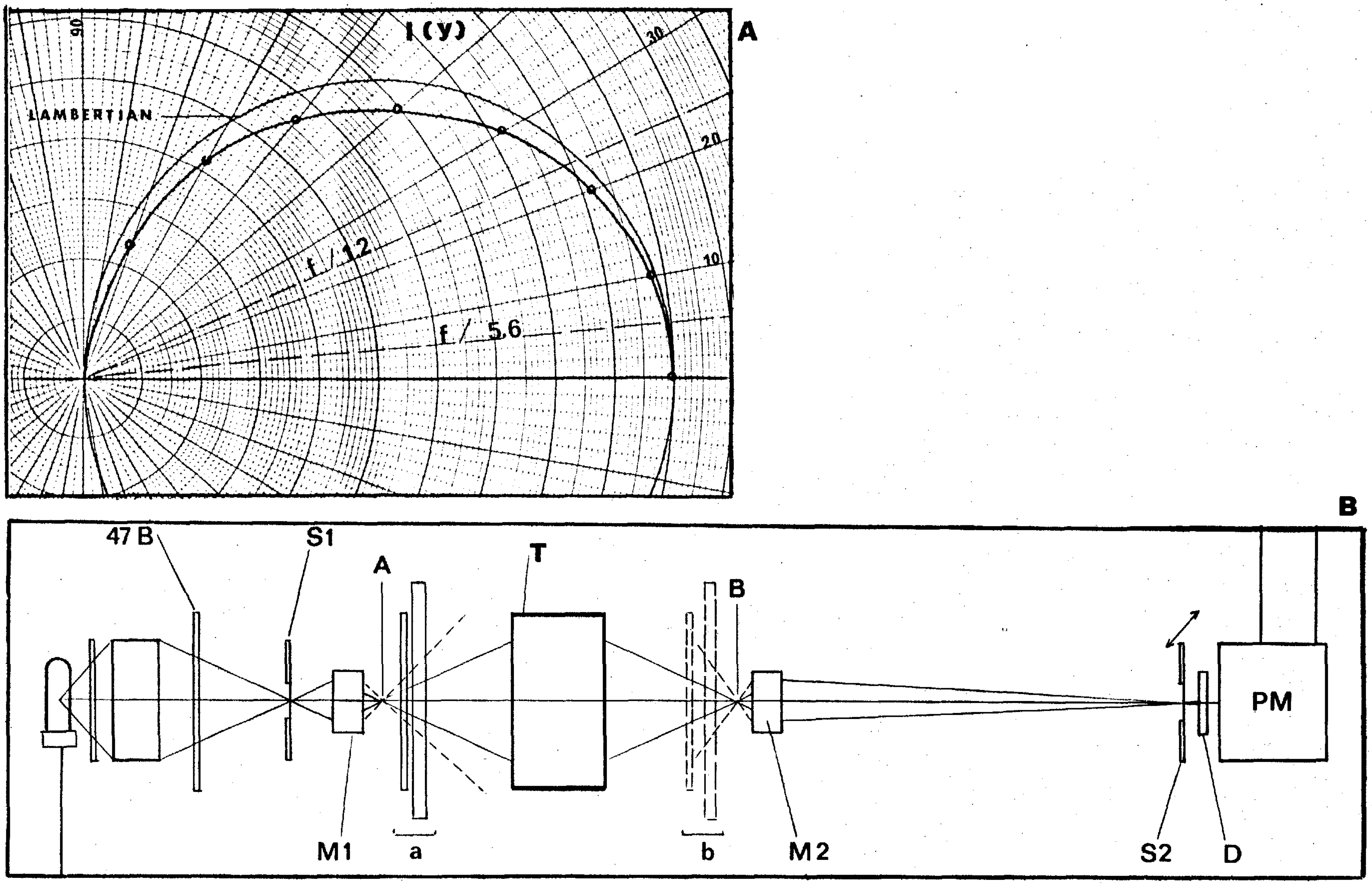

FIG 6.4 TESTS on TRANSFER LENSES

permits the calculation of this increase* in transfer efficiency for any lens of known ƒ - number. It was found that an increase of 14% can be expected for a ƒ/1.2 lens and an increase of 17% for a ƒ/5.6 lens.

The transfer efficiency of the Canon lens thus becomes $T_L = 11.4\%$ at ƒ/1.2 and 0.63% at ƒ/5.6. This is in good agreement with $T_L = 11.0 \pm 0.5\%$ found by Powell (1967) for the transfer efficiency of that lens at ƒ/1.2. The efficiency of the WW lens, used with the intensifier, becomes $T_L = 0.60\%$ (ƒ/5.6).

6.3.4. Measurements of Modulation Transfer Function on Axis

Measurement of the MTF on axis of the two lenses described above was performed by the author in the Applied Optics Section with the kind permission of Dr. Welford. The experimental arrangement is shown in Fig. 6.4 B. A slit (Sl), illuminated with blue light (Wratten 47B filter), is demagnified with a high quality microscope objective (Ml) (NA = 0.28), to form a spatial image (A). The slit width in this plane is 0.6 microns. Two glass plates (a) are placed between this image (A) and the lens under test (T) to simulate the end windows of the intensifier. The position of the lens (T) is adjusted to produce an image (B) of same dimension as image (A). Two identical glass plates (b) were placed between the lens and the image B in the case of measurements on the WW lens only. The image (B) is magnified about 100 times with an objective (M2) onto a 10 microns wide slit placed in front of a diffusing screen (D) and a photo multiplier (PM).

---

* This increase in T_L is given by:

$$1 - \frac{1}{\sin^2 \theta} \cdot \frac{\int_0^{\theta} I(y)\ \sin y\ dy}{\int_0^{\pi/2} I(y)\ \sin y\ dy}$$

where $I(y)$ is the angular distribution, y the angle to the normal on the output screen, and θ the half-angle subtended by the lens. $\mathrm{tg}\ \theta = (2.\ ƒ\text{-number})^{-1}$

It should be noted that the f-number of the lens under test was always greater than that of the two objectives ($f/1.78$), such that lens (T) was completely "filled" by rays coming from object (A) and objective (M2) collected all the rays coming from image (B). The slit (S2) was moved manually with a calibrated micrometer slide and readings of the line spread function were taken.

The normalized Fourier transform of this line spread function was then calculated using a computer program (appendix II), on the Imperial College IBM 7094 computer. The results are shown in Fig. 6.5. It appears that the MTF of the new WW lens is superior at all spatial frequencies to that of the Canon lenses. However the measured MTF of the WW lens is inferior to the one obtained by computer evaluation of the design lens (Kidger, 1969). Further efforts are being made by the manufacturers to improve on the quality of this prototype lens.

6.3.5. The Camera

A plate camera has been designed by Mr. Airey in this department (McGee et. al. 1969 B), to be used with the WW lens only. A second camera is presently under construction and will have more versatility. It will in fact be a small optical bench clamped onto the solenoid end-piece, accomodating different transfer lenses and permitting multiple exposures of one plate.

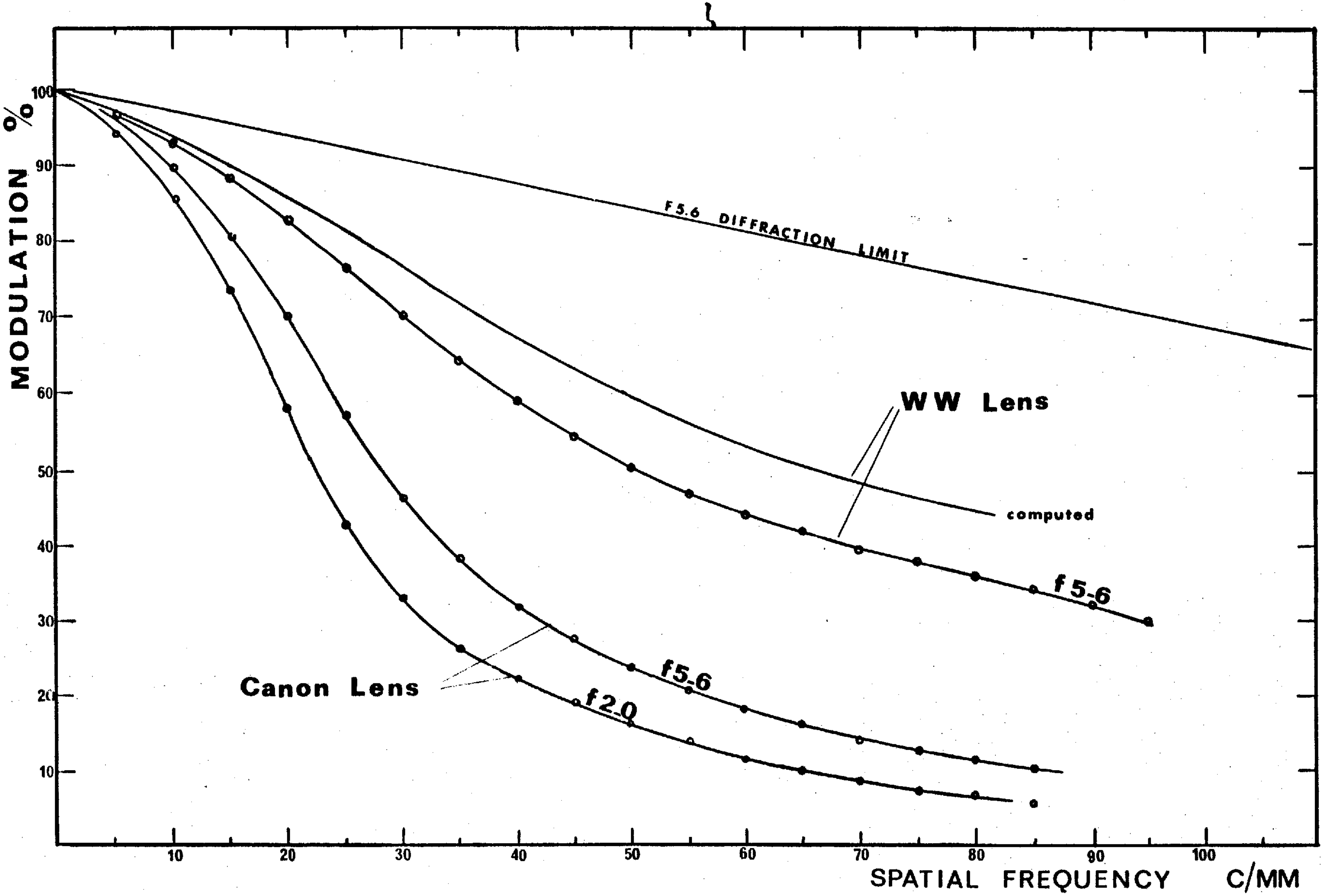

FIG 6_5 MTF of TRANSFER LENSES

CHAPTER 7.

INTENSIFICATION.

7.1 THE LIGHT GAIN OF THE CASCADE INTENSIFIER.

The light gain of an image intensifier can be conveniently defined as the ratio of the total number of photons leaving the endwindow to the number of photons in the incident radiation having spectral distribution identical to the output phosphor emission. It will be referred to in this thesis as the blue light gain (BLG) since the output phosphor emits blue light. Photon, power and luminous gain will be defined in § 7.2 and their relations with the BLG will be derived.

7.1.1 Theoretical BLG of the Cascade Intensifier.

If all photocathodes and phosphor screens of a three stage intensifier have respectively identical sensitivities and efficiencies, then the BLG can be calculated by raising the value for the dynode gain to the third power. Indeed the latter is also the light gain of a single stage illuminated with light of identical spectral distribution as its output phosphor emission. Therefore the BLG is given by: (eqn. 3.7)

$$\mathrm{BLG} = g_{\mathcal{D}}^{3} \,.\, T_{w} = \left[S_{M} \,.\, M(P11 \,.\, S11) \,.\, \eta_{\mathscr{E}} \,.\, V \right]^{3} \,.\, T_{w} \qquad (7.1)$$

where S_{M} is the maximum radiant senitivity of the cathodes, M(P11.S11) the spectral matching factor, $\eta_{\mathscr{E}}$ the effective efficiency of the phosphor screens at the stage potential V and T_{w} the transmission of the endwindows of the encapsulated intensifier. The BLG can be expressed in terms of luminous sensitivity R_{L} of the cathodes by the substitution of eqn. 3.4 with eqn. 7.1. Further substitution of the various spectral matching factors and of the measured value of T_W = 0.89 (Airey, 1970) leads to a working expression for the BLG :

$$BLG = 1.31 \,.\, 10^{-8} \,.\, R_L^3 \left[\frac{MA}{Lm}\right] \,.\, \eta^3_{gg} \left[\%\right] V^3_{\pi} \left[KV\right] \qquad (7.2)$$

where V_{TT} is the overall applied potential. Fig.7.1 shows the BLG of the cascade intensifier operated at 40KV for several values of η_{gg} as a function of the luminous sensitivity of the photocathodes*.

It is often useful to know the number of photons N_S at the output phosphor resulting from the emission of one electron at the primary cathode. This quantity is given by:

$$N_S = g_D^2 \,.\, \beta \,.\, T_w \qquad (7.3.)$$

where g_D is the dynode gain and β the quantum efficiency of the output phosphor screen. Curves of constant N_S obtained by the substitution of eqn. 3.5 by eqn. 7.3 are also shown in Fig. 7.1.

7.1.2 METHODS FOR MEASURING THE BLG .

METHOD A This method is essentially the same as that used by previous investigators working on the cascade intensifier (Powell, 1967 and Varma, 1968). The light produced by a tungsten lamp and filtered with a Wratten 47B filter is focused on the photocathode of the intensifier into a circular area of 4 mm diameter. The 47 B filter has a peak transmission at nearly the same wavelength as the peak emission of the P11 phophor. A selenium photovoltaic cell, connected to a galvanometer is first used to measure the light flux from the above source. The same cell is then placed at the output of the intensifier, behind a 1" diameter light pipe placed against the end window. The overall potential is raised until

---

*if the photocathodes have unequal sensitivities then:

$$R_L = \left[R_{L1} \,.\, R_{L2} \,.\,.\, R_{L3}\right]^{1/3}$$

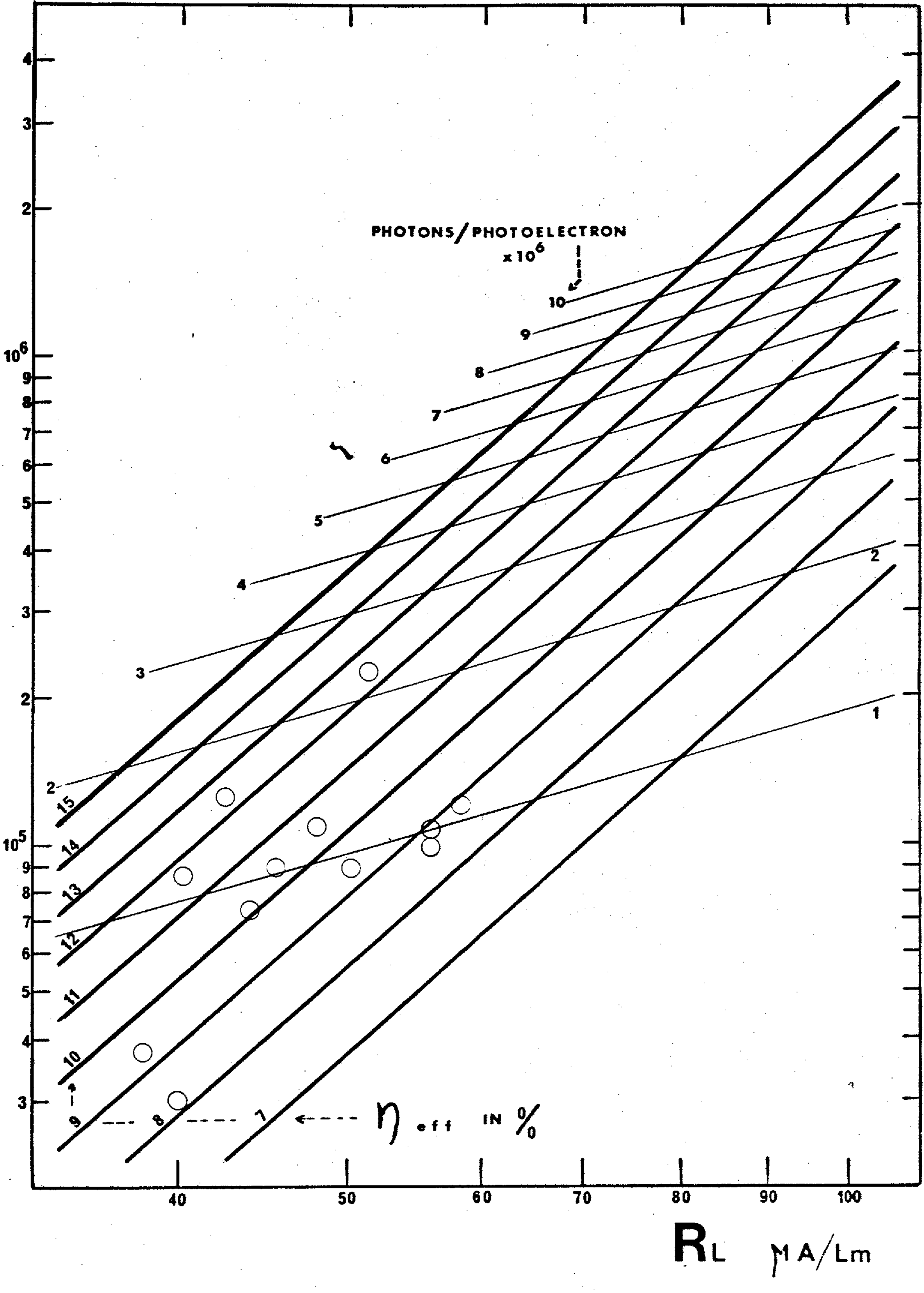

FIG 7.1 BLUE LIGHT GAIN

the galvanometer reading is the same as that obtained by direct measurement of the light flux of the source. ("Gain 1") The incident light is reduced by decreasing the voltage on the lamp so that the output light intensity is 1/5 of the previous measurement and the overall voltage, and thus the gain of the intensifier is further increased until the original reading is again measured. ("Gain 5"). This procedure is repeated until the maximum operating potential is reached ("Gain 25, 125, 625..."). A correction is made for the attenutation of the light pipe (a factor 1.8) and its separation from the output phosphor (Fig. 7.2 A: curve A).

The latter correction had been calculated from the inverse square distance law, which is not valid for such short distances and for a non-isotropic source. A much lower attentuation is obtained if one considers the fraction of light collected by the light pipe assuming a Lambertian emitting point source. The attentuation is then given by:

$$\left[\sin\left(\operatorname{arctg}\ d/2x\right)\right]^{-2}$$

where x is the distance from the phosphor to the light pipe and d the diameter of the light pipe. This attentuation factor is shown in Fig. 7.2.A (curve B) as a function of x. This lower value of attentuation was confirmed by measuring the amount of light collected by the light pipe as its distance from a 1mm diameter Lambertian emitter was increased from 0 to 12mm. (Fig. 7.2.A: curve C).

Furthermore, no allowance was made for the spectral mismatch of the different spectral sensitivity and emission characteristics of the detectors and sources used in these measurements (Fig. 7.2.B). The spectral emission characteristics of the source were computed from transmission data for the Wratten 47B filter (Kodak, 1961) and from the emission characteristics of a Planckian detector

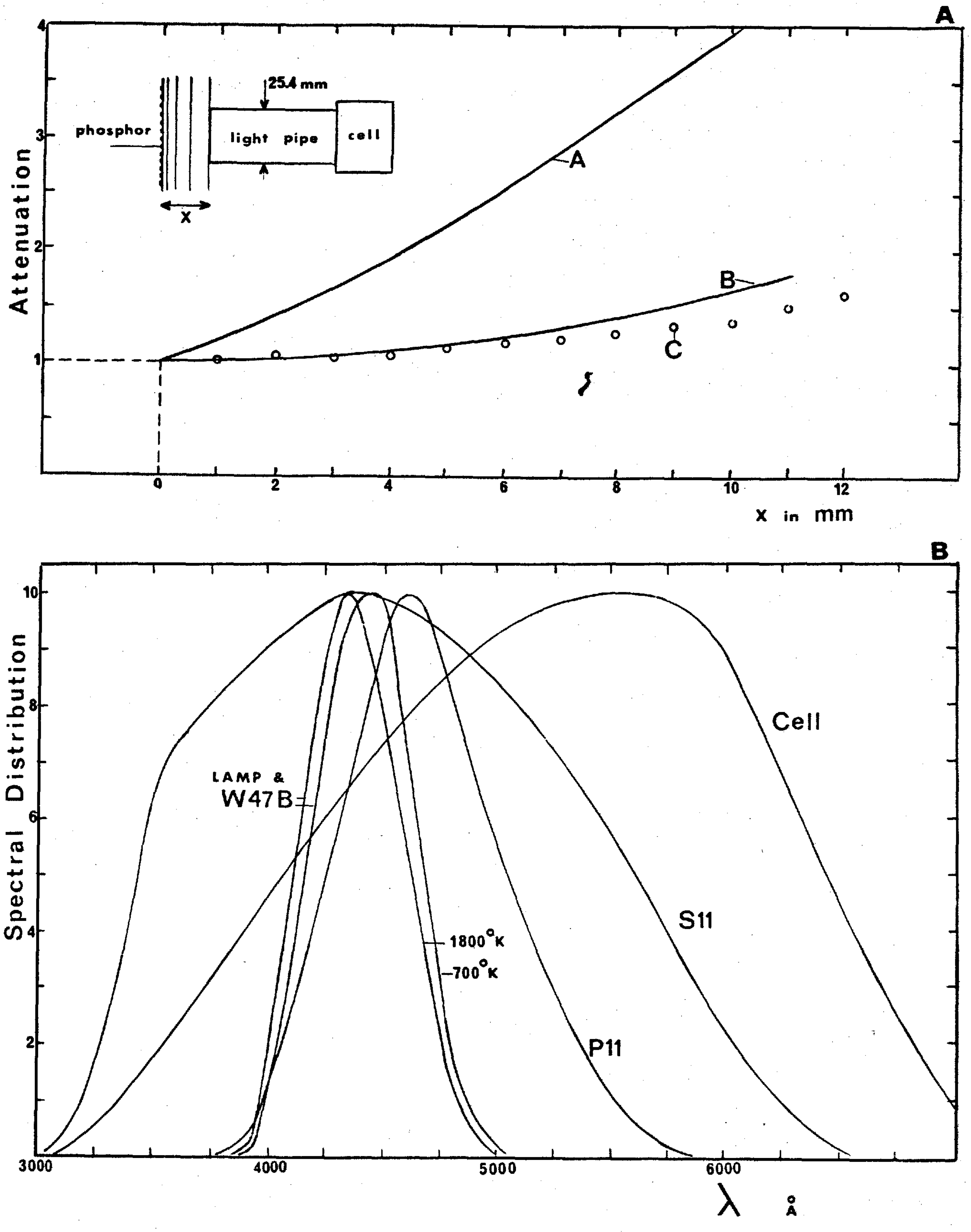

FIG 7.2 GAIN MEASUREMENTS.

(Moon 1961) operating at 1800°K and 700°K. This range of colour temperature was actually measured with a pyrometer as being that of the lamp for a typical measurement. Also shown are the characteristics of the P11 phosphor, the S11 photocathode and the photo-voltaic cell (Zworykin, et. al. 1949). The first measurement of the intensity of the source (tungsten lamp at 1800°K and W47B: $L_{\lambda B}$) with the photo voltaic cell (sensitivity D_λ) gives a reading (eqn. 3.1):

$$R_1 = D_{\lambda\ max} \cdot M\ (L_B \cdot D) \int_0^\infty L_{\lambda B}\ d\lambda$$

The equivalent reading of the output emission of the intensifier (P11 phosphor: emission intensity P_λ) with the cell is:

$$R_2 = D_{\lambda\ max} \cdot M\ (P \cdot D) \int_0^\infty P_\lambda\ d\lambda$$

The power gain of the intensifier is given by: (eqn. 7.7)

$$\int_0^\infty P_\lambda\ d\lambda \Big/ \int_0^\infty L_{\lambda B}\ d\lambda = S_M \cdot M\,(L_B \cdot S)\, g_{D1} \cdot g_{D2} \cdot \eta_{ff} \cdot V \cdot T_w$$

while the true BLG is given by eqn. 7.1. The actual BLG corresponding to the "gain 1" measurement is thus:

$$(BLG)_1 = \frac{R_2}{R_1} = \frac{M\ (L_B \cdot D)\ \ M\ \ (P \cdot S)}{M\ (P \cdot D)\ \ M\ \ (L_B \cdot S)} \qquad (7.4)$$

The four spectral matching factors were calculated by numerical integration of eqn. 3.2 and the following values were found:

$M\ (L_B . D) = 0.651$, $M(P11.\ S11) = 0.914$, $M(P11.\ D) = 0.803$ and
$M\ (L\ .\ S11) = 0.972$

Substitution in eqn. 7.4 gives $(BLG)_1 = 0.765$ As the intensity of the source is decreased, its spectral emission curve shifts towards longer wavelengths but this will not necessitate any additional correction, since, from then on, the measurements do, in fact, compare primary photocurrents.

In order to obtain the BLG, the measured values must thus be multiplied by 0.765 to account for the spectral mismatch, by 1.8 to account for the absorption in the light pipe, and by a factor given in Fig. 7.2.A (curve C) to account for the collection losses at the light pipe. Previous investigators used only the correction factors 1.8 and that given by the faulty curve A in Fig. 7.2.A , so that their BLG measurements were overestimated by a factor of about 3 .

METHOD B . An alternative method was introduced in which one measures the BLG of the complete system, consisting of the intensifier and the WW coupling lens (§ 6.3.2). The intensity of the light produced by a tungsten lamp filtered with a Wratten 47 B filter is first measured with a photomultiplier, calibrated for linearity and having a S11 photocathode. This same source is then imaged onto the photocathode of the intensifier and its output phosphor image is transformed onto the photomultiplier with the WW transfer lens working at 1:1 magnification. The overall potential is increased until the photomultiplier reading is the same as that obtained by direct measurement ("system gain 1"). The measurements are continued similarly as in the other method.

The measured system gain requires no corrections if the relative spectral sensitivity characteristics of the two S11 photocathodes are identical, since $D_{\lambda_c} = S11_{\lambda_c}$ makes the spectral correction factor of eqn. 7.4 equal unity. Measurements of these characteristics for the photocathode of the photomultiplier and that of two typical intensifiers show only slight differences in their relative spectral sensitivity characteristics. Calculations showed that the correction factor was 1.04 and 1.02 for the two photocathodes. This factor can be regarded as negligible so that the BLG of the single intensifier will be obtained by dividing the measured gain by the transfer efficiency of the coupling lens, which is $T_L = 0.006$ (§ 6.3.3) .

7.1.3 Results of the BLG Measurements.

Measurements performed on same intensifiers using the two methods described above lead to similar results within 20%. However, method B is more accurate because it involves a smaller number of corrections. It was estimated that the accuracy on the BLG measurement is ± 10% with method B and ± 25% with method A.

Two examples of measurements indicating the dependence of BLG upon overall applied voltage are shown in Fig. 7.3. Tubes 94 and 113 have respectively a BLG of 2.3×10^5. and 1.2×10^5. at 40 KV. Results of routine measurements of the BLG of other intensifiers are given in Tab. 4.3. and are also shown in Fig. 7.1 on the assumption that all photocathodes of the intensifier have a luminous sensitivity equal to that of the primary cathode. It is difficult to measure the sensitivity of the photocathodes of the two dynodes with great accuracy before the intensifier is encapsulated and it is impossible to do so after encapsulation. The measured gains are on average smaller than those predicted when using an average phosphor efficiency of 11%, as measured for 13 KeV electrons impacting on a 1.0 mg/cm^2 thick screen (§ 3.2.6). The most obvious reason for this discrepancy is that the sensitivity of the two dynode photocathodes is smaller than that of the primary cathode. Indeed only the latter is monitored for maximum sensitivity in the final step of the simultaneous activation of the cathodes (§ 5.5.4) and lower sensitivities for the other two surfaces might result.

With an intensifier gain of 10^5 one can expect about 10^6 photons to be emitted at the output phosphor for each photoelectron released from the primary cathode. If the intensifier is coupled to a photographic plate with the f/1.2 Canon lens about 10^5 photons will land on the emulsion. The limiting resolution of this complete system is approximately 30 lp/mm (§8.6) so that according to Fig. 2.1. each photoelectron will be recorded on Kodak

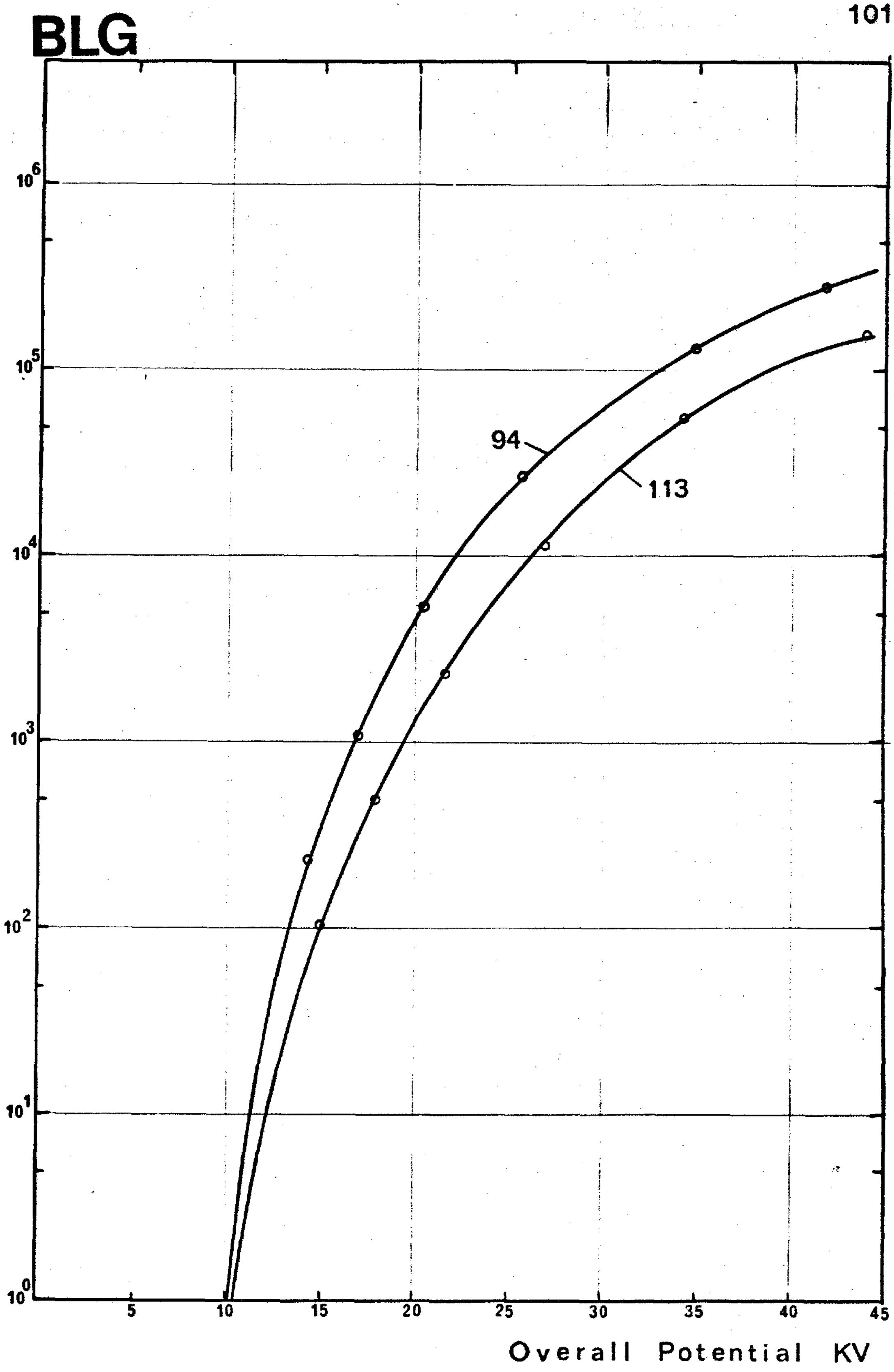

FIG 7_3 BLUE LIGHT GAIN .

TRI – X with a density of about 0.65 $\log_{10}$ units above fog. Measurements of density of recorded scintillations obtained with a system having similar characteristics confirm these results. However, the picture quality obtained with such a system is impaired by the poor optical characteristics of this fast lens and by the low signal to noise ratio in the recorded image. Indeed, each photoelectron is heavily recorded and the emulsion saturates before the noise is properly integrated. The use of an optical system with a smaller aperture, i.e. the $f/5.6$ WW lens will improve the overall picture resolution to about 40 lp/mm (§ 8.6) but only about $5 \cdot 10^3$ photons per photoelectron will land on the emulsion. Nevertheless this is sufficient to achieve detection with a certainty factor of about 5 (Fig.2.1.) without unnecessary exhaustion of the storage capacity of the emulsion, and hence, with an improved signal to noise ratio.

7.2 PHOTON, POWER AND LUMINOUS GAIN

The photon gain G_{ph} is the ratio of the total number of photons emerging from the output faceplate to the corresponding number of photons in the monochromatic input radiation. The photon gain is given by (eqn. 3.5)

$$G_{ph} = QE_{\lambda} \cdot M\left(P11 \cdot \frac{\lambda}{1200}\right) \cdot g_D^2 \cdot V_T \cdot \eta_{eff} \cdot T_W \qquad (7.5)$$

or in terms of BLG (eqn. 3.4 and 7.1)

$$G_{ph} = \frac{12395 \cdot M\left(P11 \cdot \frac{\lambda}{1200}\right)}{\lambda[\text{Å}] \cdot M(P11 \cdot S11.)} \cdot S_{\lambda z} \cdot BLG \qquad (7.6)$$

The photon gain varies with wavelength as the quantum efficiency and is thus, maximum at 4000 Å , where it equals 1.2(BLG).

The Power Gain G_w is the ratio of the total radiant light power emerging from the output faceplate to the light power in the monochromatic input radiation.

Thus:

$$G_{w.\lambda} = S_{\lambda} \cdot g_{D1} \cdot g_{D2} \cdot V_T \cdot \eta_{eff} \cdot T_w \qquad (7.7)$$

or in terms of BLG (eqn. 7.1)

$$G = \frac{S_{\lambda\tau}}{M\,(P11.\ S11)} \cdot BLG \qquad (7.8)$$

The power gain varies with wavelength as the radiant sensitivity and is thus maximum at 4300 Å, where it equals 1.09 (BLG)

The Luminous Gain G_L is the ratio of the total luminous flux emerging from the endwindow to the corresponding luminous flux in an input radiation having a spectral distribution of a 2854 °K tungsten source. It is given by : (eqn. 3.4)

$$G_L = R_L \cdot 680 \cdot M\,(P11.\ EYE)\ \ g_{D1} \cdot g_{D2} \cdot V_T\, \eta_{eff} \cdot T_W \qquad (7.9)$$

or in terms of the BLG (eqn. 3.3 and 7.1)

$$G_L = \frac{M\,(CAL.\ S11)\ \ M\,(P11.\ EYE)}{M\,(CAL. EYE)\ \ M\,(P11.\ S11)} \cdot BLG \qquad (7.10)$$

The luminous gain is thus 0.185 (BLG)
An improvement in luminous gain of a factor 6.8 can be expected if the P11 output phosphor is replaced by a P20 phosphor screen of the same effective efficiency (Tab. 3.1 and 3.4).

7.3 THE LINEARITY OF THE CASCADE INTENSIFIER.

It is desirable that the gain of an image intensifier should be independent of the intensity of the incident illumination, not only for photometric applications, but also if parameters such as modulation transfer function and recording efficiency are to be determined. Linearity will be obtained if both the sensitivities of the photocathodes and the efficiencies of the phosphor screens are unaffected by variations in the intensity of the incident illumination and the exciting current density respectively. Although no variation in photocathode sensitivity occurs in the range of illuminations currently used in intensifiers (§ 3.1.3), a decrease in phosphor efficiency may occur under certain circumstances as the electron beam current density is decreased (§ 3.2.7). Assuming that a variation in efficiency of a P11 - phosphor screen as reported by Francis et.al. (1960)[***] occurs in a typical cascade tube, it is possible to calculate that the gain would increase by about a factor of 8 between its value at very low light levels and its value at the maximum permissable input illumination (corresponding to a current of 10^{-6} A/cm^{2} in the last stage). It was felt to be quite important to investigate if such a variation in phosphor efficiency occurs with the screens used in the cascade intensifier[**].

7.3.1 Measurements.

The measurements, performed on two one-stage tubes (A and B) and on one three-stage intensifier (78), consisted in fact in measuring the relative light gain over a wide range of incident illuminations. The test apparatus is shown in Fig. 7.4. The distance between the photocathode of the image tube and the diffusing point source could be varied from 1 to 300 cm. A photomultiplier[*], calibrated for linearity, was used to verify the validity of the inverse square law over the range of position of the source. This law was obeyed to within ± 1% provided the separation was greater than 10 cm. This yielded a possible attenuation of 900. The focused intensifier was operated at constant voltage. The beam current incident on the output phosphor screen was measured with a Vibron electrometer. The light flux emitted by the output phosphor was measured

---

[*] EMI. Type 9578 A -

[***] See Fig.7.5.

[**] This investigation was published by the author in the Journal of Applied Physics (D) 4, 734, 1971.

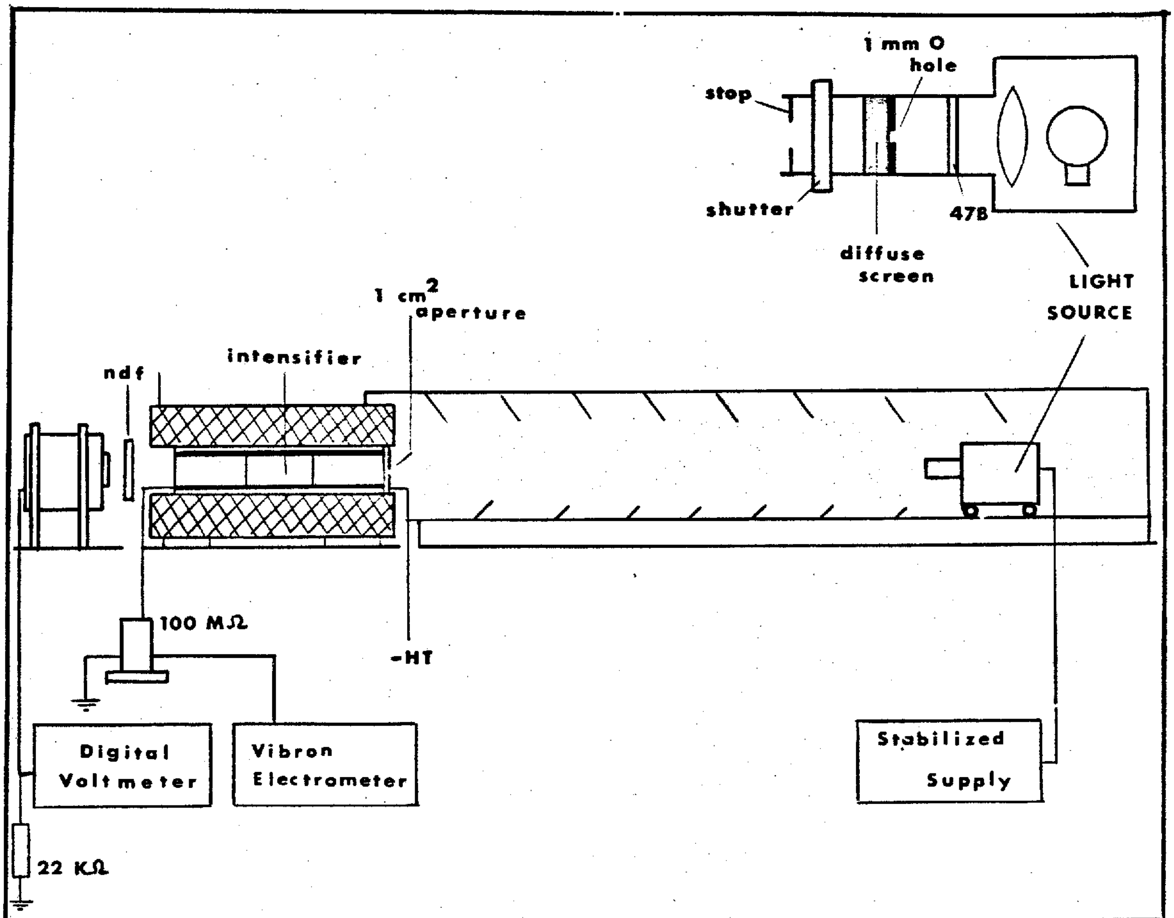

Tube	No. of Stages	Phosphor Weight	Potential applied	Range of Current Densities
		mg/cm^2	KV	A/cm^2
A	1	0.85	15.0	1.10^{-12} to 1.10^{-2}
B	1	1.00	15.0	1.10^{-13} to 1.10^{-6}
			9.0	1.10^{-14} to 1.10^{-6}
78*	3	1.05	10.8	5.10^{-16} to 1.10^{-10}
		0.90	9.4	5.10^{-14} to 1.10^{-9}
		1.00	9.8	1.10^{-12} to 1.10^{-7}

* Cascade Tube Data : BLG=78000 at 30 KV. $G_{d1}=44$ and $G_{d2}=39$. $R_1 = 43$ μA/Lm.

FIG 7.4. LINEARITY MEASUREMENTS

by means of the photmultiplier, a high stability resistor and a digital voltmeter. Neutral density filters were placed in front of the photomultiplier at high light levels to keep it operating within its calibrated range, i.e. with an anode current not higher than 10 μA. A correction was applied at low light levels to account for noise. This was done by closing the shutter provided on the light source and subtracting the residual RMS - noise level from the measured signal. The measurements began at the lowest possible light level where the signal to RMS noise ratio was about 3. The light intensity incident on the photocathode of the image tube was increased by bringing the source closer to the tube. Readings of position, current density, RMS noise level and relative output signal were taken (at a rate corresponding to 5 per decade of illumination intensity) until the distance from source to photocathode was 10 cm. The light source was then moved back to a distance of 300 cm and the lamp current increased until the photomultiplier signal was the same as that previously measured at 20 cm from the photocathode. This ensured that the ranges of incident illumination overlapped. A neutral density filter was then inserted in front of the photomultiplier. The whole procedure was repeated 3 to 4 times until the current density on the output phosphor was about 10^{-6} A/cm^2 . The current density was increased to 10^{-2} A/cm^2 in one single-stage tube (A) to investigate the occurence of saturation. The table on Fig. 7.4 gives data about the phosphors and the ranges over which the measurements were performed.

7.3.2 Results.

Fig. 7.5 shows the relative light output versus the electron beam current density for the five phosphors analysed in these measurements. The electron gains of the dynodes of the cascade tube, measured at 10^{-7} A/cm^2 , were used to calculate the current densities in the first and second stages. The computed

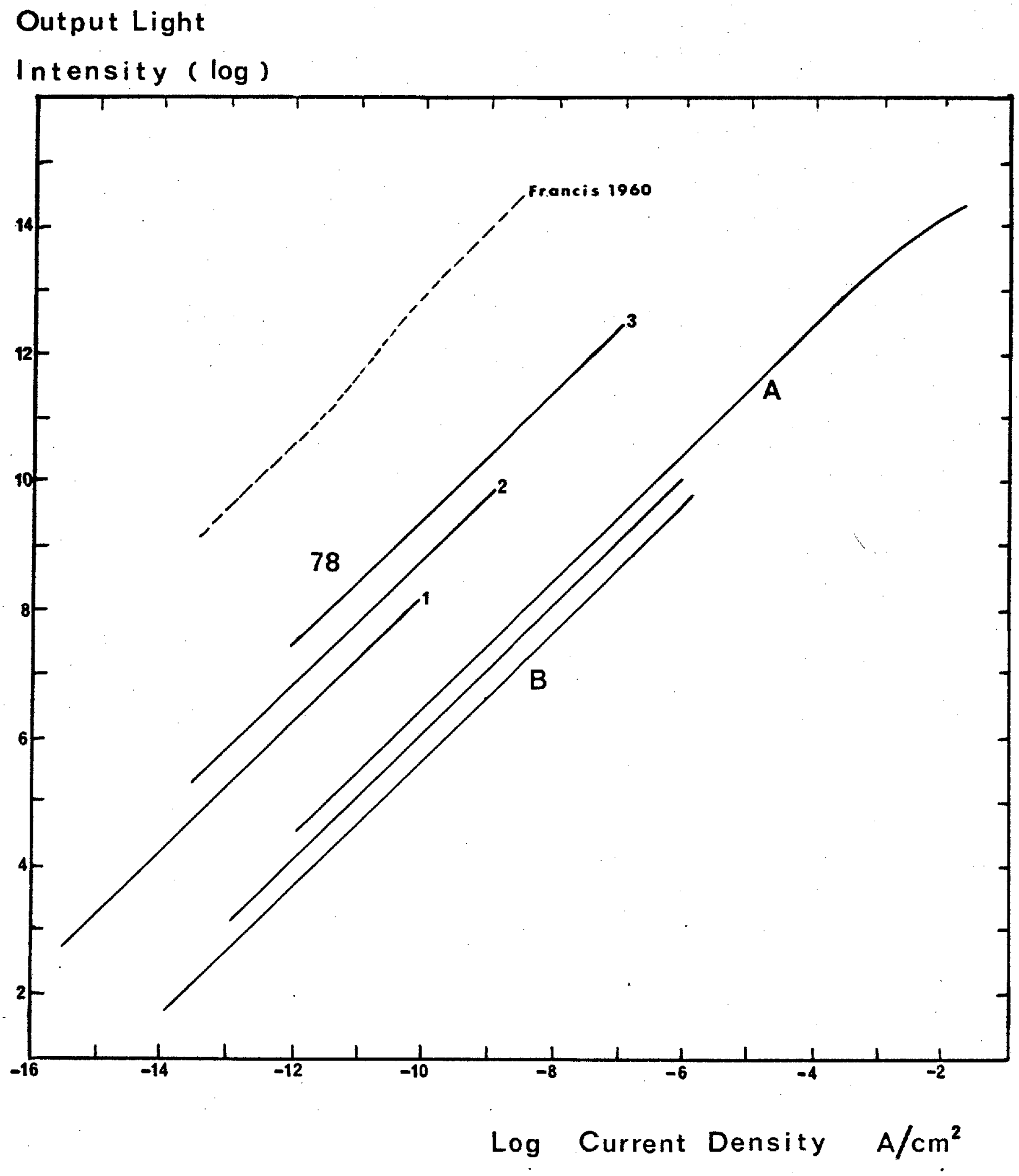

FIG 7.5. PHOSPHOR LINEARITY . RESULTS

relative efficiencies of all the phosphors were found to be constant over the range 10^{-15} to 10^{-5} A/cm^2. The RMS deviation of these efficiencies which were never higher than 3% for current densities greater than 10^{-13} A/cm^2 increased to 6% at 10^{-15} A/cm^2. A reduction in efficiency was found to occur if the current density is higher than 10^{-4} A/cm^2 (curve A).

These results indicate, as already discussed in § 3.2.7, that the phosphors used in the IC cascade intensifier are basically free from impurities and that none are introduced during backing and activation. A recent publication by Aslam, et.al. (1971) on the linearity of P11 phosphors confirms the author's results.

7.4 THE EQUIVALENT QUANTUM EFFICIENCY OF THE CASCADE INTENSIFIER.

It was shown in § 2.2.6 that if the system gain of the intensifier and coupling lens is high enough to produce a large number of developable grains in the emulsion per photoelectron leaving the primary photocathode, the EQE(o) of the detector is given by:

$$\mathrm{EQE}\ (o) = \mathrm{QE.\ RE}\ \frac{g-1}{g} \approx \mathrm{QE\ .\ RE} \qquad (2.7)$$

This relation is however derived by using the assumption that the statistics of the cathodoluminescence process obeys a near-Poisson distribution and that no noise is introduced by the granularity of the phosphor screens. In the more general case, the EQE (o) is given by :

$$\mathrm{EQE} = \frac{\mathrm{QE\ .\ RE}}{1 + \dfrac{\overline{\Delta^2 G}}{\overline{G}^2}} \qquad (1.20)$$

where $\overline{G}$ is the average number of grains in the record of a photoelectron and $\overline{\Delta^2 G}$ is the mean square deviation from $\overline{G}$.

The evaluation of EQE (o) would thus require three measurements : the quantum efficiency QE of the primary cathode, the recording efficiency RE and the intensity distribution of the recorded events which will lead to the knowledge of $\overline{\Delta^2 G} / \overline{G}^2$.

7.4.1 Quantum Efficiency QE.

The QE of the S.11 photocathode can be measured at various wavelengths with the instrumentation developed by Wilcock (1966. B) as shown in Fig. 3.3. or can be computed from the measured luminous sensitivity using equations 3.3 and 3.2. The value of QE at 4000 Å ranges from 13 to 18% for cathodes with luminous sensitivity of 60 to 80 $\mu A/Lm$ respectively.

7.4.2 Intensity Distribution.

Measurements of the intensity distribution of the output scintillations have been performed on one intensifier (94), using a bias technique in which the integral pulse height distribution is measured. A faint light source illuminates the photocathode of the intensifier. The output scintillations are recorded on Kodak TRI - X emulsion by means of the Canon lenses at different apertures and with constant shutter speed (1/100 sec). The lens-emulsion combination is used here as a discriminator with bias proportional to T_L^{-1} (transfer efficiency of the lens) or according to eqn. 6.2 proportional to $\left(1 + 4\, f^2/-\right) \sim f^2/-$. However, calibration of the Canon lenses used for these measurements show that the transfer efficiency does not vary with the f/number as it would be expected to. Table 7.6.A shows the calculated and measured values of the relative transfer efficiency of the lens for different f/numbers, normalized to the measured efficiency at f/1.2. Clearly recorded scintillations in a fixed area of the emulsion were counted for each value of the bias using a photographic enlarger. Three additional counts were made to increase the accuracy of the curve fitting

A

F/ Number	T_L Calculated	T_L Measured	Relative $\frac{1}{T_L}$ BIAS	Number of Electrons.
1.2	1.900	1.000	1.00	241
1.4	1.408	0.900	1.11	240
2.0	0.704	0.620	1.61	236
2.8	0.352	0.349	2.86	120
4.0	0.176	0.175	5.70	23
5.6	0.088	0.087	11.50	6
8.0	0.044	0.044	22.80	2
11.0	0.022	0.022	45.50	0
with neutral filter .				
1.4	-	0.690	1.45	238
2.0	-	0.470	2.13	214
2.8	-	0.260	3.85	41

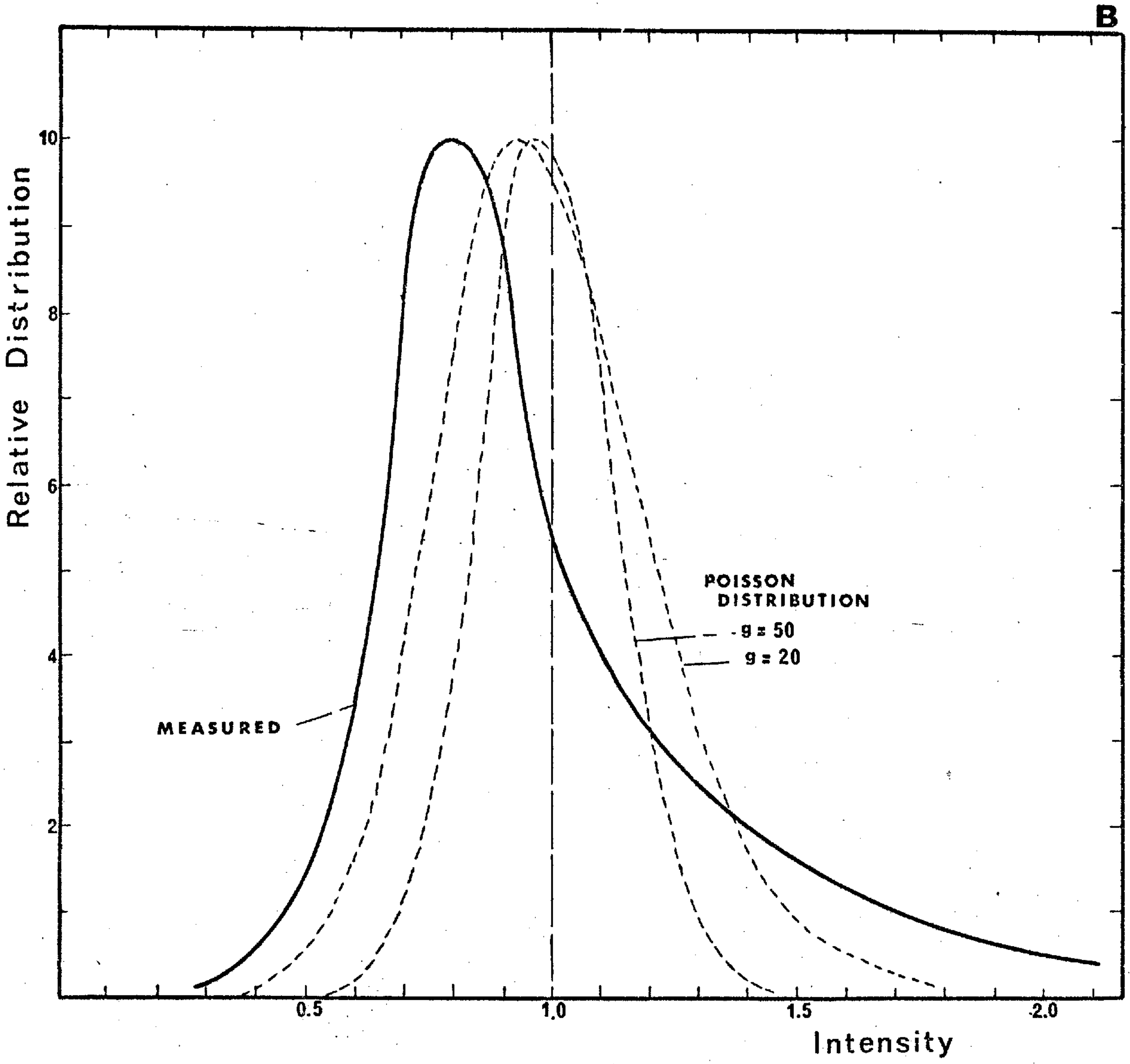

FIG 7.6 INTENSITY DISTRIBUTION.

of the integral distribution by inserting a calibrated neutral density filter in front of the recording lens. The results of these counts are shown in Table 7.6.A for the relative values of the bias. The integral distribution fitted through those 11 points was differentiated giving the intensity distribution shown in Fig. 7.6.B. Also shown in this diagram are two Poisson distributions corresponding to dynode gains of 20 and 50. These distributions are normalized to the same average intensity and the same maximum occurence as the measured curve in order to compare the shape of the distributions. Not only is the width of the peak of the distribution larger than that to be expected from a process with large average multiplication, but high occurence of brighter pulses causes the relative fluctuation to be further increased. The average intensity and the mean square deviation from the average were calculated for the measured distribution leading to a factor $\overline{\Delta^2 G}/\bar{G}^2 = 0.139$ as compared to $1/\overline{G} = 0.020$ for the Poisson distribution corresponding to a dynode gain of 50. This causes the EQE (o) to be decreased by about 12% owing to fluctuations in the output brightnesses.

It must be stressed that some doubt exists as to the accuracy of this bias technique as it does not give the distribution of eventual very faint scintillations (not recorded in the emulsion) and does not provide enough measurements for a very accurate differentiation of the integral distribution. An alternative technique for the measurement of the intensity distribution would be to measure the intensity of the scintillations with a low noise photomultiplier. The shaped signals can be analysed by a biased pulse counter or by a suitable pulse amplitude channel analyser (Reynolds, 1966, Chaman, et.al. 1966, McNall, 1970). Another method was proposed by McGee (1971) in which the output scintillations of the cascade intensifier would be recorded by a Spectracon (§ 2.1.3). The linear response of the latter device would permit the measurement of the intensity distribution by densitometry of the recorded scintillation images. It is hoped that one of these two methods will be used in the near future to assess, with more accuracy, the statistics of the cascade intensifier.

7.4.3 Photoelectron Recording Efficiency.

The recording efficiency of an IC cascade intensifier has been measured by Powell (1967) to be 73 ± 3% and by Varma (1968) to be 68 ± 5% by counting the number of recorded scintillations on Kodak TRI – X emulsion for a known primary photocurrent and exposure time. The major contribution to this loss of about 30% of primary photoelectrons is certainly the backscattering of electrons at impact with the screen of the first dynode. It will be seen in § 11.4.5 that 20 to 25% of the electrons are lost by this process. This value is lower than the 26% predictable from the average atomic number of the bombarded screen (23 for ZnS) (Holliday et. al. 1957), because of multiple electron scattering in the phosphor layer. The remaining 5 to 10% loss in photoelectron current can be explained by absorption loss in the aluminium backing which is 2 to 3% (Zworykin, et.al. 1949), by incomplete coverage of the screen and by the presence of inefficient phosphor grains. Furthermore, as already mentioned in § 7.3.2, it is possible that the intensity distribution of the output events contains photoelectron scintillations too faint to be recorded by the emulsion. This would contribute to a further decrease in the recording efficiency.

7.4.4 The Equivalent Quantum Efficiency : Interpretation and Discussion.

If the results of the different measurements mentioned above, i.e., RE = 0.70 ± 0.05 and $\overline{\Delta^2 G}/\overline{G}^2 = 0.139$, are substituted in eqn. 1.20 then the EQE (o) at zero spatial frequency can be expected to be:

$$\text{EQE (o)} = (0.62 \pm 0.05) \,.\, \text{QE}.$$

The equivalent quantum efficiency of the cascade intensifier is thus superior to that of a TSEM – intensifier (§ 2.2.4) by a factor 3 to 6 for identical primary photocathodes. This is the result of a higher recording efficiency and of better statistics of the multiplication processes. With a S11. primary photocathode having a luminous sensitivity of 60 to 80 μA/Lm, the corresponding EQE (o) of the system at low spatial frequencies will be 8 to 11% for incident light at a wavelength of 4000 Å.

It should be stressed that these values of EQE (o) only apply if the information is analysed by grain counting techniques. In that case direct photography would have an EQE (o) about equal to the quantum efficiency of the emulsion, or about 10^{-3} for Kodak TRI - X and IIa - O emulsions. The equivalent quantum efficiency of the intensifier system is thus about 80 to 110 times greater than that of the photographic plate. For identical incident signals, this improvement in EQE can be interpreted as a shortening of the exposure time required to obtain a similar signal to noise ratio in each of the recorded images, or as an improvement in the signal power to noise power ratio for similar exposure times, or as a combination of both.

If densitometry is used to analyse the recorded images, the improvement in EQE should be calculated from: (see eqn. 1.8)

$$\frac{\mathrm{EQE\,(o)\;T}}{\mathrm{EQE\,(o)\;F}} = \frac{t_F \cdot \gamma_T^2 \cdot \mathrm{NP(o)}_F}{t_T \cdot \gamma_F^2 \cdot \mathrm{NP(o)}_T}$$

where t is the exposure time needed to obtain a given density, γ the slope of the characteristic curve of the exposed emulsion and NP (o) the low frequency value of the noise power spectrum at the same density. The indices T and F correspond respectively to intensifier photography and direct photography. The ratio t_F/t_T is the relative blackening rate and will depend upon the wavelength of the incident light, the photon gain of the intensifier and the transfer efficiency of the recording lens. This ratio will increase as the exposure times are increased since direct photography requires a longer exposure to compensate for failure of the reciprocity law. The slopes of the characteristic curve at a given density for direct and intensifier photography are not identical. Indeed, the contrast for direct photography is wavelength dependent (Mees, et.al. 1966) while constant for intensifier photography, because the emulsion receives light of the same spectral distribution from the phosphor. Furthermore, signal induced background in the intensifier will lower the value of γ_T by an amount dependent upon the image content and operating condition of the intensifier (chapter 11). Finally, noise is introduced into the intensifier so that the noise power in its recorded image will be greater than that in a direct exposure. Quantitative analysis of the factors γ, t and NP (o) under controlled conditions should be the object of future investigation.

7.5 GAIN UNIFORMITY ACROSS THE FIELD.

The photometric uniformity of an intensifier should not be evaluated by measuring the output intensity profile when the primary photocathode is uniformly illuminated. Indeed, the actual sensitivity profile is smoothed by the occurence of signal induced background (chapter 11). By measuring the relative BLG of the intensifier for a spot of 1mm diameter imaged on the photocathode at various positions across the field, uniformities of ± 13% and ± 5% were measured in two intensifiers (113 and 94). These non uniformities are caused by variations in the sensitivity of the photocathodes resulting from the close evaporation of the antimony layer (§ 5.5.3) during the processing of the photoemissive surfaces.

7.6 TIME RESOLUTION.

The gain measurements discussed above are valid only for equilibrium conditions, i.e., only for long intervals compared with the response time of the intensifier. This response time depends mainly upon the persistence time of the phosphor screens, since the latter is long compared with the response time of the photoelectric effect, in the order of 10^{-11} sec (Duchet, 1966) and with the spread of transit times of the electrons in the three stages, in the order of 10^{-12} sec.* The decay characteristics of phosphors depend upon the phosphor

---

* calculated for 2 electrons leaving the photocathodes with 0 and 2 eV initial axial energy.

material, the manufacturing technique of the screens and the exiting current density. For a P11 screen the decay follows essentially a power law reaching 10% of the peak light emission after about 30 μ sec (RCA, 1969). Since three phosphor screens are cascaded in the intensifier, the overall decay characteristic must be calculated by convolution of the individual persistence characteristics of each phosphor. This has been done by Roberts (1960) making the assumption of exponential decay of the screens. Fig. 7.7. shows the result (curve A) of these calculations if a decay $e^{-t/\lambda}$, with $\lambda = 15$ μ sec, is assumed.* Since the calculations are long and tedious if a power law is considered, it was decided to measure the overall decay characteristics. The variation of the light output of a bright scintillation, resulting from the simultaneous emission at the primary photocathode of 5 to 15 electrons (§ 10.1) was measured with a photomultiplier and an oscilloscope. The average result is shown in Fig. 7.7, (curve B). The rise time is about 30 μ sec and the light output decays to 10% of the peak intensity after about 350 μ sec and to an insignificant amount after about 1 m sec. The intensity scale on the right of Fig. 7.7 gives the fraction of the total number of emitted photons which are emitted per μ sec. This was calculated by numerical integration of the measured decay characteristic. About 80% of the photons are emitted before the intensity decays to 10% of its maximum value.

Since the response to a light pulse input of the complete intensifier is known, it is possible to calculate the response of an intensifier to a sinuoidally varying incident illumination. This was done by convolution of a sine function with an analytical expression fitted to the measured decay characteristic. The sinusoidally varying output light intensity falls to 99% of the low frequency peak to peak response at 64 cycles/sec, to 70% (-3dB) at 430 cycles/sec and to 10% at 8300 cycles/sec.

---

* This corresponds to the initial decay of the P11 screen (RCA, 1969)

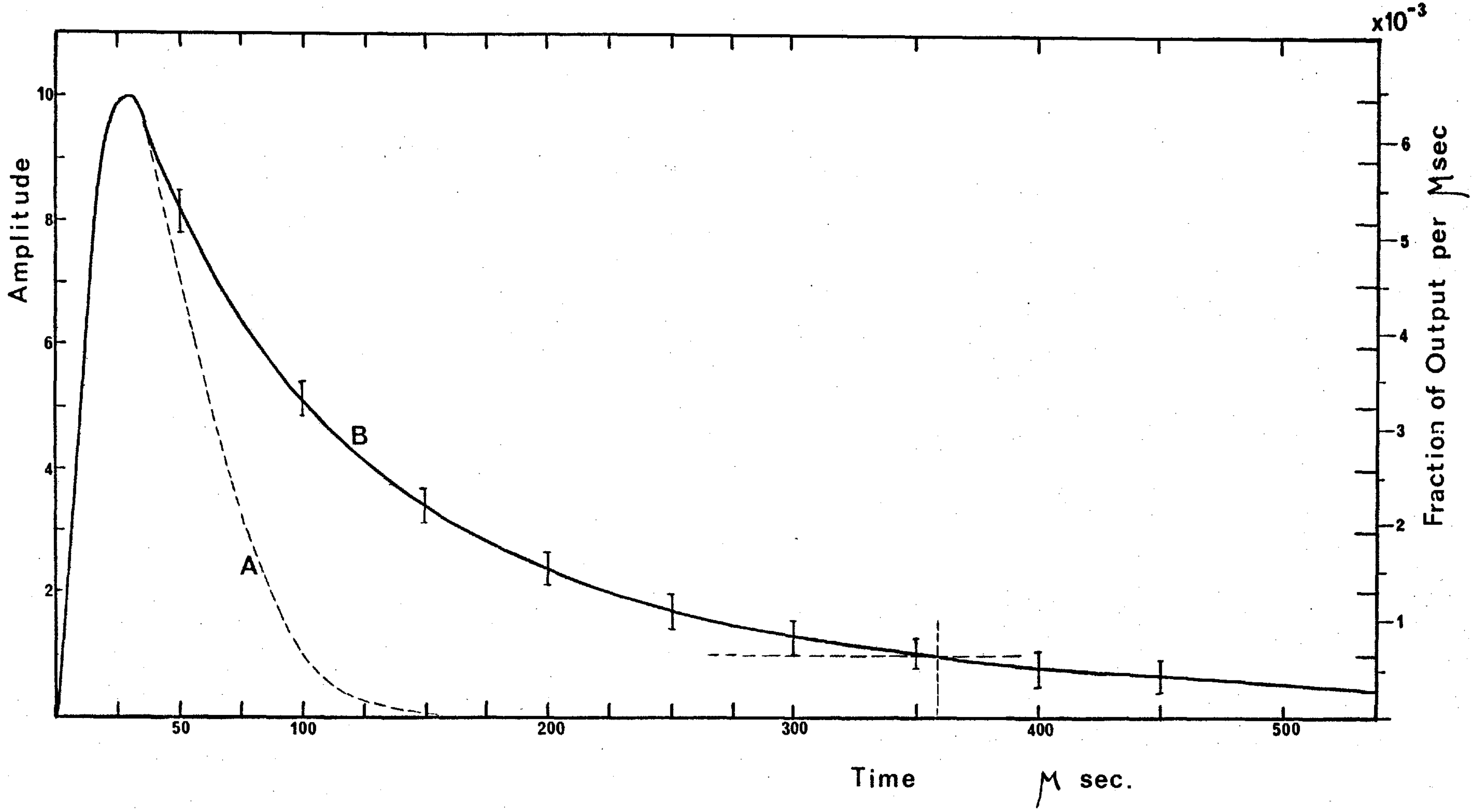

FIG 7.7 DECAY CURVE for PULSE INPUT.

7.7 STABILITY OF THE PHOTOCATHODES

The lack of stability of the S11 photocathodes in the cascade intensifier has undoubtedly been a major problem in the last years. The luminous efficiency of the cathodes of most intensifiers was 60 to 90 μA/Lm after seal-off from the pump, but decreased to 50 - 75% of that initial value after 100 days of life. The sensitivity decreased first in the first few days after processing or immediately after transfer of the cathodes. A first obvious reason of this drop is the presence of a vacuum leak in one of the 18 electrical contacts (tapes) or in the Ag Cl - seal. This has indeed been the case for several intensifiers equipped with platinum tape seals, but the occurence of leaks (or the size of the leaks?) was drastically reduced after the introduction of tungsten tape seals (§ 5.2.2). Other probable causes for the drop of sensitivity are the presence of residual oxygen which is introduced in the intensifier during processing of the S11 cathodes (§ 5.5.1) and the poisoning of the cathodes by seal-off gasses (§ 3.1.5) or by residues of chemicals used to clean the metal components. Further decrease in sensitivity was sometimes observed after operation of the intensifier. This might be caused by bombardment of the cathodes by positive ions (§ II.1.7) and gas molecules, desorbed from the internal surfaces by impact of photoelectrons and field emitted electrons.

Considerable improvements were recently obtained by evaporation of barium getter on the glass walls of the processing compartment, by avoiding any chemical procedure for cleaning the metal electrodes (sand-blasting is used instead to remove a superficial layer of the surface of these components) and by more consistent baking of the intensifier after oxidation of the manganese substrate.

7.8 CONCLUSIONS

The blue light gain of the cascade intensifier, 8.10^4 to 2.10^5, is on the average slightly lower than that of commercially available intensifiers (Tab. 2.2). The decrease in sensitivity of the cathodes in sealed off intensifiers has been responsible for these rather low gains. If initial sensitivities (60 - 90 μA/Lm) were to be maintained a BLG of 2 to 8 . 10^5 would be achieved (Fig. 7.1). Improvement of the effective efficiency of the phosphor screens, which is estimated from the gain measurements to be 9 to 12%, would similarly increase the gain of the intensifier. This could be achieved, eventually at the expense of resolution, by increasing the reflectivity of the aluminium backing (§ 3.2.5). Nevertheless, several cascade intensifiers have had a long life permiting considerable research and evaluation to be performed.

The output screen intensity of the intensifier was found to vary linearly, within the experimental error, with the intensity of the incident illumination. The equivalent quantum efficiency was calculated to be 62 ± 5% of the quantum efficiency of the primary photocathode, if the information is retrieved from the photographic plate by a grain counting technique. A slightly lower value can be expected if densitometry is used to analyze the recorded information.

Finally, the time resolution of the intensifier was analyzed. The -3dB point was calculated from measured decay characteristics to occur at 430 cycles per second.

CHAPTER 8.

RESOLUTION AND MODULATION TRANSFER FUNCTION

The fidelity with which an image intensifier reproduces image detail is usually assessed by determining its limiting resolution. This is achieved by visual observation of a calibrated resolution wedge projected onto the photocathode and observed through a low power microscope. A more complete and objective measure of image quality is the modulation transfer function (§ 1.2.1). This concept is particularly useful when imaging performance of a complex system made of cascaded elements has to be evaluated since the MTF of the complete system can be found using:

$$\text{MTF (w) system} = \prod_{n=1}^{n} \text{MTF}_n \text{ (w)} \qquad (8.1)$$

The corresponding and much used relation in terms of limiting resolutions is:

$$R_s^{-2} = \sum_{n=1}^{n} R_{en}^{-2} \qquad (8.2)$$

where R_s and R_e are respectively the limiting resolution of the system and of its components. However, the latter equation only applies if the line spread function has the shape of a Gaussian distribution, i.e. exp $(- \tau^2 y^2)$ where y is the distance and τ a constant proportional to the resolution. Indeed the relative Fourier transform or MTF is given by exp $(- \pi^2 . \xi_s^2 . \tau^{-2})$, so that the MTF of a system would be given by (eqn.8.1) exp $(- \pi^2 . \xi_s^2 \sum \tau_{en}^{-2})$ or exp $(- \pi^2 \xi_s^2 \tau_s^{-2})$ where ξ_s in the spatial frequency. Eqn. 8.2 can easily be recognized in the last two expressions.

8.1 MEASUREMENTS OF LIMITING RESOLUTION

The limiting resolution of the IC cascade intensifier operated at 40 KV is 50 to 55 lp/mm for a 100% modulated test pattern. Fig. 8.1.A shows a macrophotograph of the resolution wedge of a Baum pattern. Fig. 8.1.B indicates how the resolution of a typical intensifier varies with the overall applied voltage and with the number of loops used in focusing the stages of the intensifier. The resolution is not maintained over the whole working region but decreases to about 50% of the centre value at the edge of the field (Fig. 8.1.C left) This decrease is due principally to non-uniformities in the electric field. This can be demonstrated (Fig. 8.1.C right) by comparing the improvement in off-axis resolution obtained, at the expense of axial resolution, when the electric and magnetic fields are readjusted for optimum focus in off-axis points. Curve B shows the resolution obtained by readjusting the magnetic field keeping the stage potentials equal to those required for best focus on axis. Curve C shows that a larger improvement in resolution is obtained by readjusting the stage potentials keeping the magnetic field equal to that required for best focus on axis. Finally, curve D indicates the resolution obtained if both electric and magnetic fields are readjusted. It will be seen in § 8.3.2 that the slight drop in resolution still occurring under these conditions is caused by non-uniformities in the magnetic field.

8.2. MEASUREMENTS OF THE MODULATION TRANSFER FUNCTION

The MTF of one cascade intensifier (82) was measured on axis using two different methods.

8.2.1. The Line Spread Function Method.

This method is similar to that used for measuring the MTF of transfer lenses (§ 6.3.4), except that the line spread function is recorded photographically. The experimental arrangement is shown in Fig. 8.2.A. A slit S1, illuminated with blue light (Wratten 47B filter) is demagnified and imaged on the photocathode

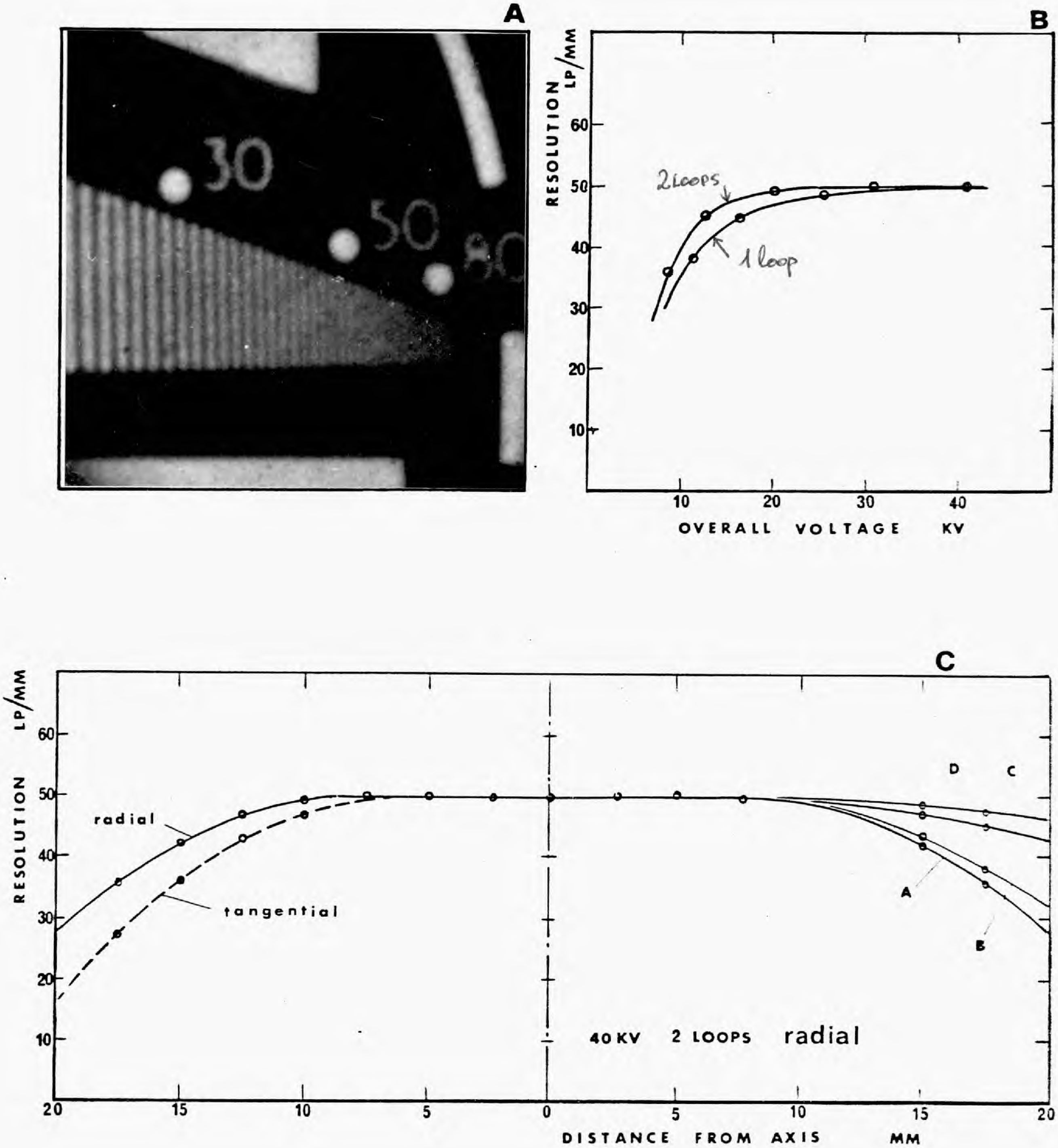

FIG 8.1 RESOLUTION

using a microscope objective M1. The slit dimensions at the photocathode plane are 4.1 microns in width and 1.35 mm in height. The cascade intensifier is focused in 2 loops at 40 KV. The magnetic field is monitored by measuring the voltage drop caused by the solenoid current over a 0.1 Ω standard resistor with a digital voltmeter (accuracy 0.05%). The phosphor slit image is magnified about 20 times with a microscope objective M2 and imaged onto a photographic plate. These plates, Ilford N30, are pre-exposed to a density of about 0.2 $\log_{10}$ units above fog. Each set of measurements consists of a focusing run in which 10 to 15 exposures of the slit are taken at various focusing currents (in steps of 0.05% around the visually observed best focus) and of an exposure run in which exposures are taken on that same plate by inserting calibrated neutral density filters in front of the slit S1. The latter exposures, taken at the visually observed best focus, are performed in order to measure the density - exposure characteristic of each plate. All exposures are of 15 sec. duration. The plates are developed, under continuous agitation, in 1:1 D76 developer (Kodak) during $6\frac{1}{2}$ minutes at 20°C and fixed in 4:1 Hypham (Ilford). Fig. 8.2.B shows a print of a typical exposure. The density profiles of the focusing run exposures, and the peak density of the exposure run profiles are measured with a microdensitometer*. Its analysing slit width is 20 μm when projected in the plate . The density - exposure characteristic of each plate is used to derive the intensity scale of the slit spread function and measurement of the recorded slit image height is used to calculate the distance scale. The sharpest intensity profiles are selected from these results and the Fourier transform of the line spread function, taking the width of the slit into account, is calculated by means of a computer programme (appendix II). The

---

*Joyce Loebl Double Beam Microdensitometer.

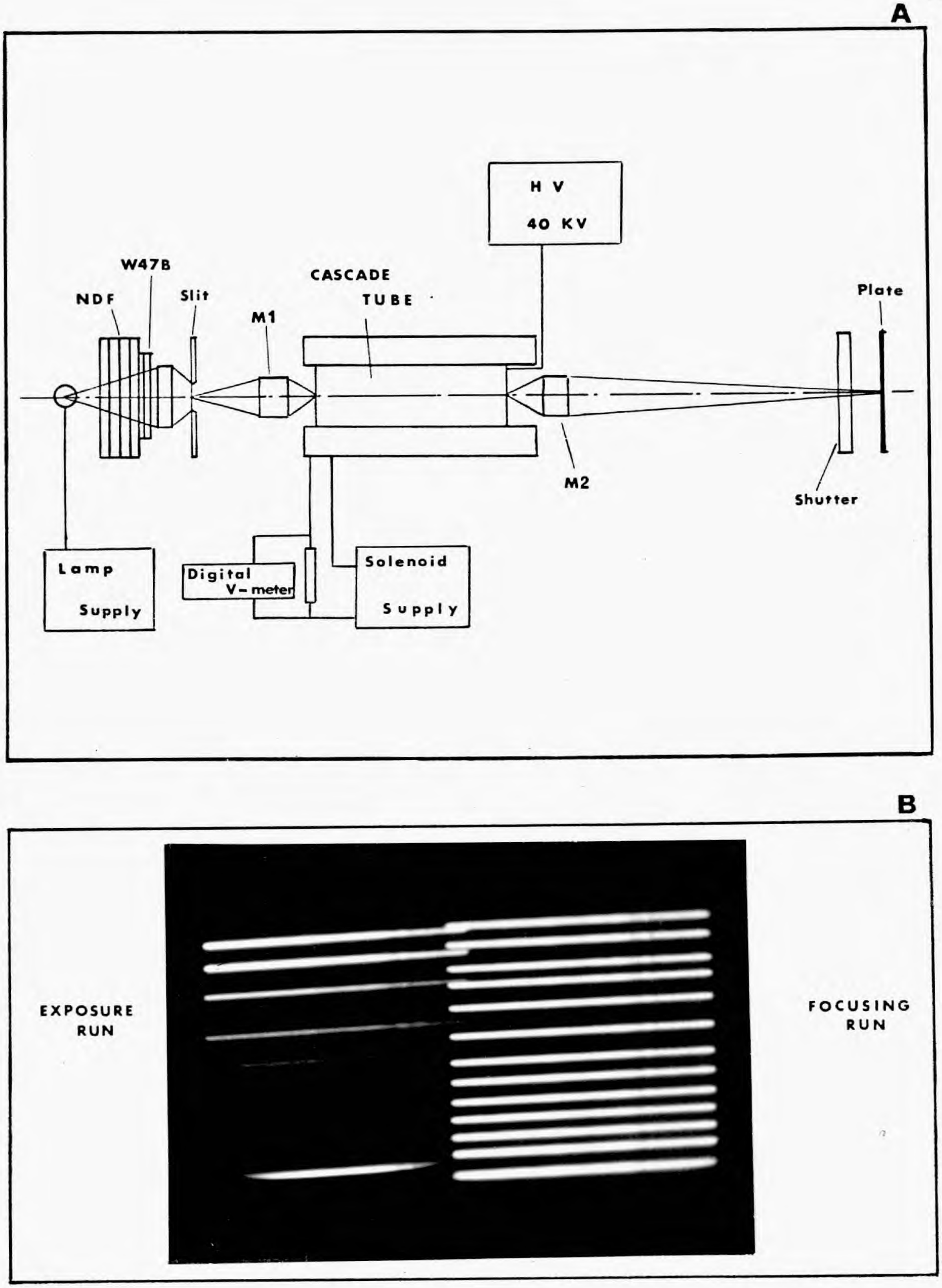

FIG 8.2. MTF. SLIT METHOD

complete measurement is repeated in order to evaluate the MTF of the input optics, the output optics and the photographic plate. The image tube is removed and the spatial image of the slit produced by M1 is focused on a plate by means of M2 with the same magnification as used in the above measurement. The $f/$ numbers of the two lenses are such that lens M2 is completely filled by the rays coming from lens M1. The MTF of the optics and that of the intensifier, calculated using eqn. 8.1 from the results of the two measurements are shown in Fig. 8.4.

8.2.2 The Sine Wave Pattern Method.

A sine wave pattern, designed by Dr. Kahan * for MTF measurements was also used by the author. It consists of a series of gratings of sine wave transmittance and of calibrated modulation corresponding to spatial frequencies of 10, 20, ... 120 c/mm, when correctly demagnified on the photocathode. The experimental arrangement and procedures are essentially the same as those used for the line spread function method. However, the plates are now pre-exposed uniformly to a density of 0.45 $\log_{10}$ units above fog. Since the modulation of the pattern is small (about 0.3) it is thereby possible by controlled exposure of the pattern from the intensifier to use the linear part of the density - log exposure characteristic. In that case the modulation of the recorded grating is given by:

$$M = \frac{10^{D_M} - 10^{D_m}}{10^{D_M} + 10^{D_m}} \qquad (8.3)$$

where D_M and D_m are the maximum and minimum measured densities above

---

*Dept. of Applied Physics, Imperial College.

A

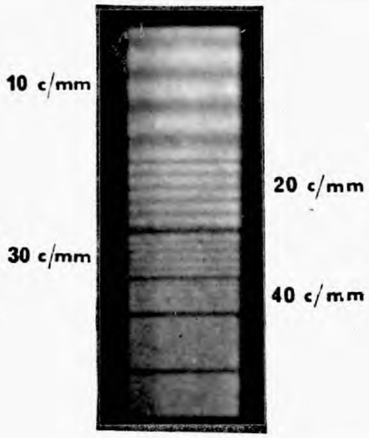

B

Spatial Frequency c/mm	10	20	30	40	50	60
Modulation of the Original Grating	0.289	0.298	0.283	0.256	0.258	0.257
Measured Modulation						
of Optics only	0.274	0.256	0.204	0.162	0.148	0.142
Of Complete system	0.216	0.116	0.048	0.024		
MTF Optics only	0.952	0.857	0.725	0.632	0.575	0.525
MTF Intensifier only	0.784	0.450	0.235	0.150		

FIG 8.3 - MTF - SINE WAVE PATTERN METHOD

the level of pre-exposure.

As previously, the measurements were performed on the complete system and on the system without the image intensifier. A microdensitometer was again used to measure D_M and D_m. The results are given in tab. 8.3.B together with a print of a typical exposure. The modulations of the original gratings were measured by Cohen (1969).

8.2.3 Discussion of the Results.

The results for the MTF of the IC intensifier obtained by the two methods are shown in Fig. 8.4 together with the measured MTF of the optical system. The visually observed limiting resolution of that same intensifier (82), measured with a 100% modulated square wave pattern, was 53 ± 2 lp/mm. The square wave response m(n) is related to the sine wave response M (w) by:

$$M(w) = \frac{\pi}{4}\left[m(n) + \frac{1}{3}m(3n) - \frac{1}{5}m(5n) + \frac{1}{7}m(7n) + \dots\right] \quad (8.4)$$

where n is expressed in lp/mm and w in cycles/mm. (Coltman, 1954). Thus for spatial frequencies close to the limiting one it can be assumed that $m(3n) \lll m(n)$, so that M(w) equals $(\pi/4).m(n)$. According to the measurements of the MTF : $M(w) = 0.040 \pm 0.015$ at 53 c/mm corresponding to a modulation $m(n) = 0.051 \pm 0.020$ at 53 lp/mm. This agrees quite well with the fact that the eye is able to discern modulation as low as 4%.

The loss of image resolution in the intensifier is the result of three major causes of aberration

- the electron optics.
- the spread of light in the mica membranes.
- the spread of light in the phosphor screens.

These contributions will be studied in the following sections.

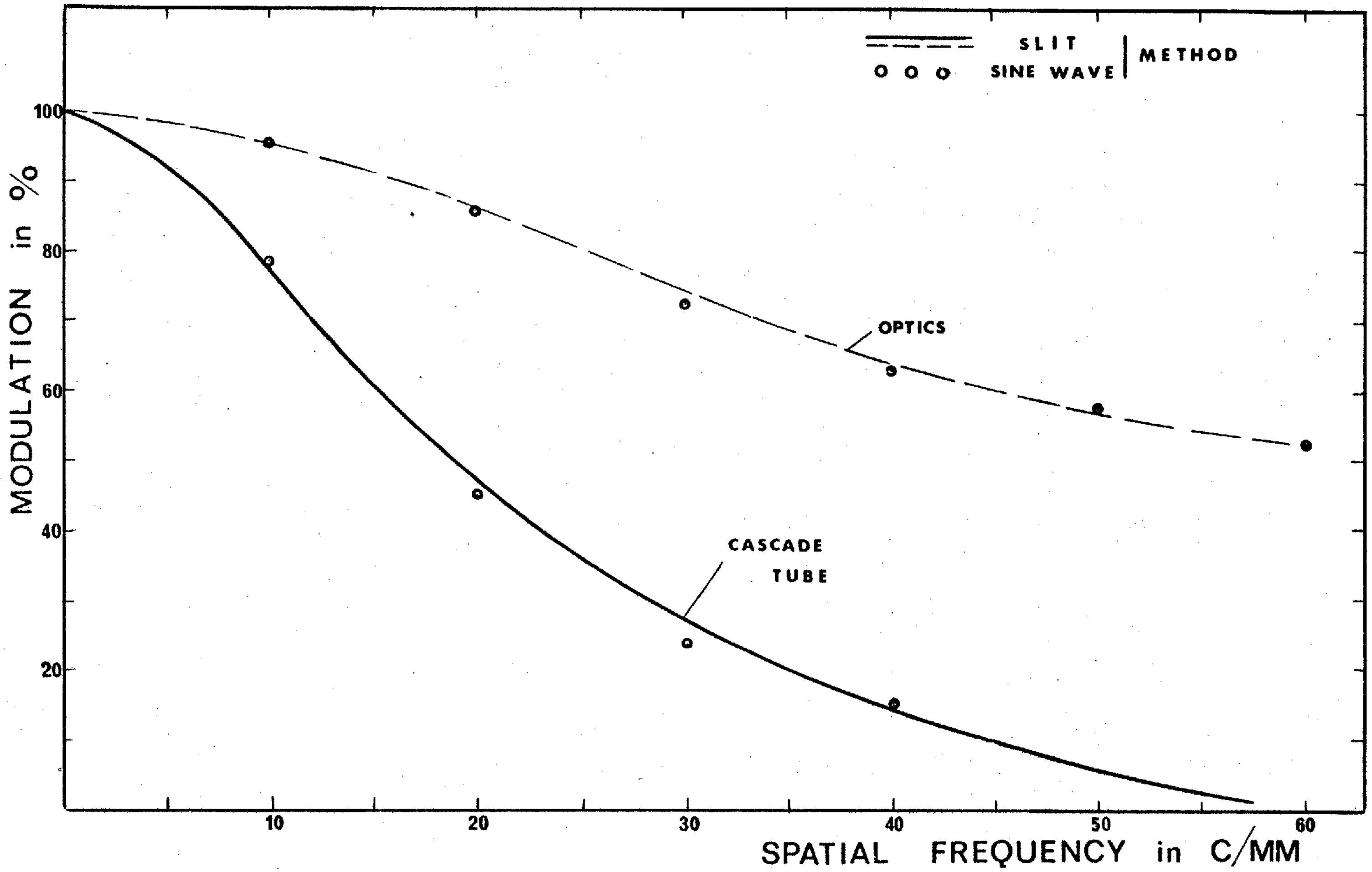

FIG 8.4 MODULATION TRANSFER FUNCTION

8.3 ABERRATIONS CAUSED BY THE ELECTRON OPTICS.

The resolution of an electro-optical system employing perfectly uniform and parallel electric and magnetic fields is only limited by chromatic aberration caused by the distribution in energies and directions of emission of the photoelectrons. However, the fields in any practical system are not uniform, hence additional aberrations will result. Although such a system has not properly speaking an axis of cylindrical symmetry, the term "on axis", used in the following sections, will refer to the centre of the field where the optimum focusing of an intensifier is normally performed.

8.3.1 Chromatic Aberrations.

The initial axial energy of photoelectrons varies between 0 and about 1.2 eV for blue light illumination of a Cs_3Sb cathode, with a maximum probability for energies between 0.5 and 0.7 eV (Shalabutov et al, 1957, Pyatnitzkii, 1957) so that the photoelectrons will focus in different planes located behind the Gaussian focal plane*. The confusion in each of these planes will depend upon the angular distribution which was found to obey essentially a cosine law for thin Cs_3Sb cathodes. (Petzel, 1965, Zheludeva, 1962). The electron density distributions in planes located behind the Gaussian focus were calculated by means of digital computer programmes by Filby (1967) and Combes et.al. (1969). They found that the radius of the disk of confusion (Rayleigh criterion) corresponding to the sharpest electron density profile is about (0.06/E)cm when E, the electric field, is expressed in V/cm. This corresponds to a limiting resolution of 0.83.E. lp/mm, which equals 1225 lp/mm for a 9 cm stage operated at 13 KV. Measurements made by Csorba (1969) confirm this high value of resolution. Indeed, he

---

*focal plane of electrons with zero initial axial energy.

found that the resolution of the electron optics of a one stage device can be expressed by 0.73 E lp/mm. (1080 lp/mm for E = 1.48 KV/cm).

8.3.2 Aberrations Caused on Axis by a Non-Uniform Magnetic Field.**

Non-uniformities in the magnetic field cause the radius of curvature of the helical trajectory projected on a plane perpendicular to the axis to vary as the electron is accelerated in a stage. No electron leaving the photocathode on axis will therefore cross the axis again when its loop is completed as is the case in a uniform magnetic field. Fig. 8.5.A.shows a sketch of such a trajectory for a continuously increasing field. The magnitude of the resulting aberration will, in general, decrease with increasing magnetic field because each loop will occur in a relatively more uniform field. This effect is detectable in the cascade intensifier as a slight increase in axial resolution when the magnetic field is increased from 1 to 2 loops focusing (Fig. 8.1.B). The field uniformity of the solenoid (D) used for this measurement is ± 0.25% on axis and increases to ± 0.35% at the edge of the field, where the occurrence of this aberration can be detected as a reduction of resolution even when both electric and magnetic fields are readjusted for optimum focus (Fig. 8.1.C, curve D).

8.3.3 Aberrations Caused by Instabilities in the Supplies.

The necessity of using highly stabilized supplies in conjunction with the image intensifier system results from the short depth of focus of electro-optical imaging. Fig. 8.5.B shows the variation of resolution when the electric and magnetic fields are varied around their optimum values. As is to be expected from eqn.4.1., a variation of the magnetic field causes a larger effect than a similar variation of the electric field. Regulations better than 0.5% for the current supply of the solenoid and better than 1.0% for the H.V. supply are thus

---

**Non uniformities in the electric field will only affect the average transit time of photoelectrons, and will therefore not inrroduce any detectable aberration.

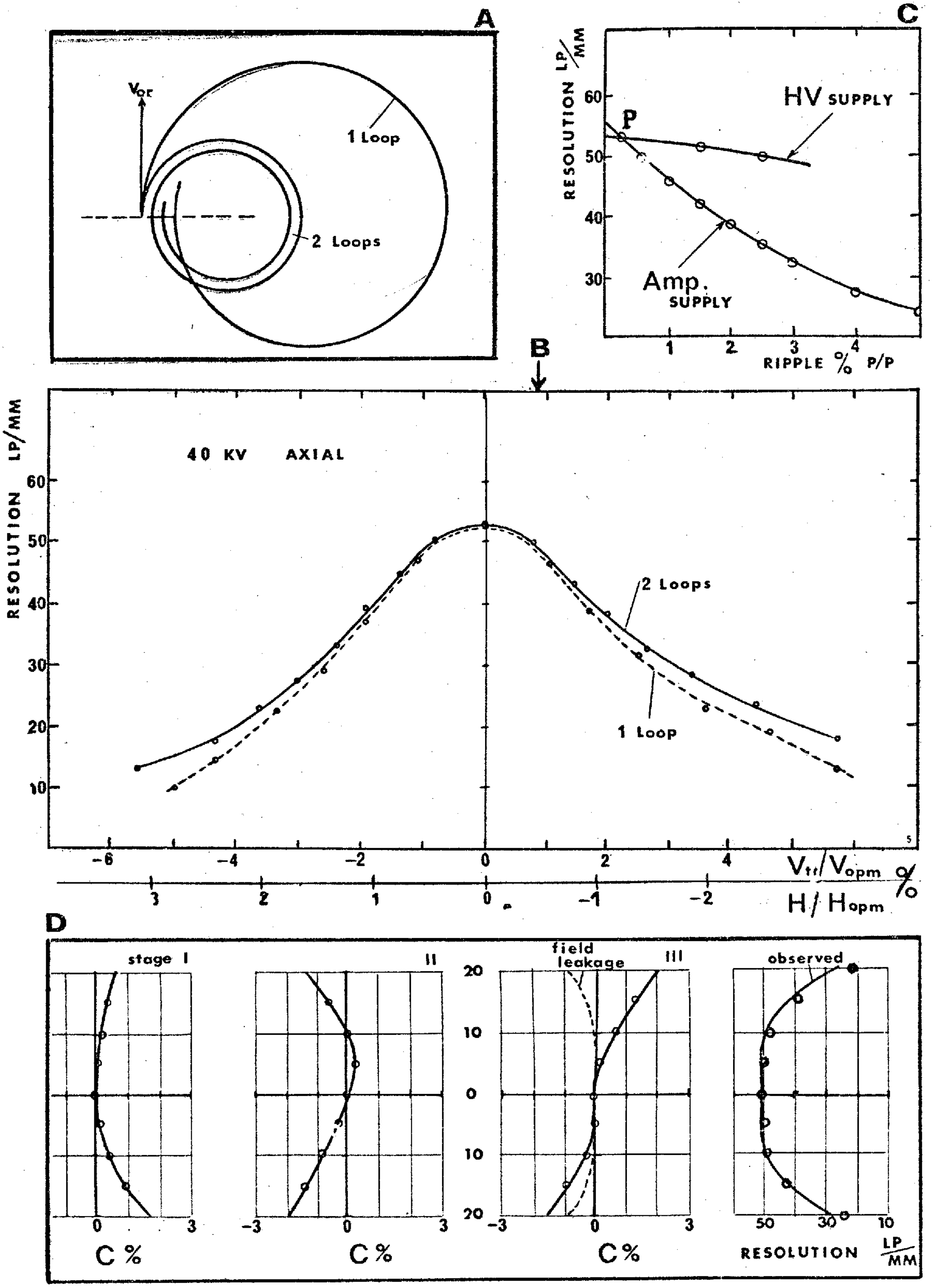

FIG 8.5 ELECTRO-OPTICAL ABERRATIONS.

required if a decrease in resolution of not more than 4% is tolerable during an exposure (§ 6.2).

The influence of ripple originating in the high voltage supply (10 Kcps ripple) and in the solenoid current supply (50 cps ripple) was also investigated. A 50 cps ripple was superimposed on the solenoid current by means of a transformer whose secondary windings were connected in series with the solenoid, while a suitable choke and capacitor protected the stabilized supply. Since a similar superposition on the H.V. supply is difficult and dangerous, several supplies of known ripple were used to investigate the effect of H.V. ripple on resolution. The results of the two measurements are shown in Fig. 8.5.C, where point P indicates the normal operating condition.

8.3.4. Off-Axis Aberrations.

If the intensifier is focus ed for optimum resolution on axis, additional aberrations will result from curvature of the image plane in each stage.

The most obvious cause of field curvature in the IC cascade intensifier is the processing compartment in the last stage. Indeed, the field of the active region of that stage leaks into the compartment onto which no potential difference is applied. The electric field distribution, calculated in § 9.3.2, was used to estimate the transit time T of electrons leaving the cathode on axis and at 10 and 20 mm from the axis. This was calculated by numerical integration of:

$$T = \int_{z=0}^{z=L'} \frac{\sqrt{m}\ dz}{\sqrt{2e\ V(z)}} \tag{8.5}$$

where V(z) is the potential distribution along the trajectory of the electron, L' the physical length of the last stage (12 cm). Values of 2.678, 2.674 and 2.663 n sec were found for electrons leaving at 0, 10 and 20 mm from the axis. This is to be compared with a transit time of 2.662 n sec for a normal stage with the same electro-optical length. If the last stage is focused on axis, then the off axial aberration can be calculated by multiplying the radial initial velocity of the electron with the transit time difference. For an initial radial energy of 0.6 eV (4.5×10^5 m/sec) the radius of confusion becomes 1.8 and 6.8 microns at 10 and 20 mm from the axis. Combined with a resolution of 50 lp/mm this should give resulting resolution of 49.5 and 42.0 lp/mm at 10 and 20 mm from the centre of the field (eqn.8.2). The field leakage in the processing compartment is thus responsible for a small part of the total off-axis aberration

An estimation of the curvature of the image plane can be obtained by comparing the stage potential V_{To} and the magnetic field H_o needed to bring an off-axial image element into optimum focus with the stage potential V_{Ta} and the field H_a needed to focus an axial image element. (Fig. 8.1.C right). Using eqn.4.1, a measure of the distance between the image plane and the phosphor plane can be found:

$$C = \frac{La - Lo}{La} 100 = \left[1 - \sqrt{\frac{V_{To}}{V_{Ta}}} \cdot \frac{Ha}{Ho} \right] 100 \qquad (8.6)$$

C is expressed in percent of the axial stage length. It is negative if the image plane is located in front of the screen and positive for the contrary case.

The measurement of C was performed on two intensifiers (78, 91) in the hope of finding an explanation for the loss of resolution in off-axis image points. However, it was found that the factor C varies considerably across the field in a very irregular way, being as high as ± 2% at the edge of the field but never higher than ± 0.5% in the central 20 mm diameter circle. Fig. 8.5.D shows an example of the image plane location for the 3 stages of an intensifier (78) measured along a diagonal across the field. It can be calculated that a factor C = 1% corresponds with a radius of confusion of about 6 microns (difference in transit time of 0.013 n sec). Using this estimation and the measured values of C for the three stages, the variation of overall resolution can be calculated (eqn.8.2) and compared with the actually observed resolution along the same diagonal across the field. It can be seen that there is a good agreeement between the two resolution curves in Fig. 8.5.D. Unfortunately, it has not been possible to correlate with sufficient accuracy the location of the image plane with possible causes of electric field disturbances, except for the field free region effect. Several potential causes will be discussed in the next chapter (§ 9.4 and 9.3) in relation to the geometry of the intensifier.

8.4 THE MODULATION TRANSFER FUNCTION OF THE MICA COUPLING.

The finite thickness of the mica membrane supporting the phosphor screen and the photocathode of a dynode causes a loss of image definition. The spread of light depends in the first instance upon the thickness of the membrane but also upon the Fresnel losses and refraction at the interface between the screen and the mica.

8.4.1 The Phosphor-Mica Interface. Optical Contact.

A small excited surface ΔS, located close to the screen side of the membrane is assumed to emit light according to a Lambertian angular distribution (Fig. 8.6.A). The light flux in the elementary solid angle $2\pi \sin\theta \, d\theta$ at an angle θ with the normal to the screen is

$$2.\pi.B.\cos\theta.\Delta S.\sin\theta.\ d\theta$$

where B is the luminance of the element ΔS. This flux is channelled into a solid angle $2\pi \sin\psi \, d\psi$ inside the mica (ψ is the angle of refraction) so that the light intensity at ψ is given by:

$$I(\psi) = B.\Delta S . \frac{\cos\theta . \sin\theta . d\theta}{\sin\psi . d\psi} . \left[1 - R(\theta.\psi)\right]$$

Using Snell's Law

$$\sin\theta = n \sin\psi \qquad \frac{d\theta}{d\psi} = n \frac{\cos\psi}{\cos\theta}$$

an expression for the angular intensity distribution inside the membrane is found after substitution of the Fresnel reflection $R(\theta.\psi)$ for natural light (Born and Wolf, 1959)

$$I(\psi) = B.\Delta S.n^2.\cos\psi \left[1 - \frac{1}{2}.\frac{tg^2(\psi - \arcsin n\sin\psi)}{tg^2(\psi + \arcsin n\sin\psi)} - \frac{1}{2}.\frac{\sin^2(\psi - \arcsin n\sin\psi)}{\sin^2(\psi + \arcsin n\sin\psi)}\right] \tag{8.7}$$

The angular distribution can be calculated using eqn. 8.7 for the following two extreme cases. All the phosphor grains are in optical contact with the mica, then $n = 1.58/2.40 = 0.66$ since the refractive index of mica is 1.58 (Rosebury, 1964) and that of Zn S is 2.4 (Handbook of physics, 1955). Or, no phosphor grain is in optical contact with the mica, then $n = 1.58/1.00 = 1.58$. The two calculated angular distributions are shown in Fig. 8.6.B. Also shown, in comparison, is a Lambertian distribution which would be obtained if the refractive index of the phosphor was equal to that of the mica.

The angular distribution in the mica membrane of an actual screen will thus quite critically depend upon the degree of optical contact of the phosphor grains with the mica surface. This will in turn depend upon the average grain size and the method of deposition of the screens. Zworykin et.al. (1954) reported that about 20 to 30% of the grains are in optical contact in the case of settled screens. A higher degree is to be expected for electrophoretically deposited screens, which are used in the intensifier, since a better packing of the grains is achieved by this method.

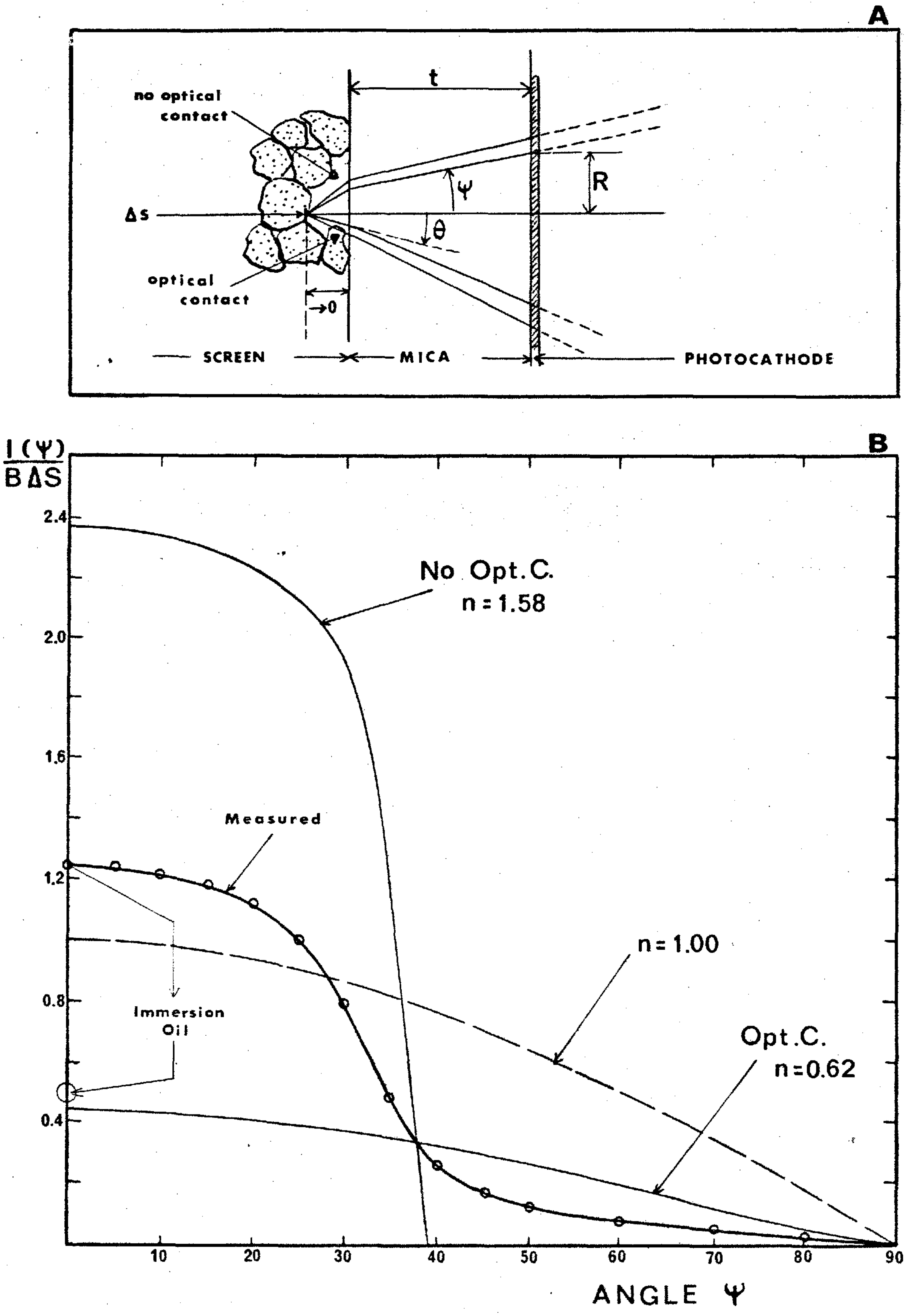

FIG_ 8.6 OPTICAL CONTACT

The following experiment was performed to measure the angular intensity distribution of the light emerging from the screen - mica interface. Total internal reflection at the mica - air interface of the membrane was eliminated by bringing a glass semi-sphere of the same refractive index into optical contact with the mica by means of immersion oil . A small area of the screen located at the centre of the sphere is excited with U.V. light and a photomultiplier is used to measure the resulting phosphorescence at varying angles Ψ to the normal on the screen. The measured distribution can be drawn on scale in Fig. 8.6.B since it should pass through the interception of the two theoretical curves ($\Psi = 38^\circ$; $I(\Psi) / B . \Delta S = 0.34$). This was verified by allowing immersion oil to diffuse between the grains and the mica while the light intensity at $\Psi = 0$ was monitored. A decrease in intensity of a factor of 2.5 was measured which corresponds approximately with the expected difference of intensity at $\Psi = 0$ between the real screen ($I(\Psi) / B . \Delta S = 1.25$) and that where grains are in full optical contact ($I(\Psi) / B . \Delta S = 0.42$).

It can thus be seen that about 60% of the light emerging perpendicularly to the screen behaves as if it originated from grains in optical contact with the substrate. This does not mean that 60% of the grains are actually in physical contact with the mica. Indeed the average phosphor grain is about 1 micron in diameter and it emits light with a wavelength of 0.40 to 0.55 microns. Therefore, light can easily "leak" through a gap and behave as if it was in optical contact. In other words, light from a grain not in physical contact, and incident on the mica with an angle higher than the critical angle (39°) could be transmitted in the membrane (frustrated transmission).

8.4.2 Point Spread Function and MTF of the Mica Membrane.

The measured angular distribution $I(\Psi)$ is now used to calculate the spread of light at the photocathode of the dynode (Fig. 8.6.A). The light flux in the solid angle sustained by a ring element dR at a distance R from the axis is $2\,\Pi\,.\,I(\Psi).\sin\Psi\,d\Psi$. The illumination of that ring of area $2\Pi\,RdR$ is thus

$$P(\Psi) = \frac{2.\Pi.\;I(\Psi)\,\sin\Psi\;d\Psi}{2\,\Pi\,RdR}$$

Now from Fig. 8.6.A : $R = t.\mathrm{tg}\,\Psi$ and thus $dR = td\Psi/\cos^2\Psi$ and also $\cos\Psi = t/(t^2 + R^2)^{1/2}$ so that the illumination at a distance R is given by:

$$P(R) = \frac{I\left(\mathrm{arctg}\,\frac{R}{t}\right)\;.\;t}{(t^2 + R^2)^{3/2}} \qquad (8.8)$$

Multiplication of P(R) by the transmission of the mica-photocathode interface which was calculated from Fresnel's equation in function of R (or Ψ), leads to the point spread function of the mica membrane. The refractive index of the photocathode was taken to be 3.00, as reported by Wallis (1956) for blue light illumination of a $Cs_3\,Sb$ cathode. Total internal reflection occurs at the photocathode - vacuum interface (critical angle : 20°). However, the resulting spread of light can be neglected owing to the thinness of the photoemissive layer (0.05 microns).

The calculated point spread function for the mica membrane using the results of the measurement of $I(\Psi)$, is shown in Fig. 8.7.A. This curve is normalised to the maximum intensity (R = 0). Also shown is the normalised line spread function obtained by numerical integration of:

$$L\left(\frac{R}{t}\right) = 2\int_0^{\infty} P\left[\sqrt{\left(\frac{R}{t}\right)^2 + \left(\frac{y}{t}\right)^2}\right]\, d\left(\frac{y}{t}\right) \qquad (8.9)$$

where y is distance along the line. Finally, the modulation tranfer function of a 4 micron thick mica membrane was calculated by taking the Fourier transform of the line spread function by means of a computer programme (Appendix II).

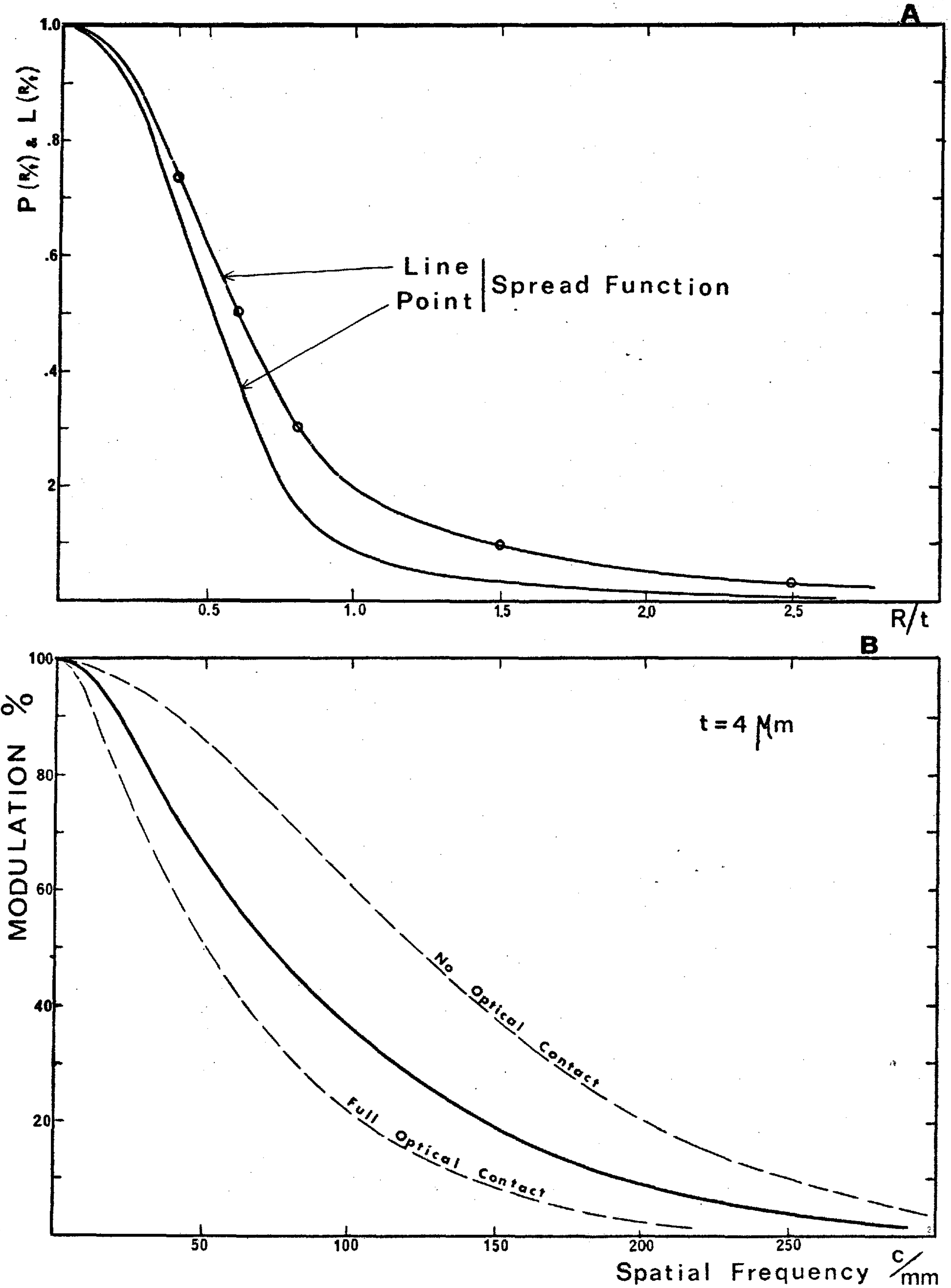

FIG 8.7 MTF of the MICA COUPLING

The resulting modulation transfer function of the mica membrane is shown in Fig. 8.7.B. The limiting spatial frequency corresponding to MTF = 0.05 is 240 cycles per mm.

8.5 MODULATION TRANSFER FUNCTION OF THE PHOSPHOR SCREENS

Limiting resolutions of the phosphor screens used in the I.C. cascade intensifier are routinely measured optically in a device in which a UV illuminated Baum pattern is projected onto the screen. Observation of the excited pattern with a low power microscope reveals limiting resolutions of 120 ± 5 lp/mm. A limiting resolution of 132 ± 3 lp/mm was observed by the author on a one stage tube (C) for a 1.0 mg/cm^2 thick screen.

8.5.1 Measurements of the MTF of the Screens.

An attempt at measuring the MTF of phosphor screens was made but it proved to be extremely difficult to obtain accurate results. The procedure used will therefore only be briefly discussed here. A phosphor screen was bombarded in a demountable vacuum system, with a narrow (10 microns) slit shaped electron beam and the luminescent slit was imaged and magnified onto a slit placed in front of a photomultiplier. The line spread function was obtained by scanning the latter slit across the image. The MTF shown in Fig. 8.8 was obtained by calculating the Fourier transform (appendix II) of the measured line spread function and correcting for the MTF of the recording optics. Two factors were responsible for the large error in the results. The poor quality of the slit used to produce the exitation of the phosphor caused an appreciable amount of electron scattering. Furthermore, the MTF of the analyzing optics was not sufficiently high at high spatial frequencies to permit an accurate correction of the MTF of the complete system.

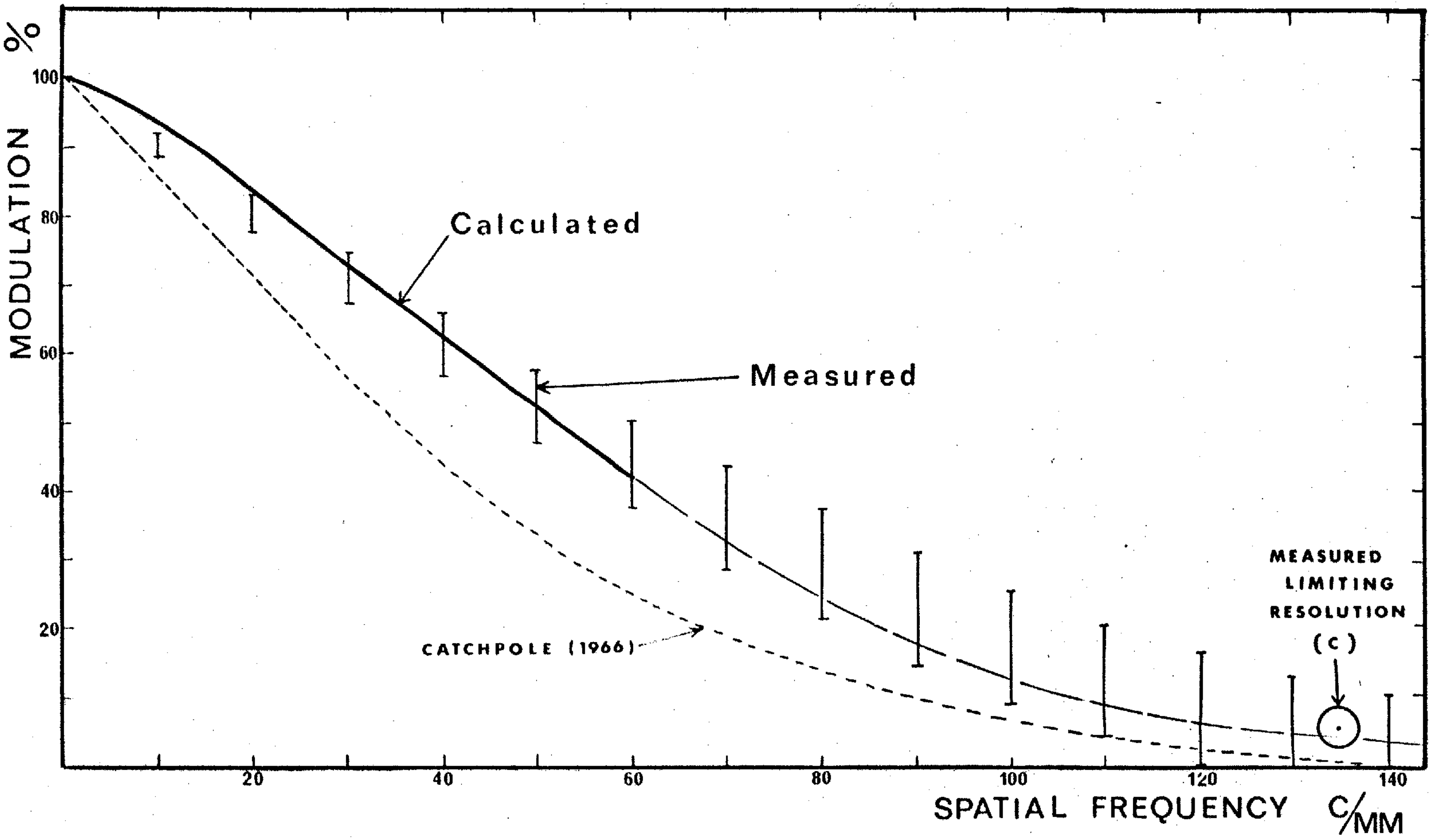

FIG 8.8 MTF of the PHOSPHOR SCREEN

8.5.2 Calculation of the MTF of the Screens.

The MTF of a phosphor screen can be calculated from the measurements of the MTF of the complete system on axis (§ 8.2) and from the MTF of the mica coupling (§ 8.4), using : (eqn.8.1)

$$\text{MTF } (w) \text{ screen} = \sqrt[3]{\frac{\text{MTF } (w) \text{ intensifier}}{\text{MTF}^2 (w) \text{ mica}}}$$

This assumes that the aberrations caused by the electron optics on axis are negligible compared to the total aberration of the system. Fig. 8.8 shows this calculated MTF being within the experimental error of the measured MTF except for very low spatial frequencies. Also shown in comparison is the result obtained by Catchpole (1966) for an electrophoretically deposited screen made of P20 phosphor grains of a slightly higher average diameter (1-3 microns).

8.6 CONCLUSION AND MTF OF THE COMPLETE SYSTEM.

The aberration caused by the electron optics on axis are very small compared with those caused by the spread of light in the phosphors and the micas. However, they become significant at distances higher than 10 mm from the centre of the field. The lack of uniformity of the electric field is mainly responsible for this aberration. It was shown that the field leakage in the processing compartment of the last stage is only responsible for a small contribution to the off-axis aberration.

The limiting resolution of the cascade intensifier could be improved to 65 - 70 lp/mm by replacing the 4 microns thick mica membranes by 500 Å thick films of self-supporting aluminium oxyde.

The modulation transfer function of the complete system, i.e. intensifier, coupling lens and emulsion can now be calculated from the results of the MTF measurements of the coupling lens (§ 6.3.4) and the intensifier (§ 8.2) and from the data presented in Tab. 1.1 for the MTF of photographic emulsions.

The results for various combinations of lens and emulsion are shown in Fig. 8.9. The system is thus able to resolve 35 to 45 lp/mm, which is sufficient for a large range of practical applications.

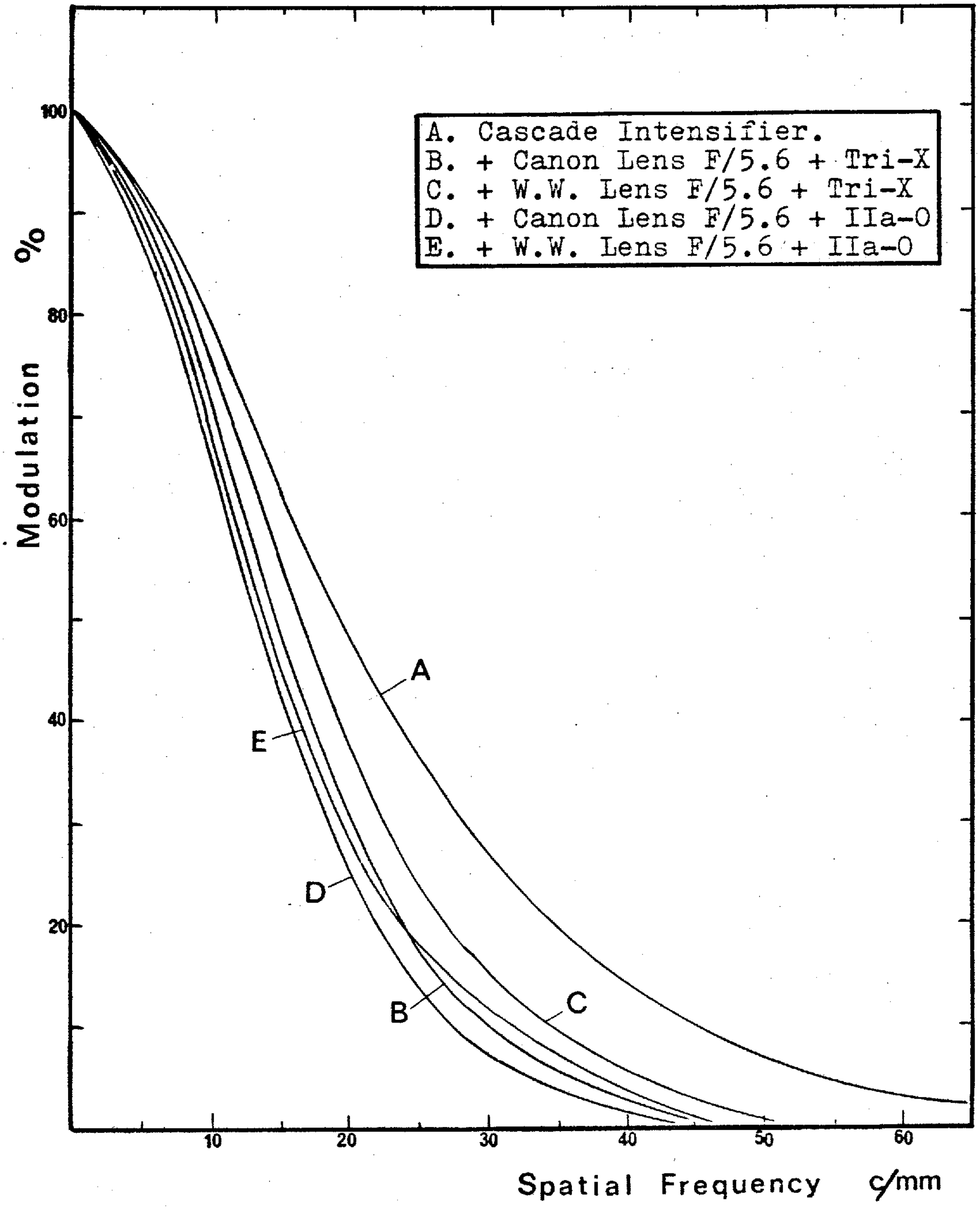

FIG 8.9 SYSTEM MTF

CHAPTER 9

THE IMAGE GEOMETRY

An ideal focusing system employing uniform and parallel electric and magnetic fields produces an erect image with unit magnification. Any disturbance causing non-uniformities in these fields will cause image distortion. It is the purpose of this chapter to analyze how well the geometry of an image is maintained as it is transfered through the intensifier, and to investigate the causes of distortions.

Several examples of image geometry are shown in Fig. 9.1. Tube 73 is a typical intensifier equipped with photocathode and dynode holders of the old design and operated in the solenoid used by previous investigators (Powell, 1967). Significant improvement of the geometry was obtained by incorporating newly designed dynode holders (§ 5.3.1) and operating the intensifiers in the new type of solenoid (§ 6.1). The geometry of tubes 76 and 109 are examples of the best geometry obtained, while tube 91 (shown for the two directions of the magnetic field) gives more average geometry quality. The geometry of tube 94 is poor and characterized by a strong shear distortion.

9.1 DISTORTION FIGURES

If the position of an image element at the photocathode is given in polar coordinates by $\tau_i \, \theta_i$ as shown in Fig. 9.2 A ($\theta_i = o$ is an arbitrary radius fixed to the image tube), then the location of the corresponding intensified image element can be described by the following coordinates:

$$\tau_o = M_L \, (\tau_i . \theta_i) \cdot \tau_i \tag{9.1}$$

$$\theta_o = \theta_i + \Theta \left(\tau_i \, \theta_i \right) \tag{9.2}$$

where $\Theta \, (\tau_i \; \theta_i)$ is the angle corresponding to the position dependent rotation of the image element around the origin and $M_L \, (\tau_i \; \theta_i)$ is the linear magnification. Perfect distortionless imaging will, in general, be obtained if $M_L(\tau_i \; \theta_i)$ and $\Theta(\tau_i \; \theta_i)$ are constant for all points of the field.

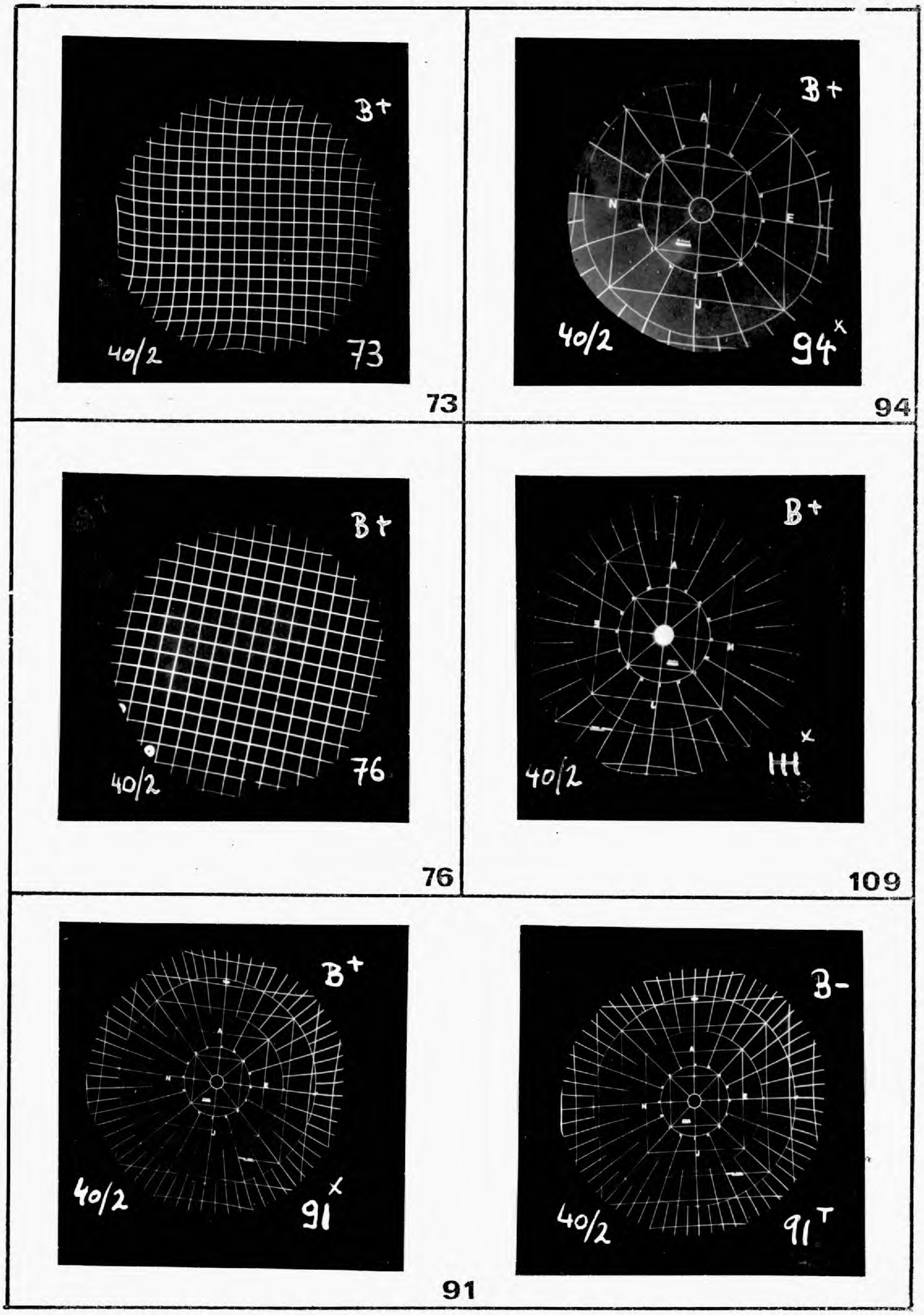

73

94

76

109

91

FIG 9.1 IMAGE GEOMETRY

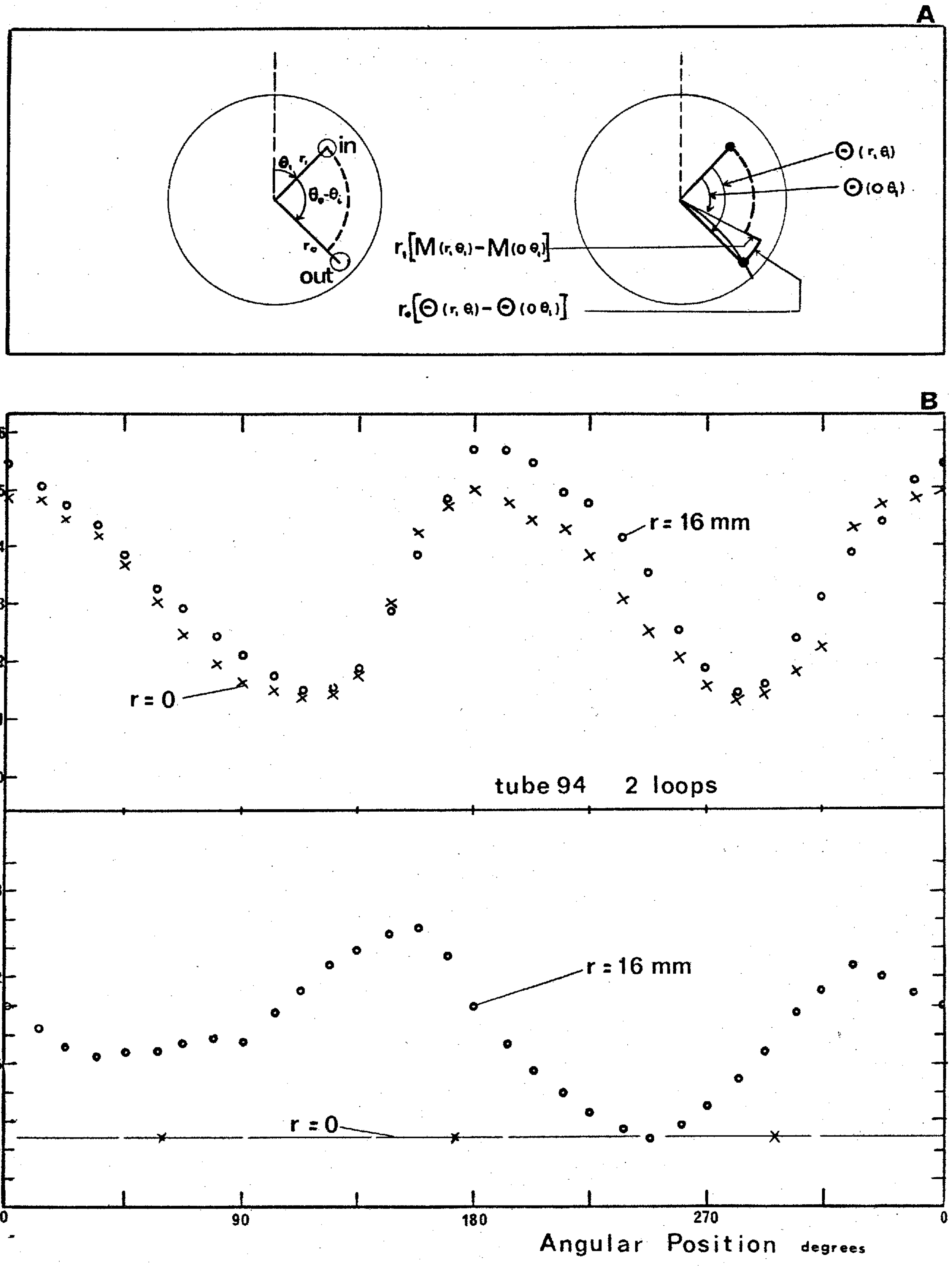

FIG 9.2 DISTORTION Measurements

If the field distributions are axially symmetric then both M and Θ are only dependent upon the radial position r_i. In that case distortions in an image are often described by three characteristic types.

_ S- distortion : in which $\Theta(r_i)$ increases or decreases with increasing r_i

_ Barrel-distortion : in which $M_L(r_i)$ decreases with increasing r_i

_Pin-cushion distortion in which $M_L(r_i)$ increases with increasing r_i

Visual analysis of the patterns of Fig. 9.1 however, shows that the system is not axially symmetric. It will therefore be necessary to measure $M_L(r_i\, \theta_i)$ and $\Theta(r_i\, \theta_i)$ for all points of the field, if a quantitative description of the image geometry is needed.

Distortion can be conveniently expressed in terms of the difference between actual output position and that predicted by paraxial imaging properties. Thus the tangential departure may be expressed in percentage of the distance to the axis:

$$S(r_i\, \theta_i) = \left[\Theta(r_i\, \theta_i) - \Theta(o\ \theta_i)\right] 100 \qquad (9.3)$$

where Θ is expressed in radians. The sagittal (radial) departure may be expressed in percentage of the distance to the axis by:

$$D(r_i\, \theta_i) = \left[\frac{M_L(r_i\, \theta_i) - M_L(o\, .\, \theta_i)}{M_L(o\, .\, \theta_i)}\right] 100 \qquad (9.4)$$

The figure D is positive for pin-cushion type distortion and negative for barrel type.

9.2 DISTORTION MEASUREMENTS

The photographed patterns are projected on polar graph paper with a magnification of about 10. Magnifications are measured by comparing the output image with that obtained by direct photography of the test pattern using identical optics. Rotations are refered to the bisector of two superimposed records of a radial line obtained for the two directions of the magnetic field.

Results of the analysis of the distortion tube 94 (poor geometry) are shown in Fig. 9.2 B. This graph shows the variation of M and Θ for all values of θ and for $r_i = o$ and $r_i = 16$ mm. Using eqn. 9.3 and 9.4 it is possible to calculate $S(16.\theta)$ and $D(16.\theta)$ whose maximum, minimum and average values in respect of the angular positions are given in Tab. 9.3. Similar measurements were made on tubes 76 and 109, and the same figures are also given in this table. Tubes

76 and 109 (considered to have good geometry) have thus about 1% S – distortion and about + 4.5% D – distortion (pin-cushion type). However tube 94 has a lower average S – distortion but a larger spread in these values at different angular position. Its D – distortion is larger and again varies considerably with angular position.

It appears thus that the worst kind of distortion occurring in these intensifiers is not S – distortion but is caused by an angular position-dependent linear magnification and rotation of the image. This causes a loss of orthogonality in the center of the working field, and a resulting distortion often characterized as "shear" distortion. The geometry of an image generally improves as the magnetic field is increased from 1 to 2 loops focusing in each stage and is expected to improve further if 3 loop focusing was used. However, this would require a magnetic field of about 400 Gauss which is not attainable with the present solenoid and current supply. The geometry also improves as the operating stage potentials are increased.

9.3 ORIGIN OF AXIALLY SYMMETRIC DISTORTIONS

Radial electric and magnetic field components give rise, in conjunction with the axial fields, to rotation and (de)-magnification of the image. The direction of rotation as well as that of radial departure depend upon the orientation of the radial field and that of the axial magnetic field.

9.3.1. Electric field in the photocathode region.

The design adopted by Powell (1967) for the photocathode and dynode holders was such that the plane of the photoemissive surface did not coincide with the plane of its holder at the cathode side, the distance between the planes being about 2 mm. Therefore the equipotential planes were bent in the vicinity of the edge of the cathode causing marked S – distortion. Modification of the design of the dynode holders (§ 5.3.1) reduced this distance to 0.5 mm. i.e. the thickness of a titanium ring, while the primary photocathode holder was redesigned so that the two planes coincide. This has led to a drastic reduction of the S – distortion at the edge of the field.

The effect of non-uniformities in the electric field caused by incorrect values

Intensifier Number	94	94	76	76	109	
Number of Loops	1	2	1	2	2	
Solenoid Used (tab.6.3)	D	D	C	C	D	
First Stage Potential	14.60	14.20	13.70	14.05	13.10	KV
Second Stage Potential	12.80	12.50	14.55	13.90	13.85	KV
Third Stage Potential	12.60	13.30	11.75	12.05	13.05	KV
Average Focusing Field	137	271	140	274	269	Gauss
Average Axial Rotation	10.2	3.1	11.7	4.9	4.2	degr
Max.Rotation at 0 mm	5.9	5.0		5.0	4.3	"
Min.Rotation at 0 mm	4.5	1.5		4.8	4.0	"
Average Rotation at 16mm	11.0	3.2	18.1	5.2	4.9	"
Max. Rotation at 16 mm	18.2	5.9		5.3	5.3	"
Min. Rotation at 16 mm	4.9	1.5		4.9	4.2	"
Average S% at 16 mm	+1.33	+0.17	+1.1	+0.52	+1.14	%
Maximum S% at 16 mm	+3.82	+1.57		+0.65	+1.80	%
Minimum S% at 16 mm	+0.70	+0.03		+0.00	+0.35	%
Paraxial Magnification	1.084	1.005	1.075	1.009	1.010	-
Average Lin.Magn.at 16mm	1.210	1.083	1.150	1.070	1.059	-
Maximum Lin.Magn.at 16mm		1.155			1.092	-
Minimum Lin.Magn.at 16mm		1.006			1.040	-
Average D% at 16 mm	+11.6	+ 7.8	+7.0	+ 4.6	+ 4.3	%
Maximum D% at 16 mm		+15.0			+ 7.6	%
Minimum D% at 16 mm		+ 0.1			+ 2.4	%
Maximum Loss of Axial Orthogonality		4.0		0.7	1.1	degr

TAB 9.3 DISTORTION DATA

of the potentials of the first and second accelerating electrode was investigated on one intensifier (76) operated in 2 loops. A 4% increase in the potential of the first annulus of the first stage from the value giving best geometry caused the S – distortion to increase from 0.5% to 2.0% (at 16 mm. of the axis) while an increase of 13% in the potential of the second annulus was needed to produce the same deterioration in geometry. Although the resistors of the external divider chain provide potentials to the electrodes within 1% of their average value, the distances between the annuli can vary as much as ± 3%. This results from the difficulty in accurately spacing the slots which locate the metal electrodes in the wall of the glass envelope. (§ 5.2.1). The potentials required to produce a uniform electric field can therefore only be obtained by the use of selected resistors producing voltage drops proportional with the measured distance between two electrodes. This was done for several intensifiers with a marginal improvement in the geometry.

9.3.2. Electric field in the last stage

No potential is applied on the processing compartment in the last stage so that field leakage from the active region of that stage occurs. The potential distribution in the last stage was calculated by solving Laplace equation with the classical relaxation method (Angot, 1961; Klemperer, 1953). Fifteen steps of relaxation were used with a mesh spacing of 10 mm. (60 variable and 44 fixed meshpoints). The results are given in Tab. 9.4 A, where the potentials are expressed in percentage of the potential applied on the last stage. The last column of this table was calculated using the relation given by Zworykin et al (1945) for the axial potential distribution in a circular aperture separating two regions of constant electric field. Good agreement is thus obtained for the axial potentials using the two methods. Fig. 9.4 B shows a plot of equipotential planes obtained by graphical interpolation of the results of the relaxation method.

The rotation $\Theta(r)$ of a picture element at a distance r from the axis is given by (Smith, 1968)

A

Distance from Cathode. (mm)	Relaxation Method.			Wall	Computed
	Axial	10 mm	20 mm		Axial
00	00.00	00.00	00.00	00.00	00.38
10	16.65	16.65	16.66	16.66	16.07
20	33.26	33.27	33.33	33.33	32.55
30	49.70	49.78	49.98	49.99	48.76
40	65.73	65.96	66.66	66.66	64.48
50	80.44	81.15	82.92	83.33	78.60
60	92.21	93.77	100.00	100.00	89.39
70	97.08	97.77	99.52	100.00	95.26
80	99.00	99.17	99.72	100.00	97.73
90	99.65	99.73	99.88	100.00	98.76
100	99.91	99.91	99.96	100.00	99.40
110	99.97	99.97	99.98	100.00	99.62
120	100.00	100.00	100.00	100.00	99.98

B

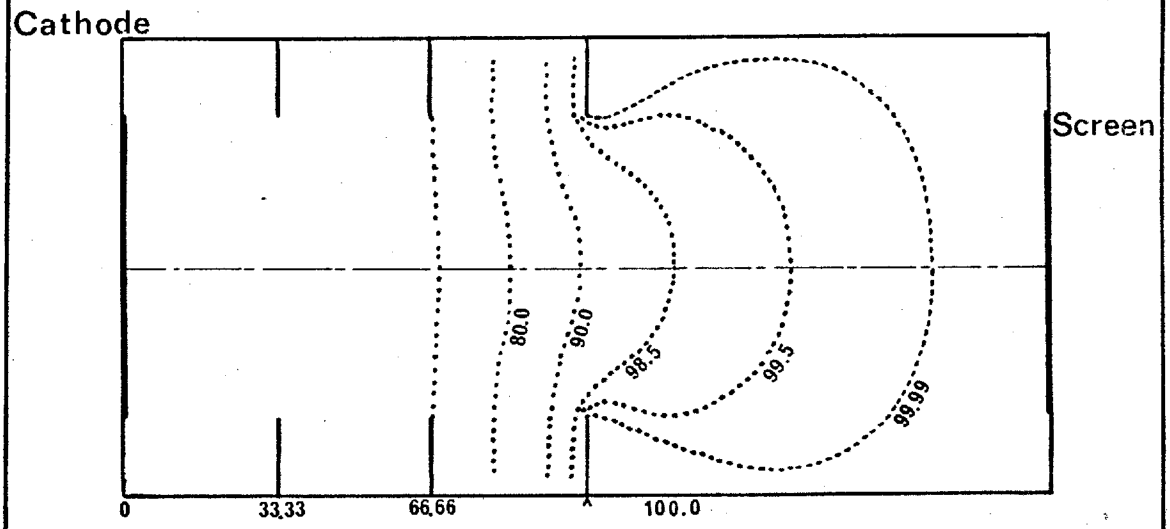

Potentials expressed in % of the potential of the processing shelf and phosphor screen.

FIG 9.4 ELECTRIC FIELD in LAST STAGE

$$\left|\Theta(r)\right| = \sqrt{\frac{m}{2e}} \cdot \frac{1}{H} \cdot \int_{z=0}^{z=L'} \frac{1}{r} \frac{E_r(z.r)}{\sqrt{V(z.r)}}\,dz \quad \text{with } E_r(z.r) = \frac{\partial V(r.z)}{\partial r} \qquad (9.4)$$

where H is the uniform magnetic field and $V(z.r)$ the electric potential and E_r the radial electric field. For paraxial electrons (r very small) $E_r(z,o)$ becomes (Klemperer, 1953):

$$E_r(z,o) = \frac{\partial V(z,o)}{\partial r} = \frac{r}{2} \cdot \frac{\partial^2 V(z,o)}{\partial^2 z} \qquad (9.5)$$

so that the axial rotation of the image is given by, after substitution of eqn. 9.5 in eqn. 9.4,:

$$\left|\Theta(o)\right| = \sqrt{\frac{m}{2e}} \cdot \frac{1}{2H} \cdot \int_{z=0}^{z=L'} \frac{\partial^2 V(z,o)}{\partial^2 z} \cdot \frac{dz}{\sqrt{V(z,o)}} \qquad (9.6)$$

Using the above data for the potential distribution it is possible to calculate $\partial^2 V(z,o) / \partial^2 z$ by numerical differentiation. Subsequent integration of eqn. 9.6 gives (using eqn. 4.1) :

$$\left|\Theta\ (o)\right| = 450 \frac{\sqrt{V_T}}{H} = \frac{6.04}{n} \text{ degrees} \qquad (9.7)$$

where V_T is the potential applied on the last stage and n the number of loops used for focusing. The paraxial rotation is thus 6.04 and 3.02 degrees for one and two loops respectively. The rotation at 15 mm from the axis was then computed by numerical integration of eqn. 9.4 in which E_r was found by numerical differentiation of the interpolated results of the relaxation method. The factor 6.04 of eqn. 9.7 increased to 6.11 so that the coefficient of S – distortion can be calculated from eqn. 9.3 to be 0.12% in 1 loop and 0.06% in 2 loop focusing at 15 mm from the center of the field. Comparing these results with those obtained by measurements on tubes (Tab. 9.3) it is possible to conclude that the field leakage in the last stage is only responsible for a very small amount of S-distortion and for part of the image rotation. This latter point was confirmed by measurements made on tube 112, which has equal stages and no region of field leakage because the output phospher is located on the processing shelf. (Observation is performed through the processing chamber). Indeed an image rotation of 2.5 degrees still occurred in 2 loop focusing. However, the axial magnification in that tube was reduced to 1.002 in two loop and to 1.015 is one loop focusing as compared to values of about 1.010 and 1.080 for standard intensifiers (Tab. 9.3).

9.3.3. Magnetic Field

Considerable improvements in the geometry of the image was obtained by operating the cascade intensifiers in the new type of solenoid (§ 6.1) in which the field uniformity is ± 0.3% on axis as compared to ± 3% for the solenoid used by previous workers (Powell, 1967; Varma, 1968). The field at 20 mm from the axis is on the average 0.1% higher than on axis and 1% higher in the region of the first photocathode. This should give rise to a slight amount of rotation and magnification.

9.4 ORIGIN OF AXIALLY ASYMMETRIC DISTORTIONS.

Attempts were made to explain the origin of asymmetric distortions by comparing the geometry patterns obtained with a plan, made before encapsulation, of the location of possible distortion causes in the cascade tube (magnetic slugs, position of tapes, dimples in processing compartment, shape of annuli, etc.). Although it is possible to correlate some type of distortions with the position of certain items, it was unfortunately very difficult to draw strong conclusions about their relative importance. The search for correlation is complicated by the presence of three cascaded stages and by the incidental allignment of distortion-causing items. Nevertheless, some cause-effect relations were found and are reported below. The distortions can be accentuated by operating the intensifier at low overall potential (25 KV) and in one loop focusing as shown in Fig. 9.5 A.

9.4.1. Magnetic Slugs

The effect of magnetic soft iron slugs, used for locking the photocathode substrate plate and dynodes in their respective holders, is clearly visible in Fig. 9.5 A, as a localized region of magnification and rotation. This distortion is still visible under normal operating conditions, but is confined to the edge of the field.

9.4.2. The "ears" in the second dynode holder

Two regions of radial magnification are observable in areas corresponding to the two holes in the second dynode holder. These two apertures (area about 0.5 cm^2 each) between the second and the third stage are the consequence of the special shape of the dynode holder that permit the transfer of the photocathode plate (Fig. 5.3). The electric field in the second stage is theoretically 1.5 times lower than that of the third stage since the same potential is applied on the 9 cm long second stage as on the 6 cm long active region of the third stage. According to stage potential data presented in Tab. 9.3, this ratio varies in practice between 1.30 and 1.70. Field leakage through these apertures will cause radial components of the electric field oriented towards the axis to be present close to the photocathode of the third stage. The electron image will therefore be magnified in these regions, leading to the type of angular position-dependent magnification as measured in Fig. 9.2 B. This effect certainly decreases as the tube is operated in normal conditions because the photoelectrons travel more rapidly through the disturbed region, but no definite conclusion could be drawn about its magnitude and its contribution to the observed shear distortion. However, two facts tend to favour this theory. Firstly, the position of maximum magnification in tube 94 (Fig. 9.2 B) corresponds approximately to that of the two apertures. Secondly, the ratio between the electric field in the third and second

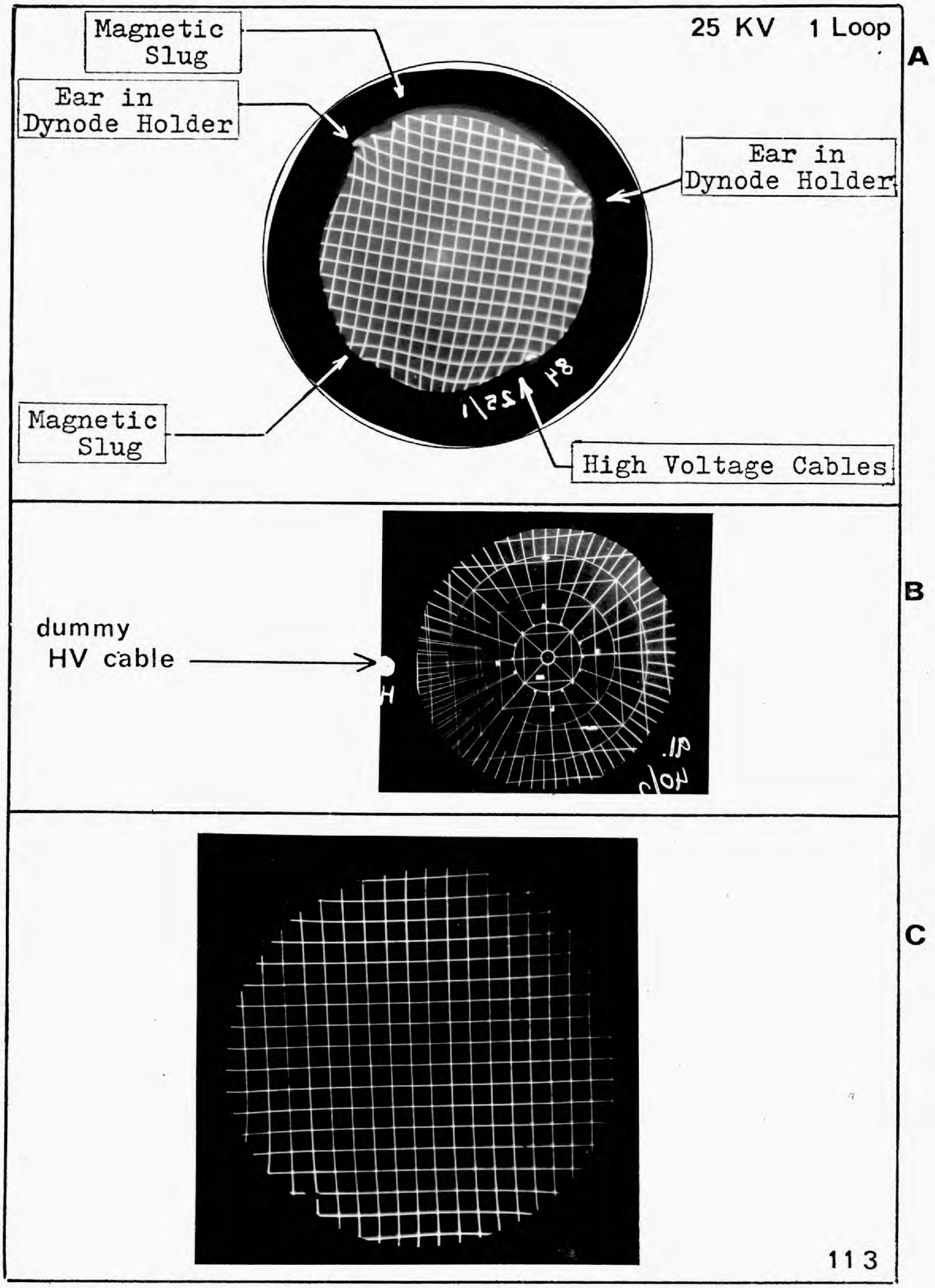

FIG 9.5 GEOMETRY

stage is higher for tube 94 than the same ratio in tubes 76 and 109, where less shear-distortion is present.

9.4.3. Field Leakage of the High Tension Leads

Severe demagnification and rotation can be observed in Fig. 9.5 A in the area close to the position of the high voltage cables that provide fixed potentials to the dynodes. This is the result of field leakage inside the envelope from these conductors, which produces a radial electric field oriented towards the cables, since the potential of the latter is always smaller than that inside the envelope. This effect can be demonstrated in a tube operated under normal conditions (40 KV, 2 loops) by placing a dummy high voltage cable along the first stage in a similar position to those in the other two stages (this cable is not connected to any point of the divider chain and is insulated at its end). Fig. 9.5 B was obtained by superimposing a pattern recorded with this cable held at zero potential with that obtained with the cable held at + 15 KV, to simulate the effect of the H T cable from the first dynode passing along the third stage. A distinct distortion affecting nearly half the working region can be observed.

Under normal operating conditions one might expect an even bigger effect since the cable from the first dynode is located along the second and third stage and that from the second dynode along the third stage (Fig. 4.1). This distortion could be minimized by efficient electrostatic screening of the envelope. Additional conductive bands were painted on the outside wall of recent intensifiers in between those making contact with the internal electrodes, but no accurate measurements have yet been performed to evaluate the eventual improvement in geometry.

9.4.4. Orthogonality of the Photocathode Plane on the Axis

If the photocathode is not perpendicular to the axis of a stage, then a cylindrical electric field will be produced between the cathode and the first equipotential plane which is perpendicular to the axis. Shear distortion will result because the displacement and rotation of the electron image leaving the cathode increases as the distance between the two planes decreases (Zworykin et. al., 1945).

The dynode holders in the intensifiers used for the measurements reported in this chapter were held in position by three spring clips, made of Inconel wire, which were engaged in a slot in the glass wall. It was noticed that these holders were often slightly tilted after backing off the intensifier on the pump, as a possible result of the high temperatures created by eddy current heating of the parts. Therefore new types of dynode and photocathode holders attachment were designed (Airey, 1971), which provide a very rigid positioning of these parts in the glass envelope.

9.5.5. Misalignments

The misalignment of the axis of the electric and magnetic fields will not, if both fields are uniform, introduce any image distortion since every point of the image is subjected to an identical displacement and rotation. However, if the fields are not uniform this will introduce asymmetric distortions. In that respect great care must be taken in the alignment of the two parts of the intensifier during the silver-chloride seal and in the axial positioning of the intensifier and its encapsulation.

9.6 CONCLUSIONS

Fig. 9.5 C shows a pattern recorded on one of the latest intensifiers (113) operated in 2 loops focusing at 40 KV. This tube incorporated the latest type of dynode holders and the additional electrostatic shielding of the envelope. The geometry is significantly better than most of the results presented in Fig. 9.1

It could be concluded that the geometry of the cascade intensifier, operated in the new solenoid, is mostly degraded by the limited mechanical tolerances used in the construction of the intensifier. It was shown that the only major deviation from ideal electrode configuration, i.e. the processing compartment in the last stage, only contributes a small amount of distortion. The shear distortion observed in several intensifiers is suspected to be caused by accidental lack of orthogonality of a photocathode on the axis of the envelope or/and by an asymmetric electric field distribution caused by the special shape of the internal electrodes.

The geometry is sufficiently good, however, for most practical applications, but corrections might be required if very accurate positioning of features in the intensified image is needed.

CHAPTER 10

BACKGROUND IN ABSENCE OF SIGNAL

Spurious background is a serious problem in high gain intensifiers. It lowers the signal to noise ratio and the equivalent quantum efficiency of the detector and sets, therefore, a limit to the detection of faint objects.

The spurious optical and electrical effects which originate in the first stage of the intensifier will be the most significant in the output image because of subsequent intensification. This background is observable in the form of scintillations (Fig. 10.1 A), and these can be divided into two distinct types:

— Scintillations which have the same intensity as photoelectron events, or single electron scintillations (SES)

— Scintillations of higher intensity, i.e. 5 to 15 times the intensity of a single scintillation, or bright electron scintillations (BES).

An extensive study of these phenomena was made by Powell (1967) on the I.C. cascade intensifier. The purpose of this chapter is to report on a few measurements and theoretical considerations about the origin of spurious background. In doing so, and for the sake of completeness, it was impossible not to repeat some of Powell's lines of thought.

10.1 BACKGROUND MEASUREMENTS

The background is normally assessed by counting the number of recorded tracks on Kodak Tri-X emulsion, coupled with the intensifier by means of the Canon f/1.2 lens. This is done, for a known area and exposure time, in a photographic enlarger.

10.1.1. Single Electron Scintillations (SES)

S.E.S. are uniformly distributed over the central region of the working field

A

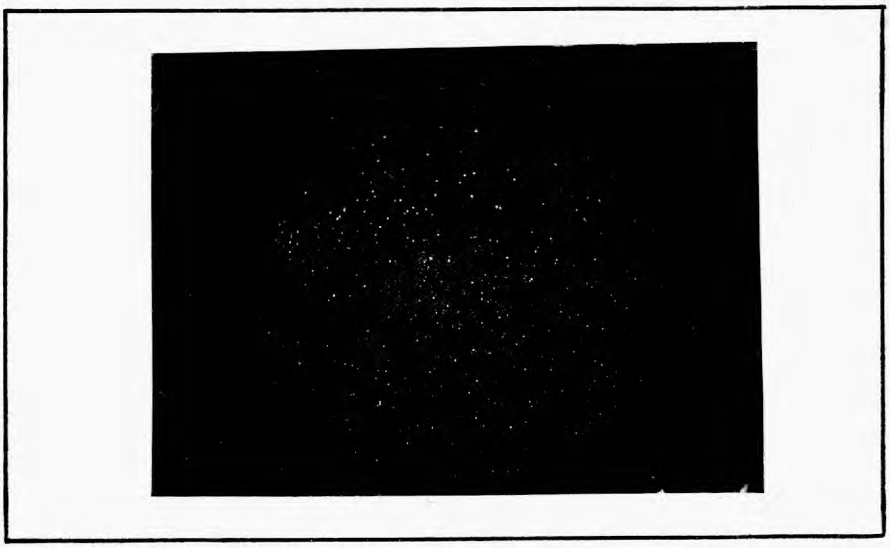

B

TUBE		35	40	45	KV
78	SES BES	70 0.2	200 0.7	2000 6.0	$/\text{cm}^2/\text{sec}$ $/\text{cm}^2/\text{sec}$
82	SES BES	95 0.5	600 3.0		$/\text{cm}^2/\text{sec}$ $/\text{cm}^2/\text{sec}$
113	SES BES	55 0.2	95 0.4	550 2.0	$/\text{cm}^2/\text{sec}$ $/\text{cm}^2/\text{sec}$

C

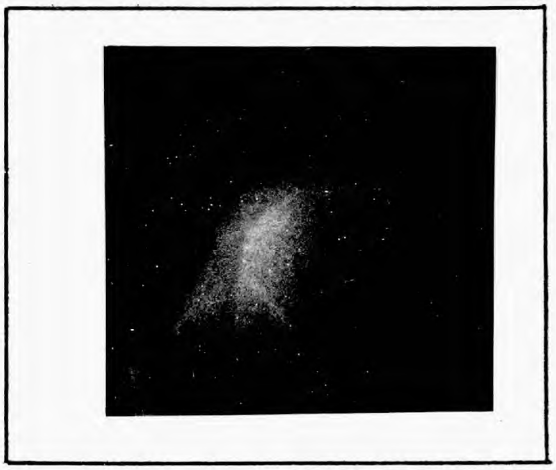

FIG 10.1 SPURIOUS BACKGROUND

and their count varies from tube to tube from 50 to 500 SES/cm^2/sec at room temperature (≈20°C). Their count decreases as the overall operating voltage is decreased as shown in Tab. 10.1.B. A slight increase in abundance of SES is usually observed at the edges of the field.

Localized patches and streaks of scintillations are sometimes observed in noisy intensifiers. The count in these regions can be as high as 3000 SES/cm^2/sec and is strongly dependent upon the focusing condition (Fig. 10.1 C).

10.1.2. Bright Electron Scintillations (BES)

The occurence of BES is very much time dependent, so that their count must be measured over a large effective exposure time. The abundance of BES is generally between 0.2 and 3 BES/cm^2/sec at 40 KV, and rises with the overall operating potential above 29 - 30 KV (Tab. 10.1 B). They are fairly well uniformly distributed across the field except at its edges where their number increases.

It is certain that BES arise from simultaneous emission of 5 to 15 electrons from the primary cathode, since they can be split up into individual electron scintillations by slight defocusing of the first stage.

10.2 PRACTICAL IMPORTANCE OF SPURIOUS BACKGROUND

By raising the noise level, any form of spurious output will reduce the signal to noise ratio of the device. This will limit the intensity of the faintest detectable object in a low contrast image. If B is the SES count (SES/cm^2/sec) at the output of the intensifier, then B/QE.RE will be the photon flux (photons/cm^2/sec) incident on the primary cathode which would produce the same scintillation count at the output. QE is the quantum efficiency of the cathode in the wavelength range of the low contrast image and RE the recording efficiency of the intensifier. With regard to threshold performance of the intensifier, the photonflux N (photons/cm^2/sec) from the image background can be said to be increased by

B/QE.RE. Therefore the minimum detectable contrast C_{min}, given by eqn. 1.17, will be multiplied by a factor :

$$\Pi C_{min} = \left[1 + \frac{B}{N \, . \, QE \, . \, RE} \right]^{+\frac{1}{2}} \qquad (10.1)$$

as the result of the instrument background. For example, with $B = 500$ SES/ cm^2/sec, an increase of at least 10% in the minimum detectable contrast can be expected if the number of image background photons incident on the detector is smaller than $2.2 \, . \, 10^4$ photons/cm^2/sec. ($QE = 0.15$; $RE = 0.70$).

10.3 ORIGIN OF SINGLE ELECTRON SCINTILLATIONS (SES)

10.3.1. Thermal Emission of the Photocathode

Most of the SES are the result of thermal emission of the primary photocathode since a count of 50 - 300 is typical of the dark current of an S11 - cathode at room temperature (Tab. 3.1). The magnitude of this dark current can be expected to decrease by about a factor 10 as the cathode is cooled to 0°C.

10.3.2. Field Emission of Electrons

The presence of high electric field in the vicinity of irregularities in the surface of the electrodes, at sharp edges (clips, slugs, foreign particles, ...) and at the interfaces between the electrodes and the glass wall, is a potential cause of field emission. These high fields narrow the potential barrier such that electrons from the metal can tunnel to the vacuum. Field emission currents become significant at fields of 10^6 to 10^7 V/cm, and are greatly increased if the surface is contaminated with caesium, or other adsorbates which lower the work function of the surface. (Muller, 1960; Essig, 1960).

Field emitted electrons originating from outside the accelerating region of the first stage have a small probability of landing on the phosphor screen. Indeed, few of them will acquire sufficient radial or tangential energy to escape from the space between the electrodes. The magnetic field will furthermore constrain the trajectory of these electrons, causing them to impact with increased energy on other annuli. Only electrons emitted at the end of the stage with sufficient radial or tangential energy will reach the phosphor screen. Several calculated trajectories of spurious electrons are shown in Fig. 10.3 to illustrate these comments.

If field emitted electrons are able to bypass several annuli before impact on an electrode, they will have acquired sufficient energy to produce backscattered electrons with high radial or tangential energy. The orbital radius of the trajectory of these electrons can now be sufficiently great to cause their impact near the center of the field (Fig. 10.3). It is thought that such a process might be responsible for the occurence of streaks and patches in the central region of the working field.

Electrons emitted near the glass wall of the tube will most probably strike the wall at glancing incidence with an energy of several hundred eV. Secondary electron emission from Pyrex, which under these conditions can have a ratio as high as 4 to 5 (Hachenberg, 1959; Matskevitch, 1957), will give rise to an avalanche process until a whole shower of electrons is stopped by the next annulus. This process could produce fluorescence from the glass wall, which may reach the photocathode to liberate spurious photoelectrons.

Furthermore the impact of field emitted electrons on internal electrodes will induce the desorption of positive ions (§ 10.4.2) and the emission of soft x-rays.

10.3.3. Other Possible Causes

The presence of radioactive decay products in the materials used for construction of the intensifier may cause spurious scintillations by fluorescence in the glass walls or phosphorescence in the phosphor screens. (Randall, 1970; Powell, 1967).

Relativistic cosmic ray particles passing through the front window and the photocathode support plate of the intensifier will produce a substantial number of Cherenkov photons (2000 - 6000 Å), and hence liberate a few tens of photoelectrons if these photons reach the photocathode (Charman, 1969). For horizontal operation of the intensifier most of the cosmic rays trajectories will be parallel to the faceplate. Therefore only Cherenkov photons emitted in the thin substrate plate will reach the photocathode while total internal reflection will prevent photons, originating in the thick faceplate, from producing any spurious effect. Indeed Cherenkov photons are emitted at an angle $\arccos(1/\beta n)$ with the particle track (n : index of refraction of glass and $1/n < \beta < 1$), such that the angle of incidence with the faceplate - vacuum interface will be $\arcsin(1/\beta n)$ which is always greater than the critical angle $\arcsin(1/n)$. (Burcham, 1963).

Any external instability or corona will give rise to spurious background. Light from a spark or corona discharge may reach the photocathode and sudden changes in potential applied to the internal electrode may enhance field emission of electrons.

10.4 ORIGIN OF BRIGHT ELECTRON SCINTILLATIONS (BES)

The simultaneous emission of a bunch of electrons from the primary photocathode is generally believed to be the result of positive ion bombardment of the cathode. Powell (1967) suggested that some BSE could result from the interaction of soft X-ray with the photocathode. (Jědlicka, 1966).

10.4.1. Dependence of BES abundance upon various parameters

Measurements of BES and SES abundance of different electromagnetically focused intensifiers are shown in Fig. 10.2. These counts were obtained from measurements made on the I.C. intensifier, but also from published data from other

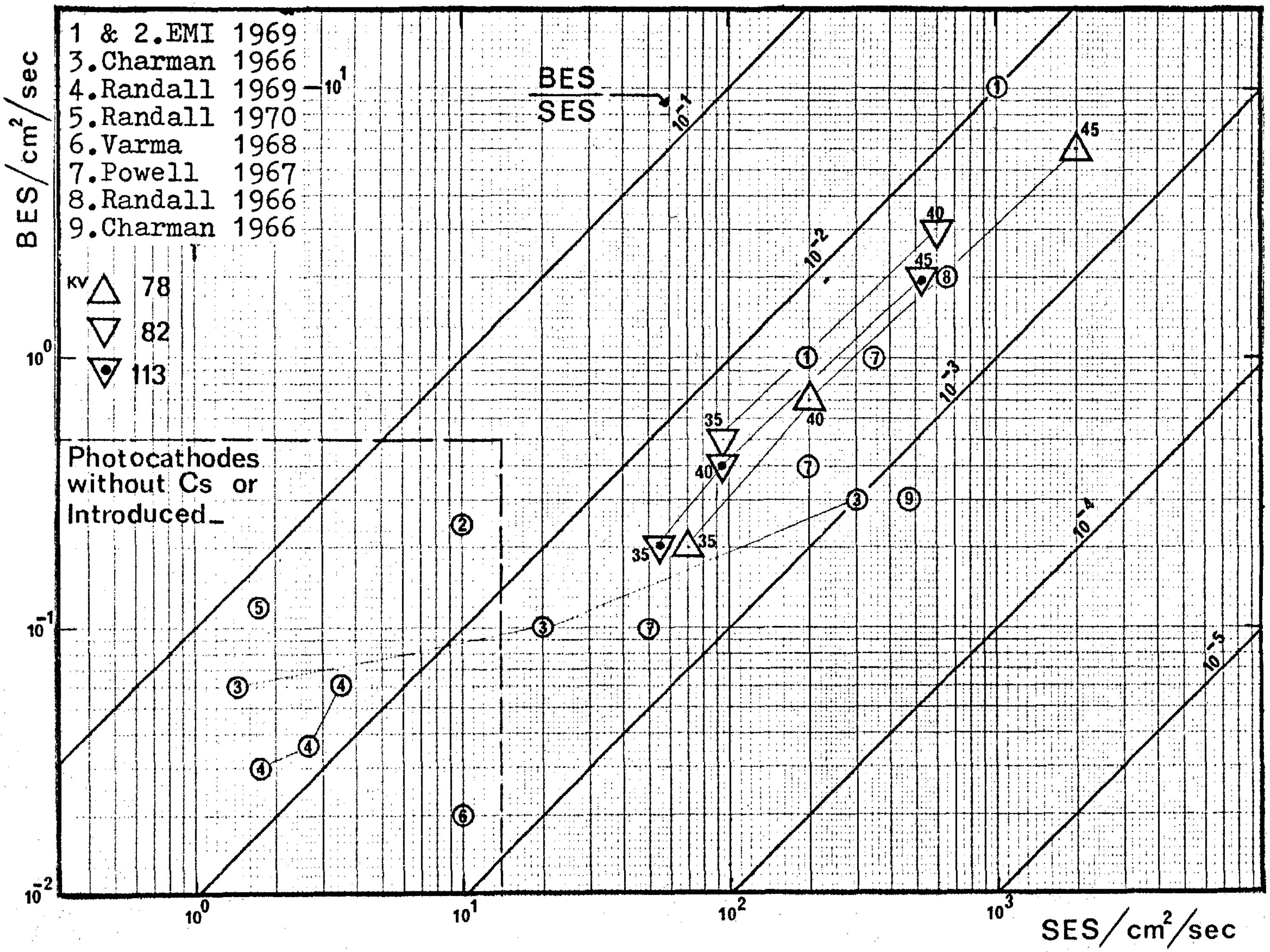

FIG 10.2 SES and BES COUNTS

investigators. It is quite remarkable that the ratio of BES to SES counts lies between 10^{-2} and 10^{-3} for intensifiers which are subjected to caesium contamination.

The abundance of BES decreases with decreasing overall potential and they are generally not visible when the field in the first stage is lower than 1 KV/cm (overall potential $\approx$ 30 KV). Similar lower limit of the electric field are reported by Randall, (1966) and Oliver (1970).

The occurence of SES and BES is strongly reduced if the metal electrodes of the intensifier have not been exposed to caesium vapour during processing, as is the case for externally processed cathodes (McGee et. al. 1969; Varma, 1968) or if no caesium is used for the in situ activation of S24 cathodes (Randall, 1969). (see also Fig. 10.2). A marked reduction in BES abundance is also observed if the electrodes are coated with a film of carbon (a poor X-ray and ion emitter under electron bombardment) or if all passive internal surfaces are coated with a layer of porous aluminium (a good ion trapper). (Randall, 1969)

Early investigators reported no dependence of BES count on temperature (Zavoiskii, 1955; Charman, 1966) but more recent measurements indicate that such dependence does in fact exist (Charman, 1969; Randall, 1969; Oliver, 1970). A decrease in count with decreasing temperature is observed at a smaller rate than the corresponding decrease in SES count.

Signal induced BES, produced by electron bombardment of residual gas molecules, is certainly negligible if the pressure in the envelope is lower than 10^{-7} torr. Indeed with this vacuum, which is believed to be typical for the intensifier, this process would yield about 10^{-6} ions/electron (Dushman, 1958). However Randall (1969) found a dependence of BES count on the number of signal electrons in the same ratio of 10^{-3} BES/electron as that of BES to SES in absence of signal. Measurements reported in § 11.1.7 also show the presence of signal induced BES at a rate of 1.3 to $1.7 \cdot 10^{-4}$ BES/electron. These bright scintillations were positively identified as caused by bombardment of the photocathode by positive ions which are impact desorbed from the phosphor screen by signal electrons.

A large number of BES can be induced by deflecting a photoelectron beam onto a metal electrode by means of saddle coils (Powell, 1967; Varma, 1968). These BES are observed at the output, concentrated near the point of impact. They are thus most probably caused by electron impact desorption of positive ions, since BES generated by soft X-rays would be uniformly distributed across the field. Powell (1967) also succeeded in inducing a large number of SES and some BES by irradiation of the primary photocathode through the faceplate with 60 KeV X-rays. However, it is not known if that experiment represents the actual situation in the intensifier, where softer X-rays (0 - 13 KeV), emitted by sudden stoppage of energetic electrons, should be present.

Most of the above discussed evidence indicates that most BES are caused by positive ion bombardment of the photocathode and that the origin of these ions is closely associated with the production of SES, or with a phenomenon like field emission. The marked correlation between BES and SES counts, the effect of lowering the work function of the internal surfaces by caesium contamination and the dependence upon applied electric field, support this theory.

10.4.2. Origin of Positive Ions Bombardment of the Photocathode

Positive ions may be emitted from the internal surfaces of the intensifier by field desorption or by electron bombardment causing impact desorption. Field ionization of residual gasses can be considered negligible at the pressure encountered in the intensifier (Muller, 1960).

Impact desorption of positive ions from adsorbed layers by electron bombardment occurs through electronic excitation or dissociation of surface molecules rather than by direct momentum transfer (Redhead et. al. 1968). The cross section for impact desorption, which is strongly dependent upon the binding state, is maximum for low energies of the impacting electrons (50 - 150 eV) and decreases slowly if the energy is increased. Ion desorption rates in vacuum systems are usually between 10^{-7} to 10^{-6} ions/electron but could be as high as 10^{-4} ions/electron for surfaces contaminated with pump oil vapour (Garbe, 1963; Trump et. al. 1947). This might well be the case in the cascade intensifier because no special precautions are taken during pumping of the device to avoid contamination of the system with back streaming oil vapour from the backing pump. Ion desorption rates ranging between 3 to 7 . 10^{-4} ions/electron were measured for the impact of 10 KeV electrons from the phosphor screens of the intensifier (§ II.1.7).

Field desorption of electropositive adsorbates occurs if sufficiently high electric fields exist in the vicinity of a surface, such that the vibrational energy of the adsorbed atoms is sufficient to overcome the reduced potential barrier. For most adsorbates, fields higher than 10^{8} V/cm are required, but in the case of caesium, field desorption is possible at fields of 10^{7} V/cm (Oliver, 1970). This field is only slightly higher than that required for field emission of electrons so that both effects could occur simultaneously. However, the field desorbed ion current originating from the cathode side of an electrode may be 10^{6} to 10^{8} smaller than the field emitted electron current from the opposite side of the electrode (similar surface conditions). (Gomer, 1961; Muller, 1941). Now since 10^{4} to 10^{7} field emitted electrons are needed to desorb an ion by impact, it can be argued that the two mechanisms for the desorption of ions might well lead to similar rates of ion desorption.

Because of the large mass of ions, as compared to electrons, their motion is much less constrained by the magnetic field. An H^{+} ion, for example, accelerated to 200 eV perpendicularly to the magnetic field will have an orbital radius of 7.5 cm in 2 loop focusing (270 Gauss). Therefore the path of even heavier ions may be considered as occuring in planes containing their initial

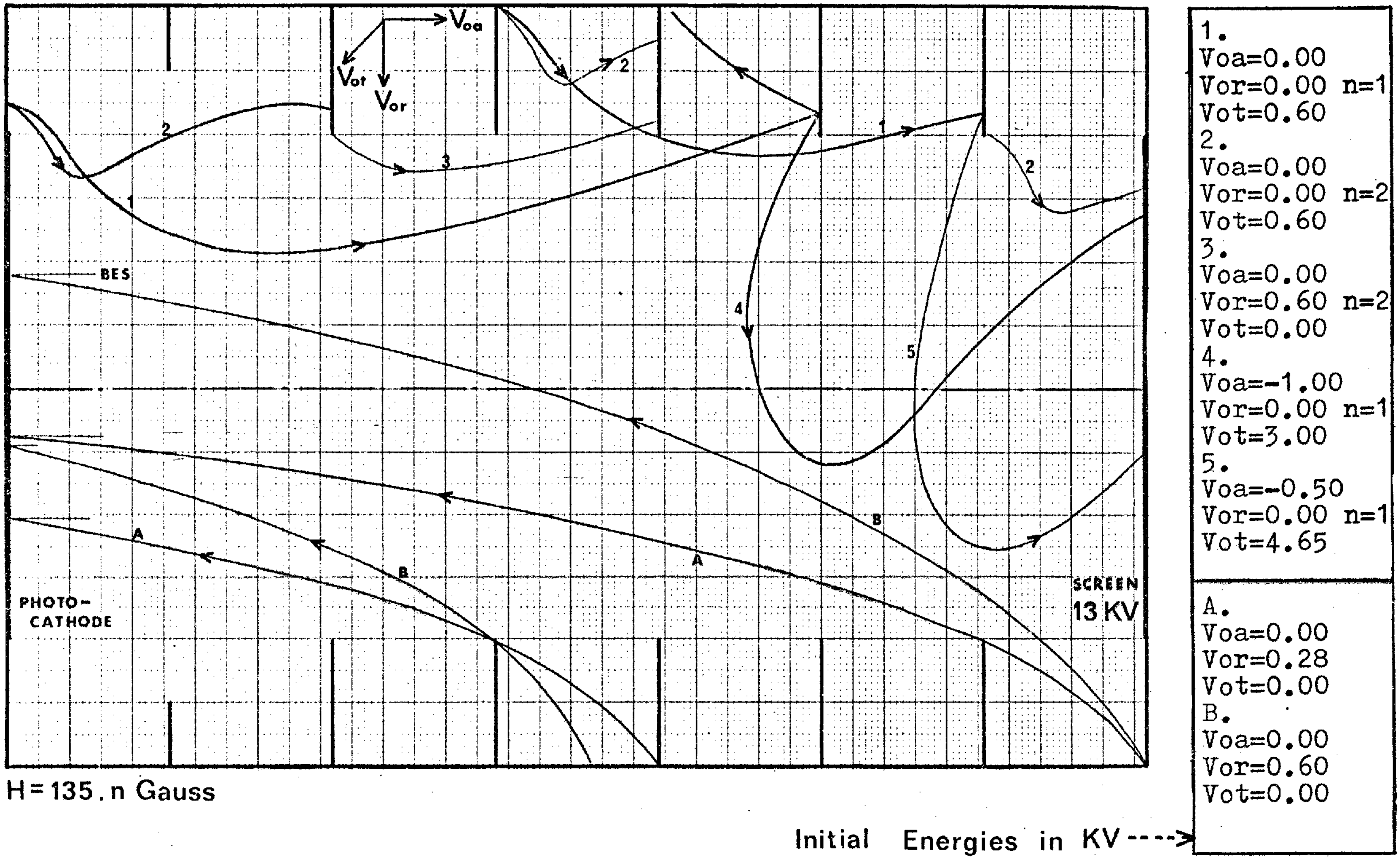

FIG 10.3 TRAJECTORIES of spurious ELECTRONS & IONS

velocity and parallel to the electric field. Several ion trajectories were calculated using the equation of motion in an electrostatic field and are shown, together with some spurious electron trajectories, in Fig. 10.3. The initial energies, acquired by the ions in regions of high radial electric field, are indicated for each trajectory. A radial acceleration to at least 280 eV is required to dislodge any ion, originating on the glass wall, from the electrode shielding system. A spurious electron with that same radial energy would not, even in I loop focusing, be able to bypass the next electrode if it originated on the glass wall. Furthermore, if an ion escapes from the space between the electrodes into the accelerating region of the stage, it will reach the photocathode with a much higher probability than an escaped electron would have to reach the phosphor screen. It is therefore not surprising that the SES count is only 10^2 to 10^3 times higher than the BES count, although 10^4 to 10^7 more field emitted electrons than ions should be emitted within the electrode shielding system.

10.4.3. Sensitivity of Photocathodes to Ion Bombardment

Little data ~~is~~ are available in the literature on the sensitivity of photocathode to ion bombardment. Morton et. al. (1967) report the ejection of 1 to 3 electrons by bombardment of S11 and S20 photocathodes with Xe^+, A^+, N_2^+ and H_2^+ ions, but no electron ejection when bombarded with O_2^+. Measurements made on metals and semiconductors indicate that "kinetic" ejection of several electrons occurs when a surface is bombarded with ions of energy higher than 1 KV (Redhead et. al. 1968). The yields (electrons/ion) increase usually linearly with ion velocity and are about an order of magnitude higher for semiconductors than those typical of metals. Yields ranging from 2 electrons /Cs^+ ion at 15 KV from germanium to 100 electrons /A^+ ion at 15 KV for oxide cathodes have been reported (Abroyan et. al. 1961 and 1963).

It is thought that a few high energy electrons are first produced by atomic excitation produced by the impact of the rapidly moving ion. These electrons then produce lower energy secondaries which escape from the surface.

10.5 CONCLUSIONS

Besides thermal emission of the primary photocathode the background in the intensifiers is thought to be the result of the presence of high electric fields in the vicinity of the metal electrodes and the glass walls. These fields induce field emission of electrons and occasionally field desorption of positive ions. The emitted electrons are accelerated by the electric field and their trajectories are constrained by the magnetic field causing them to impact on metal electrodes. The latter collision causes the desorption of positive ions and the backscattering of some of these electrons, which are then able to reach the phosphor screen. The positive ions are accelerated fowards the photocathode where they eject a large number of electrons, which are then in turn accelerated towards the screen (bright scintillation).

The background can be reduced by adequate cooling of the intensifier since this lessens both thermal and field emission phenomena. Increase of the length of the first stage, operated at the same potential, would reduce the electric field and thus field emission of electrons and field desorption of ions. However this can only be done at the expense of a larger intensifier or a higher field gradient in the second stage. Finally, a reduction of the ratio of the diameter of the working field to the inside diameter of the glass envelope,and a reduction of the distance between the metal electrodes, would also have a beneficial effect on background because it would improve the efficiency of the electrode shielding system.

CHAPTER II

SIGNAL INDUCED BACKGROUND

Observation of the output screen of a cascade intensifier in the presence of a signal, confined to small area, reveals the existence of an appreciable amount of unwanted background outside the intensified image. This background disappears if the incident signal is removed and is therefore called signal induced background (SIB). The direct consequence of this phenomenon is that the contrast in an extended image will be reduced since each picture element contributes background to all other elements in the image. This causes reductions in resolution which are dependent upon the image content. Since the intensity of the induced background increases with that of the signal, no marked improvement in signal to noise ratio will be obtained by increasing the signal intensity, as it would be the case for other sources of noise, i.e. fluctuation noise and dark background. Another fact that distinguishes SIB from these two noise components is that the induced noise from each stage of multi-stage intensifier contributes similarly to the deterioration of contrast in the final image.

It is the purpose of this chapter to analyse the different causes of SIB in the I.C. cascade intensifier and to report on experiments performed to explain their origin and relative contribution to the total background.

II.1 QUALITATIVE ASSESSMENT OF SIGNAL INDUCED BACKGROUND

Fig. II.1 shows two photographs of the output screen of a focused cascade intensifier illustrating the presence of induced background. Photograph A shows the background resulting from a small spot of light imaged on the centre of the photocathode. Besides background affecting the entire field, concentric rings

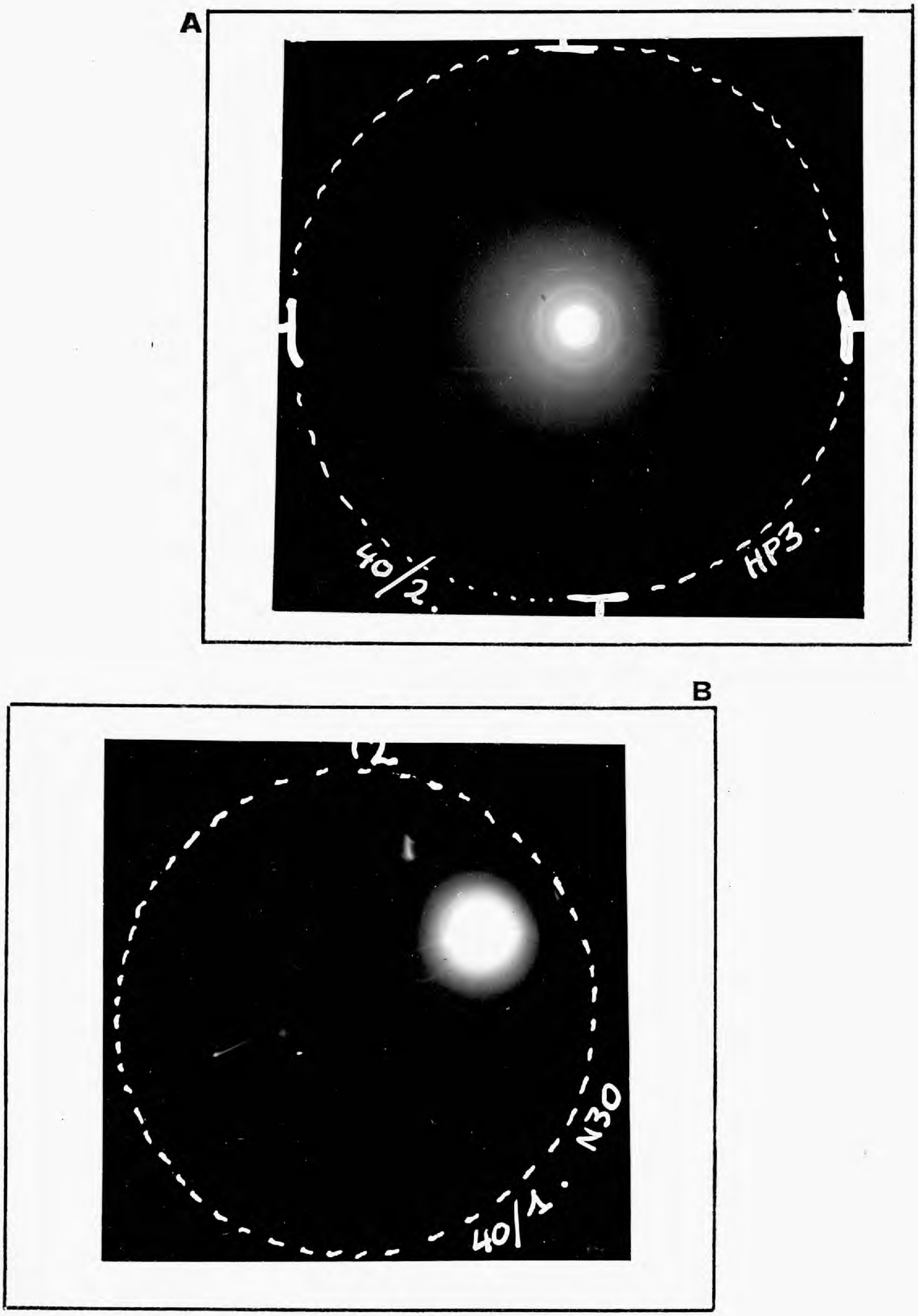

FIG 11_1 SIGNAL INDUCED BACKGROUND

around the image can clearly be observed. Photograph B, recorded on high contrast emulsion, shows two spurious images to appear when the causative image is located near the edge of the field. The first one, located above the direct image, is strongly dependent on the focusing condition of the intensifier. The second spurious image, located diametrically opposite to the causative image, is connected with the latter by a faint structure and its position is only slightly affected by the focusing conditions. Both spurious images merge with the causative image as the latter is moved towards the centre of the field.

Potential sources of SIB in cascade intensifiers will be discussed in the following paragraphs.

II.1.1. Light scattering within the end windows

The concentric rings around a small image are due to total internal reflection in the glass plate supporting the output phosphor of the intensifier. The radius of the mth ring corresponds with the theoretical radius $2\,,\,m \quad .t.\mathrm{tg}\,\theta_c$ where t is the thickness of the plate (1 mm) and θ_c the critical angle of the glass-vacuum interface (41°). The intensity of this SIB component is proportional to the signal intensity and unrecognizable from the true signal for extended images.

II.1.2. Light scattering within the photocathode windows

Multiple reflections at the various interfaces traversed by a light beam focused on the primary photocathode causes lateral spread of light. The intensity of this SIB component will depend upon the number of interfaces and their distance from the cathode, upon the numerical aperture of the incident light beam and upon the wavelength of the light. Indeed the reflectivity of the interfaces (especially the glass-photocathode and photocathode-vacuum interfaces) is dependent on wavelength and angle of incidence. Great care should be taken to avoid reflections from the back surface of the input optical system and from the metalic photocathode holder which can be a severe cause of induced background (Cromwell, 1969). The former can be minimized by antireflective coatings and the latter by placing a light absorbing ring around the entrance window of the intensifier.

II.1.3. Light scattering within the stages

A fraction of the light transmitted by the semi-transparent photocathode of each stage will be reflected back to the cathode by the glass walls, the metal electrodes and the backing of the phosphor screen of that stage. This effect is minimized by coating the metalic surfaces with a layer of evaporated carbon (§ 5.1.7). In the first stage this component can be expected to depend upon the wavelength of the incident light since both transmission of the cathode and reflectivity of the internal surfaces are wavelength dependent. Furthermore, it will depend upon the numerical aperture of the imaging beam. In the other two stages this component will be unrecognizable from the true signal and probably more important than in the first stage because of the diffuse nature of the transmitted light from the phosphor screens.

II.1.4. Optical Feedback

Imperfections and pinholes in the aluminium backing of the phosphor screens (§ 5.1.6) causes a minute amount of light, generated in these phosphors, to be fed back to the previous photocathodes. The resulting photoelectrons will, after acceleration, cause induced background over the entire field. This positive feedback component depends upon the light gain of each stage and thus upon the applied potential and sensitivity of the cathodes.

II.1.5. Backscattering of electrons from the phosphor screens.

Backscattering of signal photoelectrons at impact with the phosphor screens not only causes a loss in recording efficiency (§ 7.4.3) but also signal induced background. Indeed these rediffused electrons, which may number 15 to 25% of the impacting electrons (§ II.4.5), will describe helical trajectories, first decelerating towards the photocathode until their velocity is zero, then accelerating back towards the phosphor screen. If their flight is not interrupted by collision with a metal electrode in the stage, they will impact on the screen with their initial energy but at an off focus position (fig. II.2 A).

This process has been suspected by several investigators (Emberson, 1966; Randall, 1966) to be an important source of SIB in cascade intensifiers, but the author is not aware of any qualitative or quantitative investigation into this matter.

The occurence of backscattering of electrons is visually observable in the I.C. cascade intensifier as the spurious image located in the vicinity of the causative image (fig. II.1 B). It comes into sharp focus for values of the magnetic field slightly higher (2 - 4 %) than those required to focus the causative image, i.e. at nH_I, but also at values close to $^n/_2\ H_I$. (H_I is the field required for one loop focusing and n is the number of loops). The spurious image is still clearly visible when the direct image is in sharp focus but disperses itself radially as the magnetic field is increased or decreased. Three exposures of the output phosphor screen are shown in fig. II.2 B, for different magnetic fields corresponding to 1, 1.5 and 2 loops focusing of the direct image. These spurious images originate in the last stage of the intensifier since a change of the potential applied on that stage causes the image to defocus.

Transit time of backscattered electrons (BSE) : The refocusing of BSE in the last stage can be understood from the calculation of their time of flight. If a BSE is emitted at the phosphor of the first or second focused stage (length L; applied potential V_T), with an energy ξV_T $(0 \leqslant \xi \leqslant 1)$ and at an angle θ with the normal to the screen, then its transit time $T_{1,2}$ can be calculated to be: (Appendix IV)

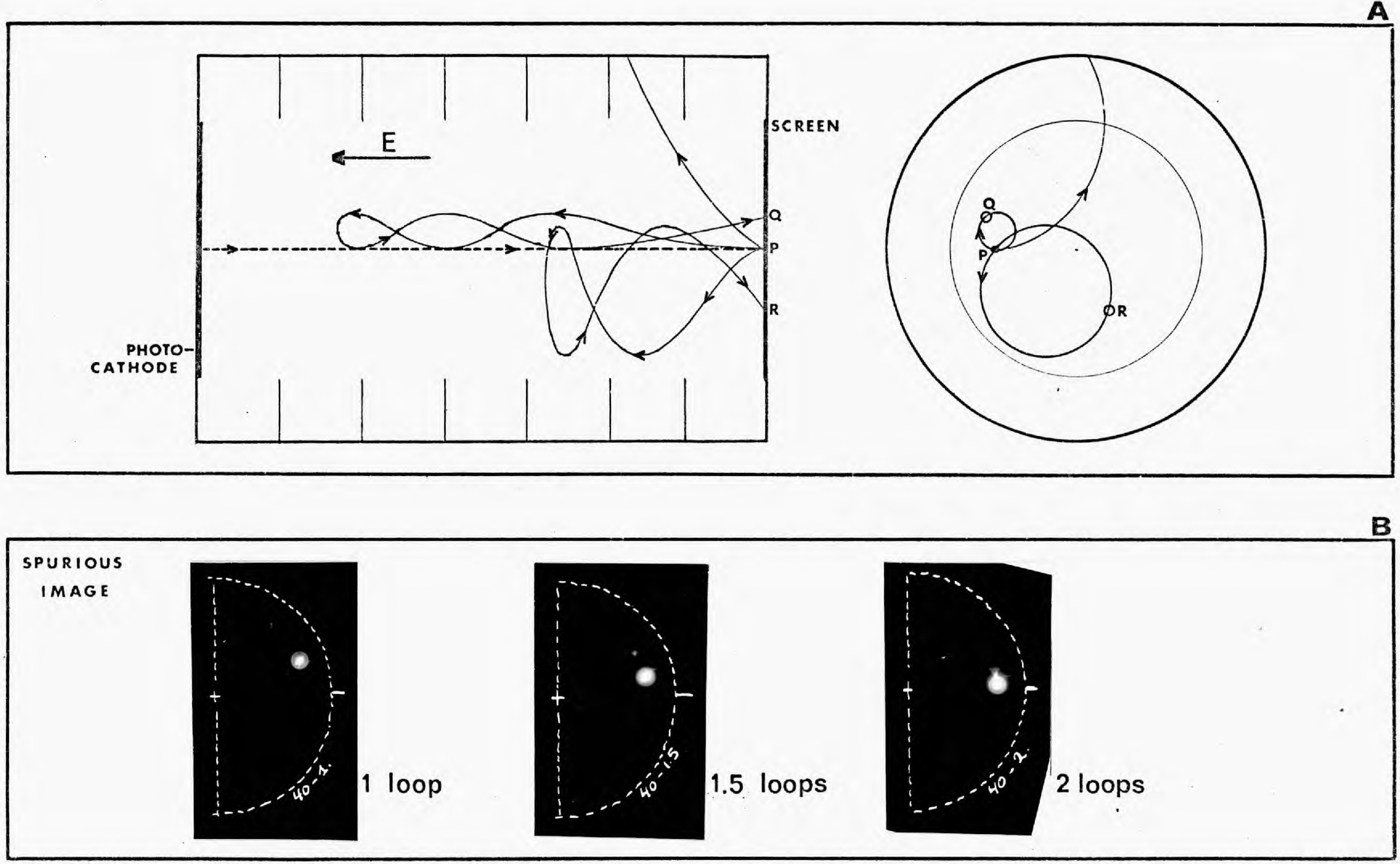

FIG 11.2 BACKSCATTERED ELECTRONS

$$T_{1,2} = 2n \cdot \sqrt{\xi} \cdot \cos\theta \cdot T_{loop} \qquad (11.1)$$

where n is the number of loops used to focus the direct image and T_{loop} the orbital time, which depends solely upon the magnetic field. However, in the last stage the situation is quite different since the backscattered electrons have to traverse the processing compartment, onto which no potential difference is applied. It was seen in § 8.3.4 that the resulting field leakage in that chamber only caused a reduction of at most 0.6% in the transit time of photoelectrons, as compared to the transit time in the ideal stage with uniform field in the active region and zero field in the processing chamber. The time of flight of the BSE can therefore be calculated in the latter assumption without any large error. If A is the length of the active region and 2F the length of the field free region, then the transit time T_3 of BSE in the last stage becomes: (Appendix IV)

$$T_3 = \frac{2n}{A+F}\left[\frac{F}{\sqrt{\xi}\cos\theta} + A\sqrt{\xi}\cos\theta\right] T_{loop} \qquad (11.2)$$

The variation of relative transit time $T_i/n\,T_{loop}$ was calculated as a function of the initial axial energy $\xi\cos^2\theta$, for * A = 6 cm and 2F = 6 cm, and the results are shown in Fig. 11.3 A. It can be seen that if the transit time of the BSE in the first two stages varies quite rapidly with the initial axial energy, the flight time in the last stage is fairly constant for axial energies ranging from 0.25 to 1.00 $V_T\cos^2\theta$

The backscattered electrons are emitted with initial energies ranging from $\xi = 0$ to $\xi = 1$ (elastically reflected) with a continuous energy distribution peaking around $\xi = 0.5$ to 0.9, and with an angular distribution that obeys essentially a cosine law (§ 11.4.5). A large fraction of the BSE emitted in the last stage with initial axial energies between 0.25 and 1.00 V_T, will practically

---

* A + F is the electro-optical length of the last stage (eqn. 4.1).

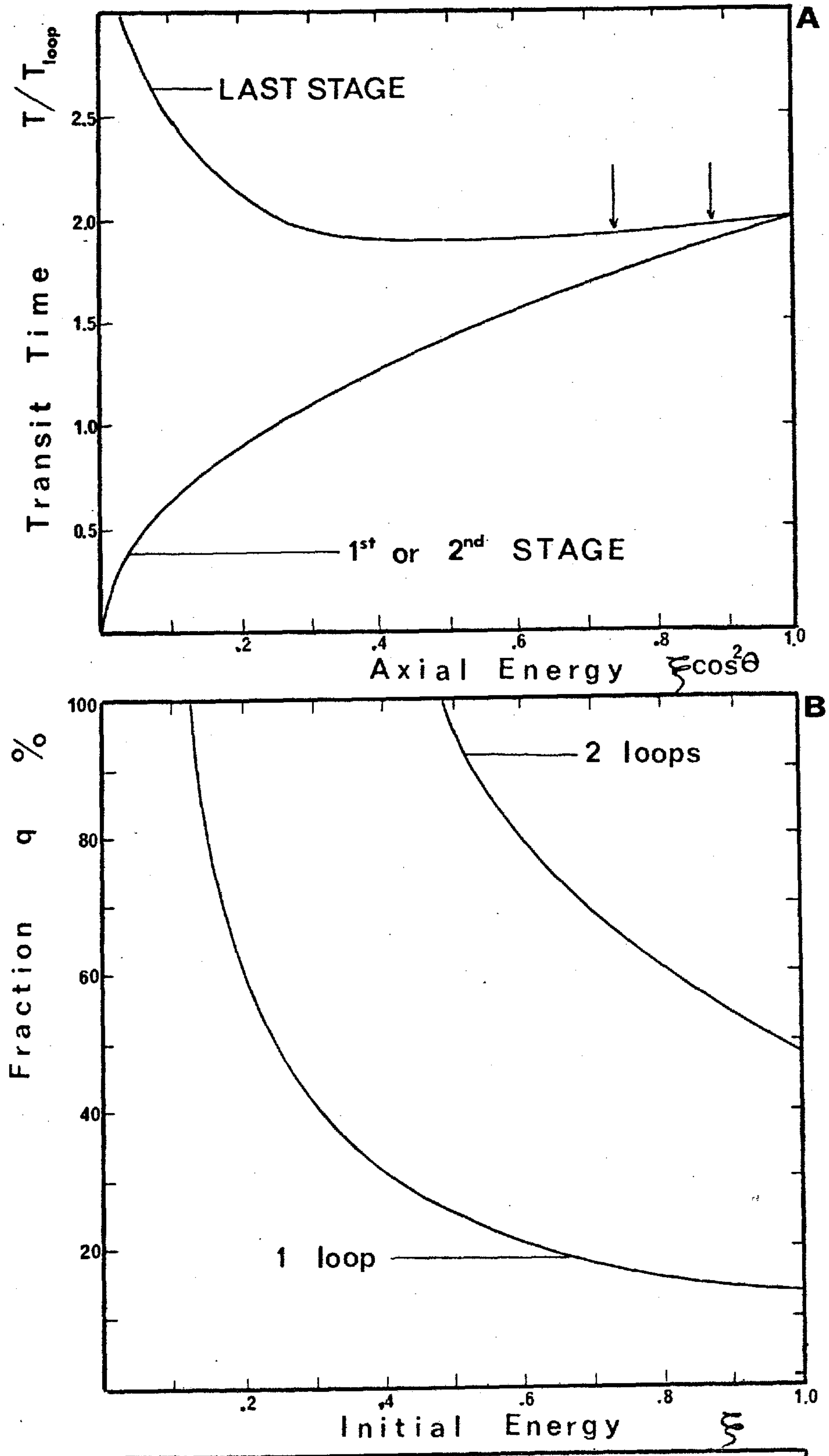
A
LAST STAGE
1st or 2nd STAGE
Transit Time T/T_loop
2.5
2.0
1.5
1.0
0.5
.2
.4
.6
.8
1.0
Axial Energy ξcos²θ
B
2 loops
1 loop
Fraction q %
100
80
60
40
20
.2
.4
.6
.8
1.0
Initial Energy ξ

FIG 11.3 BSE

complete their (2n - 1)th loop at the time of impact with the screen. They should thus focus near the causative image at a magnetic field slightly higher than that required to focus the direct image, as is indeed observed in the intensifier. In the other two stages, only BSE with $\xi \cos^2 \approx 0.25$ and 1.00 will focus close to the direct image while those with axial energy between these values, or the majority of BSE, will impact on the phosphor screen during their (2n - 1)th loop and thus distribute across the field.

The tangential displacement of the spurious image is caused by the field leakage in the processing compartment of the last stage (§ 9.3.2). The rotation of the spurious image is higher than twice the rotation of the direct image indicating that the BSE travel twice through the electron lens with smaller speeds than the photoelectrons.

Fraction of BSE which contribute to SIB. Not all BSE, emitted from the phosphor screens, will contribute directly to SIB, since BSE with sufficiently high orbital radius (high radial initial energy: $\xi \sin^2 \theta$) will collide with the metal electrodes of the stage. The occurence of this collision will not only depend on the energy and direction of emission but also on the location of the causative image element. Furthermore, it will depend upon the strength of the magnetic field (number of loops) since the orbital radius decreases with increasing magnetic field. An increase of the SIB component associated with BSE can thus be expected when the field is increased from 1 to 2 loops focusing.

It can be shown that the fraction $\underline{q}$ of monoenergetic BSE, originating from the centre of the field, which remain in the accelerating region of a stage is given in first approximation by: (Appendix IV)

$$\underline{q} = \frac{\Pi^2 \, . \, n^2 \, . \, R^2}{4 L^2 \, \xi} \qquad (11.3)$$

where R and L are respectively the radius of the field and the electro-optical length of the stage, n the number of loops used to focus the stage and ξ the relative initial energy of the BSE $(0 \leqslant \xi \leqslant 1)$. This equation is only valid for $\xi \geqslant \pi^2 n^2/4L^2$ and $\underline{q}$ equals 1.0 for $\xi \leqslant \pi^2 n^2/4L^2$. The variation of $\underline{q}$ with ξ is shown in Fig. II.3 B for n = 1 and n = 2. (calculated with R = 2 cm and L = 9 cm). The fraction $\underline{q}$ is thus 12.2% and 48.6% for elastically rediffused electrons in one and two loops respectively and increases to 100% as the initial energy is decreased. For three loop focusing of that same stage, all the BSE originating from the centre of the field will remain in the accelerating region and thus contribute to background. (Indeed $\pi^2 n^2 R^2/4L^2 = 1$ when n = 2.89).

The accurate calculation of the fraction $\underline{q}$ for BSE originating from any location on the phosphor screen can not be done analytically as will be pointed out in § II.4.6. The results of the computer calculation of this fraction will be shown in Fig. II.13 (dotted curves).

It can be concluded that the contribution of BSE to the SIB of the intensifier can be expected to increase by at most a factor 4.0 when the magnetic field is increased from 1 to 2 loops focusing. The exact value of this factor will depend upon the energy distribution of the BSE and upon the content of the image projected on the intensifier. The actual magnitude of the SIB component associated with BSE will depend on the same two factors, but also on the fraction of photoelectrons which is backscattered at the phosphor screens (rediffusion coefficient) and upon the dependence of the efficiency of the phosphor screens on the energy of the BSE.

II.1.6 Secondary effects caused by backscattered electrons

A considerable fraction $(1 - \underline{q})$ of the high energy backscattered electrons will thus impact on the metal electrodes of the intensifier. Some of these electrons will further be backscattered and reaccelerated to the phosphor screen. Soft X-rays will be emitted by sudden stoppage of these electrons and could produce roentgenoluminescence in the screens. Finally, the impact of energetic BSE on the metal electrodes, might cause the desorption of positive ions, which after acceleration and impact on the photocathode will liberate several electrons (§ 10.4.3). The contribution of these effects should decrease with increasing magnetic field since fewer BSE will impact on the metal electrodes.

11.1.7. Ionic Feedback

It was seen in § 10. .2 that the impact of energetic electrons causes the desorption of positive ions from a surface. This effect can be expected to occur when signal electrons impact on the phosphor screen in each stage. These ions, emitted with very low initial energies (Redhead, 1968), are accelerated towards the photocathode, where each liberates 5 to 15 electrons. If this occurs in the first stage, signal induced bright electron scintillations should appear at the output screen in the vicinity of the causative image. This is indeed the case, but can only be observed if a sufficiently small image is projected on the primary photocathode.

The situation in the last stage is again quite different because of the presence of radial electric field components oriented towards the axis and resulting from field leakage in the processing compartment (§ 9.3.2). A desorbed ion, from an off-centre location of the phosphor screen, is deflected towards the axis while accelerated towards the cathode. The trajectory, which is only slightly affected by the magnetic field, intercepts the photocathode at a point which is nearly diametrically opposite to the direct image (Fig. 11.4 B). The group of electrons generated by impact of that ion on the cathode (§ 10.4.3) is in turn accelerated towards the screen producing the second spurious image visible in Fig. 11.1.B.

The determination of the origin of this spurious image has not been as simple as it appears from the above considerations. It was only after the following experiment that the responsible mechanism became obvious. The last three annuli of the first stage of an intensifier were externally connected to the first dynode, creating a region of field leakage in the first stage. The intensifier was then operated with 10 KV (2 loops) on that stage and 16 KV (2 loops) on the other two stages. A new spurious image, similar to that already occuring in the intensifier and definitely composed of individual bright electron scintillations, appeared on the output screen as shown on the photograph II.4.A.* The yield of ion production was measured by comparing the photoelectron current in the first stage with the number of recorded bright electron scintillations which constituted the spurious image. It was found that 1.3 to 1.9 . 10^{-4} ions/electron were produced in the most intense region of the ion image.

The occurence of this ion feedback was investigated on several intensifiers. Its intensity varies considerably from tube to tube which is believed to be associated with varying degrees of adsorption of gasses in the phosphor screens.

Some work was performed to explain the shape and fine structures visible on the ion feedback image. Fig. II.4 B shows a section of the last stage where several ion trajectories have been drawn. This was done by means of a simple graphical ray tracing method (Musson-Genon, 1946), and with the electric field distribution calculated in § 9.3.2. The trajectory of these ions depends solely upon their initial energy and angle of emission, and not upon the mass of the ions. Keeping in mind that the accuracy of this ray tracing method is not very high, it can be seen that the ions with low initial velocity approximately land in the most intense region (SI) of the ion image (Fig. II.4B,C) The faint structure (FS) connecting the direct image to (SI), would then be caused by ions desorbed with higher initial energies. As for the diffuse structure (BB) which is located nearer to the centre of the field it might be caused by ions emitted at high emission angles and/or in planes not coinciding with the meridional plane. The latter structure is quite important in regard to SIB, since its position is only slightly affected by the position of the causative image (Fig. II.4 D). Therefore, if the entire field is illuminated it will cause a marked increase in SIB around the centre of the field.

---

* A spurious streak appeared on the output screen as the result of the excessive electric field in the last stage.

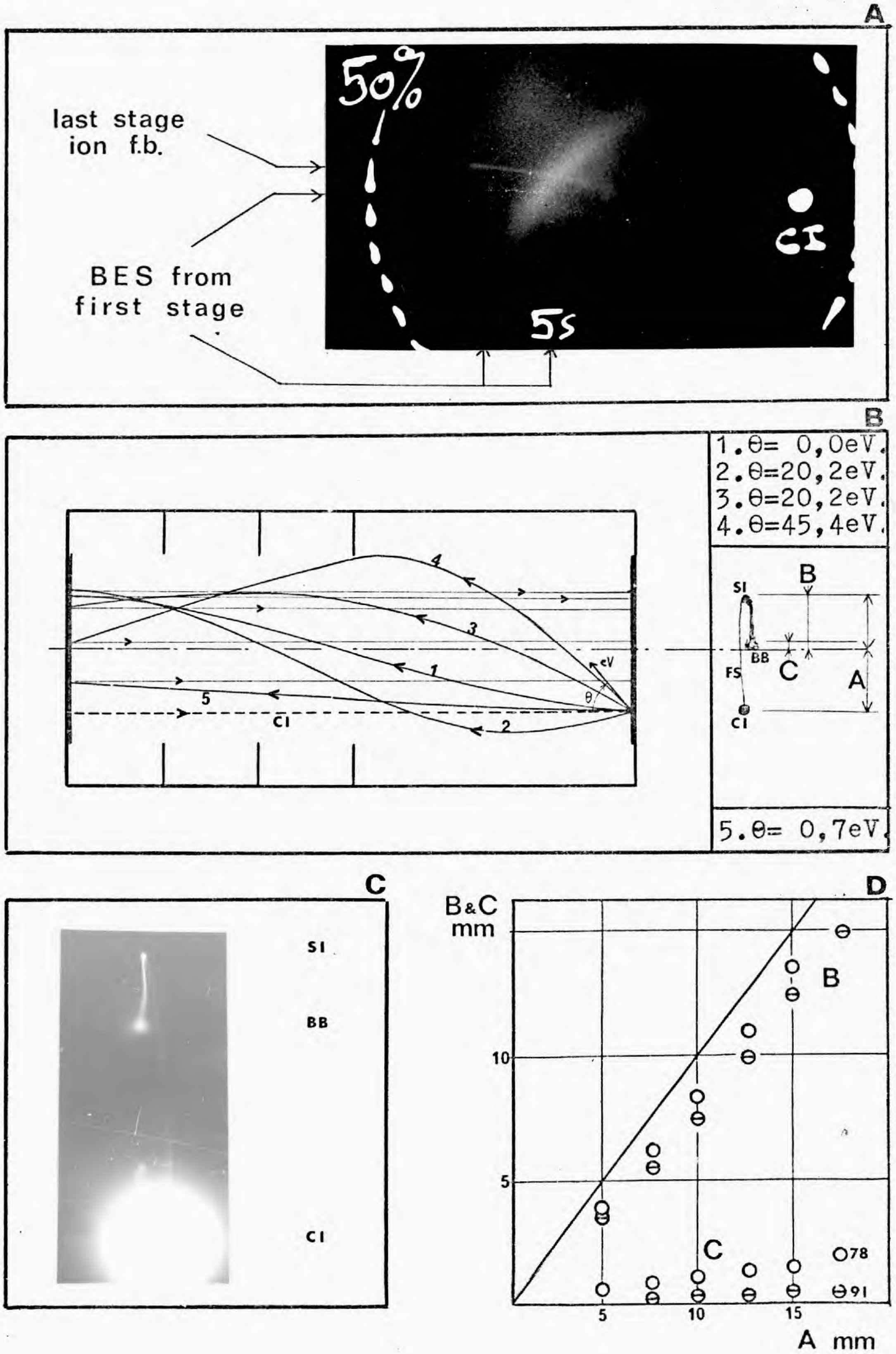

FIG 11.4 ION FEEDBACK

The other component (SI) of this ion image will be more uniformly distributed over the field.

II.2 THEORY RELATED TO SIGNAL INDUCED BACKGROUND

A rigourous treatment of SIB of a detector would require the convolution of the incident signal distribution with the point spread functions for every image element of the field. The following less rigourous treatment has the advantage of separating a priori the signal from the background. Indeed the latter is generally caused by the loss of a fraction of the signal which is then partially redistributed to other picture elements in the field. This fraction is a physical quantity which can be measured or calculated for most sources of background (transmission of the photocathodes, rediffusion coefficient of BSE, etc ...)

II.2.1. One source of SIB

If $S_i(r\varphi)$ is the signal density in a picture element $(r\varphi)$ of an image incident on an image detector, and if K is the fraction of that signal which is lost, then $G'(1-K)\,S_i(r\varphi)$ will be the signal density in that element at the output, where G' is the gain of the device in absence of signal loss. K is assumed to be independent of the position in the field. If the function $\underline{g}(r\varphi\ r_1\ \varphi_1)$ describes how the lost signal from $(r\varphi)$ redistributes itself over the field then

$$G' \,.\, K \,.\, S_i(r\varphi)\ \underline{g}(r\,\varphi\,r_1\ \varphi_1)\ r dr\, d\varphi$$

will be the density of the SIB in an element $(r_1\ \varphi_1)$. The function $\underline{g}$ is a probability function and has a dimension of (length)$^{-2}$. It should be noted that $\underline{g}(r_1 .\, \varphi_1 .\, r_1 .\, \varphi_1)$, i.e. the contribution of an element to itself, is strictly speaking not induced background. However, to avoid discontinuities in the following integrations, this will not be taken into account. Therefore the measurable gain G in a picture element will be $G = G'(1 - K)$. The factor K and $\underline{q}$ have been assumed to be independent of the signal density. Indeed no deviation in proportionality between the SIB and signal intensity have been detected in the measurements.

The total output density $S_o(r_1\ \varphi_1)$ at $(r_1\ \varphi_1)$ is, after integration over the image:

$$S_o(r_1\ \varphi_1) = G'(1 - K)\, S_i(r_1\ \varphi_1) + K\, G' \iint\limits_{\text{image}} S_i(r\ \varphi)\, q(r\ \varphi\ r_1\ \varphi_1)\, r dr d\varphi \qquad \underset{}{(r_1\ \varphi_1 = ct)} \tag{II.4}$$

The ratio of actual output density in a picture element $(r_1\ \varphi_1)$ to that of the signal density is then:

$$\frac{S_o(r_1\ \varphi_1)}{G'(1-K)\, S_i(r_1\ \varphi_1)} = 1 + \frac{K \iint S_i(r\ \varphi)\, \underline{q}(r\ \varphi\ r_1\ \varphi_1)\, r dr d\varphi}{(1-K)\, .\, S_i(r_1\ \varphi_1)} \tag{II.5}$$

The output signal is thus increased as the result of induced background by an amount dependent upon K, $\underline{q}$ and the distribution across the field of the intensity of the incident image.

II.2.2. The signal induced background index Z

The SIB-index $Z(r_1\ \varphi_1)$ of a device is defined here as the ratio of the increase in output density to the signal density for every output image element of a uniformly illuminated device. Thus $S_i(r\ \varphi) = \underline{Si}$ *. The SIB-index is thus:

$$Z(r_1\ \varphi_1) = \frac{K}{1 - K} \int_{r=0}^{R} \int_{\varphi=0}^{2\pi} \underline{q}(r\ \varphi\ r_1\ \varphi_1)\, r dr\, d\varphi \tag{II.6}$$

R is the radius of the working field

---

* A bar under a letter denotes uniformity across the field, in contrast to a bar above a letter which denotes average.

or

$$Z(r_1\ \varphi_1) = \frac{K \cdot Q(r_1\ \varphi_1)}{1 - K} \qquad (II.6)$$

where $Q(r_1\ \varphi_1)$ is the total fraction of lost signal from all elements of the field which contributes to an element $(r_1\ \varphi_1)$. The index Z will be used in this thesis as a measure for the magnitude of the induced background. The output density in a picture element $(r_1\ \varphi_1)$ of a uniformly illuminated device is given by:

$$S_o(r_1\ \varphi_1) = \left[1 + Z\ (r_1\ \varphi_1) \right]\ G\ \underline{Si} \qquad (II.7)$$

II.2.3. Reciprocity and Uniformity

It is sometimes easy to calculate or to measure the total amount of lost signal which contributes to the output over the entire field when only a small area of the field is subjected to an input signal. This quantity $T(r\ \varphi)$ is given, relative to the real output signal, by

$$T(r\ \varphi) = \frac{K}{1 - K} \int_{r_1=0}^{R} \int_{\varphi_1=0}^{2\pi} \underset{(r\ \varphi\ =\ ct)}{\underline{q}\ (r\ \varphi\ r_1\ \varphi_1)\ r_1\ dr_1\ d\varphi_1}$$

or

$$T\ (r\ \varphi) = \frac{K\ \ Q'(r\ \varphi)}{1 - K} \qquad (II.8)$$

and is a function of the position of the causative element $(r\ \varphi)$. The two quantities $Z(r_1\ \varphi_1)$ and $T(r\ \varphi)$ are equal in a given picture element $(r_1\ \varphi_1)$ if

$$Q\ (r_1\ \varphi_1) = \Big[Q'\ (r\ \varphi) \Big]_{\substack{r = r_1 \\ \varphi = \varphi_1}} \qquad (II.9)$$

„ condition for reciprocity „

This condition is satisfied if $\underline{q}$ is a symetric function in respect to $r\ \varphi$ and $r_1\ \varphi_1$, or if the contribution of $(r\ \varphi)$ to $(r_1\ \varphi_1)$ is equal to that of $(r_1\ \varphi_1)$ to $(r\ \varphi)$.

A source of SIB whose contribution of one element to another is a function of their distance only, will obey the reciprocity condition. In that case it is sufficient to know the total contribution $T(r\,\varphi)$ of one element $(r\,\varphi)$ to all the elements in the field in order to derive the relative increase in output density $Z(r\,\varphi)$ in that element due to a uniformly distributed signal.

The increase in output intensity resulting from SIB will be uniformly distributed across the field if

$$Q\,(r_1\,\varphi_1) = \underline{Q} = \underline{q}\,\Pi R^2 \qquad \text{(II.10)}$$

„ condition of uniformity „

This can only be true if the contribution of any element to any other element is identical. If the condition for uniformity is satisfied, so will the condition for reciprocity. However, the contrary is not necessarily true, because of finite boundary conditions.

II.2.4. Two sources of SIB

If the output of a device A, with SIB-index Z_A, is made to be incident onto a second device B, with SIB-index Z_B, then it can be shown that the SIB-index Z_{AB} of the two devices is:

$$Z_{AB}(r_1\,\varphi_1) = Z_A(r_1\,\varphi_1) + Z_B(r_1\,\varphi_1) + \frac{K_B}{1-K_B}\int_{r=o}^{R}\int_{\varphi=o}^{2\Pi} Z_A(r\,\varphi)\,\underline{q}_B(r\,\varphi\,r_1\,\varphi_1)\,r\,dr\,d\varphi \qquad \text{(II.11)}$$

where the last term denotes the SIB generated in the second device by the SIB of the first device.

Special Cases:

-- if the SIB in both devices is uniform:

$$\underline{Z_{AB}} = \underline{Z_A} + \underline{Z_B} + \underline{Z_A} \cdot \underline{Z_B} \quad . \tag{II.12}$$

-- if the SIB in the first device is uniform:

$$Z_{AB}\,(r_1\ \varphi_1) = \underline{Z_A} + Z_B\,(r_1\ \varphi_1) + \underline{Z_A}\, Z_B\,(r_1\ \varphi_1) \quad . \tag{II.13}$$

-- if the SIB in the second device is uniform:

$$Z_{AB}\,(r_1\ \varphi_1) = Z_A\,(r_1\ \varphi_1) + \underline{Z_B} + \underline{Z_B} \cdot \overline{Z_A} \quad , \tag{II.14}$$

where $\overline{Z_A}$ is the field averaged SIB-index of the first device.

-- if at least one of the two detectors is uniform:

$$\overline{Z_{AB}} = \overline{Z_A} + \overline{Z_B} + \overline{Z_A}\ \overline{Z_B} \tag{II.15}$$

Eqn. II.15 will be used in § II.4 to sum up various individually calculated or measured sources of SIB, even in cases where the distribution is not strictly uniform. Only the contribution of BSE will be calculated on a digital computer using eqn. II.II, since its distribution across the field is very non-uniform. The results of the computer calculation showed that the eventual use of eqn. II.15 to sum up these non-uniform contributions would only cause a very small error.

II.3 MEASUREMENTS OF THE SIB OF CASCADE INTENSIFIERS

The SIB-index Z, defined in § II.2.2, is used as a measure for the magnitude of the induced background. Two methods were used to measure Z on several intensifiers.

II.3.I. "Spot" Method

The SIB produced by a small spot of light imaged at the centre of the photocathode was first analyzed. The experimental arrangement is shown in Fig. II.5. A small aperture (A), located in a slide carrier, is diffusely illuminated with blue light from a tungsten lamp (L) filtered with a Wratten 47B filter (F). The aperture is imaged on the photocathode of the intensifier with the f/5.6 WW lens (W), to produce a disc of I mm in diameter. With the intensifier adjusted for optimum resolution, the output image on the phosphor screen is imaged with a microscope objective (M) onto a circular aperture (B) placed in front of a photomultiplier* (PM) A set of blue light calibrated density filters are used to keep the photomultiplier within its calibrated range. The lens, aperture and multiplier are mounted on a traversing carriage so that the light distribution in the phosphor plane can be determined. Prior to the measurements on the intensifier (91), the contrast performance of the input and output optical system alone were determined as shown in Fig. II.6 (curve A). It can be seen that the impairment of contrast due to the optics alone is small as compared to that of the intensifier and optics together. Curve B shows the variation of the induced background intensity across the field for 2 loops focusing of the intensifier operated at an overall potential of 40 KV. The background shows a rapid variation with distance from the centre of the field which is not what one would expect if optical feedback or light scattering were the main causes of induced background. The measurements were repeated with I loop focusing of the intensifier. The comparison of these results with those obtained in 2 loop focusing, requires a correction in order to take into account the small differences in differential and linear magnification occuring in the intensifier in I and 2 loops focusing (Tab. 9.3). The corrected results are shown in Fig. II.6 (curve C). A marked increase in background intensity thus occurs when the magnetic field is increased from I to 2 loops focusing, as would be expected from the contribution of backscattered electrons (§ II.I.5).

---

*EMI 9578 A. Calibrated for linearity.

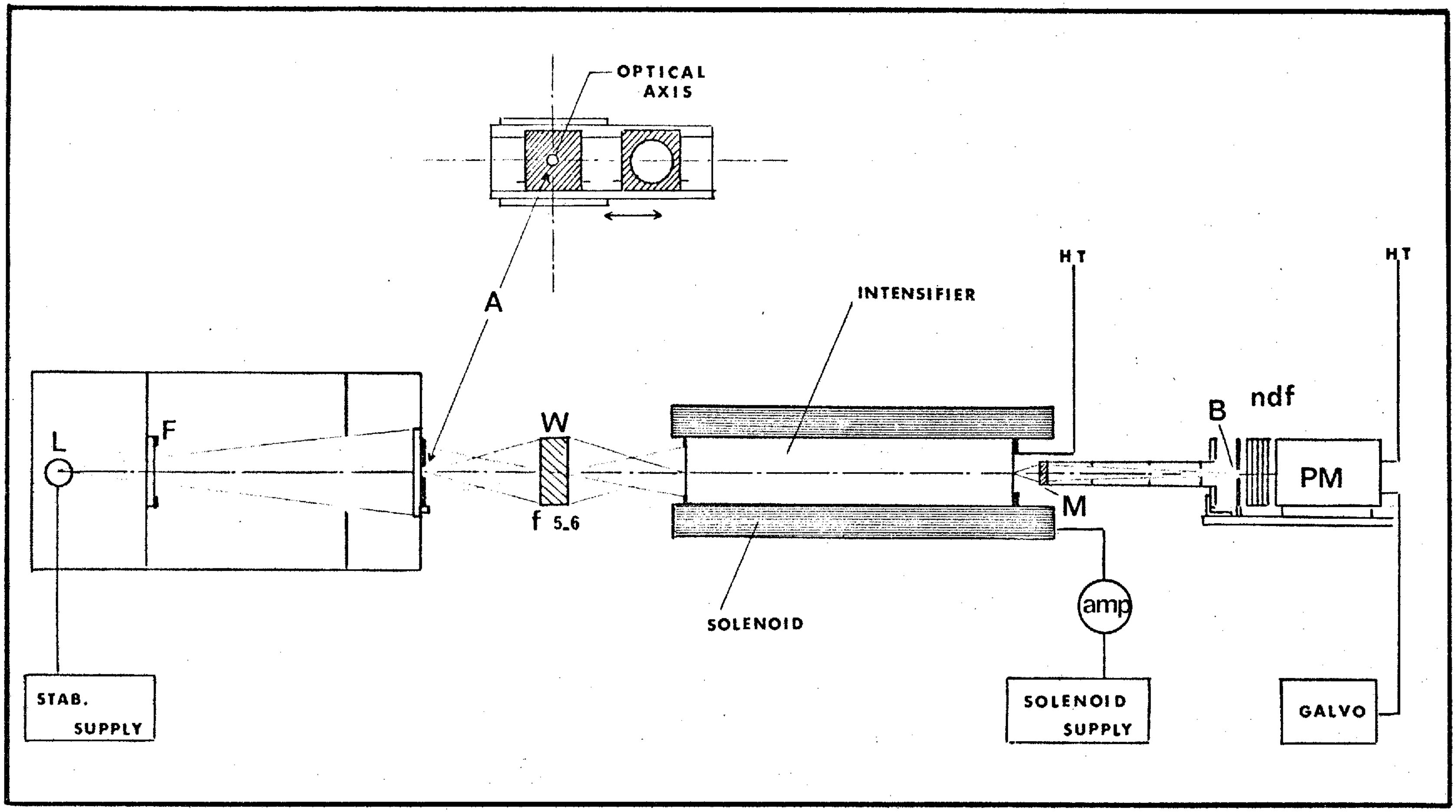

FIG 11-5 SIB MEASUREMENTS

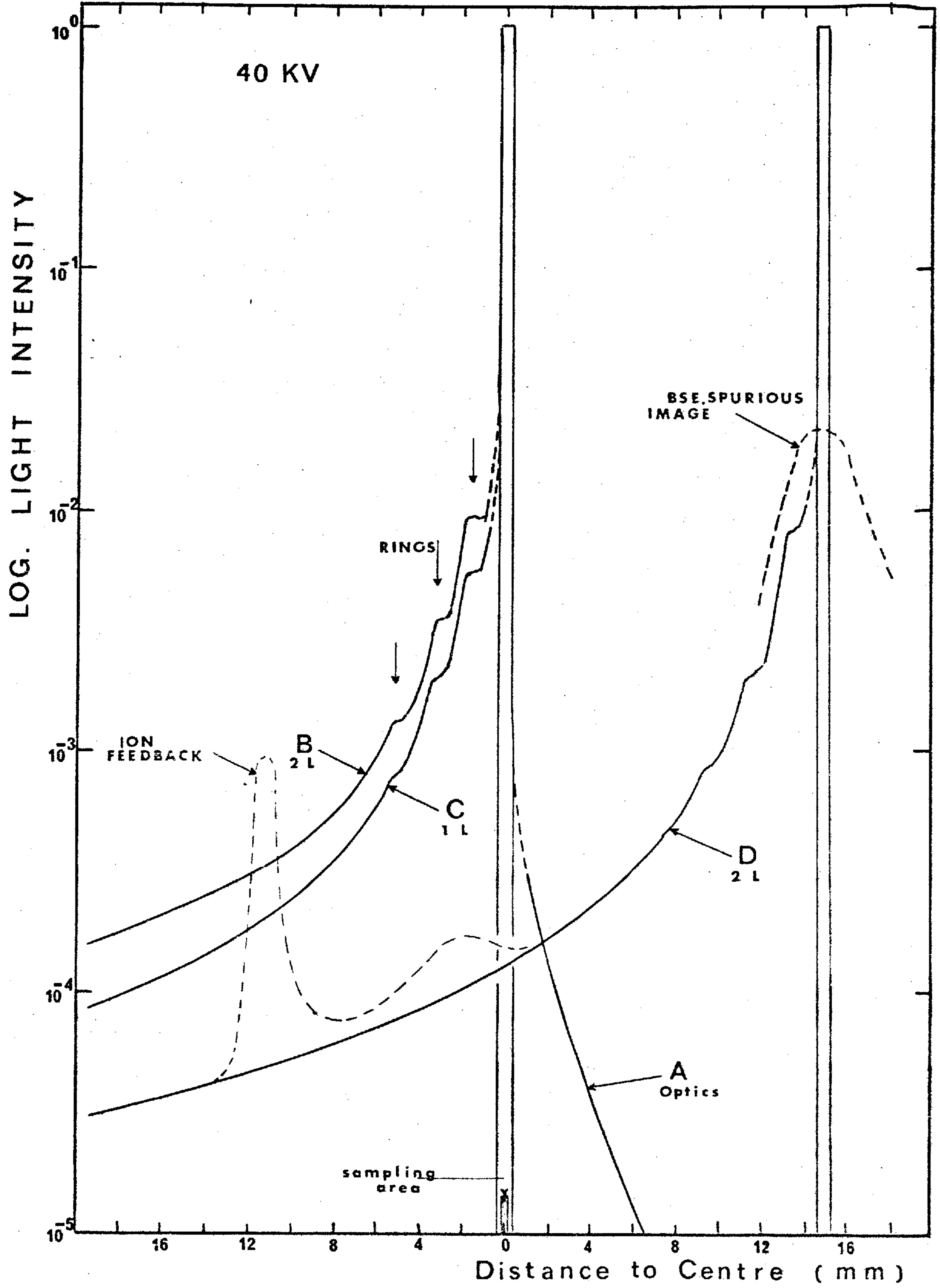

FIG 11.6 SIB produced by a SPOT

The fraction of the total phosphor emission that occurs outside the true image area, can be calculated by numerical integration of the two curves. Values of 41% and 30% were found for 2 and 1 loop focusing respectively. In other words, the integrated intensity of the background over the entire field is

$$T = \frac{0.41}{0.59} = 69.5\% \text{ (2 loops) and } T = \frac{0.30}{0.70} = 42.9\% \text{ (1 loop)}$$

of the total intensity of the circular image at the centre of the field. If the condition of reciprocity was satisfied, (§ II.2.3) this would also represent the SIB-index in the centre of the field. However, measurements of the background of the light spot located at 15 mm from the centre of the field (Fig. II.6, curve D) indicates that the contribution of off-centre picture points decreases slowly as the distance to the centre of the field is increased. Therefore a smaller value of the SIB-index can be expected, but it is difficult to calculate this factor because the boundary conditions become rather complex for any point other than the centre. The measurements were repeated with red light illumination (Wratten 25 filter) but no detectable difference in the results were obtained.

The major problems involved with this type of measurements is that of accurately measuring a wide range of intensities and that of integrating the results. Furthermore, any change of focusing condition alters sufficiently the differential magnification of the intensifier, so that elaborate corrections must be performed if a comparison of the SIB intensity at different focusing conditions is desired.

II.3.2. "Apertures" Method

In order to overcome the above difficulties in measuring the SIB index, another method was introduced which is based on the following principles. If the photocathode is uniformly illuminated, then the intensity S_{oR} in a picture element at the output phosphor will be that of the real signal in that element, increased by the SIB contribution of all elements of the field. If however only that element is illuminated at the input, then the output intensity S_{oo} in that element will be that of the real signal only. Therefore $S_{oR} - S_{oo}$ is the total contribution of SIB to that element and the SIB-index is given by

$$Z = \frac{S_{oR} - S_{oo}}{S_{oo}} = \frac{1 - S_{oo}/S_{oR}}{S_{oo}/S_{oR}} \qquad (II.16)$$

If S_{oR} can readily be measured, S_{oo} can only be obtained by extrapolation because a finite detecting area must be used to measure the intensity. A uniformly illuminated circle of radius r is imaged on the photocathode and the detecting aperture is located at the centre of the intensified circular image (Fig. II.7 A). The measured output intensity S_{or} in this detecting aperture is that of the signal increased by the SIB of the elements within the circle. The latter component decreases as r is decreased and extrapolation of the plot of S_{or} versus r to r=o gives the value of S_{oo}. If the output intensity S_{oR} for complete illumination is known, then the SIB-index can readily be calculated with eqn. II.16.

The experimental arrangement is essentially the same as that used above (Fig. II.5). Circular apertures (13 in total) of different diameter are placed in turn in one position of the dual slide carrier. The other position is occupied by an aperture that permits the complete illumination of the cathode, such that the measurement of S_{or} and S_{oR} can rapidly be performed. The position of the photomultiplier assembly is adjusted so as to measure the light intensity at the centre of the intensified image of the smallest aperture (radius 0.8 mm). The detecting area has a diameter of 0.6 mm and is the image of aperture B on the phosphor screen. A plot of S_{or}/S_{oR} in function of r/R permits the extrapolation to r/R = 0. Fig. II.7B shows the results of the measurements obtained for the centre of the field for an intensifier (91) focused in 1 and 2 loops and at an operating potential of 40 KV.

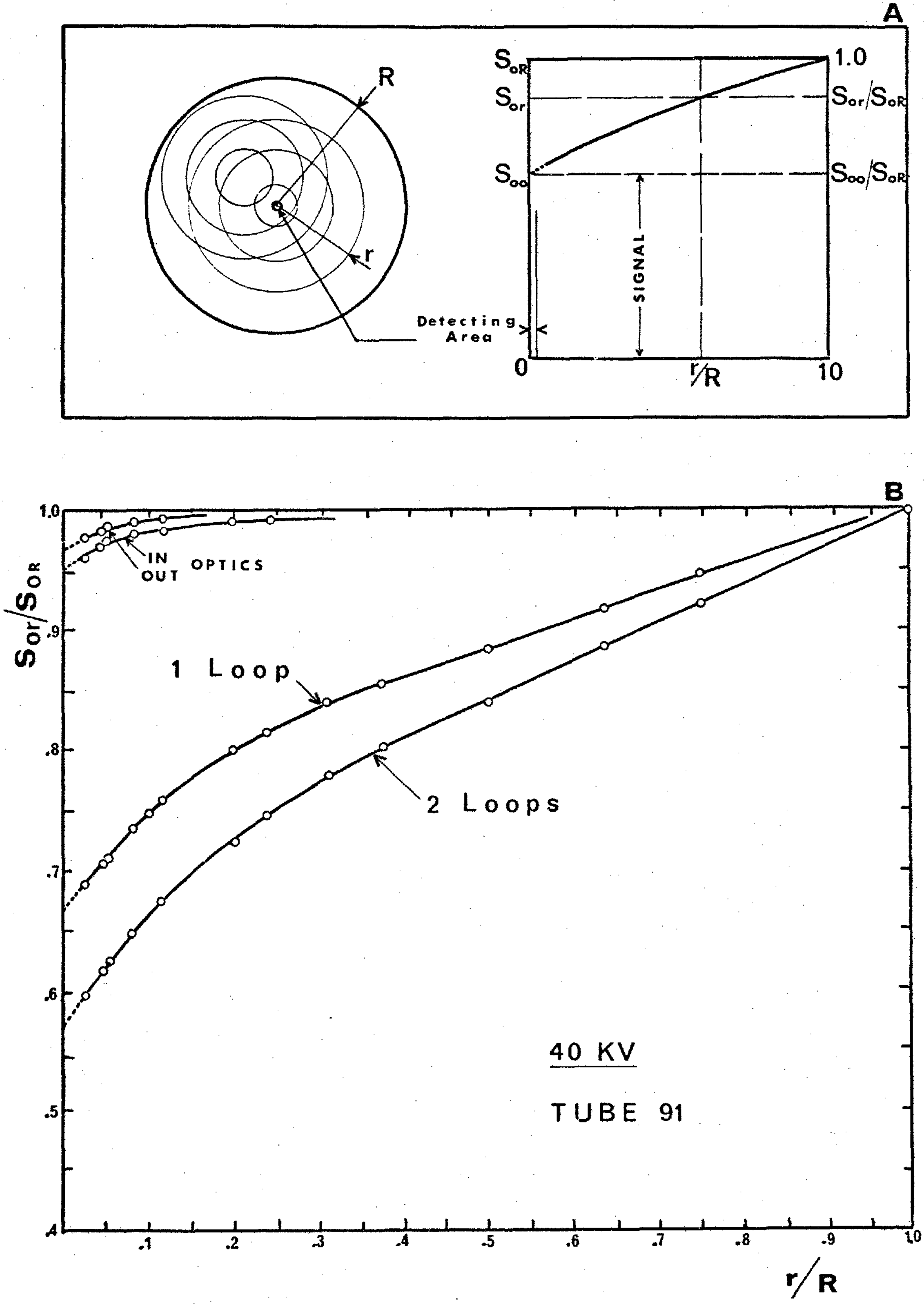

FIG 11.7 SIB - INDEX Measurements

The ratios S_{oo}/S_{oR} are respectively 0.67 ($Z_{iTo} = 0.49$) and 0.57 ($Z_{iTo} = 0.74$). Also shown are the results obtained for the assessment of the SIB in the input optics and the output optics in absence of imaging tube. The former was performed by placing the aperture B in the image plane of the WW lens, the latter by focusing the photomultiplier assembly directly on the apertures in the plane of the slide carrier (Fig. II.5). The SIB-indices, calculated with eqn. II.16, are $Z_i = 0.047$ for the input optics and $Z_o = 0.034$ for the output optics in the centre of the field.

The measurements were repeated for off centre locations in the field of the intensifier and for the separate optics in order to assess the field uniformity of the background, and at different overall operating potentials of the focused intensifier in order to investigate the voltage dependence. Only five small apertures were used for these measurements since this provides enough points to extrapolate to $r/R = 0$. The results of all these measurements performed on one intensifier (91) are shown in Tab. II.8.

Correction of the results

The SIB-index of the sole intensifier must now be calculated from the measured indices for the complete system Z_{iTo}, for the input optics Z_i and the output optics Z_o. It can be seen from Tab. II.8 that Z_i is fairly constant across the field such that, using eqn. II.13

$$Z_{To} = \frac{Z_{iTo} - \underline{Z_i}}{1 + \underline{Z_i}} \qquad (II.17)$$

where Z_{To} is the SIB-index of the intensifier and output optics. Furthermore, because Z_o is also practically constant across the field, it is possible to calculate Z_T, using eqn. II.14 and II.15 by

$$Z_T = Z_{To} - \underline{Z_o} - \underline{Z_o}\,\frac{\overline{Z_{To}} - \underline{Z_o}}{1 + \underline{Z_o}} \qquad (II.18)$$

SIB ACROSS THE FIELD. OPTICS & TUBE 91.(40 KV)							
Distance to the centre of the field (in mm)		Input optics Z_i	Output optics Z_o	System 1 loop Z_{iTo}	System 2loops Z_{iTo}	Tube 1 loop Z_T	Tube 2loops Z_T
0		0.047	0.034	0.493	0.739	0.378	0.604
1				0.460	0.695	0.349	0.564
2		0.047	0.034	0.450	0.660	0.337	0.531
3				0.440	0.652	0.329	0.524
4		0.047	0.035	0.435	0.648	0.325	0.519
6		0.047	0.034	0.426	0.648	0.315	0.518
8		0.047	0.035	0.420	0.640	0.310	0.514
10		0.047	0.034	0.480	0.615	0.299	0.490
12		0.046	0.034	0.377	0.575	0.271	0.454
14		0.046	0.035	0.324	0.493	0.222	0.378
16		0.044	0.034	0.282	0.409	0.203	0.301
18		0.043	0.034	0.242	0.324	0.146	0.222
SIB DEPENDENCE ON OVERALL POTENTIAL.CENTRE.TUBE91							
Applied overall potential (in KV)							
40		0.047	0.034	0.493	0.739	0.378	0.604
35				0.470	0.704	0.358	0.583
30				0.450	0.653	0.338	0.525
25				0.417	0.595	0.318	0.473
20				0.360	0.516	0.256	0.399
15				0.290	0.419	0.191	0.322
SIB OF DIFFERENT TUBES.(40 KV)							
Intensifier Number.	Distance to the centre of the field (in mm)						
78	0	0.047	0.034	0.551	0.840	0.432	0.701
	10			0.422	0.650	0.310	0.520
91	0			0.493	0.739	0.378	0.604
	10			0.408	0.615	0.299	0.490
94	0			0.470	0.710	0.360	0.580
	10			0.392	0.605	0.280	0.490
99	0			0.515	0.762	0.399	0.623
	10			0.410	0.630	0.305	0.507

TAB II.8 SIB-index . RESULTS

where $\overline{Z_{T_0}}$ is the field average of Z_{T_0} obtained by numerical integration of the results of eqn. II.17. The results for the SIB-index Z_T are shown in Tab. II.8 and in graphical form in Fig. II.9. This diagram shows the variation of Z_T with the position in the field for 1 and 2 loops focusing of the intensifier operated at 40 KV (A) and the variation of Z_T in the centre of the field with varying overall applied potential in 1 and 2 loops focusing (B).

Measurements on other intensifiers

Measurements were repeated on three other intensifiers (94, 78, 99), but only the SIB-index at the centre of the field and at 10 mm from the centre was measured when the intensifier was operated at 40 KV in 1 and 2 loop focusing. The results were corrected with eqn. II.17 and II.18.

II.3.3. Conclusion of the measurements

The increase in output intensity of a uniformly illuminated intensifier, occuring as a result of signal induced background and characterized by the SIB-index, depends upon the position in the field, on the overall applied potential and on the number of loops used to focus each stage. Furthermore, it varies from tube to tube as the result of non-uniformities in the sensitivity of the cathodes, differences in light gain and variations in the importance of ion feedback.

The index Z_T is maximum in the centre of the field where it equals 58 to 70% in 2 loops focusing and 36 to 43% in 1 loop focusing for an overall potential of 40 KV. It decreases to about 15% at the edges of the field. The field averaged SIB-indices, calculated by numerical integration of the distribution across the field, was found to be 22 and 36% for tube 91 in 1 and 2 loops focusing (40 KV). The variation of Z_T with position in the field indicates the predominance of electronic causes of SIB, since the optical causes should lead to a fairly uniform distribution of the background. The localized increase in the centre of the field is caused by ion feedback as already indicated in § II.1.7. (It is caused in particular

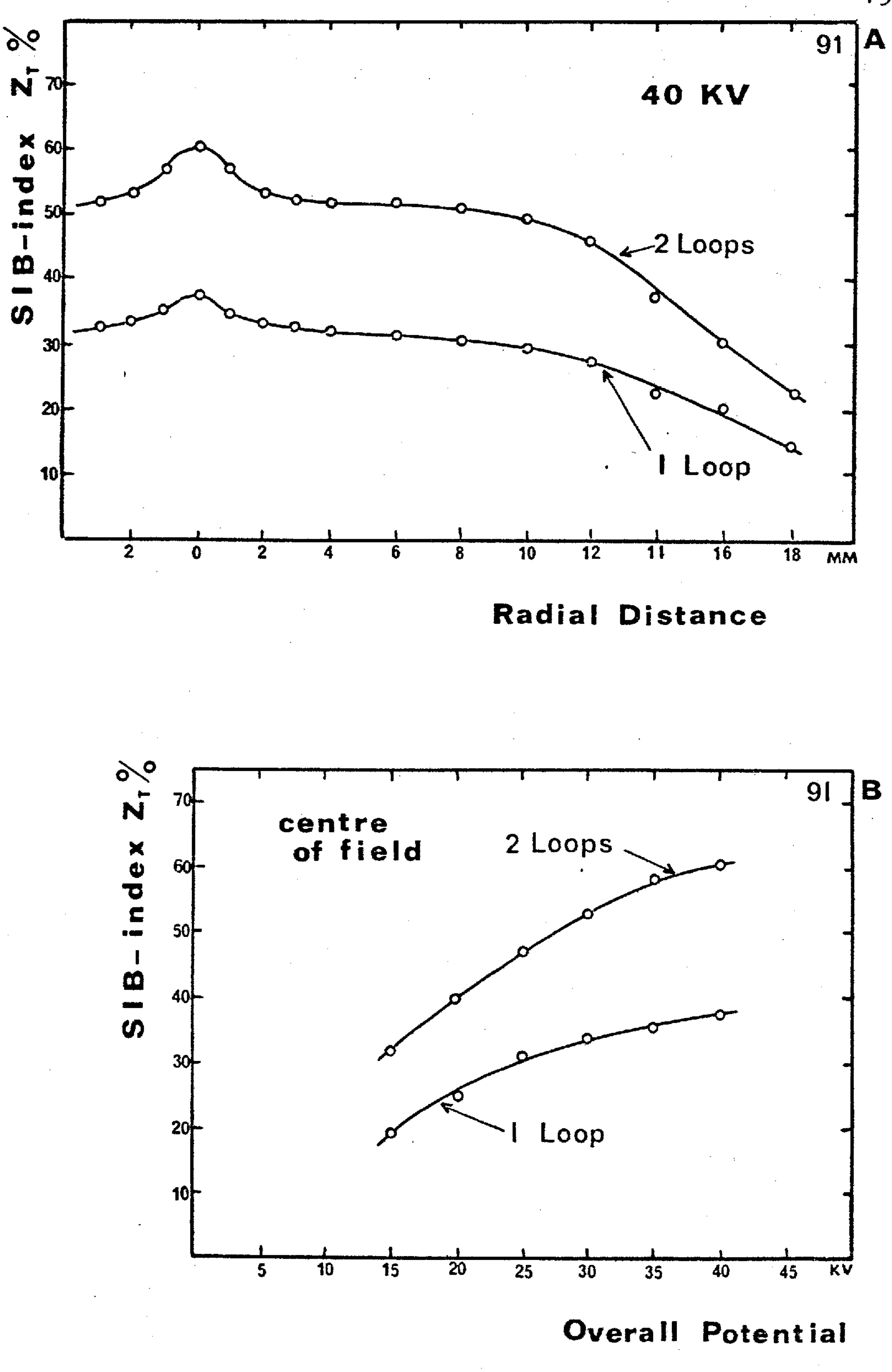

FIG II. 9 SIB-index Z_T

by the structure BB of the ion image in Fig. II.4 C).

The dependence of Z_T upon the magnetic field strength results from the contribution to background of the backscattered electrons since the other background components would not be significantly affected by such a change. The dependence of Z_T upon applied potential results from the combined effect of voltage on the backscattered electrons component (§ II.4.5) and the optical and ionic feedback (§ II.4.4 and § II.4.9).

It is interesting to compare these results with those obtained by Cromwell (1969) on the two stage Carnegie Intensifier (RCA . C33011 . see Tab. 2.2). This intensifier was operated in 1 loop focusing (data from RCA . 1966) with probably an overall potential of 20 KV. Cromwell used a simple technique which should give an underestimation of the SIB-index.* He found that the background was dependent upon the wavelength of the incident illumination, increasing continuously from Z = 21% at 3500 Å to Z = 36% at 8000 Å at the centre of the field and from 13 to 31% at the edge of the field. The wavelength dependence and the relative uniformity of the background at long wavelengths indicate that light scattering in the stages is an important contribution to SIB in that intensifier. It can be estimated that at practically all wavelengths the SIB-index of a two stage version of the I.C. intensifier operated in 1 loop at an overall potential of 20 KV would only be 22% in the centre of the field and 7% at its edge (field average of 13%). This would be about the magnitude of the SIB of the Carnegie tube at short wavelengths, where the contribution of light scattering in the stages is the smallest (§ II.4.3).

---

* He illuminated uniformly a 180° sector of the photocathode and measured the background B near the boundary of the illuminated region. The resulting values were multiplied by 2 in order to approximate the background for full cathode illumination.

11.3.4. Practical importance of SIB

For low contrast images, and in absence of any bright objects in the field, the average intensity of the output image will be increased by a factor (1+Z), where Z is the SIB-index which is dependent upon the position in the field. Therefore, the contrast of a faint object will be reduced approximately by that same factor. The modulation transfer function, which was measured in § 8.2 for a single small image on a dark background (100% modulation) will have to be divided by (1+Z) at all spatial frequencies. The modulation at zero frequency therefore becomes $(1+Z)^{-1}$ and represents the large scale loss of contrast. The limiting spatial frequency, which was found to be 53 c/mm (MTF = 0.05), can be calculated from the data presented in Fig. 8.4. The limiting spatial frequency decreases to 46 c/mm in 2 loop focusing (Z = 60%) and to 49 c/mm in 1 loop focusing (Z = 38%) at the centre of the field.

The intensity of the faintest detectable object will increase by a factor $\sqrt{1+Z}$ since this represents the increase in the statistical fluctuations of the average intensity of the image. This would mean, for example, that the magnitude of the faintest star detectable on the sky background will be increased by $\log_{2.51} \sqrt{1+Z}$ magnitudes. For the intensifier operated under normal focusing conditions (2 loops, 40 KV) this would correspond to a reduction of at most 0.25 magnitudes (centre of the field, Z = 60%).

As already pointed out in § 7.5 the SIB prevents the determination of the true sensitivity profile of the intensifier from the measurement of the variation in output intensity when the primary photocathode is uniformly illuminated. Indeed the SIB tends to smooth out the true sensitivity profile and large errors could result from such a calibration if the intensifier is used for photometric applications. The true sensitivity profile can only be estimated by measuring the output intensity of a small light spot imaged in turn on all points of the primary photocathode (Cromwell, 1969).

Whenever a bright object happens to be in the field the signal induced background it produces may seriously compromise the photometric capability of the intensifier. The radial variation of the background of a bright object will limit the accuracy with which the intensity of a faint feature, located near the bright object, can be measured. (Fig. II.6). For example, the accuracy of the photometric measurement of a faint star, located at 3 mm from a bright star, will not be better than ±0.05 magnitudes if the bright star is 10.5 magnitudes higher than the faint one.* Therefore an 9.5 magnitude star should be avoided or masked from the photocathode, if photometry of a 20 magnitude star is to be made.

II.4 QUALITATIVE ANALYSIS OF THE INDIVIDUAL SOURCES OF SIGNAL INDUCED BACKGROUND

The importance of the different sources of SIB in the cascade intensifier will now be investigated. Each SIB-producing mechanism will be considered to occur individually in the intensifier, and the magnitude of the background at the output will be evaluated by measurements and/or calculations.

This evaluation will be performed in the following assumptions:

-- The sensitivity of all photocathodes and the effective efficiency of all phosphor screens are constant over the entire area of these surfaces.

-- The intensifier has perfect performance in regard to geometry.

-- The contribution of any picture element to itself is considered here as SIB.

---

*This was calculated from the data presented in Fig. II.6, in the assumption that only one sky background measurement is made at a distance of 0.5 mm from the faint star.

II.4.1. Light scattering in the phosphor end-windows

The fraction of light emitted by the output screen which is internally reflected at the glass-vacuum interface of the output phosphor support plate, can be calculated from the angular intensity distribution $I(\Psi)$ of the light inside the glass plate. Indeed this fraction is given by:

$$K_p = \int_{\theta_c}^{90} I(\Psi)\sin\Psi \quad d\Psi \Bigg/ \int_{\theta_t}^{90} I(\Psi)\sin\Psi \quad d\Psi \tag{II.19}$$

where θ_c is the critical angle of the interface ($\theta_c = 41^{\circ}$). Numerical integration of this expression using the distribution $I(\Psi)$ as measured in § 8.4.1 leads to a value for K_p of 23%. Considering the multiple reflections and the absorption in the glass and phosphor screen it was calculated by Law (1939) that about $Q'_p = 20\%$ of the initially reflected light emerges from the glass plate in the forward direction. (a degree of optical contact of 60% as estimated in § 8.4.1 was assumed). The SIB contribution from a phosphor screen element to the entire field will thus, according to eqn. II.8, be equal to $T_p = K_p\, Q'_p / 1 - K_p = 0.059$. This figure of 5.9% is also a good approximation for the SIB-index Z_p, associated with this type of background. Indeed the condition of reciprocity (§ II.2.3) is practically satisfied for most points of the field. (neglecting edge effects).

The SIB-index Z_p was measured using the aperture method (§ II.3.2) on a single backed screen. Ultra-violet light, illuminating the screen against which the apertures were placed, provided the uniform excitation of the phosphor. The photomultiplier assembly was used to measure the intensity of the excited light at the centre of the screen. After correction of the extrapolated measurement for the SIB contribution of the photomultiplier assembly (Z_o) a value of $Z_p = 0.063 \pm 0.004$ was found.

It can easily be calculated that the reflections at the end-window of the envelope cause a further increase of 0.5% of the background. Therefore the total contribution of the end-window can be estimated to be $Z_p = 6.8 \pm 0.4\%$ (eqn. II.15).

II.4.2. Light scattering in the photocathode windows

The interfaces traversed by a light beam focused on the primary photocathode cause about 20 to 30% of that light to be lost by reflection. Indeed a reflection of 4% can be accounted for each of the three interfaces between vacuum (or air) and glass, and 15 to 25% of the remaining light will be reflected by the photocathode (Wallis, 1956; Wlerick et. al. 1966). The exact amount depends upon the thickness and processing method of the photocathode and upon the wavelength and numerical aperture of the incident light beam. Considering the multiple reflections in the various interfaces it is possible to calculate the fraction of light which is actually transmitted to the photocathode as signal (S), the fraction which is transmitted to the cathode after multiple reflections as SIB (B), and the fraction which is reflected from the window by the complete system of interfaces (R). This was done as a function of the combined reflectivity of the glass-cathode and cathode-vacuum interfaces. Since the condition of reciprocity (§ II.2.3) is practically obeyed for most points of the field (edge effects neglected), the SIB-index Z_E, associated to this component, is given by the ratio B/S. The results of these calculations, performed for three possible configurations of photocathode windows, are shown in Fig. II.10 A. Also shown is the percentage of light (R), which is reflected by the entire system of interfaces towards the input optical system.

The reflection coefficients used in these calculations are valid for angles of incidence of the light up to about 30° for the glass-vacuum interfaces and probably up to 15° for the photocathode-vacuum interface (critical angle: 19.5° if the refractive index of the photocathode is 3.00). Therefore the values for Z_E obtained in Fig. II.10 A should be valid for numerical apertures of the input optical system up to 0.25 or for effective f/- numbers greater than f/2.0.

The amount of light reflected by the system of interfaces (R) was measured for several intensifiers and ranged between 23 and 30% of the incident light. A very slight increase of this figure with increasing wavelength was observed. Therefore, it can be seen from Fig. II.10.A that the SIB index Z_E corresponding to this type of background will be 2.3 to 3.2%, and practically independent of the wavelength. (dotted lines with arrows)

II.4.3. Light scattering within the stages

A fraction of the light transmitted by the photocathode of each stage will be reflected to it by the electrodes, the glass walls and the backing of the phosphor screen. The average SIB-index associated with this type of background can be factorized as:

$$\overline{Z_s} = \frac{K_s \cdot \overleftarrow{R} \cdot \overline{Q_s}}{\overrightarrow{R}} \qquad (II.20)$$

where K is the transmission of the photocathode for light which has the spectral distribution of the incident illumination (first stage) or that of the PII phosphor emission (second and third stage). $\overleftarrow{R}$ and $\overrightarrow{R}$ are the sensitivities of the cathode for illumination from the vacuum side and from the substrate side respectively. $\overline{Q_s}$ is the average fraction of light, transmitted by the cathode, which is reflected to it by the internal surfaces of each stage. This factor depends upon the geometry of the stage, the angular distribution of the transmitted light and the reflectivity of the internal surfaces.

<u>The Transmission K_s and the Ratio $\overleftarrow{R}/\overrightarrow{R}$.</u> The results of measurements of K_s and $\overleftarrow{R}/\overrightarrow{R}$ made on three SII photocathodes are given in Tab. II.10 B These measurements were performed on one intensifier (the dynodes and output phosphor screen were stored in the processing compartment) and on two photocells. Wratten filters

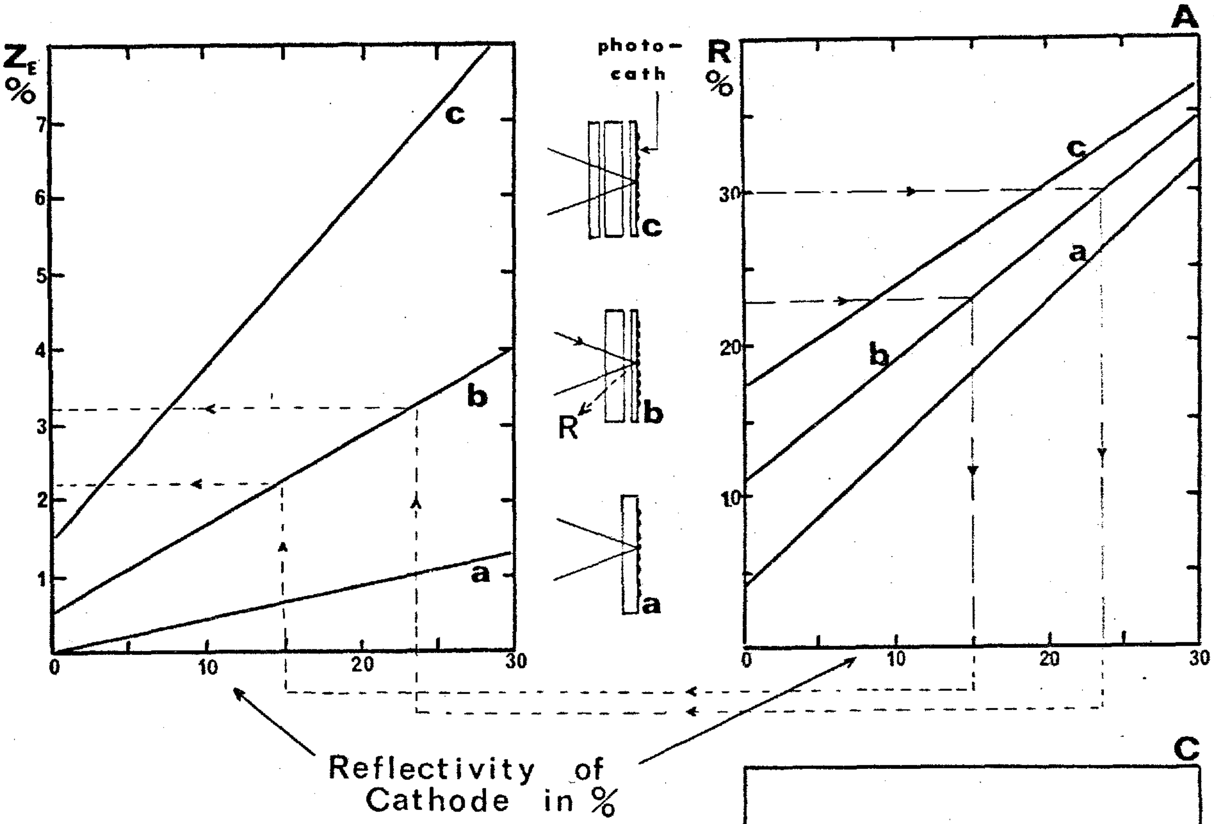

B

Photocathodes	No.1	No.2	No.3
TRANSMISSION K_s %			
Blue (47B)b	24	30	19
Green (58)	29	37	
Yellow (73)	40		
Red (25)r	69	52	61
RATIO $\overleftarrow{R} / \overrightarrow{R}$			
Blue b	0.90	0.83	0.95
Green	0.76	0.81	
Yellow	0.59		
Red r	0.50	0.76	0.52
RATIO $\frac{K_{sr}\overleftarrow{R}_r\overrightarrow{R}_b}{K_{sb}\overrightarrow{R}_r\overleftarrow{R}_b}$	1.60	1.59	1.52

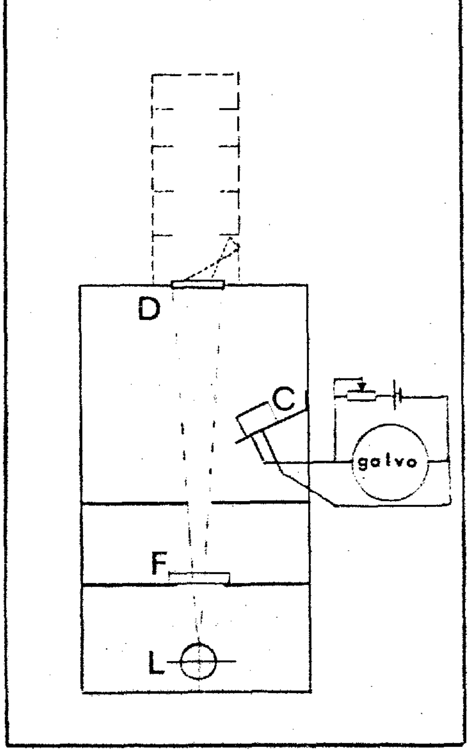

FIG II.10 LIGHT SCATTERING

were used to vary the colour of the incident light. The results indicate the expected increase in transmission with increasing wavelength from about 25% for blue light to about 65% for red light. The ratio $\overleftarrow{R} / \overrightarrow{R}$ decreases with increasing wavelength from about 0.90 for blue light to about 0.55 for red light.

The opposite effect would be expected from considerations of escape depth of photoelectrons and absorption of light in the photoemissive layer. Indeed, a higher sensitivity of the cathode at all wavelengths for illumination from the vacuum side would result from the high absorption at the vacuum side of the photoemissive layer from where the photoelectrons easily escape. On the other hand, it was suggested by Bǎćik (1971) that more light should be trapped in the cathode if it is illuminated from the substrate side rather than from the vacuum side. Indeed the reflectivity of the photocathode-vacuum interface is very high (12 - 25%) owing to the large refractive index of the $Cs_3 Sb$ layer. ($n = 2$ to 3). Therefore an appreciable fraction of the light incident from substrate side on the photocathode-vacuum interface will be reflected in the cathode to produce more photoelectrons. In the case of illumination from the vacuum side, only light which is transmitted by that interface will contribute to photoemission. Therefore, on these considerations only, one would expect a higher sensitivity for illumination from the substrate side ($\overrightarrow{R}$) as compared to the sensitivity for illumination from the vacuum side ($\overleftarrow{R}$). The ratio $\overleftarrow{R} / \overrightarrow{R}$ should decrease with increasing wavelength, since the reflectivity of the interface increases with wavelength (Sommer, 1968; Wlerick et. al. 1966). The differences in the spectral characteristics measured on three photocathodes for the two directions of illumination (Tab. II.10 B) tend to indicate that the effect of reflections at the photocathode-vacuum interface is more important than that based on considerations of escape depth and absorption.

The fraction $\bar{Q}_s$. A simple instrument was designed to evaluate the average fraction $\bar{Q}_s$ or the amount of light, transmitted by the cathode, which is reflected back to it by the internal surfaces. (Fig. II.10.C). A circular diffuse screen (D), uniformly illuminated with blue light from a tungsten lamp (L) filtered by a Wratten 47B filter (F), simulates the diffuse phosphor screen emission in the second and third stage of the intensifier. A photovoltaic cell (C), connected to a galvanometer, measures the average brightness of the screen. The experiment is performed is three steps:

-- The galvanometer is first zeroed, by balancing the cell current with a small DC current from a battery, when no obstacle above the screen (D) reflects light to the screen (the room is in complete darkness).

-- A mirror is then placed against the screen such that nearly all the light emitted by the screen is reflected to it. The galvanometer reading then represents nearly $\bar{Q}_s = 100\%$.

-- A dummy stage is placed facing the screen which then simulates the phosphor screen in the intensifier. The galvanometer reading is compared with the previous measurement to yield a value of $\bar{Q}_s$ for the actual intensifier. It was found that $1.0 \pm 0.1\%$ of the light, transmitted by the cathode, was reflected back to it by the internal surfaces of the stage when all the metalic surfaces were coated with a layer of evaporated carbon. This figure increased to $3.3 \pm 0.1\%$ if clean molybdenum annuli were substituted in the dummy stage.

The fraction $\bar{Q}_s$ for the first stage of the intensifier will depend on the numerical aperture and wavelength of the incident light beam, and will certainly not be greater than that estimated above for the other stages.

The SIB-index Z_s. Substitution of the above data in eqn. II.20 permits the calculation of the SIB-index associated with light scattering within the stages. For the last two stages $Z_s = 0.15$ to 0.28% since the spectral transmission of the Wratten 47 B filter is similar to the spectral emission of the P11 phosphor screen. (§ 7.1.2). The SIB-index for the first stage will be at most that of the other two stages for blue light illumination, and at most $\overline{Z_s} = 0.26$ to 0.52% for red light illumination. The total contribution of this type of background for the entire intensifier can now be calculated using eqn. II.15 to be at most 0.9% for blue light illumination and 1.1% for red light illumination of the intensifier.

II.4.4. Optical Feedback

The SIB produced by optical feedback in a uniformly illuminated stage can be considered to be uniformly distributed across the field. Indeed each pinhole or imperfection in the aluminium backing of a phosphor screen will practically produce a uniform illumination of the previous photocathode. The SIB-index can then be expressed by

$$\underline{Z}_F = K_F \cdot \underline{\underline{q}} \quad \overleftarrow{S_M} \; M(PII \;.\; \overleftarrow{SII}) \cdot \eta_{eff}(V).V \qquad - (II.21)$$

where K_F is the fraction of light emitted by the screen in the forward direction, which is transmitted by the backing towards the previous photocathode, $\underline{\underline{q}}$ is the fraction of the latter light which reaches the cathode and the other terms represent the light gain $\overleftarrow{G}$ of the stage for illumination from the vacuum side (eqn. 3.7).

A first attempt at evaluating this SIB component for the first stage (G of an intensifier (97) consisted in measuring the photocurrent - applied voltage characteristic of the primary cathode. Indeed if the photocurrent caused by the signal should remain constant after complete photoelectron collection, the current produced by optical feedback should increase with applied voltage as the light gain of the stage. An increase in photocurrent of 2% at 13 KV over the current at 1 KV was measured for blue light illumination of the cathode (Wratten 47 B). Complete collection of the photoelectrons was recognized by a plateau in the characteristic between 1 and 3 KV. The SIB-index of that stage would thus be $\underline{Z}_F = 2.0\%$. However, when red light illumination was used (Wratten 25) an increase of 2.9% was observed for the same measurement. This would indicate that photoemission is somewhat enhanced as a result of the applied field, i.e. the photoelectric Schottky effect (§ 3.1.3). Therefore there is some doubt about the accuracy of the measurement made with blue light, although this effect should not appreciably affect the short wavelength response of the cathode.

A second evaluation of the magnitude of optical feedback was performed by comparing the amount of light emitted in the forward direction with that emitted through the aluminium backing. This was done in the demountable system shown in Fig. II.11 A, by comparing the current from a photovoltaic cell (C) placed alternatively at right angle with the screen in the two directions. An average ratio of $K_F = 0.009 \pm 0.001$ was found for several screens. Assuming that the light emitted through the backing is Lambertian, the ratio $\underline{q}$ can be evaluated to be $\sin^2$ (arctg R/L), where R is the radius of the photocathode and L the length of the stage. This factor is $\underline{q} = 4.7\%$ for the first two stages and $\underline{q} = 2.7\%$ for the last stage.

According to the results presented in Tab. II.10.B, it can be said that the <u>blue</u> light gain of a stage is practically equal for front or back illumination of the cathode, thus $\overleftarrow{G} = \overrightarrow{G}$. (The effective sensitivity for vacuum side illumination of the cathode of a multiplying dynode will be slightly increased by the reflections of the transmitted light by the phosphor screen). The SIB-index $\underline{Z_F}$ can thus be calculated as a function of the blue light gain of the stage, by substitution of the above results in eqn. II.21. The SIB-index of the complete intensifier is further calculated using eqn. II.15, as a function of the blue light gain of the intensifier. The results are shown in Fig. II.11.B. Thus for a BLG = 10^5 a value $\underline{Z_F} = 4.5$ to 5.6% can be expected as a result of optical feedback.

The presence of pinholes and cracks in the backing of the first dynode can be observed by operating the first stage of the intensifier at about 1 KV (11 loops). Only electrons landing in these pinholes will produce luminescence in the screen because those landing on the aluminium will not penetrate the backing. The two other stages of the intensifier are operated under normal conditions. Fig. II.11.C

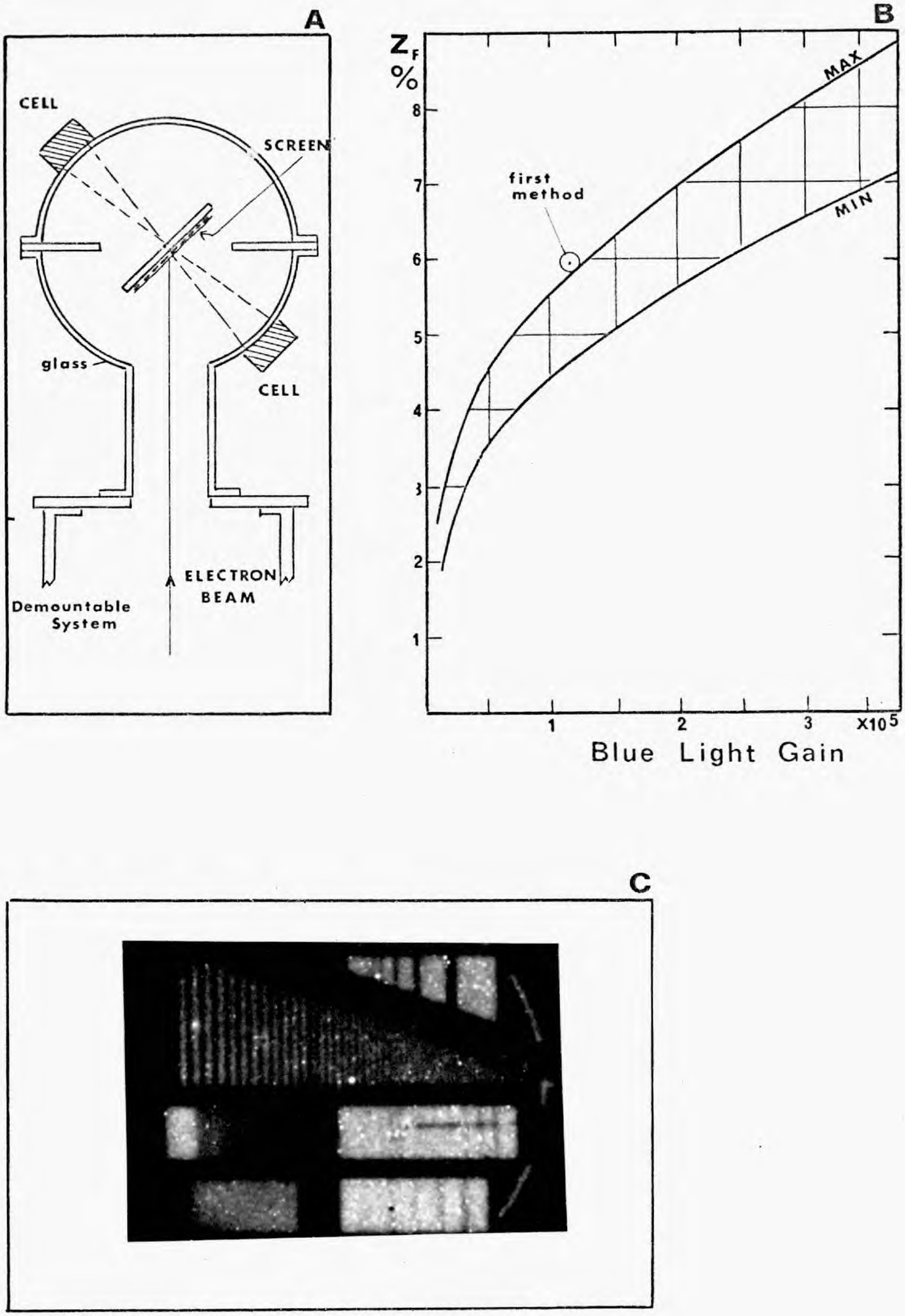

FIG II.II OPTICAL FEEDBACK

shows a macrophotograph obtained in this manner. The average pinhole size measured at the output screen is about that of the disc of confusion, indicating that those pinholes are very small.

II.4.5. Backscattering of electrons from the screens

The magnitude of the SIB produced by backscattered electrons depends upon the magnetic field strength, the dimensions of each stage and quite critically upon the rediffusion coefficient of the screens and the energy distribution of the backscattered electrons (BSE). The fraction of BSE which are able to contribute to the background increases with decreasing energy of these electrons (§ II.1.5) while the efficiency of the phosphor screen decreases.

It has unfortunately not been possible to measure the rediffusion coefficient and the energy distribution of the backscattered electrons. This would require sophisticated equipment which must be designed for the analysis of the backscattered electron current caused by high energy primary electrons. However, estimations for these properties can be made from data published in the literature.

Coefficient of Rediffusion (K_B). The rediffusion coefficient is the ratio of backscattered current* to the incident current. The rediffusion coefficient for uniform surfaces of metals and insulators increases slightly with the primary energy for energies higher than 5 KeV and depends mainly upon the average atomic number of the bombarded material (Holliday et. al. 1957; Sternglass, 1954). This ratio is

---

*strictly speaking, the total rediffusion current can be divided into three components: (a) elastically reflected primaries, (b) inelastically reflected primaries, and (c) true secondary electrons. No clear border line exists between (b) and (c). However, in case of primary electrons energies of several hundred volts, electrons with more than 50 eV energy are, as a whole regarded as backscattered (Sternglass, 1954).

about 26% for zinc sulphide (average atomic number: 23).

The phosphor screens used in the intensifier consist of a very tightly packed layer of phosphor grains (average diameter of 1 micron) onto which a 500 to 700 Å thick layer of aluminium is deposited. Very few electrons are backscattered from this backing at high energy of the primary electrons (> 10 KeV) because this layer is thin and made of low atomic number material. The rediffusion coefficient of the phosphor screen itself should be smaller than that of a smooth Zn S surface, because of multiple scattering in the polycrystalline screen. This reduction will depend upon the shape, size and packing of the phosphor grains. This fact was recently confirmed by Meyer (1970) who measured a rediffusion coefficient of 26% for a single Zn S crystal, but a reduction to 15 ± 2% when an actual screen, made of settled Zn S powder and backed with a 500 Å thick film of aluminium was bombarded with 13 KeV electrons. The average grain size of that screen was 15 microns. A higher rediffusion coefficient can be expected for the screens used in the cascade intensifier. The much smaller average grain size (1 micron) will cause the surface to be smoother and reduce the number of electrons which, after having been scattered back from a single crystallite, strike the surface of another grain. Furthermore, the packing of the electrophoretically deposited screens is higher than the packing of settled screens.

Analysis on one phosphor screen made at the Analytical Services Laboratory* indicated however that the ratio of total backscattered current to incident beam current (15 KeV) was 25 to 30%. There is some doubt about the accuracy of that measurement since that particular sample showed signs of defective surface conductivity. A spectrum of the soft X-rays emitted by the screen as a result of impact of 40 KeV electrons showed that no foreign material with high atomic number was

---

* These measurements were performed by Mr. P.R. Monk.
Imperial College. Microprobe report ASL 7410.

accidentally present in the screen (accuracy: 1 part in 1000).

Energy distribution of the BSE's. The major features of the energy distribution of BSE's from smooth surfaces under electron bombardment of 2 - 30 KeV electrons are the predominance of electrons which have experienced energy losses between 10 and 50% of the primary energy, the absence of a large group of elastically scattered electrons and an increase in the mean energy of the BSE with increasing atomic number of the bombarded material, and with increasing energy of the primary electrons (Sternglass, 1954; Redhead, 1968). The results of measurements made by Meyer (1970) of the energy distribution of the BSE from the settled screen described above are shown in Fig. II.12 A (curve M). The average energy is about 50% of the primary energy and the peak in the distribution occurs at about 65% of the primary energy. Since lower losses in the energy of the BSE can be expected for the screens used in the cascade intensifier, one could also expect an energy distribution for these screens which has a larger average energy and a peak occuring at a higher energy than that measured by Meyer. This assumption is confirmed by the following fact. The spurious image, resulting from the refocusing of the electrons in the last stage of the intensifier, comes into focus at a magnetic field which is 2 to 4% higher than the field required to focus the causative image. This would correspond with a transit time of BSE of about 1.96 to 1.92 times the orbital period for photoelectrons in the last stage. According to Fig. II.3 A this would mean that a large number of BSE have an initial axial energy of 88 to 74% of the energy of the primary electrons (two arrows indicate the position of these extreme values of the axial energy). It was seen in § II.1.5 that only high energy BSE with small emission angle with the normal to the screen (θ) are able to contribute to the production of the spurious image since BSE with higher angle of emission are captured by the electrode system. Therefore the peak of the actual energy distribution will be slightly higher than the 88 to 74% predicted for the axial energy distribution.

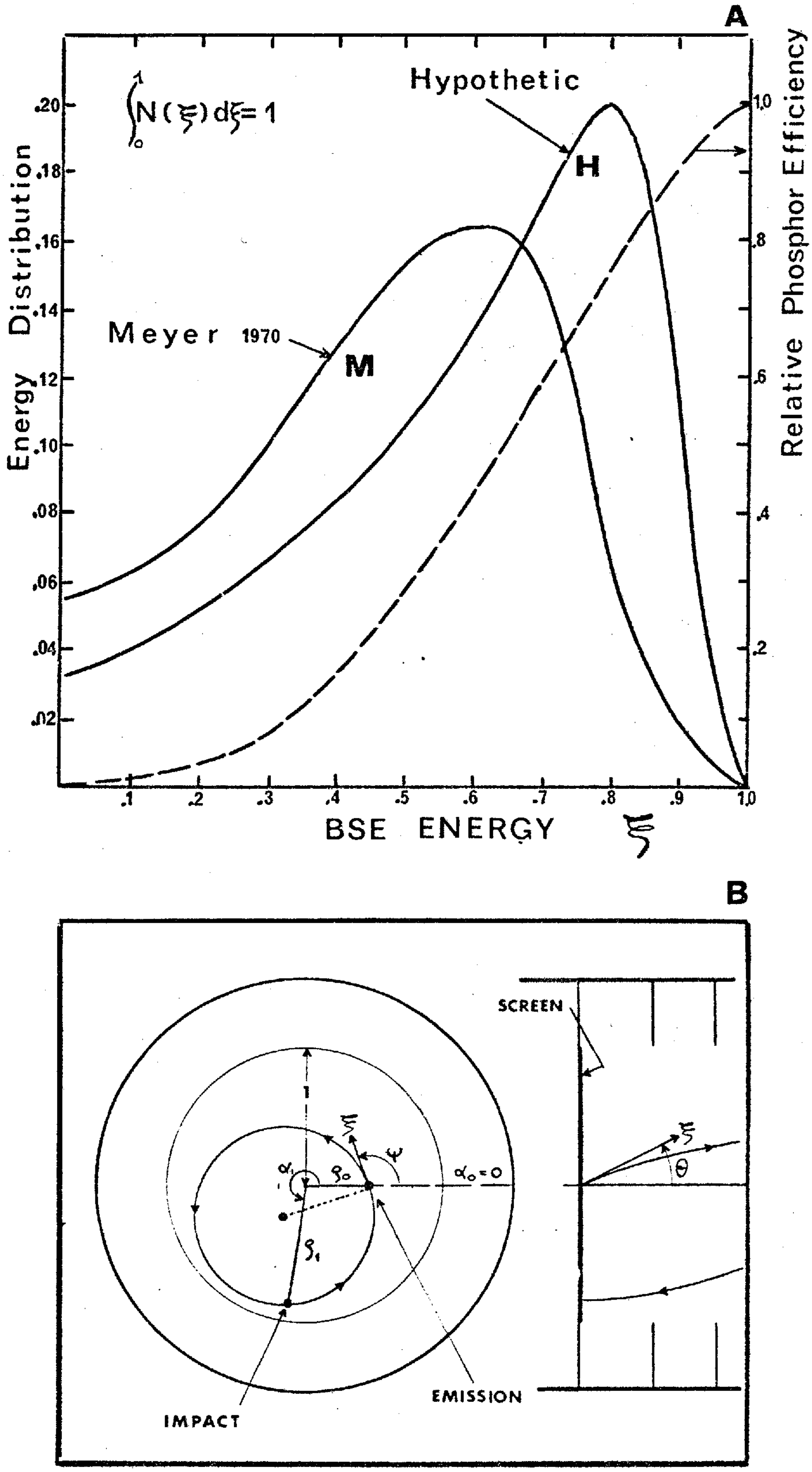

FIG II_12 BS-ELECTRONS

On the other hand, the fact that the spurious image on the output phosphor screen is observed as photons would cause the peak of the distribution to be slightly lower since the efficiency of the screens increases with increasing energy of the BSE.

An hypothetical distribution, based on the above speculations, was chosen, together with that measured by Meyer, for the purpose of the calculation of induced background. This distribution, shown in Fig. II.12 A (curve H), peaks at 80% of the energy of the primary electrons and has a shape similar to that measured by Meyer.

Angular distribution of BSE. The angular distribution of BSE has been shown by Kanter (1957 and 1961) to obey essentially a cosine law for electrons incident on the surface with angles smaller than 45°. Furthermore, the shape of the energy distribution is independent of the angle of emission of the BSE. (Sternglass, 1954).

II.4.6. SIB-index associated with backscattered electrons

Location of the point of impact of a BSE

The location of the point of impact of a BSE depends upon the position of the point of emission of that electron, its initial energy and direction of emission and upon the focusing conditions. The complete calculations are given in Appendix IV and only the results will be given here in so far as it is necessary for the understanding of this section.

A BSE is emitted at the relative distance ρ_o from the centre of the field of radius R (ρ_o is the actual distance divided by R). Its relative initial energy is ξ ($\xi = V_o/V_T$ where V_o is its actual energy in eV and V_T the stage potential) and it is emitted at an angle θ with the normal to the screen and at an angle ψ (azimuth) with the radius connecting the centre of the field to the point of emission. (Fig. II.12 B). The primary electron image is focused in n loops by correct adjustment of the magnetic field (eqn. 4.1). The position $\rho_1 \alpha_1$ of the point of impact of that BSE is then given by

$$\rho_1 = \frac{1}{n}\left[\xi(P \sin\theta \, \sin B)^2 + (\rho_o n)^2 + 2.P.n.\rho_o \sqrt{\xi} \, \sin\theta \, \sin B \cos(\psi + B)\right]^{1/2} \tag{II.22}$$

$$\alpha_1 = \text{ARcos} \, \frac{\rho_o + P \, \sqrt{\xi} \, \sin\theta \, \sin B \cos(\psi + B)}{\rho_1} + \alpha_o \tag{II.23}$$

where P is a constant depending on the dimensions of the stage, i.e. $P = 2L/\pi R$, where L is the electro-optical length of the stage (eqn. 4.1). The angle B is half the angle of rotation of the BSE around the centre of curvature of its trajectory, and thus equals $\pi \, T/T_{loop}$ where T is the transit time of the BSE in a particular stage and T_{loop} the orbital period for any electron. The transit times for the three stages were given by eqn. II.2 and II.3 such that

$$B = 2 \pi \, n \, \sqrt{\xi} \, \cos \theta \tag{II.24}$$

for the first and second stage, and

$$B = \frac{2 \pi n}{A + F}\left[\frac{F}{\sqrt{\xi} \, \cos \theta} + A \, \sqrt{\xi} \, \cos \theta \right] \tag{II.25}$$

for the last stage. (A is the length of the active region of the last stage and F half the length of the processing compartment.)

The next problem is to find the condition which the initial parameters (ξ, θ, ψ) of a BSE must satisfy, in order to remain in the accelerating region of a stage. Therefore the normalized distance ρ between the electron and the centre of the field should never be greater than 1.0, for all values of B between zero and that given by eqn. II.24 or II.25, or at all times between emission and impact on the phosphor. However examination of eqn. II.22 indicates that it is not possible to extract explicitly any of the initial parameters (ξ, θ or ψ). Hence, it is not possible to derive an analytical expression for the condition mentioned above. It will therefore be necessary to calculate ϱ at various times during the flight of the BSE, and to reject any electron if ϱ becomes greater than unity.

The SIB-index of one stage. The calculation of the SIB associated with backscattering of electrons was accomplished by programming a digital computer.* This program, which calculates the background in one stage, was devised to accomodate any energy distribution and rediffusion coefficient of the BSE and any axially symmetrically distributed input illumination. This was done so that the output intensity distribution of the first stage of the uniformly illuminated intensifier could be fed directly into the second stage, and its output in the third stage, without the need of using explicitly eqn. II.II to calculate the SIB-index of the complete intensifier.

If $F(\varrho_o)$ is the causative electron density incident on the phosphor screen in a ring $(\varrho_o ; \varrho_o + \Delta\varrho_o)$, and if $K(1)$ is the rediffusion coefficient of the screen for the incident electrons $(\xi = 1)$, then the number of electrons backscattered from that ring with an initial energy ξ is given by:

$$2.\Pi.R^2.\varrho_o.\Delta\varrho_o.F(\varrho_o).K(1).N(\xi).\Delta\xi.$$

where $N(\xi)$ is the energy distribution of the BSE and $\sum_0^1 N(\xi)\Delta\xi = 1$. An equal fraction of these electrons can be thought to be emitted from the centre of the ring (at a distance $\varrho_o + \Delta\varrho_o/2$ from the centre of the field) in M different directions. Therefore E possible values of the azimuth ψ and T possible values of the angle Θ with the normal on the screen are chosen such that each combination of ψ and Θ represents an equal fraction $1/M$ of the electrons scattered from

---

* with the invaluable help of Mr. M. Cohen (Applied Physics Department)

the ring with energy ξ . The possible angles <u>must</u> thus obey: (M = E . T)

$$\Psi(e) = \frac{2\pi}{E}\ .\ e \qquad e = 0, 1, 2 \ldots E - 1.$$

and since the angular distribution is Lambertian

$$\theta(t) = \tfrac{1}{2}\,\mathrm{arcos}\,\left(1 - \frac{2t}{T}\right) \qquad t = 0, 1, 2 \ldots T - 1.$$

Eqn. II.24 is then used for each combination of Ψ and θ to calculate the distance to the centre of the field at different times during the flight of the BSE (ξ, Ψ, θ). This is done by replacing B in eqn. II.25 or II.26 by kB and by calculating ρ ... for $k = {}^{1}/_{K}, {}^{2}/_{K}, \ldots\ {}^{K-1}/_{K}, 1$. If any of these results yields a value of $\rho \geqslant 1$, then this electron is rejected since it impacts on a metal electrode and hence does not contribute directly to this type of SIB. If this is not the case, then the electron lands at ρ_1 as given by eqn. II.24. The computer is programmed to count the number of electrons which land on the screen inside a ring ($\rho_a; \rho_a + \Delta\rho_a$) or the number $N_a(\xi . \rho_o . \rho_a)$ of the M electrons emitted at $\rho_0 + \Delta\rho_0/2$ with an energy ξ for which

$$\rho_a < \rho_1 \leqslant \rho_a + \Delta\rho_a .$$

The number of electrons landing in a ring ($\rho_a; \rho_a + \Delta\rho_a$) is then

$$\frac{1}{M}\cdot 2\pi R^2\cdot \rho_0 \cdot \Delta\rho_0 \cdot F(\rho_0).K(1).N(\xi).\ \Delta\xi \,.\, N_a(\xi \cdot \rho_0 \cdot \rho_a)$$

Part of these electrons are again backscattered with a rediffusion coefficient $K(\xi)$ such that the number of photons produced in the ($\rho_a; \rho_a + \Delta\rho_a$) by the electrons with energy ξ from a ring ($\rho_0; \rho_0 + \Delta\rho_0$) becomes:

$$\frac{1}{M}\cdot 2\pi R^2 \cdot \rho_0 \cdot \Delta\rho_0 . F(\rho_0).K(1).\left[1 - K(\xi)\right].\beta(\xi.\theta).N(\xi).\Delta\xi . N_a(\xi.\rho_0.\rho_a)$$

where $\beta(\xi,\theta)$ is the quantum efficiency of the screen in absence of electron losses by backscattering. This is a function of both the energy of the BSE and its angle of incidence on the screen, which is equal to the angle of emission. Indeed, the thickness of the screen, as seen by the electron, is always higher than the actual screen thickness. It can be seen from Fig. 3.5 that the efficiency of the phosphor screens decreases slowly as the thickness of the screen is increased above 1.0 mg/cm^2 (as used in the intensifier). However the effect of the angle of incidence was not taken into account and therefore the resulting background should be slightly overestimated. On the other hand, a slight underestimation results from assuming that no re-backscattered electrons contribute to the background.

The total number of photons produced in a ring $(\rho_a, \rho_a + \Delta\rho_a)$ by the backscattered electrons from all picture elements of the field can now be obtained by sumation for all values of ρ_o and ξ. The number of photons produced by the causative electron flux in that ring is

$$2\pi R^2 \cdot \rho_a \cdot \Delta\rho_a \cdot F(\rho_a) \cdot \beta(1) \cdot \left[1 - K(1) \right]$$

so that the relative increase in output intensity, or the SIB-index in a ring ρ_a is given by :

$$Z_B(\rho_a) = K(1) \frac{\sum\limits_{\rho_o=0}^{\rho_o=1} \sum\limits_{\xi=0}^{\xi=1} \frac{1}{M} \cdot \rho_o \cdot F(\rho_o) \cdot \beta_r(\xi) \cdot N(\xi) \cdot \Delta\xi \cdot N_a(\xi\ \rho_o\ \rho_a)}{\rho_a \cdot F(\rho_a)} \qquad (II.26)$$

The relative quantum efficiency $\beta_r(\xi)$ of the phosphor screens is given by

$$\beta_r(\xi) = \frac{\beta(\xi)\ \left[1 - K(\xi)\right]}{\beta(1)\left[1 - K(1)\right]} \qquad (II.27)$$

and is the efficiency of the screens which is actually measured at an energy ξ, divided by that at an energy $\xi = 1$ corresponding to the stage voltage. The radial thickness of the rings $\Delta\rho_o$ and $\Delta\rho_a$ were taken as equal.

Computer Program

The SIB-index associated with BSE was calculated using eqn. II.27 on the Imperial College IBM 7094 digital computer. (Appendix IV). The following values of the above parameters were used:

- stage dimensions: $R = 2$ cm $L = 9$ cm thus $P = 2.864$.
  last stage $A = 6$ cm $F = 3$ cm.
- number of loops: $n = 1, 2$ and 3.
- number of elementary rings: 10 thus $\Delta\rho_o = \Delta\rho_a = 0.1$
- number of BSE/ring/energy value: 361 with $E = 19$ and $T = 19$
- number of intermediate calculations $K = 11$
- energy distribution: with $\Delta\xi = 0.1$
  - (M) distribution measured by Meyer] Fig. II.12 A
  - (H) hypothetical distribution] Fig. II.12 A
  - (E) all electrons are elastically backscattered
- relative phosphor efficiency $\eta_r(\xi)$; $\Delta\xi = 0.1$

This was found by evaluating the variation of gain with overall applied voltage of several intensifiers. The third root of the gain is proportional to the quantum efficiency of the phosphor screens. $\eta_r(\xi)$ is shown in Fig. II.12 A as a dotted curve.

- rediffusion coefficient $K(1)$: 0.10 to 0.30.

II.4.7. Results of computations of Z_B

The first results presented in Fig. II.13, for one and two loop focusing of a single stage, are independent of the energy distribution and rediffusion coefficient. The dotted curves in these diagrams represent the fraction of BSE of initial energy ξ and originating at a distance ρ_o from the centre of the field (curves of equal

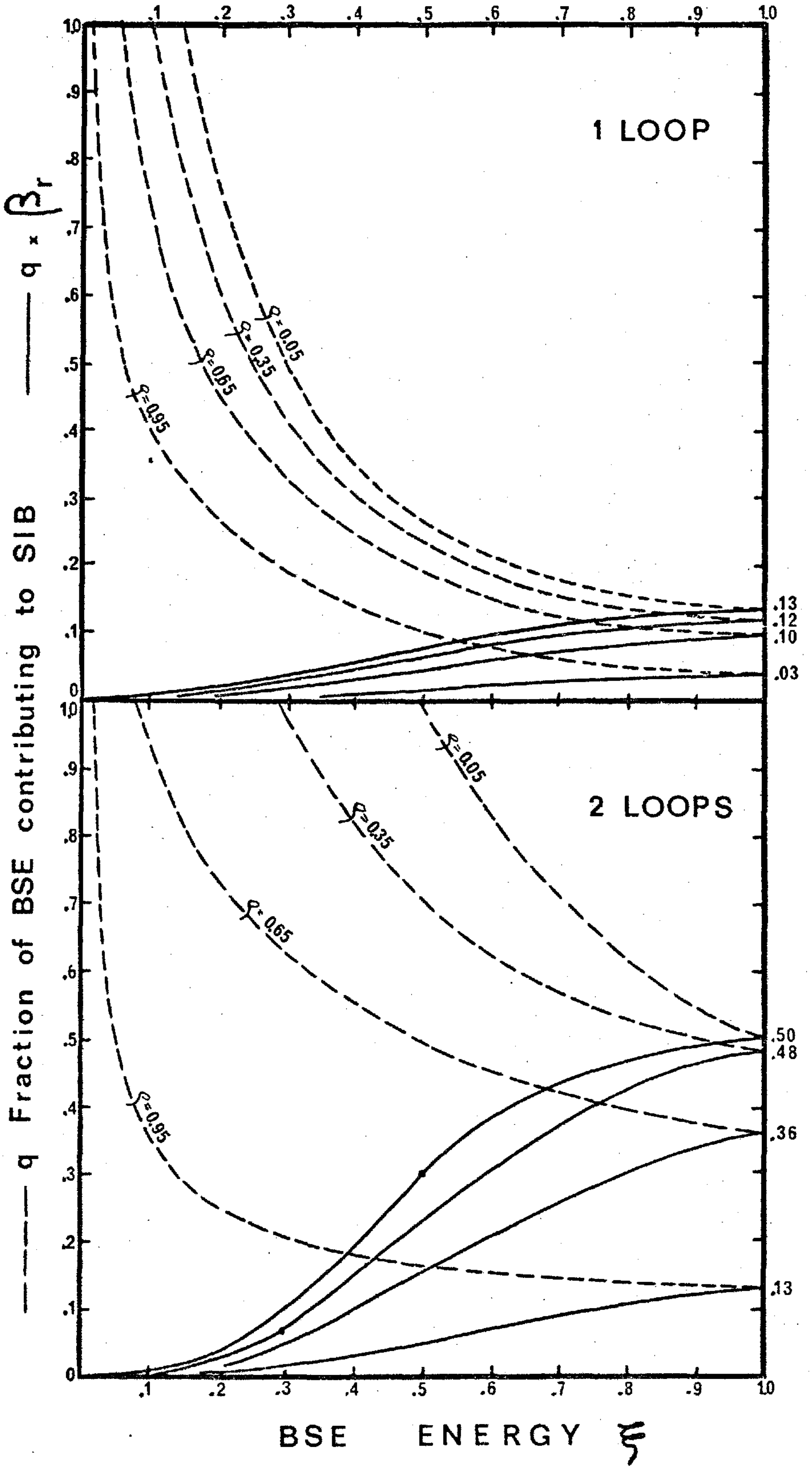

FIG II_13 COMPUTER RESULTS ONE STAGE value of $\rho_0 = 0.05$, 0.35, 0.65 and 0.95), which are able to remain in the accelerating region of the stage and thus contribute to background over the entire field. The solid curves were obtained by multiplying the above fraction by the relative quantum efficiency of the phosphor screen. They represent thus the number of photons produced on average in the field by backscattered photoelectrons (with energy ξ from a point located at ρ_0 from the centre). This number is expressed as a fraction of the number of photons that would have been produced if these incident photoelectrons had not been backscattered.

The results of the computer calculation of the SIB-index are presented in Fig. II.14 to II.16. The energy distributions are designated by "H" (hypothetical distribution), by "M" (distribution measured by Meyer) and by "E" (all BSE are elastically rediffused).

Fig. II.14 A shows the variation of the SIB-index across the field of the uniformly illuminated first stage, for two energy distributions and using 1, 2 or 3 loops focusing. The SIB intensity varies quite considerably across the working field, being maximum at the centre and nearly zero at the edge of the field. Fig. II.14 B and C give the maximum value $Z_B(o)$ and the field averaged value $\overline{Z}_B$ as a function of the rediffusion coefficient K_B. The maximum value of Z_B increases by a factor of nearly 4 when the magnetic field is increased from 1 to 2 loops focusing, while the average index $\overline{Z}$ only increases by a factor 2.9 (distribution M), a factor 3.3 (distribution H) and a factor 4.0 if all electrons were elastically backscattered.

Fig. II.15 shows an example (distribution H with $K_B = 0.20$) of how the background associated with backscattering of electrons increases when a uniform illumination of the primary photocathode is gradually intensified in the three stage of the intensifier. Thus in the case of 2 loops focusing the SIB will cause the intensity at the centre of the field to be 22% higher than the uniform intensified signal.

Fig. II.16 shows the maximum and average values of the SIB-index of a three stage intensifier, for the two types of energy distribution of BSE, as a function of

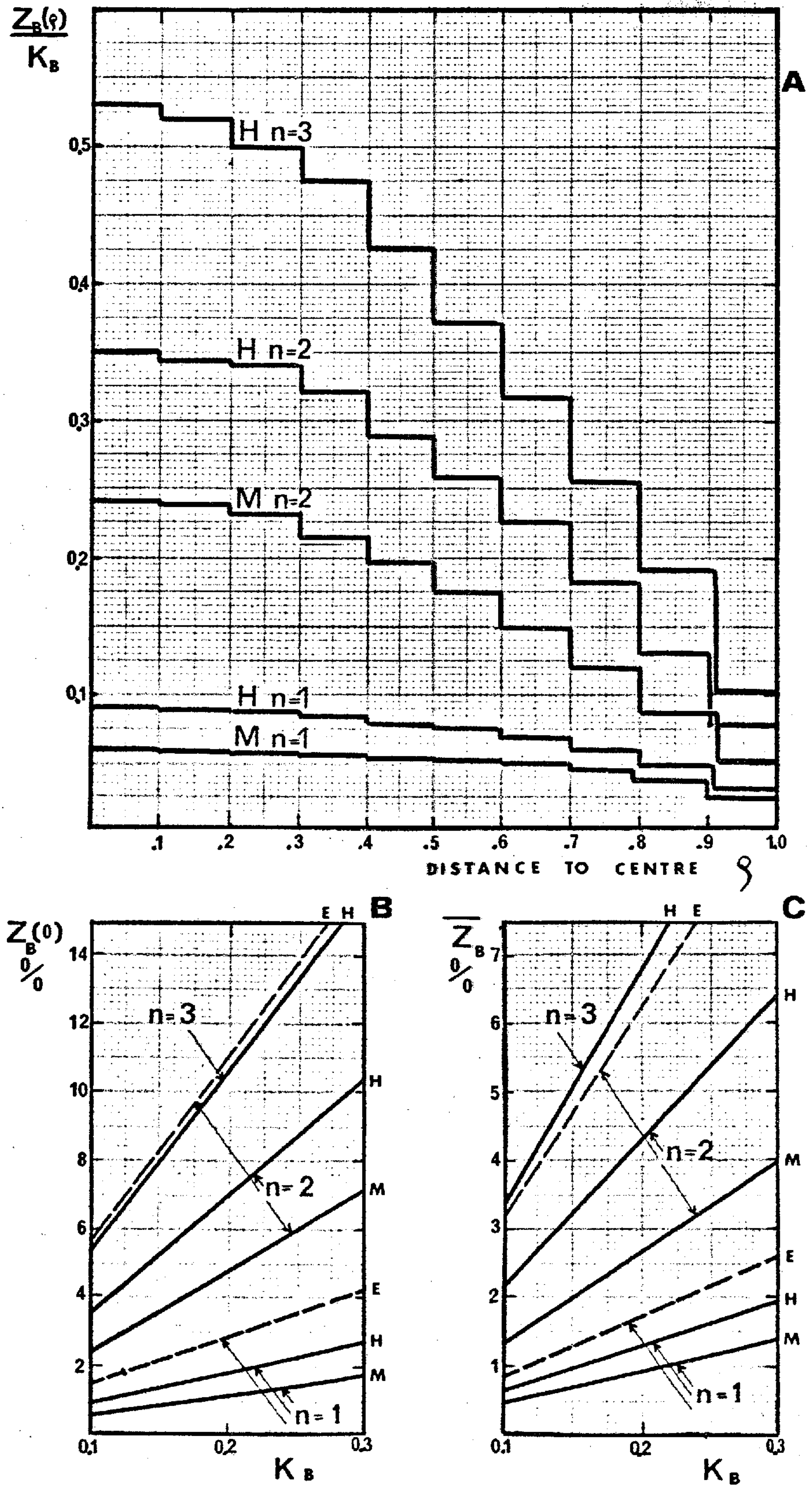

FIG II_14 COMPUTER RESULTS ONE STAGE

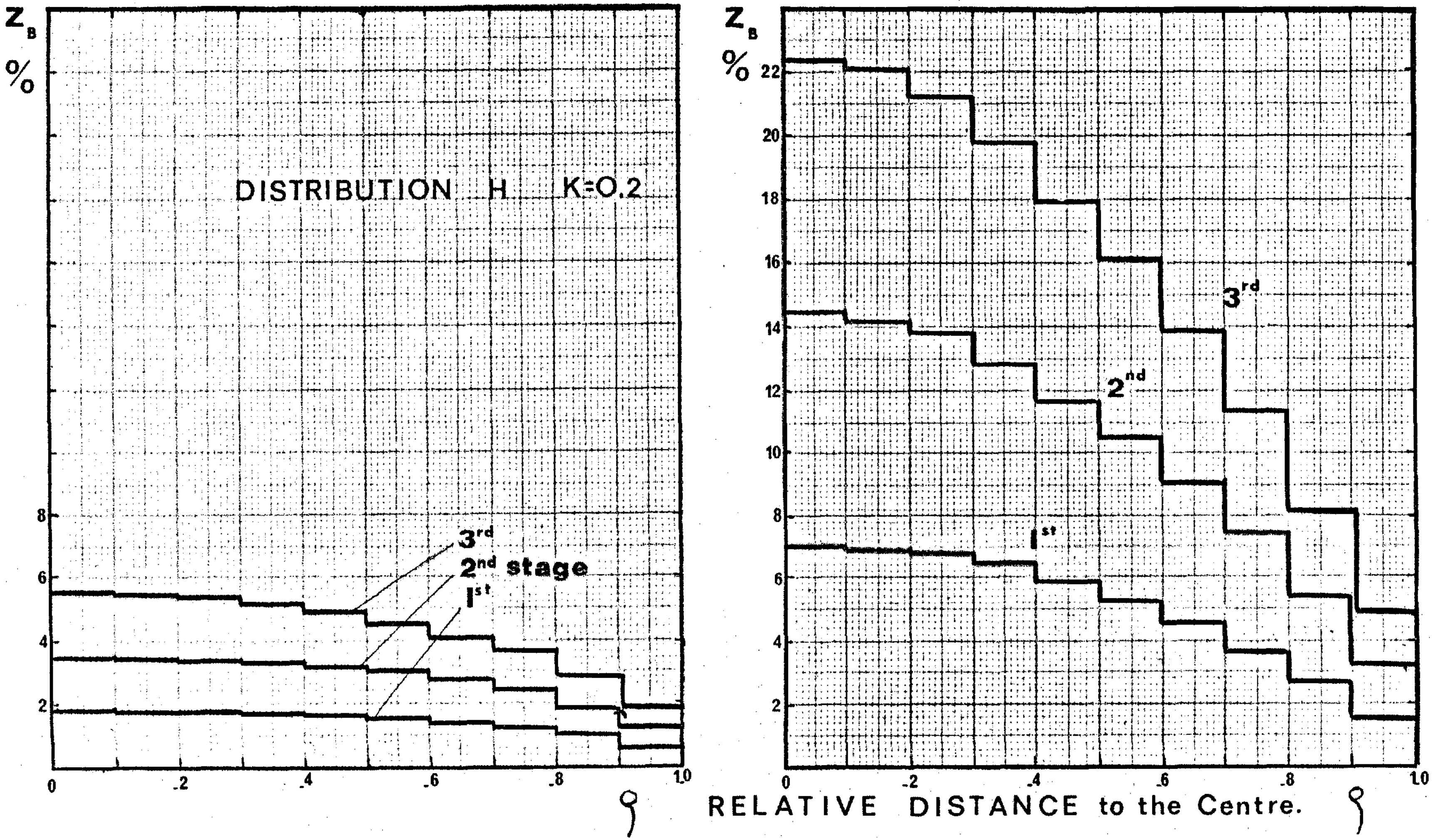

FIG II.15 BUILD-UP of SIB(BSE) in a CASCADE INTENSIFIER

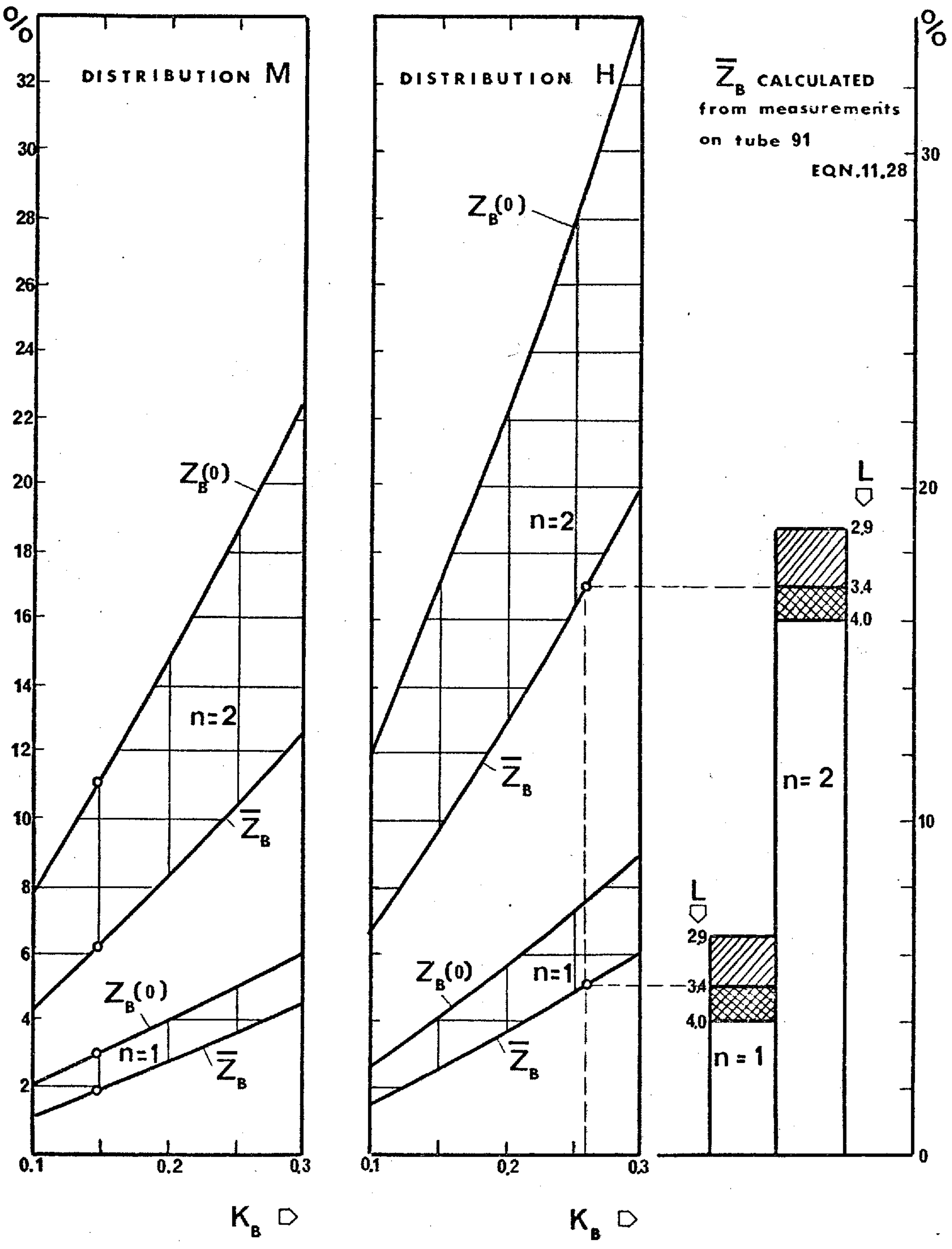

FIG 11.16 SIB-index (BES) of a 3-STAGE TUBE.

the rediffusion coefficient of the screens.

Notwithstanding the uncertainties concerning the shape of the energy distribution of the BSE, and concerning the value of the rediffusion coefficient, it can be concluded that BSE are an important source of SIB in cascade intensifiers. Indeed considering what are thought to be the most optimistic assumptions concerning the above parameters, i.e. an energy distribution and a rediffusion coefficient ($K_B = 0.15$) as measured by Meyer (1970), it can be seen that the output intensity of a uniformly illuminated three stage intensifier operated in 2 loops focusing would be on the average $\bar{Z}_B = 6\%$ higher than the true signal intensity, and $Z_B(o) = 11\%$ higher in the centre of the field. However, if the energy distribution of the BSE is similar to the suspected one (H), much higher values of the SIB-index would have to be associated with backscattering of electrons. An average increase of $\bar{Z}_B = 10$ to 16% ($K_B = 0.15$ to 0.25) and a peak increase $Z_B(o) = 16$ to 28% would occur in a three stage intensifier focused in 2 loops.

Partial confirmation of the latter estimation will be obtained in § II.5, by direct evaluation of the BSE-component from the measurements on the complete intensifier.

II.4.8. Secondary effects of BSE

A considerable fraction of the backscattered electrons impact on the metal electrodes of the intensifier. Indeed as much as 90% (60 %) of the BSE will on the average collide with the electrodes in 1 loop (2 loops) focusing of a single stage. However, the combined effect of the resulting rediffused electrons, the emitted soft X-rays (1 - 10 Å) and the desorbed positive ions will not cause an increase of more than 0.5% in the output intensity of a three stage intensifier. Indeed very few electrons, which are backscattered from the metal electrodes outside the accelerating space of the intensifier, are able to reach the phosphor screen as is the case for field emitted electrons (§ 10.3.2). Furthermore, the energy conversion efficiency for the production of soft X-rays and the numerical conversion for the production of positive ions are both very small, i.e. 1 to 4 . 10^{-4} (Compton and Allison, 1948) and 10^{-4} to 10^{-5} (§ 10.3.2) respectively.

11.4.8. Ionic Feedback

Measurements reported in § 11.1.7 of the yield of ion production by electron impact desorption from the phosphor screen indicated that on the average 1.3 to 1.9 . 10^{-4} ions were desorbed by impact of one 10 KeV photoelectron. These ions are accelerated towards the photocathode of the first and second stage along trajectories which are practically parallel to the axis of the intensifier. They will therefore produce a uniform component of SIB. Each ion will liberate 6 to 12 electrons from the cathode so that the SIB-index, associated to ionic feedback, can be estimated to be $\underline{Z} = 0.00078$ to 0.0023 % for each of the first and second stage. However, in the last stage of the intensifier this background is quite non uniformly distributed across the field as already seen in § 11.1.7. In particular about 30% of the desorbed ions from each picture element of the field concentrates in a small circle of about 2 mm diameter around the centre of the field. Therefore a local increase in output intensity of about

$$0.30\ (1.3 \text{ to } 1.9 \,.\, 10^{-4})\ (6 \text{ to } 12)\ \frac{\pi . 2^2}{\pi . 20^2} = 2 \text{ to } 6\ \%$$

can be expected at the centre of the field. This is indeed the magnitude of the local rise in output intensity above the level of signal and other sources of SIB (Fig. 11.9).

The contribution of ionic feedback to the SIB of the complete intensifier can thus be estimated to be 0.2 to 0.7% (eqn. 11.15).

11.5 SYNTHESIS OF MEASUREMENTS AND CALCULATIONS

It was seen in § 11.4.7. that the average SIB-index associated to BSE can be expected to increase by a factor 2.9 to 4.0 as the magnetic field is increased from 1 to 2 loops focusing. No other source of background is significantly affected by such a change, so that it is possible to separate the average SIB-index measured on a complete intensifier ($\overline{Z_{T1}}$ in one loop and $\overline{Z_{T2}}$ in two loops focusing) into a component associated to BSE ($\overline{Z_{B1}}$ in one loop and $\overline{Z_{B2}}$ in two loops focusing) and into a component which does not depend on the magnetic focusing condition ($\overline{Z_c}$). The latter component represents the total contribution of all sources of background except BSE. It is possible to estimate these components by successive calculation of: (eqn. 11.15) (§ 11.4.7)

$$\overline{Z_c} = \frac{\ell\,\overline{Z_{T1}} - \overline{Z_{T2}}}{\ell - 1} \; ; \quad \overline{Z_{B1}} = \frac{\overline{Z_{T1}} - \overline{Z_c}}{1 + \overline{Z_c}} \quad \text{and} \quad \overline{Z_{B2}} = \ell\,\overline{Z_{B1}} \qquad (11.28)$$

ℓ is the ratio of the SIB produced in 2 loops to that produced in 1 loop

where ℓ ranges from 2.9 to 4.0. With $\overline{Z_{T1}} = 22\%$ and $\overline{Z_{T2}} = 36\%$ as measured in § 11.3 for the intensifier (91) one finds the value of the three components

$$\overline{Z_c} = 14.5 \text{ to } 17.3\% \; ; \quad \overline{Z_{B1}} = 6.5 \text{ to } 4.0\% \quad \text{and} \quad \overline{Z_{B2}} = 18.8 \text{ to } 16.0\%$$

These results are compared in Fig. 11.16 with those obtained by computer evaluation of the average SIB-index associated to BSE. It can be seen that for the ratio $\ell = 3.4$, which would correspond to the hypothetical energy distribution, agreement is obtained for a rediffusion coefficient slightly higher than 25%. However, since a lower rediffusion coefficient can be expected for the screens used in the intensifier (§ 11.4.5), the agreement could only be reached if the actual energy distribution of BSE had a higher average energy than that of the hypothetical distribution.* In other words the hypothetical distribution used

---

* It can be calculated that agreement would be reached for $K_B = 15\%$, if all BSE were elastically rediffused ($\ell = 4$).

in the computer calculations, leads to a slightly optimistic assessment of the SIB associated to BSE. The probable range of the values for the factor ℓ would therefore be restricted to 3.4 to 4.0.

The various results for the average SIB-indices of the sources of background are given in Fig. II.17. The most important contribution, besides that of backscattering of electrons, are light scattering in the output phosphor windows and optical feedback. The latter component, shown in this diagram for a blue light gain of $8 \cdot 10^4$ (intensifier 91), becomes comparable to the contribution of the output windows for an intensifier with BLG of $3 \cdot 10^5$.

The total average SIB-index of all contributions except BSE was calculated by summation of the individual components (eqn. II.15), and is compared in Fig. II.17 with the value $\bar{Z}_c$ obtained above from the measurements on the intensifier (91). It can be seen that using the restricted range for the values of ℓ (3.4 to 4.0) the total contribution $\bar{Z}_c$ is slightly higher than the average component obtained from the summation of the individual components. This could be the consequence of the effect of non-uniformities in the sensitivities of the photocathodes on the measured SIB-index of the intensifier. Furthermore, the existence of an as yet undetected background component can not be ruled out.

It can be concluded that the results shown in Fig. II.17 represent a fairly good estimation of the contribution of the various sources of background in the cascade intensifier.

II.6 CONCLUSIONS

Signal induced background causes loss of contrast in extended images and reductions of resolution which are dependent on the image content. It furthermore affects the photometric capability of the intensifier, especially if the incident image contains a large range of light intensities.

A major contribution to background was found to be the backscattering

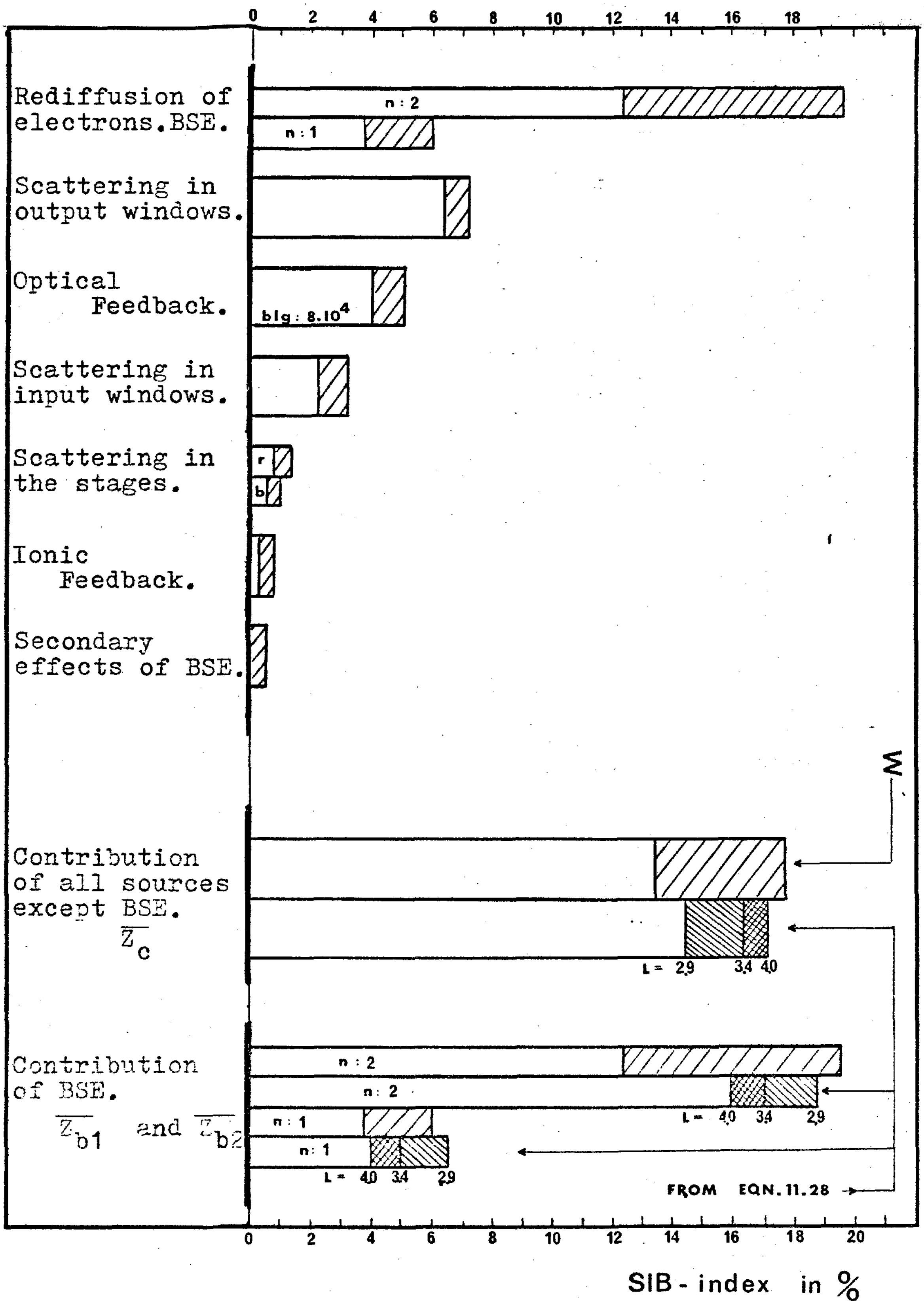

FIG 11.17 RELATIVE CONTRIBUTIONS TO SIB

of electrons from the phosphor screens. Little can be done to reduce this component until accurate measurements of the rediffusion coefficient and the energy distribution of the backscattered electrons are made. It might be possible then to understand which materials in the screen cause the rediffusion of electrons with the suspected low losses in energy.

The effect of scattering of light in the end-window of the intensifier could be reduced by depositing the output phosphor screen either on a very thick end-window of the vacuum envelope, such that all internally reflected light falls outside the picture area*, or on a very thin membrane, such that the reflected light falls in close proximity to each causative picture element.

Scattering of light in the photocathode windows can be reduced by evaporating the photocathode on the front window of the vacuum envelope. However, this would not be compatible with transfer techniques, which are known to reduce the occurence of spurious background.

Optical feedback would be eliminated by the production of a backing which is opaque to light generated in the phosphor. However, it is believed that the actual method of deposition of the backing (§ 5.1.6) can probably not be optimized in that respect. Indeed the phosphor grains tend to puncture the organic film onto which the aluminium backing is evaporated (Airey, 1970). Additional pinholes and cracks are probably caused during the removal of the organic film by baking. Optical feedback is the only contribution to background which increases significantly with the gain of the intensifier. It might therefore become a major component if very high gain (better than $3 \cdot 10^5$) could be achieved.

Light scattering within the stages was found to be a small component of the total signal induced background. Absence of blackening of the metalic internal

---

*such a technique is used in CRT.

surfaces could lead to a significant wavelength dependent contribution to the signal induced background.

The two spurious images observable in the I.C. cascade intensifier are characteristic of this tube, since they are both caused by the electron optics in the last stage.

CHAPTER 12

APPLICATIONS

The equivalent quantum efficiency of the cascade intensifier system may be at most 100 times higher than that of photographic emulsions, depending on the method used to retrieve the recorded information (§ 7.4.4). This improvement could be used to shorten the exposure time required to obtain a given signal to noise ratio or to improve the signal to noise ratio for a given exposure time. Alternatively it would permit observations to be performed using slower and less expensive input optical systems and at very low light levels where direct photography may be limited by failure of the reciprocity law. The storage capacity of the system may be improved by the use of fine grain emulsion or by magnetic scanning of the electron image (§ 6.1.5). The limiting resolution of the cascade intensifier system, (including lens and plate) i.e.: 35 to 45 lp/mm (§ 8.6), is only slightly lower than that of common fast emulsions. The use of a fine grain emulsion to record the intensified image may improve the limiting resolution to about 50 lp/mm and allow probably more information to be recorded. The geometry of the output image is sufficiently faithful for most practical applications (§ 9.2) but corrections may be required if very accurate positioning of features in the image is needed. The incidence of spurious background should be analyzed for every application in particular (§ 10.2 and § 11.3.4). These spurious effects will limit the detection of low contrast images and may compromise the photometric capability of the intensifier.

The intensified image can alternatively be directly observed on the output screen or transfered to a television system. The latter would permit the enhancement of contrast and the use of data processing and photon counting techniques.

The compactness, reasonable weight (about 20 kg) and flexibility of use of the equipment should make its incorporation possible in many systems where it may be required.

12.1 GENERAL APPLICATIONS

Although, in astronomy, the cascade intensifier does not compete with electronography (§ 2.1) for the detection of faint stars under sky background limited conditions, it could nevertheless be used successfully in several instances. The high speed of the system as compared to direct photography would permit the rapid detection of high contrast sources and extended objects (Cromwell, 1969), spectroscopic work at high dispersion (Livingston, 1966; Varma, 1968), the study of emission objects through very narrow band interference filters (Ford, 1966), the observation of spectra or objects which vary in time (Powell, 1969), and, quite important, the use of moderate size telescopes for observations which, hereto, could only be carried out on large telescopes. The use of a cascade intensifier for visual observation of star fields would facilitate the tracking of faint stars with a telescope.

Cascade intensifiers are further applicable in many fields of experimental sciences, where normal techniques are limited by low photon fluxes. Examples of applications, where cascade intensifiers have been used are: field-ion microscopy for studies in crystallography and metallurgy (Whitmell, 1966; Cranstoun, 1969), the photography of spark and streamers chambers (Jones, L. 1966) and the detection of Cherenkov photons (Giese, 1969) in nuclear physics, the study of bioluminescent phenomena (Reynolds, 1964), and Raman spectroscopy (An I.C. cascade image intensifier system is actually used for that purpose by Professor Long at Bradford University.

Image intensification has found very valuable applications in the medical sciences. Specially designed X-ray image intensifier systems have been available for a number of years and permit the reduction of the radiation dosage to the patient and at the same time provide the radiologist with a bright image which can be viewed without dark adaption (Combee, 1971). Furthermore, cine-radiography has made it possible to study internal body motion (Tolan, 1958) while telefluoroscopy permits contrast enhancement and magnetic tape recording of the radiograms. Cascade intensifiers have been used in conjunction with X-ray equipment (Catchpole, 1962, 1963) and with medical scintillation cameras (Wilks, 1967).

A more specific medical application of the cascade intensifier, which has been of considerable interest to the author, is discussed in the following section.

12.2 RETINAL CINE ANGIOGRAPHY

This project was initiated by Professor C.T. Dollery and his team at the Royal Postgraduate Medical School (Hammersmith) for the purpose of observing the blood circulation in the retina of the human eye. Study of the blood circulation in the retina, which is the only part of the human body where living blood vessels can be observed without surgery, is important for the diagnosis and understanding of many systemic vascular diseases such as hypertension and diabetes (Dollery et. al. 1962; Kohner et. al. 1968).

The normal technique of retinal angiography consists in injecting fluorescein in the blood stream and in projecting an intense flash of blue light on the retina through the pupil, or order to excite the fluorescein present in the vessels. The emitted green light is separated from the scattered blue light with a suitable filter, and an image of the fundus is formed by a retinal camera onto a photographic emulsion. This technique is limited on humans to a single exposure because the retina can only be exposed to the required intense illumination for a very short time, without discomfort for the patient or even retinal damage. The only result that can be obtained with such a technique is thus a complete map of retinal vessels after they are completely filled with fluorescein.

However, of particular interest is to study how rapidly the vessels are filled by the fluorescein or to measure the actual blood flow. Indeed, this gives a qualitative assessment of the circulation changes associated with a vascular disease, or with the treatment of a disease. Cine photography will allow the measurements of the speed of advance of the dye front in the vessels by frame to frame analysis. The average intensity of the light source, which provides the blue excitation of the fluorescein, must be reduced by a factor of 300 to 500 for studies on humans. The use of a cascade intensifier system lends itself quite well to the purpose of increasing the brightness of the fluorescence image to permit its recording on cine-film.

A first version of the instrument which permits cine angiography was developed at Hammersmith Hospital in close collaboration with workers of the Applied Physics Section and is described by Powell (1967) and Bulpitt et. al. (1970). The first clinical tests were promising, but the equipment proved to be very difficult to use, and unsatisfactory resolution and geometry in the recorded image were often a limiting factor to the analysis of the results. The author has been responsible for modification and improvements of the equipment*, including the incorporation of a new light-weight and magnetically shielded solenoid (Tab. 6.3) and the design of a moving-mirror system which has greatly facilitated the use of the equipment.

12.2.1. Description of the equipment

Fig. 12.1 shows a photograph and a schematic drawing of the modified equipment. The equipment is mounted vertically above the head of the patient, who is lying on a couch. Independent vertical movements of the different

---

*The mechanical modifications were made by Mr. J.N. Beckwith in the Applied Physics Workshop of Imperial College parts of the instrument and some lateral movement are made possible by a suitable system of coaxial guides, pulleys and contraweights.

A Zeiss Fundus Camera (I) is mounted above the eye of the patient (1). The illumination of the retina is provided by a viewing lamp (2) for the observation and focusing of the system, and by a Xenon-arc lamp (3) which is pulsed during the actual filming of the fluorescein pattern. A blue filter (4) (§ 12.2.2), which transmits the required exciting light, is inserted automatically in the light path when filming is started. The light sources are imaged by an aspherical lens (5) in the centre of the dilated pupil of the patient by horizontal adjustment of the fundus camera. The retina is thereby illuminated and an image of the retina is formed in the focal plane of the same aspheric lens. This intermediate image is then reproduced by a photographic objective (6) onto a fine cross-hair (7) after deflection by a 45° hinged mirror (8). The observer, looking through the observation eyepiece (9), adjusts the fundus image to a sharp focus by vertical adjustment of the entire top part of the instrument (mirror box + intensifier + camera) while the Zeiss camera is locked in position. The other side of the hinged mirror, which is made of a thin glass plate ($^1/_{10}$ mm thick), is also aluminized. This permits the projection of a small resolution pattern (10) onto the photocathode (12) of the intensifier. (III). The green filter (11) (§ 12.2.2), which separates the fluorescent light from the blue scattered light, is mounted permanently in front of the intensifier. The distance between the centre of mirror and the cross-hair is adjusted beforehand to equal the optical distance between the centre of the mirror and the photocathode of the cascade intensifier, so that the fundus image is in focus on the photocathode after the mirror is moved out of the path of the light beam. The image has a diameter of 22 mm on the photocathode which corresponds with a field of 30° on the retina (as seen from the pupil). The moving mirror assembly (II) has greatly facilitated the use of the instrument because it permits simultaneous focusing of the fundus image on the cross-hair

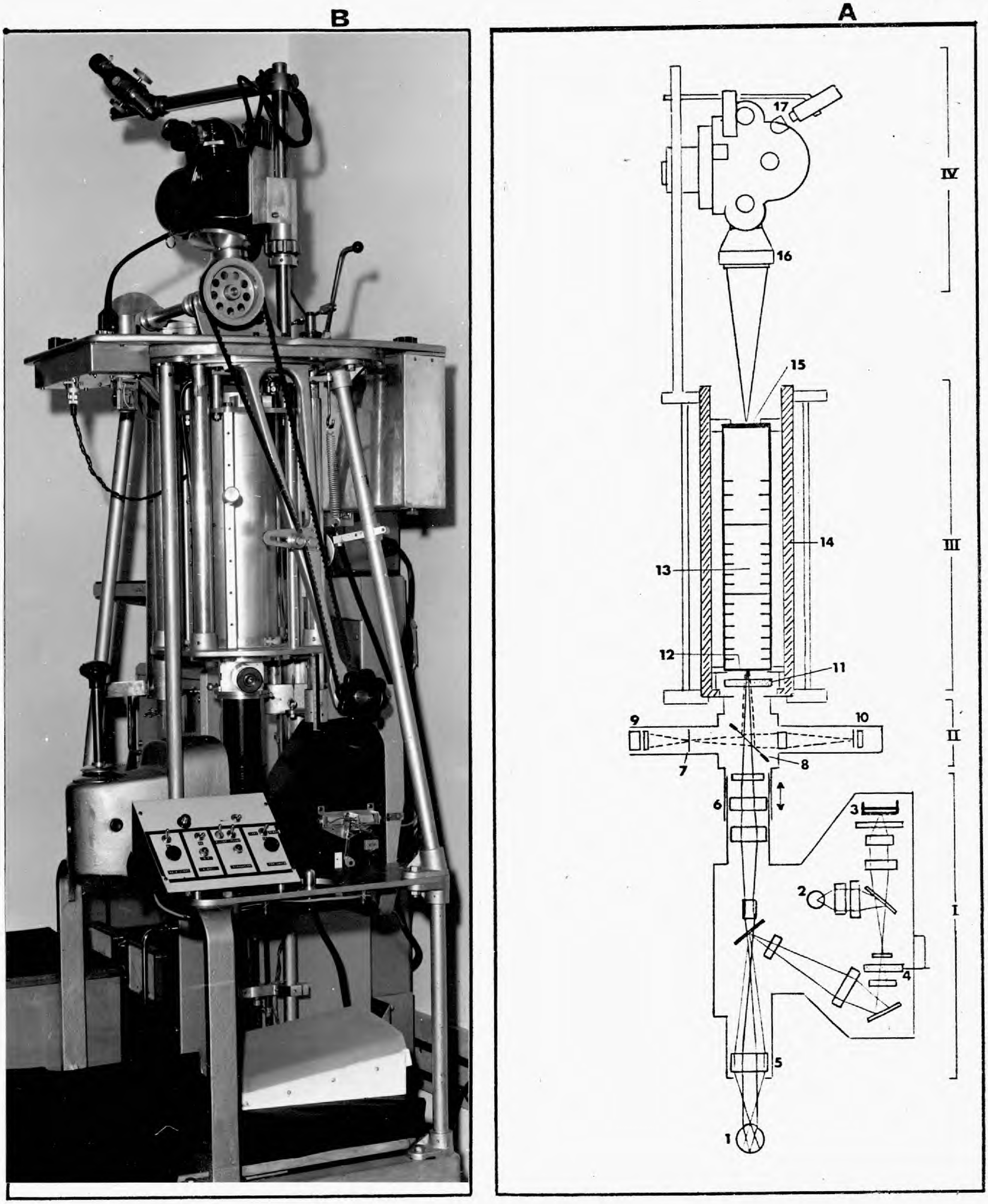

FIG 12.1 RETINAL CINE ANGIOGRAPHY

and fine adjustment of the intensifier focus by an assistant operator. Micro-switches, operated by the movement of the mirror, causes the insertion of the blue filter (4) and sets the cine camera in motion. The latter, an Arriflex 16 mm professional camera, is mounted on top of the instrument by means of an adjustable screw thread and locking system. The intensified image on the output phosphor screen (15) is transfered to the film by means of a Wray f/2 lens (16), designed to work with a demagnification of 3 : 1. Sharp focus is obtained by means of a low power (x 30) microscope focused on the cross-hair of the viewing system of the cine camera (17). The latter, operated electrically, triggers the power supply* of the Xenon-arc lamp in synchronism with the aperture of the camera shutter. The controls of the system are centralized on two panels located conveniently to the hands of the observer and the assistant operator.

12.2.2. Laboratory Evaluation

Several experiments were performed to evaluate and optimize the performance of the system.

The success of the technique depends partially on the correct choice of the two optical filters. Fluorescein, when dissolved in blood, has a peak absorption in the 4700 - 4900 Å wavelength region. The peak of the emission band (fluorescence) occurs at about 5250 Å but this band extends from 5100 to 5400 Å (Novotny et. al. 1961; Dollery, 1970). The closeness of the two peaks makes it difficult to find a set of filters sufficiently selective so that the photocathode does not receive the large amount of blue excitation light reflected from the optical surfaces in the Zeiss Camera, the cornea, the edge of the pupil and especially from the retina. This optical leak between the two filters would cause background in the fluorescent image and therefore reduce the contrast.

---

* designed by Mr. E. Eamons, Hammersmith Hospital.

Several combinations of commercially available filters were tried in the past and have been investigated by the author. The combination Baird Atomic B5 (blue) - Zeiss 300976 (green-yellow) was found to give the best results. The blue filter has an average transmission of 70.3% in the 4700 - 4900 Å region, while the green filter transmits an average of 82.5% in the 5150 - 5350 Å region. Maximum transmission for the two filters in juxtaposition is about 0.3% at 4940 Å. This combination is superior to the combination Baird Atomic B5 - Ilford 109, which was used in the past, having an average transmission of 70.3% in the blue region, 81.4% in the green region but a maximum leak transmission of 1.5% at 4880 Å. It should be noted that the sensitivity of the SII photocathode is about 1.25 times more sensitive for the leakage light than for the signal. It is thought that further improvement could be obtained by specially designed interference filters.

Several types of 16 mm cine films were analyzed from the point of view of limiting resolution, speed and contrast characteristics. The Ilford Mk V film was found to be superior to Ilford HPS, Kodak Tri-X and Plus-X for this specific application. The development procedure of the cine-film was adjusted to obtain optimum contrast and fog.

Measurements of the limiting resolution of the complete system indicated that about 55 lp/mm could be resolved in the plane of the retina. This would correspond to a detail of 18 microns on the retina (100% contrast). The arterioles and veins of the optic disc of the eye are about 120 to 150 microns in diameter and their smallest visible branches about 20 microns. However the contrast of these vessels against the background will not be very high, so that some loss of image detail can be expected.

The geometry of the image of the retina on film was found to be excellent. This is important if accurate measurements of the blood flow are required.

12.2.3. Clinical Evaluation

Cine angiography has up to now been performed on 14 patients with the modified equipment. The fluorescein is either injected in a vein in the arm of the patient (veinous injection) or through a catheter which terminates in the heart of the patient (arterial injection). The latter method used on 8 patients gives excellent results because the fluorescein has little chance to diffuse in the blood before it reaches the eye. A print of the initial frames of the cine-film taken using an arterial injection is shown in Fig. 12.2. The dye front can easily be seen, progressing in the arteries of the retina. The time between two frames is about $^1/_{50}$ sec. The background is caused principally by the fluorescence in the choroid, which is located underneath the blood vessels of the retina and which is filled by the fluorescein prior to the retinal arteries. This is of course a fundamental source of background which will limit the contrast in the initial frames. This background is further increased by the leakage between the two optical filters, by the signal induced background in the intensifier and the scattering of light in the optical systems. Examination of the results shows that the smallest detectable vessel of the retina is 50 to 70 microns in diameter, for a contrast of 25 to 50%. The results of arterial injection are very promising and a medical research program has been undertaken using the equipment.

Veinous injection (6 patients), which requires less time, skill and discomfort for the patient, is not as satisfactory as arterial injection. The dye front was only recorded on film with sufficient clarity for two patients. The high dilution of the fluorescein after its passage through the heart and the background caused by the choroid are certainly the major causes for the low contrast in the recorded films. However, it is possible that further improvements in the optical filters, reduction of light scattering in the optical systems and of signal induced background in the intensifier, and improvement of the contrast characteristic of the cine film might make the use of this instrument more successful with veinous

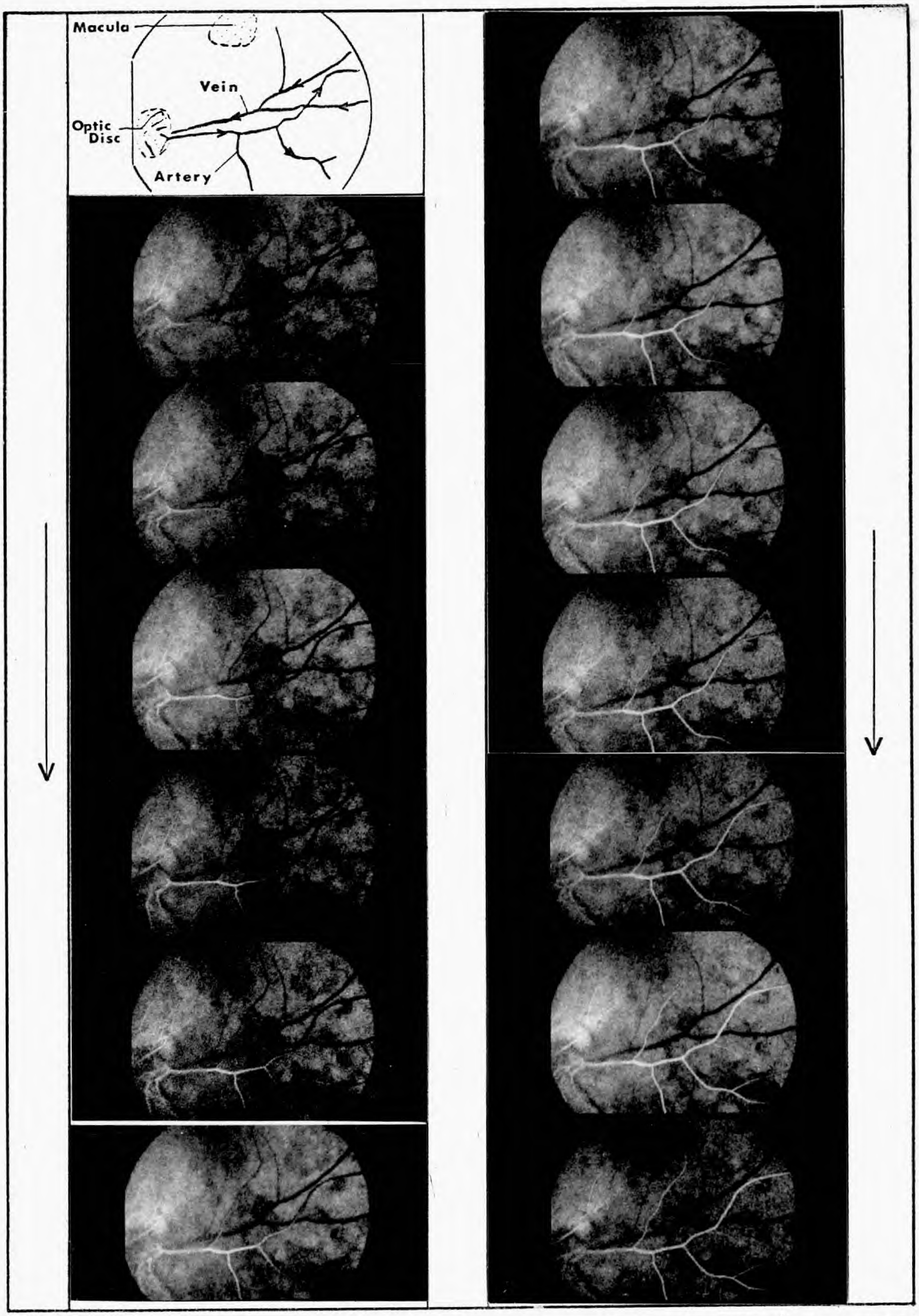

FIG 12.2 ANGIOGRAM . (Arterial injection)

injection. Contrast enhancement could be achieved by the use of a television system coupled to the output of the intensifier. This would furthermore permit the recording of the angiograms onto magnetic tape, and their analysis by digital computer techniques.

This instrument, or any further improved version, could become a powerful tool for diagnosis in routine work and for further study of systemic vascular diseases.

CHAPTER 13

GENERAL CONCLUSIONS

While the relatively modest sensitivities (40 – 55 μA/Lm) of the S11 photocathodes have prevented the achievement of very high light gains, considerable improvements can be expected as more control of processing techniques and especially stability of the cathodes is gained. The highest blue light gains obtained during the present investigation were 1 to 2 . 10^5 at an overall potential of 40 KV. However, the internal electron multiplication corresponding to these gains should permit the recording of about 70% (recording efficiency) of the primary photoelectrons with a sufficient degree of certainty on the photographic plate, even if a rather slow f/5.6 lens is used to couple the intensifier to the emulsion. The gain of the intensifier was furthermore found to be constant within 6% over seven decades of incident illumination intensities. The response of the intensifier to a sinusoidally varying input illumination was calculated to fall to 70% (-3dB) of the low frequency peak to peak output intensity at about 430 cycles per second.

The equivalent quantum efficiency at zero spatial frequency was found to be 62 ± 5% of the quantum efficiency of the primary photocathode, if information retrieval by photographic grain counting is performed. A slightly lower value can be expected if densitometry is used to analyze the recorded information.

The modulation transfer function on axis was measured on one intensifier to be 50% at 18.5 cycles per mm. and 5% at 53 cycles per mm. This corresponds with the limiting resolutions of 48 to 55 line pairs per mm. observed off axis on all intensifiers. This resolution, which is maintained over the working field up to a distance of 10 mm. from the centre of the output screen, decreases to about 25 - 30 line pairs per mm. at the edge of the field. The modulation transfer function of the complete intensifier system, including coupling lens and emulsion, is about 50% at 15 cycles per mm. and 5% at 33 to 43 cycles per mm., depending on the coupling lens and emulsion used. The geometry in the intensified image is satisfactory for most practical applications. The radial displacement at 16 mm. from the centre of the field is typically about 5% of the distance to the centre of the field (Pincushion distortion) while the tangential displacement is small and typically about 1% of the distance to the centre of the field (S-distortion).

The spurious instrument background, which limits the detection of faint objects on an image background, was found to correspond at room temperature to an incident illumination producing at most 500 photoelectrons per square cm. per second from the primary photocathode (about 2.10^{-10} lumens per square cm. or 2.10^{-15} Watts per square cm. at a wavelength of 4300 Å.) The signal induced background affects the photometric capability of the intensifier and causes a loss of contrast in extended images. A detailed analysis of this phenomenon indicated that backscattering of signal electrons, light scattering in the output and input windows of the intensifier and optical feedback are the major contributions to signal induced background. It was found that when the primary photocathode is uniformly illuminated, the output intensity in the centre of the field is raised above the level of the intensified signal by as much as 38 and 60% in 1 and 2 loops focusing respectively. Field averaged values of this rise were found to be 22 and 36% in 1 and 2 loops focusing.

Higher equivalent quantum efficiencies and light gains would undoubtedly be achieved by the use of multi-alkali photocathodes. This should improve the use of the system in the visible range and eventually extend it to the near infra-red. The introduction of externally processed cathodes would permit the use of different preselected cathodes and would lower the instrument background of the intensifier because of the absence of contamination of the internal surfaces by alkali vapour. Furthermore, the absence of processing compartment will reduce the total length of the tube and lower the image rotation.

Amelioration of the characteristics of the phosphor screens and the phosphor-photocathode sandwitches is probably the most challenging problem associated with cascade intensifiers. The effective efficiency of the phosphor screens could be increased by the use of a more reflective aluminium backing, but this would impair the limiting resolution of the screens which are already the major limiting factor for the overall resolution of the intensifier. Similarly, the number of imperfections and pinholes in the aluminium backing, which cause signal induced background by optical feedbadk, may be decreased by the use of a thicker backing and a more viscous filming solution, again at the expense of resolution and effective efficiency. An analysis of the problem of "optical contact" of the phosphor grains with the glass or mica substrates indicated that an eventual decrease of the optical contact of the grains would lead to an improvement of the limiting resolution associated with the mica coupling, to a more peaked angular intensity distribution of the light emerging from the end-window of the intensifier and thus to a higher transfer efficiency of the coupling lens, and to a decrease of the signal induced background component associated with scattering of light in the output phosphor window. Furthermore, a reduction of the backscattering of signal electrons from the phosphor screens would improve the effective efficiency of the screens, reduce the loss in recording efficiency of photoelectrons and lower the signal induced background of the intensifier. Considerable improvements in screen resolutions would be obtained by the development of non-granular, evaporated phosphor screens. Such screens, deposited on thin aluminium oxyde films, may lead to limiting resolutions of 90 - 120 line pairs per mm. for complete three stage intensifiers.

Improvements in the construction of the intensifier, leading to more uniform electric fields, should make it possible to operate the intensifier in single loop focusing of the electron images in the three stages, without deterioration in the quality of image geometry and resolution. This would not only reduce the signal induced background component associated to back-scattered electrons, but also decrease the power consumption, size and cooling requirements of the focusing solenoid.

It is hoped that further developments in the manufacturing and processing techniques, and increased research into the many remaining problems associated with the operation of cascade intensifiers, will further improve their performance and increase their success in many practical applications.

APPENDICES

APPENDIX I: RELATIVE FLUCTUATIONS IN A MULTISTAGE INTENSIFIER SYSTEM.

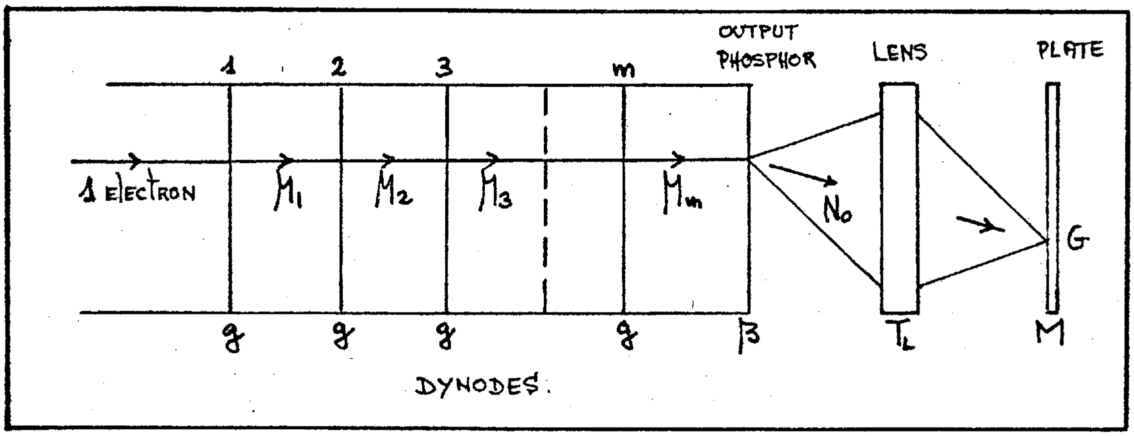

Symbols g dynode gain; $\mathcal{M}_i$ number of electrons leaving the ith dynode; m number of dynodes; β quantum efficiency of output phosphor; T_L transfer efficiency of the coupling lens; M quantum efficiency of the emulsion; G number of developable grains.

The mean square deviations in the different processes are given by:

$$\overline{\Delta^2 g}$$

$$\overline{\Delta^2 \beta} = k\bar{\beta} \qquad \text{quasi Poisson statistics } (k \approx 1)$$

$$\left.\begin{aligned} \overline{\Delta^2 T_L} &= \bar{T}_L \left(1 - \bar{T}_L\right) \\ \overline{\Delta^2 M} &= \bar{M}\left(1 - \bar{M}\right) \end{aligned}\right] \qquad \text{"go-not-go" processes.}$$

Consecutive use of eqn. 1.9, which permits the calculation of the mean value and the mean square deviation of the output of each interaction, gives:

-- for the first dynode

$$\begin{aligned} \bar{\mathcal{M}}_1 &= \bar{g} \\ \overline{\Delta^2 \mathcal{M}_1} &= \overline{\Delta^2 g} \end{aligned} \qquad \text{(a)}$$

-- for the second dynode

$$\overline{M}_2 = \overline{g}^2$$

$$\overline{\Delta^2 M_2} = \overline{\Delta^2 g}\left(\overline{g}^2 + \overline{g}\right) \qquad \text{(b)}$$

-- ....

-- for the m th dynode

$$\overline{M}_m = \overline{g}^m$$

$$\overline{\Delta^2 M_m} = \overline{\Delta^2 g}\left[\overline{g}^{m-1} + \overline{g}^{m-2} + \ldots\ldots + \overline{g}^2 + 1\right] \qquad \text{(c)}$$

$$\overline{\Delta^2 M_m} = \overline{\Delta^2 g}\ \overline{g}^{m-1}\ \frac{1-\overline{g}^m}{1-\overline{g}}$$

-- for the photons leaving the output screen

$$\overline{N_o} = \overline{\beta}\ \overline{g}^m$$

$$\overline{\Delta^2 N_o} = \overline{\beta}^2\ \overline{\Delta^2 g}\ \overline{g}^{m-1}\ \frac{1-\overline{g}^m}{1-\overline{g}} + \overline{g}^m k\ \overline{\beta} \qquad \text{(d)}$$

-- for the number of developable grains

$$\overline{G} = \overline{T}_L \,.\, \overline{M} \,.\, \overline{N}_o$$

$$\overline{\Delta^2 G} = \overline{T}_L^2\ \overline{M}^2\ \overline{\Delta^2 N_o} + \overline{N}_o\,\overline{T}_L\,\overline{M}\left(1-\overline{T}\,\overline{M}\right) \qquad \text{(e)}$$

Substitution of eqn. (d) in eqn. (e) gives

$$\frac{\overline{\Delta^2 G}}{\overline{G}^2} = \frac{\overline{T}_L^2\,\overline{M}^2\left[\overline{\beta}^2\,\overline{\Delta^2 g}\ \overline{g}^{m-1}\frac{1-\overline{g}^m}{1-\overline{g}} + \overline{g}^m k\,\overline{\beta}\right] + \overline{\beta}\,\overline{g}^m\,\overline{T}\,\overline{M}\left(1-\overline{T}\,\overline{M}\right)}{\overline{T}^2\,\overline{M}^2\,\overline{\beta}^2\,\overline{g}^{2m}} \qquad \text{(f)}$$

The relative fluctuations in the number of developable grains is given, after simplification of eqn. (f), by

$$\frac{\overline{\Delta^2 G}}{\overline{G}^2} = \overline{\Delta^2 g}\,\frac{1-\bar{g}^{-m}}{\bar{g}(\bar{g}-1)} + \frac{k}{\bar{\beta}\bar{g}^m} + \frac{1-\bar{T}.\bar{M}}{\bar{T}.\bar{M}.\bar{\beta}.\bar{g}^m} \qquad (2.4)$$

APPENDIX II : COMPUTER PROGRAM FOR THE CALCULATION OF THE MODULATION TRANSFER FUNCTION

The following computer program permits the calculation of the Fourier transform of a line spread function. The language used is Fortran IV and the computations were made on the IBM 7094 installation at Imperial College.

```
      DIMENSION   YGRMM(1001)
      NOFY  =  55
      RNOFY   =   NOFY
      READ(5,1001) (  YGRMM(N),    N   =   1,NOFY )
 1001 FORMAT   (  F5.1  )
      HGRMM  =  10.0
      XSCALE  =  20000.0
      TLOPMM   =    HGRMM*  (RNOFY-1.0)/XSCALE
      HNREFL  =  (RNOFY  -  1.0)/2.0
      CYREFL   =    HNREFL/TLOPMM
      CYSTEP  =  10.0
      NOFSTP   =     (CYREFL/CYSTEP)   +   6.0
      NOFSTP  =  60
      AGRMM  = -  270.0
      AOPMM     =     AGRMM/XSCALE
      HOPMM    =    TLOPMM/(RNOFY  -  1.0  )
      PIE   =    3.141592653
      YSCALE   =    1.0
      YSQMM  =  120.0
      FCNIP    =    YSQMM  *  YSCALE
      WDSQMM  =  0.0
      WDIPMM    =    WDSQMM/XSCALE
      DO  101  M  =  1,NOFSTP
      RM  =  M
      CPMM  =  CYSTEP*(RM-1.0)
      OMEGA  =  2.0*PIE*CPMM
      C   =   0.0
      S   =   0.0
      DO  102  N  =  1,NOFY
      RN    =    N
      XOPMM    =    HOPMM  *  (RN-1.0)  +  AOPMM
      FCNOP    =    YGRMM(N)*  YSCALE
```

```
C
       IF (M.NE.1)  GO TO 5
       NQ   =  N/26
       NREM   =  N - (NQ*26)
       IF(NREM.NE.1)  GO  TO  1
       WRITE ( 6,1002 )
 1002 FORMAT (1H1,15HOUTPUT ORDINATE,10X,16HABSCISSA IN MMS.,9X,
     A14HHEIGHT IN MMS.,11X,15HOUTPUT FUNCTION //)
 1     WRITE (6,1003) N,XOPMM,YGRMM(N),FCNOP
 1003 FORMAT (1X,I3,22X,F10.5,15X,F7.2,18X,F11.7 / )
 5     CONTINUE
C
C
       NHALF   =   N/2
       IF (N- (2*NHALF).EQ.0)  GO TO 2
       WEIGHT   =   2.0
       IF (N.EQ.1.OR.N.EQ.NOFY) WEIGHT  =  1.0
       GO  TO  3
 2     WEIGHT   =   4.0
 3     CONTINUE
       C =C+WEIGHT*FCNOP*COS(OMEGA*XOPMM)
       S =S+WEIGHT*FCNOP*SIN(OMEGA*XOPMM)
 102  CONTINUE
       CI   =   C*HOPMM/3.0
       SI   =   S*HOPMM/3.0
       RMODOP   =   SQRT(CI**2 + SI**2 )




       BETA   =  OMEGA* (WDIPMM/2.0)
       FOTRIP = WDIPMM*FCNIP
       IF ( OMEGA.EQ.0.0 )  AREAOP = RMODOP
       FOTRIP   =   AREAOP
       IF(BETA.NE.0.0) FOTRIP = FOTRIP*(SIN(BETA)/BETA)
       RMODIP = SQRT(FOTRIP**2)
       TRFFCN = 6.666666
       IF(RMODIP.NE.0.0) TRFFCN = RMODOP/RMODIP
       IF (M.EQ.1) ZEROTF    =    TRFFCN
       RLVMTF   =   TRFFCN/ZEROTF
       MQ   =  M/26
       MREM   =   M - (MQ*26)
       IF (MREM.NE.1)  GO TO 4
       WRITE (6,1004)
 1004 FORMAT (1H1,9HCYCLES/MM,3X,12HC.I.(OUTPUT),8X,12HS.I.(OUTPUT),8
     A12HMOD.(OUTPUT),8X,11HC.I.(INPUT),9X,12HM.T.FUNCTION,8X,
     B15HRELATIVE M.T.F. //)
 4     WRITE (6,1005) CPMM, CI, SI, RMODOP, FOTRIP, TRFFCN, RLVMTF
 1005 FORMAT (1X,F6.1,6X,6(F11.7,9X) / )
 101  CONTINUE
       STOP
       END
```

APPENDIX III : PHOTOELECTRON FOCUSING

Symbols H magnetic field strength; E electric field strength; L length of a stage; A length of the active region of the last stage; 2F length of the field free region; m and e mass and charge of an electron; $\mathcal{E}$ initial energy of a photoelectron; θ angle of emission to the normal of the photocathode; V_T stage potential.

Photoelectrons describe helical trajectories in uniform electric and magnetic fields. The orbital radius is given by:

$$r_{Phe} = \frac{\sqrt{2m\mathcal{E}}\,\sin\theta}{\sqrt{e}\,H} \qquad \text{(a)}$$

$$r_{Phe} = 3.35\frac{\sqrt{\mathcal{E}}\,\sin\theta}{H}$$ with r_{Phe} in cm, $\mathcal{E}$ in eV & H in Gauss.

while the orbital period is:

$$T_{loop} = \frac{2\pi m}{eH} \qquad \text{(b)}$$

Photoelectrons will focus on the phosphor screen when the magnetic field is adjusted to make the orbital period an integer fraction of the electron transit time in the stage. The latter is, neglecting initial energies of the photoelectrons as compared to the energy they acquire by acceleration ($V_T \gg \mathcal{E}\cos^2\theta$), equal to

$$T_{I\,II} = \sqrt{\frac{2m}{e}}\cdot\frac{L}{\sqrt{V_T}} \qquad \text{(c)}$$

in the first two stages. In the last stage, the transit time equals the sum of the transit time in the active region (length A) and the transit time in the "field free" region (length 2F). Thus :

$$T_{\text{III}} = \sqrt{\frac{2m}{e}}\ \frac{A}{\sqrt{V_T}} + 2F \cdot \frac{\sqrt{m}}{\sqrt{2e\,V_T}} = \sqrt{\frac{2m}{e}} \cdot \frac{A+F}{\sqrt{V_T}} \quad \text{(d)}$$

The transit time is thus equal in all stages if $L = A + F$. (L is the electro-optical length of the last stage).

Focus is obtained if

$$n \cdot \frac{2\pi m}{eH} = \sqrt{\frac{2m}{e}} \cdot \frac{L}{\sqrt{V_T}}$$

or if

$$H = \frac{2\pi^2 m}{e} \cdot n \cdot \frac{\sqrt{V_T}}{L}$$

$$H = 335.19 \cdot n \ \frac{\sqrt{V_T}}{L} \qquad (4.1)$$

where n is an integer or the number or focusing loops. H is expressed in Gauss, V_T in KV and L in cm

APPENDIX IV : ELECTRON - OPTICS OF BACKSCATTERED ELECTRONS

Symbols same as in appendix III ... and ...
ξ initial energy of backscattered electrons relative to the stage potential; θ angle of emission to the normal on the phosphor screen; ψ azimuthal angle of emission; R radius of the working field.

Transit Time of BSE in a Focused Stage:

The transit time of a BSE in the first and second stage is twice the time required for it to come to a stop...

speed = 0 = $$-\frac{V_T}{L}\cdot\frac{e}{m}\cdot t + \sqrt{\frac{2e\xi V_T}{m}}\cdot\cos\theta$$

Thus $$T_{1,2} = 2t = 2\cdot\sqrt{\frac{2m}{e}}\cdot\sqrt{\frac{\xi}{V_T}}\cdot L\cdot\cos\theta \qquad \text{(a)}$$

Using eqn. (III b) and eqn. 4.1, $T_{1,2}$ becomes:

$$T_{1,2} = 2.n.\sqrt{\xi}\cdot\cos\theta\cdot T_{loop} \qquad \text{(II.1)}$$

In the last stage, a BSE first drifts through the field free region during a time

$$t_1 = 2F\sqrt{\frac{m}{2e\xi V_T}}\cdot\frac{1}{\cos\theta} \qquad \text{(b)}$$

and is then brought to a stop after a further time:

$$t_2 = \sqrt{\frac{2m}{e}}\cdot\sqrt{\frac{\xi}{V_T}}\cdot A\cdot\cos\theta \qquad \text{(c)}$$

Therefore the total transit time is

$$T_3 = 2\left(t_1 + t_2\right) = 2\,\frac{2m}{e}\left[\frac{F \quad 1}{\cos\theta\sqrt{\xi V_T}} + A\cos\theta\sqrt{\frac{\xi}{V_T}}\right] \qquad \text{(d)}$$

Using again eqn. (III b) and eqn. 4.1, T_3 becomes

$$T_3 = \frac{2n}{A+F}\left[\frac{F}{\sqrt{\xi}\cos\theta} + A\,\xi\cos\theta\right]T_{loop} \qquad \text{(II.2)}$$

Orbital Radius of BSE in a focused stage

The orbital radius is, from eqn. (III a), given by:

$$r_{BSE} = \frac{\sqrt{2m\xi V_T}\;\sin\theta}{\sqrt{e}\quad H} \tag{e}$$

and substitution of H from eqn. 4.1 gives

$$r_{BSE} = \frac{L}{\pi n}\sqrt{\xi}\;\sin\theta \tag{f}$$

Fraction of BSE (from the centre of the field) contributing to SIB

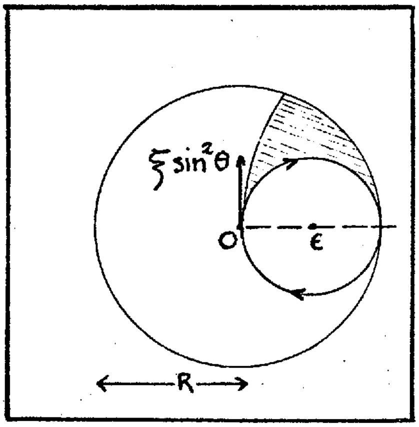

A BSE will remain in the field if the radius R of the field is larger than the diameter of its helical trajectory. Thus if $2r_{BSE} \leqslant R$

Therefore, from eqn. (f), the maximum angle θ_{max} that a BSE can have in order to remain in the working field is:

$$\theta_{max} = \arcsin\frac{\pi n R}{2L\sqrt{\xi}} \tag{g}$$

If a cosine angular distribution of emission of the BSE electrons is assumed (§ II.4.5) then the fraction of BSE that contributes to the background is given by:

$$q = \frac{1}{\pi}\int_0^{2\pi}\int_0^{\theta_{max}} \sin\theta\cos\theta\, d\theta\, d\varphi = \frac{\pi^2 n^2 R^2}{4L^2\xi} \tag{II.3}$$

This relation is a good approximation for BSE leaving the centre of the field. No account was taken of BSE, with low axial initial energy, which land in the shaded region of the above diagram, before half of their first loop is completed.

Point of impact of a BSE

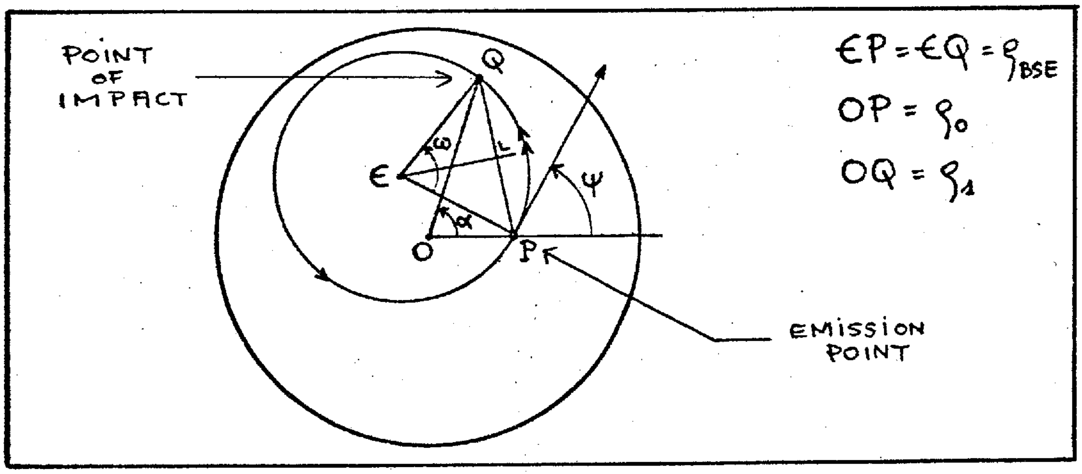

This diagram shows the trajectory of a BSE projected on the phosphor screen. All the distances are relative to the radius of the working field.

In triangle CPM
$$MP = \rho_{BSE} \sin \frac{\omega}{2} \tag{h}$$

In triangle OPQ
$$\rho_1^2 = \rho_0^2 + (2\,MP)^2 - 4\rho_0\, MP \cos\left[\pi - \left(\psi + \frac{\omega}{2}\right)\right] \tag{i}$$

Substitution of eqn. (h) in eqn. (i) gives:

$$\rho_1^2 = \rho_0^2 + 4\rho_{BSE}^2 \sin^2\frac{\omega}{2} + 4\rho_0\rho_{BSE} \sin\frac{\omega}{2} \cos\left(\psi + \frac{\omega}{2}\right) \tag{j}$$

In triangle OPQ
$$(2.MP)^2 = \rho_1^2 + \rho_0^2 - 2\rho_1\rho_0 \cos\alpha \tag{k}$$

Substitution of eqn. (h) in eqn. (k) gives

$$\cos \alpha = \frac{-4 \rho_{BSE}^{2} \sin^{2} \frac{\omega}{2} + \rho_0^{2} + \rho_1^{2}}{2 \rho_0 \rho_1} \qquad (l)$$

and substitution of eqn. (j) in eqn. (l) gives

$$\cos \alpha = \frac{\rho_0 + 2 \rho_{BSE} \sin \frac{\omega}{2} \cos\left(\varphi + \frac{\omega}{2}\right)}{\left[\rho_0^{2} + 4 \rho_{BSE}^{2} \sin^{2} \frac{\omega}{2} + 4 \rho_0 \rho_{BSE} \sin \frac{\omega}{2} \cos\left(\varphi + \frac{\omega}{2}\right)\right]^{1/2}} \qquad (m)$$

The angle $\omega/2$, which is half the angle of rotation of the BSE around the centre of curvature of its trajectory, equals $\pi T / T_{loop}$ where T is the transit time of the BSE in a particular stage. $T_{1,2}$ is given by eqn. II.1 and T_3 by eqn. II.2.

The relative radius $\rho_{BSE} = r_{BSE} / R$ is given by eqn. (f).

Substitution of ρ_{BSE} in eqn. (j) gives, after rearrangement

$$\rho_1 = \frac{1}{n} \left[\xi \left(P \sin \theta \sin B\right)^2 + \left(\rho_0 n\right)^2 + 2 . P . n . \rho_0 \sqrt{\xi} \sin \theta \sin B \cos\left(\varphi + B\right) \right]^{1/2} \qquad (II.22)$$

where $P = 2L/\pi R$, and $B = \omega/2$, which is given by

$$B = 2 \pi n . \sqrt{\xi} . \cos \theta \qquad (II.24)$$

for the first two stages, and by

$$B = \frac{2 \pi n}{A + F} \left[\frac{F}{\sqrt{\xi} \cos \theta} + A \sqrt{\xi} \cos \theta \right] \qquad (II.25)$$

for the last stage.

Computer Program for the calculation of the SIB-index associated to BSE in a single stage.

The principles of calculation are explained in § II.4.6. The language is Fortran IV and the computations were made on the IBM 7094 installation at Imperial College.

```
      DIMENSION   RSUM(10),NC(320,10),FCRZ(20), FCE(16), RNC(320,10)
      NFCRZ = 10
      NFCE = 11
      PIE = 3.141592653
      A = 2.86478
      G = 1.0 / 3.0
      READ (5,5001)    (FCRZ(I),I=1,NFCRZ)
 5001 FORMAT (F7.3)
      READ (5,5002)    (FCE(I), I=1,NFCE)
 5002 FORMAT (  F6.4)
      WRITE (6,5003)
 5003 FORMAT  (1H1)
      WRITE (6,5004)    (I,FCRZ(I), I=1,NFCRZ)
 5004 FORMAT (1H0,5HFCRZ(,I2,1H),4X,F7.3)
      WRITE (  6,5003)
      WRITE (  6,5005)    ( I,FCE(I), I=1,NFCE)
 5005 FORMAT (1H0,4HFCE(,I2,1H),4X,F6.4)
      N = 2
      EN = N
      NI = 0
      DO 1    JP =1,NFCRZ
      P = JP-1
      RZ = 0.05 + P* 0.1
      DO 2    JM =1,NFCE
      RM= JM -1
      E = RM/10.0
      NI = NI+ 1
      DO 12    I= 1,10
      NC(NI, I) =0
 12   CONTINUE
      DO 10           JF =  1,19
      F = JF - 1
      PSI = ( PIE*F)/ 9.5
      DO  11    JT = 1,19
      T = (  2 * JT ) - 1
      THETA = 0.5 * ARCOS (  1.0 -  T/19.0))
      BB = 2.0 * PIE * EN * SQRT(E) * COS(THETA)
      DO  21          KB = 1,11
      FKB = KB - 1
      B = BB * FKB/10.0
      Z=E*((A*SIN(THETA)*SIN(B))**2)+(RZ*EN)**2
     1   +2.0*RZ*EN* SQRT(E)* SIN( THETA)*SIN(B)*A*COS(PSI+B)
```

```
      W = ABS (Z)
      R = SQRT (W) / EN
      IF (R.GE.1.0)      GO TO 11
21    CONTINUE
      IF(R.GE.0.0.AND.R.LE.0.1)    NC(NI, 1) = NC(NI, 1)+1



          DC0495        10050C89                                           DATE
           SABM        -   EFN   SOURCE STATEMENT  -  IFN(S)  -

      IF(R.GT.0.1.AND.R.LE.0.2)    NC(NI, 2) = NC(NI, 2)+1
      IF(R.GT.0.2.AND.R.LE.0.3)    NC(NI, 3) = NC(NI, 3)+1
      IF(R.GT.0.3.AND.R.LE.0.4)    NC(NI, 4) = NC(NI, 4)+1
      IF(R.GT.0.4.AND.R.LE.0.5)    NC(NI, 5) = NC(NI, 5)+1
      IF(R.GT.0.5.AND.R.LE.0.6)    NC(NI, 6) = NC(NI, 6)+1
      IF(R.GT.0.6.AND.R.LE.0.7)    NC(NI, 7) = NC(NI, 7)+1
      IF(R.GT.0.7.AND.R.LE.0.8)    NC(NI, 8) = NC(NI, 8)+1
      IF(R.GT.0.8.AND.R.LE.0.9)    NC(NI, 9) = NC(NI, 9)+1
      IF(R.GT.0.9.AND.R.LE.1.0)    NC(NI,10) = NC(NI,10)+1
11    CONTINUE
10    CONTINUE
      DO 13     III = 1,10
      ZNC = NC (NI,III)
      RNC ( NI, III) = ZNC*FCPZ(JP)*FCE(JM)  /  361.0
13    CONTINUE
      IF ((NI-(NI/25)*25).NE.1)    GO TO 101
      WRITE (6,1001)    (I,I=1,10)
1001  FORMAT (1H1,2HRZ,6X,1HE,2X,10(3X,1H(,I2,1H),5X))
101   CONTINUE
      WRITE (6,1002)   RZ,E,  (RNC(NI,I),  I= 1,10)
1002  FORMAT (1H0,F5.2,2X,F4.1,10(3X,F9.4))
2     CONTINUE
1     CONTINUE
      DO 3  I=1, 10
      RSUM  (I)  =0
      DO 4    J=1,NI
      RSUM  (I)  = RSUM(I) + RNC(J,I)
4     CONTINUE
3     CONTINUE
      WRITE  (6,1003)    (RSUM  (I)  , I=1,10)
1003  FORMAT (  1H0/1H0,5X,  6HTOTALS,10(3X,F9.4))
      STOP
      END
```

APPENDIX V: LIST OF PRODUCTS AND MANUFACTURERS

This list refers to indices in Chapter 5.

a.	Mica Sheets	Ruby mica (B.Q)	3M Ltd. - Germany
b.	Solder glass	Type X88	Glass Tubes & Co.Ltd. - UK.
c.	Bright Platinum	Type GA	Johnson Matthews Ltd. - UK.
d.	Phosphor Powder	Type MA214(MAP)	EMI Ltd. - UK
e.	Filming solution	Type D	EMI Ltd. - UK
f.	Glass tubing	-----	Jencons Sc. Ltd. - UK
g.	Tungsten tapes	-----	Goodfellow Metals Ltd. - UK
h.	Platinum paste	Type T177	Johnson Matthews Ltd. - UK
j.	Silver paste	Type FSP411,412	" " " "
k.	Nimonic	Type 90	Henry Wiggen Ltd. - UK
l.	Inconel(soft)	Type 600	Gilby Brunton Ltd. - UK
m.	Inconel(hard)	Type 1/8	" " " "
n.	Resistors	Type GB	Allen Bradley Ltd. - USA
p.	Black paint	VALSPAR SG	Goodlass Ltd. - UK
q.	Silica window	Spectrosil B	The Thermal Syndicate - UK
r.	Resin	Type BP 4116	BIP Chemicals Ltd. - UK
s.	HV cable	uniradio Type 39	Radio Spares - UK
t.	Primer	Type MS 2650	Midland Silicones Ltd. - UK
v.	Silicone rubber	Type 9161	" " " "

ACKNOWLEDGEMENTS

The author would like to express his gratitude to Professor J.D. McGee for his interest and guidance throughout this work.

It is also a pleasure to thank Mr. R.W. Airey for his continuous assistance, and Mr. H. Băčik, Dr. B.L. Morgan, Dr. E. Kahan and Mr. M. Cohen for their help and stimulating interest in this work.

Technical co-operation, assistance and suggestions from Messrs. G.L. Busby, B. Weekley, R. Ranger, J. Beseigel, R. Barr and J. Osborn were gratefully received.

The author wishes to acknowledge the receipt of a British Council Scholarship for a period of eighteen months.

REFERENCES

Abroyan, I.A., Mounin, S.M. (1961) Sov. Phys. Solid State, 3, 416.

Abroyan, I.A., Lavrov, V.P. (1963) Sov. Phys. Solid State, 4, 2382.

Adams, J. (1962) Adv. in Elec. and El. Phys.* 22, 139.

Adams, J., Manley, B.W. (1966) IEEE Trans. Nucl. Sci. 13, 88.

Adams, J., Manley, B.W. (1967) Philips Tech. Rev. 28, 156.

Airey, R.W. (1964) Brit. Pat. Appl. No. 2060/64.

Airey, R.W. (1970-71) Private communications.

Angot, A. (1961) Compléments de Mathématiques, Editions Revue d'Optique, Paris.

Aslam, M. (1965) PhD Thesis, University of London.

Aslam, M., Bartolini, L., Haber, R. (1971) Rev. Sci. Instr. 42, 519.

Bǎćik, H. (1970-71) Private communications.

Backwill, J.T., Folkes, J.R. (1959) Brit. Pat. Appl. No. 23148/59.

Baldwin, G.C., Friedman, S.I. (1965) Rev. Sci. Instr. 36, 16.

Barr, W.E., Anhorn, V.J. (1949) Scientific Glass Blowing Inst. Publ. Co. Pittsburg.

Baum, W.A. (1962) Adv. in Elec. and El. Phys.* 16, 391.

Bayford, L.J. (1952) Proc. I.E.E. 99, 516.

Beckman, J.E. (1966) Adv. in Elec. and El. Phys.* 22, 369.

Bied-Charreton, P., Bijaoui, A., Duchesne, M., Le Contel, J.M. (1969) Adv. in Elec. and El. Phys.* 28, 27.

Binnie, D.M., Jane, M., Newth, J.A., Potter, D.C. (1963) Nucl. Inst. and Methods, 20, 221.

Born, M., Wolf, E. (1959) Principles of Optics, Pergamon Press, London.

Bril, A., Klassens, H.A. (1952) Philips Res. Rep. 7, 401.

Bulpitt, C.J., Dollery, C.T. (1970) Brit. Kinematography Sound and Telev. Jan 14.

Burcham, W.E. (1963) Nuclear Physics, Longmans, London.

Burns, J., Neuman, M.J. (1960) Adv. in Elec. and El. Phys.* 12, 97.

Catchpole, C.E. (1962) Adv. in Elec. and El. Phys.* 16, 567.

Catchpole, C.E. (1963) PhD thesis, University of London.

Catchpole, C.E. (1966) Adv. in Elec. and El. Phys.* 22, 425.

Charman, W.N., Hewitt, A.V. (1966) Adv. in Elec. and El. Phys.* 22, 101.

Charman, W.N. (1969) Adv. in Elec. and El. Phys.* 28, 705.

Charrier, S., Wlerick, G. (1962) Adv. in Elec. and El. Phys.* 16, 5.

Cohen, M. (1969) Private communication.

Collings, P.R., Beyer, R.R., Kalafut, J.S., Gaetze, G.W. (1969) Adv. in Elec. and El. Phys.* 28, 105.

Coltman, J.W. (1954) J.O.S.A. 44, 468.

Combee, B., Botden, P.J.M., Kuhl, W. (1971) in Photoelectric Imaging Devices, ed. by L.M. Biberman and S. Nudelman, Plenum Press, N.Y. 2, p.149.

Combes, M., Felenbock, P., Guerin, J., Picat, J.P. (1969) Adv. in Elec. and El. Phys.* 28, 39.

Compton, A.H., Allison, S.K. (1948) X-rays in theory and experiments, Van Nostrand, N.Y.

Cranstoun, G.K.L. (1969) Adv. in Elec. and El. Phys.* 28, 875.

Cromwell, R.H. (1969) Optical Sciences, Tech. Rep. 38, University of Arizona, Austin, Tx., USA.

Crowe, K.R., Gummick, J.L. (1967) Appl. Phys. Letters 11, 249.

Csorba, I.P. (1969) R.C.A. Rev. 30, 36.

Davis, E.J. (1958) J. Sci. Instr. 35, 308.

Davis, E.J. (1959) PhD Thesis, University of London.

Davis, G.P. (1962) Adv. in Elec. and El. Phys.* 16, 119.

Decker, R.W., Mestwerdt, H (1969) Adv. in Elec. and El. Phys.* 28, 19.

Decker, R.W. (1969) Adv. in Elec. and El. Phys.* 28, 357.

de Haan, E.F., van der Drift, A. (1964) Philips Tech. Rev. 25, 136.

Dietz, L.A., Hanrahan, L.R., Hance, A.B. (1967) Rev. Sci. Instr. 38, 176.

Dolizy, P., Legoux, R. (1969) Adv. in Elec. and El. Phys.* 28, 367.

Dollery, C.T., Hodge, J.V., Engel, M. (1962) Brit. Med. J. 2, 1210.

Dollery, C.T. (1970) Private communication.

Dolon, P.J., Niklas, W.F. (1961) Image Intensifier Symposium, NASA, Fort Belvoir, Va. p.93.

Duchesne, M. (1962) Adv. in Elec. and El. Phys.* 16, 27.

Duchet, M. (1966) Adv. in Elec. and El. Phys.* 22, 499.

Dushman, S. (1958) Vacuum Techniques, J. Wiley and Sons, London.

Eberhardt, E.H. (1968) Appl. Optics 7, 2037.

Eckart, F. (1954) Ann. Phys. 14, 98.

Ehrenberg, W., Franks, J. (1953) Proc. Phys. Soc. 66, 1057.

Ehrenberg, W., King, D.E.N. (1963) Proc. Phys. Soc. 81, 751.

Emberson, D.L., Todkill, A., Wilcock, W.L. (1962) Adv. in Elec. and El. Phys.* 16, 127.

Emberson, D.L. (1966) Adv. in Elec. and El. Phys.* 22, 129.

(E.M.I. data) (1969) Photocathodes. 30M/6-67 (PMT).

Engstrom, R.W. (1947) J.O.S.A. 37, 420.

Epstein, D.W., Pensak, L. (1946) R.C.A. Rev. 7, 5.

Eschard, G., Graf, J. (1969) Adv. in Elec. and El. Phys.* 28, 1969.

Essig, S.F. (1960) Adv. in Elec. and El. Phys.* 12, 1960.

Felgett, P.B. (1956) The Present and Future of the Telescope of Moderate Size, Ed. F.B. Wood, University of Pennsylvania Press, P.51.

Felgett, P.B. (1958) Monthly Notices, R.A.S., 118, 223.

Filby, R.S. (1967) PhD Thesis, University of London.

Flinn, E.A. (1962) Adv. in Elec. and El. Phys.* 16, 155.

Ford, W.K. Jr. (1966) Adv. in Elec. and El. Phys.* 22, 697.

Francis, G.W., Stoudenheimer, R.G. (1960), Rev. Sci. Instr. 31, 1246.

Fry, T.C. (1929) Probability and its Engineering Uses, Van Nostrand, N.Y.

Garbe (1963) Vakuum Technik 12, 201.

Garlick, G.E.J. (1949) Luminescent Materials, Clarendon Press, Oxford.

Gaucher, F.S. (1950) Phys. Rev. 78, 816.

Giese, R., Gildermeister, O., Schuster, G. (1969) Adv. in Elec. and El. Phys.* 28, 919.

Gildermeister, O., Giese, R. (1962) Adv. in Elec. and El. Phys.* 16, 113.

Glaser, A., Henneberg, W. (1935) Z. Tech. Physik, 16, 229.

Goetze, G.W. (1962) Adv. in Elec. and El. Phys.* 16, 145.

Goetze, G.W. (1969) Adv. in Elec. and El. Phys.* 28, 219.

Gomer, R. (1961) Field Emission and Field Ionization, Havard University Press, Cambridge, Mass.

Gorlich, P. (1936) Z. Physik 101, 335.

Habel, R. (1966) Alta Frequenza 35, 197.

Hachenberg, O., Braver, W. (1959) Adv. in Elec. and El. Phys.* 11, 413.

Handbook of Physics (1955) 36th Edition. Chemical Rubber Publ. Co. Cleveland.

Hiltner, W.A. (1956) The Present and Future of the Telescope of Moderate Size, Ed. F.B. Wood, University of Pennsylvania Press, p.11.

Hiltner, W.A., Pesh, P. (1960) Adv. in Elec. and El. Phys.* 12, 17.

Hiltner, W.A., Niklas, W.F. (1962) Adv. in Elec. and El. Phys.* 16, 37.

Holliday, J.E., Sternglass, E.J. (1957) J. Appl. Phys. 28, 1189.

Hopmann, W. (1966) Adv. in Elec. and El. Phys.* 22, 591.

(Ilford data) (1962) photographic plates

Irendale, P. (1964) IEEE Trans. Nucl. Sci. 11, 139.

(I.T.T. data) (1971) ERMA-cathodes. ITT, Easton, Pa.

(JEDEC) (P-) (1960) E.I.A. Publication No.16.

(JEDEC) (S-) (1964) E.I.A. Publication No. 50.

Jedlička, M. (1966) Czech. J. Phys. 16, 132.

Jedlička, M. (1969) Adv. in Elec. and El. Phys.* 28, 323.

Jeffers, S. (1968) PhD Thesis, University of London.

Jones, L.W., Loo, B.W. (1966) Adv. in Elec. and El. Phys.* 22, 813.

Jones, R.C. (1955) Phot. Sci. and Eng. 2, 56.

Jones, R.C. (1958) Phot. Sci. and Eng. 2, 57.

Jones, R.C. (1959) Adv. in Elec. and El. Phys.* 11, 88.

Kahan, E., Cohen, M. (1969) Adv. in Elec. and El. Phys.* 28, 725.

Kanter, H. (1957) Ann. Physik 20, 144.

Kanter, H. (1961) Westinghouse Res. Labs. Sc. paper 112 - BOO - PI.

Kapany, N.S. (1961) Image Intensifier Symposium, NASA, Fort Belvoir, Va, p.143.

Kapany, N.S. (1967) Fibre Optics, Principle and Applications. Academic Press, N.Y.

Kazan, B. (1957) Proc. I.R.E. 45, 1358.

Khogali, A. (1964) PhD Thesis, University of London.

Kidger, M.J. (1969) Private communication.

Kiepenheur (1934) Die Sterne 9, 190.

Klassens, H.A., Ramsden, W., Chow Quantie (1948) J.O.S.A. 38, 60.

Klemperer, O. (1953) Electron Optics, Cambridge University Press.

(Kodak data) (1961) Wratten Filters.

(Kodak data) (1962) Photographic Plates, Publ. P-9.

Kohner, E.M., Bulpitt, C.J., Dollery, C.T. (1968) Hospital Medicine, April 858.

Koller, L.R. (1930) Phys. Rev. 36, 1639.

Koller, L.R, Alden, E.D. (1951) Phys. Rev. 83, 684.

Krizek, V., Vand, V. (1946) Electr. Engng. 18, 316.

Kroon, D.J. (1968) Laboratory Magnets, Philips Tech. Library, Eindhoven.

Kron, G.E. (1962) Adv. in Elec. and El. Phys.* 16, 25.

Kron, G.E., Papiashvili, I.I. (1966) Adv. in Elec. and El. Phys.* 22, 59.

Kron, G.E., Ables, H.D., Hewitt, A.V. (1969) Adv. in Elec. and El. Phys.* 28, 1.

Lallemand, A. (1936) C.R. Acad. Sci. (Paris) 203, 243.

Lallemand, A., Duchesne, M., Wlerick, G. (1960) Adv. in Elec. and El. Phys.* 12, 5.

Lallemand, A. (1962) Adv. in Elec. and El. Phys.* 16, 1.

Lallemand, A. (1966) Adv. in Elec. and El. Phys.* 22, 1.

Lamberts, R.L., Higgins, G.C., Wolfe, R.W. (1958) J.O.S.A. 48, 487.

Lasof, S. (1947) Phys. Rev. 72, 165.

Law, R.R. (1939) Proc. I.R.E. 27, 511.

Lawrence, E.O., Beams, J.W. (1930) Phys. Rev. 36, 482.

Lawrence, E.O., Linford (1942) Photoelectric Phenomena by Hughes and Dubridge, McGraw Hill, N.Y.

Lehmann, W. (1958) J.O.S.A. 48, 647.

Leverenz, H.W. (1950) Luminescence of Solids; J.Wiley and Sons, Inc. N.Y.

Livingstone, W.C., Lynds, C.R., Doe, L.A. (1966) Adv. in Elec. and El. Phys.* 22, 705.

Longini, R.L. (1949) J.O.S.A. 39, 877.

Malherbe, A., Tessier, M., Veron, S. (1966) Adv. in Elec. and El. Phys.* 22, 1966.

Mandel, L. (1959) Brit. J. of Appl. Phys. 10, 233.

Manley, B.W., Guest, A., Holmshaw, R.T. (1969) Adv. in Elec. and El. Phys.* 28, 471.

Martin, S.T., Headrick, L.B. (1939) J. Appl. Phys. 10, 116.

Matskevitch (1957) Sov. Phys. Tech. Phys. 2, 255.

McGee, J.D. (1955) Arch. Elektr. Ubert. 9, 355.

McGee, J.D. (1956 A) The Present and Future of the Telescope of Moderate Size. Ed. F.B. Wood, University of Pennsylvania Press, P.31.

McGee, J.D. (1956 B) Brit. Pat. Appl. No. 9796/56.

McGee, J.D., Flinn, E.A., Evans, H.D. (1960) Adv. in Elec. and El. Phys.* 12, 87.

McGee, J.D., Wheeler, B.E. (1962) Adv. in Elec. and El. Phys.* 16, 47.

McGee, J.D., Khogali, A., Ganson, A., Baum, W.A. (1966 A) Adv. in Elec. and El. Phys.* 22, 11.

McGee, J.D., Airey, R.W., Aslam, M., Powell, J.R., Catchpole, C.E. (1966 C) Adv. in Elec. and El. Phys.* 22, 113.

McGee, J.D., Aslam, M., Airey, R.W. (1966 D) Adv. in Elec. and El. Phys.* 22, 407.

McGee, J.D., Airey, R.W., Aslam, M. (1966 E) Adv. in Elec. and El. Phys.* 22, 571.

McGee, J.D., McMullan, D., Bǎćik, H., Oliver, M. (1969 A) Adv. in Elec. and El. Phys.* 28, 61.

McGee, J.D., Airey, R.W., Varma, B.P. (1969 B) Adv. in Elec. and El. Phys.* 28, 89.

McGee, J.D. 1970-71. Private communication.

McMullan, D., Oliver, M. (1968) J. Sci. Instr. (E) 1, 1255

McMullan, D. (1970) Private communication.

McNall, J., Robinson, L., Wampler, E.J. (1970) Publ. Astron. Soc. Pacif. 82, 837.

Mees, K.C., James, T.H. (1966) The Theory of the photographic process. MacMillan Publ. Co. N.Y.

Meyer, V.D. (1970) J. Appl. Phys. 41, 4059.

Miller, K.S. (1956) Engineering Mathematics, Dover Publ. Inc. N.Y.

Montgomery, D.B. (1969) Solenoid Magnet Design. Wiley Inter Science, N.Y.

Moon, P. (1961) The Scientific Basis of Illuminating Engineering. Dover Publ. Inc. N.Y.

Morton, G.A. (1955) Trans. I.A.U. 9, 679.

Morton, G.A., Smith, H.M., Wasserman, (1967) IEEE Trans. Nucl. Sci. 14, 443.

Muller, E.W. (1941) Naturwissen schafter, 29, 533.

Muller, E.W. (1960) Adv. in Elec. and El. Phys.* 13, 83.

Murray, R.B., Manning, J.J. (1960) I.R.E. Trans. Nucl. Sci. 7, 80.

Musson-Genon, R. (1946) C.R. Acad. Sci. (Paris), 222, 1946.

Nail, N.R., Urback, F., Pearlan, D. (1949) J.O.S.A. 39, 690.

Novotny, H.D., Alvis, D.L. (1961) Circulation. 24, 82.

Oliver, M.B., (1970) PhD thesis, University of London.

Orvin, L.T. (1934) Brit. Pat. No. 445, 156.

Petzel, B. (1965) Phys. Status. Solidi 12, 103.

(Philips) (1928) Philips Gloeilampen Fabrieken, Brit. Pat. Appl. No. 326.200

Pniewski, J. (1951) Acta Physica Polonica 11, 230.

Polkosky, J.J. (1951) U.S. Patent No. 2,676,282.

Powell, J.R. (1967) PhD Thesis, University of London.

Powell, J.R., Trumbo, D.E., Lynds, C.R. (1969) Publ. Astron. Soc. Pacif. 81, 601.

Pyatnitzkii, A.I. (1957) Radioteknika i Electr. 2, 714.

Randall, R.P. (1966) Adv. in Elec. and El. Phys.* 22, 87.

Randall, R.P. (1969) Adv. in Elec. and El. Phys.* 28, 713.

Randall, R.P. (1970) EMI Report R/S 014 V 70.

(R.C.A.) (1961) RCA Report DH 44009, Eng. 4590.

(R.C.A.) (1963) RCA Manual, Tech. PT-60.

(R.C.A. data) (1962) Phosphors TPM-1508 A.

Redhead, P.A., Hobson, J.P. and Kornelsen, E.V. (1968) The Physical Basis of U.H.V. Chapman and Hall, London.

Reynolds, G.T. (1964) IEEE Trans. Nucl. Sci. 11, 147.

Reynolds, G.T. (1966 A) Appl. Optics, 5, 577.

Reynolds, G.T. (1966 B) Adv. in Elec. and El. Phys.* 22, 71.

Rhoads, H.U., Weber, A.H. (1962) Rev. Sci. Instr. 33, 250.

Roberts, A. (1960) Adv. in Elec. and El. Phys.* 12, 135.

Rose, A., Weimar, P.K., Law, H.B. (1946) Proc. IRE 34, 424.

Rose, A. (1948 A) Adv. in Elec. and El. Phys.* 1, 131.

Rose, A. (1948 B) J.O.S.A., 38, 196.

Rosebury, Fr. (1964) Handbook of Electron Tube and Vacuum Techniques. Addison-Wesley Publ. Co. Mass. U.S.A.

Sackinger, W.M., Johnson, J.M. (1969) Adv. in Elec. and El. Phys.* 28, 487.

Sauter, F. (1949) Z. Naturforsche 4, 682.

Schaffernicht, W. (1948) Electronics 1, 96.

Schön, H. (1942) Zeits. fur Physik 119, 463.

Shalabutov, Iu.K., Maslennikova, N.A. (1957) Sov. Physics. Techn. 1, 1137.

Shaw, R. (1962) Phot. Sci. and Eng. 6, 281.

Shaw, R. (1963) J. Phot. Sci. 11, 199.

Shaw, R. (1965) J. Phot. Sci. 13, 308.

Slark N.A., Woolgar, A.J. (1962) Adv. in Elec. and El. Phys.* 16, 141.

Smith, R. (1968) PhD Thesis, University of London.

Sommer, A.H. (1955) Rev. Sci. Instr. 26, 725.

Sommer, A.H. (1968) Photoemmisive Materials, J. Wiley and Sons, N.Y.

Spencer, H.E. (1958) Phys. Rev. 109, 1074.

Spicer, W.E. (1958) Phys. Rev. 112, 114.

Sternglass, E.J. (1954) Phys. Rev. 95, 345.

Stoudenheimer, R.G. (1960) Adv. in Elec. and El. Phys.* 12, 41.

Stoudenheimer, R.G. (1961) Image Intensifier Symposium, Fort Belvoir, Va. USA p. 35.

Szepesi, Z., Novice, M. (1969) Adv. in Elec. and El. Phys.* 28, 1087.

Theodorov, D.G. (1966) Adv. in Elec. and El. Phys.* 22, 477.

Tolan, J.H. (1958) Phot. Sci. and Eng. 2, 154.

Trump, G.T., van de Graaff (1947) J. Appl. Phys. 18, 327.

Urbach, F., Urbach, A., Schwartz, M. (1947) J.O.S.A. 37, 122.

Varma, B.P. (1968) PhD Thesis, University of London.

(Varo data) (1971) S-25 cathode. Varo Inc. Garland, Texas.

Wallis, G., (1956) Ann. Physik. 17, 401.

Watchtel, M.M., Doughty, D.D., Goetze, G., Anderson, A.E., Sternglass, E.J., (1960) Rev. Sci. Instr. 31, 576.

Waters, J.R., Reynolds, G.T., Scarl, D.B., Zdanis, R.E. (1962) IRE Trans. Nucl. Sci. 9, 239.

Weimer, P.K., Forque, S.V., Goodrich, R.R. (1950) Electronics 23, 70.

(Westinghouse data) (1964) Phosphors. ETD-6101.

Westlake, J. (1970) Private communication.

Whitmell, D.S., Southon, M.J. (1966) Adv. in Elec. and El. Phys.* 22, 903.

Wilcock, W.L., Emberson, D.L., Weekley, B. (1960) Trans. IRE. Nucl. Sci. 7, 126.

Wilcock, W.L. (1964) Private communication in Khogali (1964).

Wilcock, W.L. (1966 A) Adv. in Elec. and El. Phys.* 22, 629.

Wilcock, W.L. (1966 B) Adv. in Elec. and El. Phys.* 22, 535.

Wilcock, W.L., Miller, D.E. (1969) Adv. in Elec. and El. Phys.* 28, 513.

Wilks, R.J., Mallard, J.R. (1967) Phys. Med. Biol. 12, 251.

Wlérick, G., Grosse, A. (1966) Adv. in Elec. and El. Phys.* 22, 465.

Wooten, F. (1966) J. Appl. Phys. 37, 2965.

Wynne, C.G., Kidger, M.J. (1969) Adv. in Elec. and El. Phys.* 28, 759.

Zavoiskii, E.K., Butslov, M.M., Smolkin, G.E. (1956) Sov. Phys. Dokl. 1, 743.

Zheludeva, G.A. (1962) Radio. Eng. Electronic. Phys. 7, 1525.

Zworykin, V.K., Morton, G.A., Ramberg, E.G., Hillier, J., Vance, A.W. (1945) Electron Optics and Electron Microscope, J. Wiley and Sons, N.Y.

Zworykin, V.K., Ramberg, E.G. (1949) Photoelectricity and Applications, J. Wiley and Sons, N.Y.

Zworykin, V.K., Morton, G.A. (1954) Television. J. Wiley and Sons, N.Y.

---

* "Advances in Electronics and Electron Physics" are edited by L. Marton.

Proceedings of the symposii on Photo-Electronic Image Devices:

12 (First Symposium) ed. by J.D. McGee and W.L. Wilcock.

16 (Second Symposium) ed. by J.D. McGee, W.L. Wilcock and L. Mandel.

22 (Third Symposium) ed. by J.D. McGee, D. McMullan and E. Kahan.

28 (Fourth Symposium) ed. by J.D. McGee, D. McMullan, E. Kahan and B.L. Morgan.

Academic Press, New York and London.